

7-10-2013

Spectroscopic and Computational Electronic Structure Studies of Donor-Acceptor Systems

Diana Habel-Rodriguez

Follow this and additional works at: https://digitalrepository.unm.edu/chem_etds

Recommended Citation

Habel-Rodriguez, Diana. "Spectroscopic and Computational Electronic Structure Studies of Donor-Acceptor Systems." (2013). https://digitalrepository.unm.edu/chem_etds/28

This Dissertation is brought to you for free and open access by the Electronic Theses and Dissertations at UNM Digital Repository. It has been accepted for inclusion in Chemistry ETDs by an authorized administrator of UNM Digital Repository. For more information, please contact disc@unm.edu.

Diana Habel-Rodriguez

Candidate

Chemistry and Chemical Biology

Department

This dissertation is approved, and it is acceptable in quality and form for publication:

Approved by the Dissertation Committee:

Dr. Martin L. Kirk, Chairperson

Dr. Susan R. Atlas

Dr. Hua Guo

Dr. Richard A. Kemp

**SPECTROSCOPIC AND COMPUTATIONAL
ELECTRONIC STRUCTURE STUDIES
OF DONOR-ACCEPTOR SYSTEMS**

by

DIANA HABEL-RODRIGUEZ

B.S. Biology, B.S. Chemistry, University of New Mexico, 2003

DISSERTATION

Submitted in Partial Fulfillment of the
Requirements for the Degree of

**Doctor of Philosophy
Chemistry**

The University of New Mexico
Albuquerque, New Mexico

May, 2013

DEDICATION

To my parents, Eberhard and Petra,

To my husband, Marco,

To my grandparents Lotte, Margarete, Günther, and Waldemar,

To my great-aunt, Johanna.

ACKNOWLEDGEMENTS

I would like to thank the people that have given me their advice and support for this work. I want to thank my graduate advisor, Prof. Martin L. Kirk, for his patience, enthusiasm for our work, advice on our research, and valuable discussions of the data, as well as for his financial support. I would like to thank the members of my graduate committee, Prof. Susan R. Atlas, Prof. Hua Guo and Prof. Richard A. Kemp, for their time and advice on the completion of my doctoral thesis.

My thanks also go to the past and current graduate students and postdoctoral fellows of Prof. Kirk's research group, who have been very supportive over the years: Dr. Sushilla Z. Knottenbelt, Dr. Nick Rubie, Meita Fulton, Antonio William, Dr. Abebe Berhane, Dr. Regina Peter Mtei, Dr. Joseph Sempombe, Dr. Jing Yang, Benjamin W. Stein, Chao Dong, Dominic Kofl Kersi, and Dr. Logan J. Giles. Thank you for your support: you have helped me with your suggestions for experimental procedures or computational methods, with our discussions of the research results in meetings and group meeting, with running of the instruments with me when I was unfamiliar, and with being another pair of hands when I needed help in the lab.

I would like to acknowledge and thank our collaborators without whom a large part of my research would not have been possible. Prof. Charles G. Young and his students from the University of Melbourne synthesized the MoSCu model compounds and provided them to us, obtained crystallographic data and room temperature EPR for the compounds. Prof. David A. Shultz and his students from North Carolina State University synthesized the donor-bridge-acceptor biradical compounds and provided

them to us. They have also obtained crystallographic data, magnetic susceptibility data, room temperature electronic absorption and EPR spectra. Dr. Alfred Sattelberger from Argonne National Laboratories, and Dr. Frederic Poineau and Erick V. Johnstone from the University of Nevada have synthesized the $\text{Re}_2\text{X}_4\text{P}(\text{Me}_3)_4\text{PF}_6$ compounds and provided them to us, and also obtained room temperature electronic absorption spectra. We have also had shared discussions of our (our collaborator's and our group's) research results with all our collaborators on the respective research problems.

I gratefully acknowledge the friendly help and support from the Center for Advanced Research Computing (CARC) at UNM, who set up and maintained the multi-node clusters that were used for the majority of the DFT calculations in my work, as well as installed the appropriate computational codes and resolved numerous help requests. In particular I would like to acknowledge Prof. Susan Atlas for her time and support.

I thank the Department of Chemistry and Chemical Biology at UNM for the opportunity to be a part of the graduate program and financial support. I would also like to thank the graduate coordinator Karen McElveny for her patience and help, as well as Dr. Sylvie Pailloux for teaching me the fractional distillation of butyronitrile, and Prof. Dave Tierney for training us on the X-band and Q-band EPR and providing us with help and advice on EPR experiments. I would like to thank the IGERT fellowship that has provided financial support for me, as well as additional training for my research, and the program coordinator, Heather Armstrong, for her friendly support of the students in the IGERT program.

Last, but not least, I want to thank my family for their support and encouragement, in particular my husband Marco V. Rodriguez, my mother Petra Habel, my father Eberhard Habel, my grandparents Lotte Mehlhose, Margarete Habel and Günther Habel, and my great aunt Johanna Brückner. Without you I would not have had this opportunity.

**SPECTROSCOPIC AND COMPUTATIONAL ELECTRONIC
STRUCTURE STUDIES OF DONOR-ACCEPTOR SYSTEMS**

by

Diana Habel-Rodriguez

B.S. Biology, B.S. Chemistry, University of New Mexico, 2003

Ph.D. Chemistry, University of New Mexico, 2013

ABSTRACT

Three molecular systems have been studied, which exhibit strong intramolecular electronic communication between constituent moieties. Experimental results for electronic absorption, resonance Raman, electron paramagnetic resonance (EPR), and magnetic circular dichroism (MCD) spectroscopies are presented. Density functional theory (DFT) electronic structure calculations were employed to augment the interpretation of experimental results. Using a valence bond configuration interaction (VBCI) model we show that the ground state properties of the molecules are influenced by excited state configurations.

Donor (= semiquinone)-bridge-acceptor (= nitronylnitroxide) biradicals show strong ferromagnetic donor-acceptor coupling, and contributions to the ferromagnetic coupling from spin delocalization and spin polarization mechanisms are discussed. We explore effects of bridge substitutions on donor-acceptor coupling, where the bridge can be phenyl, thiophene, biphenyl, bithiophene, xylene, or other sterically hindered phenyl-derivatives. Meta connectivity of the Donor and Acceptor on a phenyl bridge results in antiferromagnetic donor-acceptor coupling, while para connectivity results in

ferromagnetic exchange coupling. In this dissertation we discuss in detail the mechanisms for the observed exchange coupling.

The heterobimetallic active site of the carbon monoxide dehydrogenase (CODH) enzyme catalyzes the oxidation of carbon monoxide to carbon dioxide in presence of water. Mechanisms presented in the literature differ in their description of how the [MoSCu] unit functions to catalyze CO oxidation. Computational and spectroscopic studies of synthetic CODH active site models show that electronic transitions below $\sim 27000\text{ cm}^{-1}$ are Cu \rightarrow Mo charge transfer in nature, and the observation of large isotropic Cu hyperfine coupling to the Mo(V) confirms the importance of Cu \rightarrow Mo charge transfer excited states to covalency within the [MoSCu] unit. The large covalency across the [MoSCu] unit in both the enzyme and models points to a likely role of the [MoSCu] unit in the transfer of electrons between CO and Mo(VI). Calculated geometric and electronic changes for CO binding to the Cu(I) site are discussed.

The $\text{Re}_2\text{X}_4(\text{PMe}_3)_4\text{PF}_6$ compounds (X = Cl, Br) are highly symmetric Re dimers with a bond order of 3.5 that includes a partial δ bond. Spectroscopic and computational data of the $\delta \rightarrow \delta^*$ band show that the contribution of the δ bond to the Re-Re bonding is small. Bonding calculations show that antibonding interactions of the halide and trimethylphosphine ligands with the Re d-orbital manifold dictate the energetic ordering of the Re d-orbitals.

TABLE OF CONTENTS

LIST OF FIGURES	xiii
LIST OF TABLES.....	xxi
1. INTRODUCTORY REMARKS.....	1
1.1 Valence Bond Configuration Interaction	1
1.2 Robin-Day Classification.....	7
2. SPECTROSCOPIC AND COMPUTATIONAL STUDIES OF DONOR-BRIDGE-ACCEPTOR BIRADICALS AND (EXTENDED) MOLECULAR ASSEMBLIES UTILIZING DONOR-BRIDGE- ACCEPTOR BIRADICALS.....	11
2.1 Introduction.....	11
2.2 Experimental Details.....	17
2.2.1 Electronic Structure Calculations	17
2.2.2 Electron Paramagnetic Resonance Spectroscopy (EPR)	19
2.2.3 Variable-Temperature Electronic Absorption.....	20
2.2.4 Resonance Raman Spectroscopy	23
2.3 Extending Previous Studies on $\text{Tp}^{\text{Cum,Me}}\text{Zn}(\text{SQ-Ph-NN})$	25
2.3.1 Strong Acceptor-Bridge Interactions	26
2.3.2 Spin Polarization and Spin Delocalization	32
2.3.2.1 Spin Polarization on Allyl- and the Nitronyl Nitroxide Radical ..	32
2.3.2.2 Donor-Bridge-Acceptor Bond Torsions and the Resulting Spin Density Distributions	34
2.3.2.3 Correlation Between DFT Calculated Spin Densities, Experimental Nitrogen Hyperfine Coupling Constants, and Magnetic Susceptibility Data	40
2.3.3 Excited States and Excited State Distortions: TD-DFT Band Assignments, the Nature of the DA-CT Band and Bridge During the DA-CT Transition	45
2.4 Changing the Electronic Nature of the Bridge: Replacing Phenylene with Thiophene	52
2.4.1 Frontier Molecular Orbitals, Spin Density Distribution, and the Molecular Orbital Diagram for $\text{Tp}^{\text{Cum,Me}}\text{Zn}(\text{SQ-Thp-NN})$	53
2.4.2 Electronic Absorption Spectra and TD-DFT Band Assignments for $\text{Tp}^{\text{Cum,Me}}\text{Zn}(\text{SQ-Thp-NN})$	59
2.4.3 Resonance Raman Spectra and DFT Frequency Calculations for $\text{Tp}^{\text{Cum,Me}}\text{Zn}(\text{SQ-Thp-NN})$	62
2.5 Extending the Length of the Bridge: Biphenyl and Bithiophene.....	67
2.5.1 Maintaining Ferromagnetic Coupling Over Longer Distances.....	67
2.5.2 Frontier Molecular Orbitals and Orbital Compositions for $\text{Tp}^{\text{Cum,Me}}\text{Zn}(\text{SQ-Thp}_2\text{-NN})$ and $\text{Tp}^{\text{Cum,Me}}\text{Zn}(\text{SQ-Ph}_2\text{-NN})$	72
2.5.3 Room-Temperature Electronic Absorption Spectra, Time-Dependent DFT Results and Band Assignments for $\text{Tp}^{\text{Cum,Me}}\text{Zn}(\text{SQ-Thp}_2\text{-NN})$ and $\text{Tp}^{\text{Cum,Me}}\text{Zn}(\text{SQ-Ph}_2\text{-NN})$	76

2.5.4	Variable Temperature Electronic Absorption Experiments for $\text{Tp}^{\text{Cum,Me}}\text{Zn}(\text{SQ-Thp}_2\text{-NN})$ and $\text{Tp}^{\text{Cum,Me}}\text{Zn}(\text{SQ-Ph}_2\text{-NN})$	81
2.5.5	Resonance Raman Spectra and Frequency Calculations for $\text{Tp}^{\text{Cum,Me}}\text{Zn}(\text{SQ-Thp}_2\text{-NN})$ and $\text{Tp}^{\text{Cum,Me}}\text{Zn}(\text{SQ-Ph}_2\text{-NN})$	89
2.6	Sterically-Hindered Bridges.....	97
2.6.1	Dependence of Overlap and Spin Populations as Functions of Donor, Bridge, and Acceptor Dihedral Angles	97
2.6.2	Optimized Geometries, DFT Spin Densities, and Frontier Molecular Orbitals.....	101
2.6.3	Electronic Absorption Spectra and Computational Studies of Sterically Hindered D-B-A Biradicals	104
2.6.4	Resonance Raman Spectra and DFT Frequency Calculations of Sterically Hindered DBA Biradicals	115
2.7	Computational and Experimental Studies of a Cross-Conjugated D-B-A Biradical: $\text{Tp}^{\text{Cum,Me}}\text{Zn}(\text{SQ-mPh-NN})$	119
2.7.1	$\text{Tp}^{\text{Cum,Me}}\text{Zn}(\text{SQ-mPh-NN})$ Shows Antiferromagnetic D-A Biradical Exchange Coupling	119
2.7.2	DFT Optimized Geometry and Frontier Molecular Orbitals of $\text{Tp}^{\text{Cum,Me}}\text{Zn}(\text{SQ-mPh-NN})$	120
2.7.3	Experimental and Calculated Electronic Absorption of $\text{Tp}^{\text{Cum,Me}}\text{Zn}(\text{SQ-mPh-NN})$ Compared to $\text{Tp}^{\text{Cum,Me}}\text{Zn}(\text{SQ-pPh-NN})$	124
2.7.4	Variable-Temperature Electronic Absorption of $\text{Tp}^{\text{Cum,Me}}\text{Zn}(\text{SQ-mPh-NN})$	129
2.7.5	Configuration Interaction States Contributing to the Antiferromagnetic Coupling in $\text{Tp}^{\text{Cum,Me}}\text{Zn}(\text{SQ-mPh-NN})$	132
2.8	Computational Studies of a Mixed-Valent Ligand Co Complex.....	137
2.8.1	Longe-Range Ferromagnetic Coupling in $\text{NN-Ph-SQCo}^{\text{III}}(\text{py})_2\text{Cat-Ph-NN}$	137
2.8.2	Description of Delocalization in $\text{NN-Ph-SQCo}^{\text{III}}(\text{py})_2\text{Cat-Ph-NN}$	139
2.9	Conclusions.....	142
3.	SPECTROSCOPIC AND COMPUTATIONAL STUDIES OF THE BIMETALLIC ENZYME ACTIVE SITE OF CARBON MONOXIDE DEHYDROGENASE AND A SERIES OF ACTIVE SITE MODELS THAT ARE ELECTRONIC STRUCTURE AND GEOMETRY MIMICS OF THE ACTIVE SITE	150
3.1	Introduction.....	150
3.2	Experimental Details.....	158
3.2.1	Sample Handling.....	158
3.2.2	Multifrequency Electron Paramagnetic Resonance Spectroscopy (EPR) .	158
3.2.3	Density Functional Calculations	159
3.2.4	Electronic Absorption Spectroscopy.....	160
3.2.5	MCD Spectroscopy	161
3.3	Computational Studies of the Enzyme Active Site.....	163
3.3.1	Equatorial Oxo Ligand vs. Equatorial Hydroxy Ligand	163

3.3.2	Geometry Changes at the Cu Site upon CO Binding.....	172
3.3.3	Alternative Geometries for CO Binding	179
3.3.4	Bicarbonate as the Equatorial Ligand	180
3.4	Computational and Experimental Studies of the Active Site Model Compounds	181
3.4.1	Frontier Orbitals and Electronic Structure of CODH Model Compounds	183
3.4.2	Covalency versus Spin Density Distribution Across the [MoSCu] Unit... ..	189
3.4.3	Electron Paramagnetic Resonance Spectroscopy of CODH Model Compounds	191
3.4.4	Electronic Absorption and Magnetic Circular Dichroism of CODH Model Compounds	196
3.5	Conclusion	212
4.	SPECTROSCOPIC AND COMPUTATIONAL STUDIES OF CLASS III VALENCE DELOCALIZED RHENIUM DIMER MOLECULES.....	216
4.1	Introduction.....	216
4.2	Experimental Details.....	224
4.2.1	Sample Preparation	224
4.2.2	Electronic Absorption Measurements.....	225
4.2.3	Magnetic Circular Dichroism Measurements	226
4.2.4	Resonance Raman Measurements.....	228
4.2.5	Density Functional Theory Electronic Structure Calculations	230
4.3	Spectroscopic and Computational Studies of Re Dimers: Effects of Ligand Substitution	231
4.3.1	Room Temperature Electronic Absorption of $\text{Re}_2\text{Cl}_4(\text{PMe}_3)_4\text{PF}_6$ and $\text{Re}_2\text{Br}_4(\text{PMe}_3)_4\text{PF}_6$	231
4.3.2	C-term MCD of $\text{Re}_2\text{Cl}_4(\text{PMe}_3)_4\text{PF}_6$ and $\text{Re}_2\text{Br}_4(\text{PMe}_3)_4\text{PF}_6$	240
4.3.3	DFT Calculated Electronic Structure of $\text{Re}_2\text{Cl}_4(\text{PMe}_3)_4\text{PF}_6$ and $\text{Re}_2\text{Br}_4(\text{PMe}_3)_4\text{PF}_6$	251
4.4	Spectroscopic and Computational Studies of Re Dimers: the Vibronic Structure of the δ - δ^* Band	260
4.4.1	Vibronic Progressions Resolved in Low-Temperature Optical Spectroscopy	260
4.4.2	Resonance Raman Spectra and DFT Calculated Vibrational Frequencies of $\text{Re}_2\text{Cl}_4(\text{PMe}_3)_4\text{PF}_6$ and $\text{Re}_2\text{Br}_4(\text{PMe}_3)_4\text{PF}_6$	265
	Figure 4.19: Resonance Raman spectrum of $\text{Re}_2\text{Br}_4(\text{PMe}_3)_4\text{PF}_6$ in a NaCl/ Na_2SO_4 matrix at 458 nm excitation.	266
4.5	Conclusion	274
5.	CONCLUDING REMARKS.....	278
6.	APPENDICES	286
6.1	Appendix A: Supporting Information for Chapter 2.....	287
6.1.1	Resonance Raman Spectra of D-B-A Biradicals	287
6.1.2	Coordinates of DFT Optimized Geometries and Final Energies of D-B-A Biradicals of Table 2.4.....	291
6.2	Appendix B: Supporting Information for Chapter 3.....	299

6.2.1 Variable-Temperature MCD Spectra for CODH Model Compounds	299
6.2.2 Low-Temperature Electronic Absorption Spectra for CODH Model Compounds “Post-MCD”	300
6.2.3 X-band EPR Spectra and Simulations for CODH Model Compounds.....	300
6.2.4 Aerobic and Anaerobic Electronic Absorption for CODH Model Compounds	301
6.2.5 Variable-Temperature Sample Cell Assembly	302
6.3 Appendix C: Supporting Information for Chapter 4.....	303
6.3.1 Resonance Raman Spectra of $\text{Re}_2\text{Cl}_4(\text{PMe}_3)_4^+$ and $\text{Re}_2\text{Br}_4(\text{PMe}_3)_4^+$	303
6.3.2 D_{2d} Character Table	304
7. REFERENCES CITED.....	305

LIST OF FIGURES

Figure 1.1: VBCI description of ferromagnetic coupling in [SQ-NN] ⁻ biradicals. Adapted from reference ³	4
Figure 1.2: Potential energy surfaces of class I (a), II (b), and III (c) mixed-valent compounds in the Robin-Day classification, adapted from Kahn. ⁶	7
Figure 2.1: ChemDraw rendition of Tp ^{Cum,Me} Zn(SQ-Ph-NN).	26
Figure 2.2: DFT-optimized structure of Tp ^{Cum,Me} Zn(SQ-Ph-NN). Carbons are gray, nitrogens are blue, oxygens are red, hydrogens are white, boron is rose, and zinc is light-blue.	27
Figure 2.3: Fragment molecular orbitals of [SQ-Ph-NN] ⁻ , SOMO = singly occupied molecular orbital, LUMO = lowest unoccupied molecular orbital. Molecular orbitals are plotted at a contour isovalue of 0.05. Percentages are the molecular orbital contributions of each ring moiety to the total for each molecular orbital.	28
Figure 2.4: Molecular orbital diagram and DFT-calculated molecular orbitals and their compositions. Energies are not drawn to scale, orbitals are α orbitals and are displayed at an contour isovalue of 0.05.	31
Figure 2.5: Spin polarization in the nitronyl nitroxide radical (energies and orbital coefficient not drawn to scale).	33
Figure 2.6: Spin density distribution of Tp ^{Cum,Me} Zn(SQ-Ph-NN) (positive spin density blue, negative spin density red).	34
Figure 2.7: Calculated spin populations on the NN nitrogens (dashed lines) and bridging carbon (solid lines) of NN in [SQ-Ph-NN] ⁻ in the triplet state as a function of rotating the donor (red), bridge (green), or acceptor (blue) individually away from a planar D-B-A geometry in 15° increments.	37
Figure 2.8: ChemDraw representations of the D-A, D-B-A, and B-A molecules.	40
Figure 2.9: Room temperature EPR Spectra of Tp ^{Cum,Me} Zn(SQ-NN) (1), Tp ^{Cum,Me} Zn(SQ-Ph-NN) (2), Tp ^{Cum,Me} Zn(SQ-Thp-NN) (3), Tp ^{Cum,Me} Zn(SQ-Xyl-NN) (4), NN-Ph (5), and NN-Ph(OMe) ₂ (6). Experimental data are in red and simulations in blue.	41
Figure 2.10: Correlation of experimental isotropic nitrogen hyperfine coupling constants and DFT-calculated nitrogen spin populations.	44
Figure 2.11: TD-DFT low-energy transitions for Tp ^{Cum,Me} Zn(SQ-Ph-NN): bars are oscillator strengths, line spectra are calculated oscillator strengths widened into bands of 4000 cm ⁻¹ bandwidth (black). Experimental spectrum from reference ^{4,90} (red).	46
Figure 2.12: Orbital contributions (top, white/blue, first row: HOMO → SQ SOMO, second row HOMO-1 → SQ SOMO) and EDDMs (bottom, red = loss and blue = gain of electron density during the transition, contour isovalue is 0.002): Band 1 at the left, band 2 at the right.	46
Figure 2.13: Orbital contributions (top, white/blue, contour isovalue 0.05) and EDDMs (bottom, red = loss of electron density during the transition, blue = gain of electron density during the transition, contour isovalue is 0.002) for band 3, the donor-acceptor charge transfer band.	48
Figure 2.14: DFT-calculated vibrations and their frequencies. Left: [SQ-Ph-NN] ⁻ , right: benzene. Modes are shown as overlays of the extrema of the vibrational mode.	51

Figure 2.15: Top: SQ SOMO (left) and NN-Phe ₁ LUMO (right) (Tp ^{Cum,Me} and Zn were omitted for clarity, contour isovalue 0.05). Bottom: excited state distortion accompanying the removal of an electron from the SQ SOMO (red) and the addition of that electron to the NN-Phe ₁ LUMO (blue), adapted from reference ⁴	51
Figure 2.16: DFT frontier molecular orbitals and orbital compositions for Tp ^{Cum,Me} Zn(SQ-Thp-NN). Note that no information about the relative energies of the orbitals with respect to each other is intended (i.e. α and β orbitals are not degenerate in the calculation). ZnTp denotes Tp ^{Cum,Me} Zn for space purposes in the diagram.	54
Figure 2.17: Molecular orbital diagram of NN-bridge mixing in Tp ^{Cum,Me} Zn(SQ-Ph-NN) (left) and Tp ^{Cum,Me} Zn(SQ-Thp-NN) (right). Energy levels are not drawn to scale. Percent contributions are obtained from the AOMix Mulliken Population Analysis of the DFT-calculated molecular orbitals of the full Tp ^{Cum,Me} Zn(SQ-Bridge-NN) molecule.	56
Figure 2.18: Molecular orbital diagram of Tp ^{Cum,Me} Zn(SQ-Thp-NN). Energy levels are not drawn to scale. Thiophene sulfur points to the bottom.	57
Figure 2.19: DFT-calculated spin density distribution for Tp ^{Cum,Me} Zn(SQ-Thp-NN), where blue is positive spin density, red is negative spin density, and the contour isovalue is 0.004.	58
Figure 2.20: DFT-calculated (black) and experimental solution (red) spectra of Tp ^{Cum,Me} Zn(SQ-Thp-NN). DFT bands were widened to 4000 cm ⁻¹ , bars represent calculated oscillator strengths.	59
Figure 2.21: Resonance Raman spectrum of Tp ^{Cum,Me} Zn(SQ-Thp-NN) in a NaCl/Na ₂ SO ₄ matrix using a 458 nm excitation wavelength. Internal standard sulfate peak(s) are marked in red, and sample modes are marked in black and blue (most enhanced).	63
Figure 2.22: Resonance Raman enhancement profile for selected modes (blue 626 cm ⁻¹ , green 1400 cm ⁻¹ , black 1420 cm ⁻¹) as a function of laser excitation energy and overlaid on the electronic absorption spectrum (red). The Tp ^{Cum,Me} Zn(SQ-Thp-NN) sample was in the solid state in a NaCl/Na ₂ SO ₄ matrix.	64
Figure 2.23: Raman active DFT-calculated vibrations of thiophene. Modes are shown as overlays of the extrema of the vibrational mode.	65
Figure 2.24: Selected DFT-calculated vibrations of [SQ-Thp-NN] ⁻ . Modes are shown as overlays of the extrema of the vibrational mode.	66
Figure 2.25: Room-temperature EPR of Tp ^{Cum,Me} Zn(SQ-Ph ₂ -NN). Data (black), spectral simulation (red).	68
Figure 2.26: Tp ^{Cum,Me} Zn(SQ-Thp ₂ -NN) in a cis-conformation (left) or trans-conformation (right).	69
Figure 2.27: Experimental nitrogen hyperfine coupling constants as a function of J from experimental magnetic susceptibility measurements for Tp ^{Cum,Me} Zn(SQ-Ph _n -NN), where n = 0, 1, and 2.	71
Figure 2.28: Frontier molecular orbitals and orbital composition for Tp ^{Cum,Me} Zn(SQ-Thp ₂ -NN).	73
Figure 2.29: Frontier molecular orbitals and orbital composition for Tp ^{Cum,Me} Zn(SQ-Ph ₂ -NN).	75
Figure 2.30: DFT-calculated (black for trans-, blue for cis-geometry) and experimental solution (red) spectra of Tp ^{Cum,Me} Zn(SQ-Thp ₂ -NN). DFT bands were widened to 4000	

cm ⁻¹ , bars represent calculated oscillator strengths for the trans -geometry. Calculated extinction coefficients were divided by 3 in order to be on scale with the experimental data.....	77
Figure 2.31: DFT-calculated (black) and experimental solution (red) spectra of Tp ^{Cum,Me} Zn(SQ-Ph ₂ -NN). Computed bands have 4000 cm ⁻¹ bandwidth. Bars represent calculated oscillator strengths. Calculated extinction coefficients were divided by 2 in order to be on scale with the experimental data.....	79
Figure 2.32: Variable-temperature electronic absorption spectra of Tp ^{Cum,Me} Zn(SQ-Thp ₂ -NN) in a polystyrene film matrix. Temperatures from 5 K (blue) to 290 K (red). Expanded view of the temperature-dependent peaks from ~18500 cm ⁻¹ to ~20500 cm ⁻¹ (inset).	82
Figure 2.33: Variable-temperature electronic absorption spectra of Tp ^{Cum,Me} Zn(SQ-Ph ₂ -NN) in a polystyrene film matrix. Top: using a liquid-helium cryostat, temperatures from 10 K (blue) to 211 K (red), inset: expanded view of the temperature-dependent peaks from ~23500 cm ⁻¹ to ~27000 cm ⁻¹ ; bottom: using a liquid-nitrogen cryostat, temperatures from 74 K (blue) to 290 K (red), inset: expanded view of the temperature-dependent peaks from ~23000 cm ⁻¹ to ~27500 cm ⁻¹	83
Figure 2.34: Variable-temperature electronic absorption spectra of Tp ^{Cum,Me} Zn(SQ-Thp ₂ -NN) in a polystyrene film matrix. Temperatures from 5 K (blue) to 273 K (violet).....	85
Figure 2.35: Theoretical Boltzmann populations (triplet state degeneracy of 3 and singlet state with degeneracy of 1) and an energy gap of 170 cm ⁻¹ between them. Lines are the Boltzmann-predicted depopulations of the triplet. Red dots are temperature-dependent electronic absorption intensities for the band at 18832 cm ⁻¹	86
Figure 2.36: singlet (orange) and triplet (blue) electronic absorption spectra for Tp ^{Cum,Me} Zn(SQ-Ph ₂ -NN). Left: data set from liquid helium cryostat, right: data set from liquid nitrogen cryostat.	87
Figure 2.37: singlet (orange) and triplet (red) electronic absorption spectra for Tp ^{Cum,Me} Zn(SQ-Thp ₂ -NN).	88
Figure 2.38: Resonance Raman spectrum of Tp ^{Cum,Me} Zn(SQ-Ph ₂ -NN) in a NaCl/Na ₂ SO ₄ matrix using a 407 nm excitation wavelength. Internal standard sulfate peak(s) are marked in red, and sample modes are marked in black and blue (most enhanced).	90
Figure 2.39: Resonance Raman spectrum of Tp ^{Cum,Me} Zn(SQ-Ph ₂ -NN) in dichloromethane using a 407 nm excitation wavelength. Sample modes are marked in black and blue (most enhanced), and are labeled the same as for the solid state sample since shifts were within 1-2 cm ⁻¹	90
Figure 2.40: Resonance Raman enhancement profile for the 1600 cm ⁻¹ mode as a function of laser excitation energy and overlaid onto the electronic absorption spectrum (black). Red dots: resonance enhancement in a NaCl/Na ₂ SO ₄ matrix, blue dots resonance enhancement in dichloromethane.	91
Figure 2.41: DFT-calculated vibration in [SQ-Ph ₂ -NN] ⁻ . The mode is shown as overlays of the extrema of the vibrational mode.	92
Figure 2.42: Resonance Raman spectrum of Tp ^{Cum,Me} Zn(SQ-Thp ₂ -NN) in a NaCl/Na ₂ SO ₄ matrix using a 514 nm excitation wavelength. Internal standard sulfate peak(s) are marked in red, and sample modes are marked in black and blue (most enhanced).	94

Figure 2.43: Resonance Raman enhancement profile for selected modes (blue 1046 cm^{-1} , green 1066 cm^{-1} , black 1405 cm^{-1} , pink 1435 cm^{-1} , light blue 1517 cm^{-1}) as a function of laser excitation energy and overlaid onto the electronic absorption spectrum (red). The $\text{Tp}^{\text{Cum,Me}}\text{Zn}(\text{SQ-Thp}_2\text{-NN})$ sample was in the solid state in a $\text{NaCl}/\text{Na}_2\text{SO}_4$ matrix.	94
Figure 2.44: Selected DFT-calculated vibrations of $[\text{SQ-Thp}_2\text{-NN}]^-$. Modes are shown as overlays of the extrema of the vibrational mode.	96
Figure 2.45: DFT-calculated correlation between ring torsion angles and the square of the $2p_z$ orbital coefficient for the NN-bridging carbon where in red are the data points and their fit and in blue is a $\cos^2\theta$ function for reference. Top: rotation of the SQ from planarity; middle: rotation of the Ph from planarity; bottom: rotation of the NN from planarity.	98
Figure 2.46: DFT-optimized structures of sterically-hindered D-B-A biradicals.....	101
Figure 2.47: DFT-calculated spin density distributions of sterically-hindered DBA biradicals. Blue = positive spin density, red = negative spin density, contour isovalue = 0.004.....	103
Figure 2.48: DFT-calculated (black) and experimental solution (red) spectra of $\text{Tp}^{\text{Cum,Me}}\text{Zn}(\text{SQ-Xyl-NN})$. DFT bands were widened to 4000 cm^{-1} , bars represent calculated oscillator strengths.	105
Figure 2.49: Variable-temperature electronic absorption spectra of $\text{Tp}^{\text{Cum,Me}}\text{Zn}(\text{SQ-Xyl-NN})$ in a polystyrene polymer matrix. Temperatures range from 5 K (dark blue) to 292 K (red), and data were baseline corrected to align with the temperature-independent polystyrene reference peak at $\sim 6000 \text{ cm}^{-1}$	108
Figure 2.50: Computed (black) and experimental solution (red) spectra for $\text{Tp}^{\text{Cum,Me}}\text{Zn}(\text{SQ-PhMe-NN})$. Computed bands have bandwidths of 4000 cm^{-1} , and bars lengths represent calculated oscillator strengths.....	108
Figure 2.51: Variable-temperature electronic absorption spectra for $\text{Tp}^{\text{Cum,Me}}\text{Zn}(\text{SQ-PhMe-NN})$ in a polystyrene matrix. Temperatures are 4 K (blue), 76 K (green), and 295 K (red), and the data were baseline corrected to align the temperature-independent polystyrene reference peak at $\sim 6000 \text{ cm}^{-1}$	110
Figure 2.52: DFT-calculated (black) and experimental solution (red) spectra for $\text{Tp}^{\text{Cum,Me}}\text{Zn}(\text{SQ-MePh-NN})$. Computed transitions are shown with a 4000 cm^{-1} bandwidth, and bar heights represent calculated oscillator strengths.	111
Figure 2.53: Variable-temperature electronic absorption spectra of $\text{Tp}^{\text{Cum,Me}}\text{Zn}(\text{SQ-MePh-NN})$ in a polystyrene polymer matrix. Temperatures range from 5 K (dark blue) to 319 K (red), and data were baseline corrected to align the temperature-independent polystyrene reference peak at $\sim 6000 \text{ cm}^{-1}$	113
Figure 2.54: Absorbance at 23670 cm^{-1} for $\text{Tp}^{\text{Cum,Me}}\text{Zn}(\text{SQ-MePh-NN})$ as a function of temperature (red circles) and theoretical Boltzmann populations for ferromagnetic exchange couplings of $2J = 20\text{-}50 \text{ cm}^{-1}$	114
Figure 2.55: Resonance Raman data for $\text{Tp}^{\text{Cum,Me}}\text{Zn}(\text{SQ-Xyl-NN})$ (top) and $\text{Tp}^{\text{Cum,Me}}\text{Zn}(\text{SQ-MePh-NN})$ (bottom) in a solid state $\text{NaCl}/\text{Na}_2\text{SO}_4$ matrix using 407 nm excitation.....	116
Figure 2.56: Overlay of Resonance Raman spectra for $\text{Tp}^{\text{Cum,Me}}\text{Cu}(\text{SQ-NN})$ (black, left y-axis, 413 nm excitation, in CH_2Cl_2) ⁴ , $\text{Tp}^{\text{Cum,Me}}\text{Zn}(\text{SQ-Ph-NN})$ (red, right y-axis, 413 nm	

excitation, in CH ₂ Cl ₂) ⁴ , Tp ^{Cum,Me} Zn(SQ-MePh-NN) (green, right y-axis, 407 nm excitation, in NaCl/Na ₂ SO ₄), and Tp ^{Cum,Me} Zn(SQ-Xyl-NN) (blue, right y-axis, 407 nm excitation, in NaCl/Na ₂ SO ₄), solvent/sulfate peaks are marked with stars.....	117
Figure 2.57: Chemical structure of Tp ^{Cum,Me} Zn(SQ-mPh-NN).	120
Figure 2.58: Frontier molecular orbitals and orbital compositions for Tp ^{Cum,Me} Zn(SQ-mPh-NN) (broken-symmetry singlet).	122
Figure 2.59: Frontier molecular orbitals and orbital compositions for Tp ^{Cum,Me} Zn(SQ-mPh-NN) (triplet).	123
Figure 2.60: Orbital interactions in Tp ^{Cum,Me} Zn(SQ-mPh-NN) versus Tp ^{Cum,Me} Zn(SQ-pPh-NN).	124
Figure 2.61: Overlay of room temperature electronic absorption spectra for Tp ^{Cum,Me} Zn(SQ-mPh-NN) (black) and Tp ^{Cum,Me} Zn(SQ-pPh-NN) (green) as well as DFT-calculated oscillator strengths (blue bars = triplet Tp ^{Cum,Me} Zn(SQ-mPh-NN), pink bars = bss Tp ^{Cum,Me} Zn(SQ-mPh-NN)).	125
Figure 2.62: Molecular orbital diagram depicting electronic transitions in Tp ^{Cum,Me} Zn(SQ-mPh-NN).	128
Figure 2.63: Variable-temperature electronic absorption of Tp ^{Cum,Me} Zn(SQ-mPh-NN) as a film in a polystyrene matrix. Temperatures range from 5 K (blue) to 298 K (red), and spectra were normalized to a polystyrene reference peak at ~6000 cm ⁻¹	130
Figure 2.64: Theoretical Boltzmann populations and electronic absorption intensities as a function of temperature for Tp ^{Cum,Me} Zn(SQ-mPh-NN).	131
Figure 2.65: singlet (blue) and triplet (red) electronic absorption spectra for Tp ^{Cum,Me} Zn(SQ-mPh-NN).	132
Figure 2.66: Various configurations for singlet and triplet Tp ^{Cum,Me} Zn(SQ-mPh-NN)..	133
Figure 2.67: Spin polarization mechanism leads to antiferromagnetic coupling in Tp ^{Cum,Me} Zn(SQ-mPh-NN).	134
Figure 2.68: The SQ-Co ^{III} -Cat core of NN-Ph-SQCo ^{III} (py) ₂ Cat-Ph-NN.....	138
Figure 2.69: Stationary and itinerant electrons in NN-Ph-SQCo ^{III} (py) ₂ Cat-Ph-NN.....	138
Figure 2.70: DFT-calculated spin density distribution of NN-Ph-SQCo ^{III} (py) ₂ Cat-Ph-NN for an S = 3/2 ground state where blue represents positive spin density and red negative spin density at an contour isovalue of 0.005.	140
Figure 2.71: Lowest-energy TD-DFT-calculated transition of NN-Ph-SQCo ^{III} (py) ₂ Cat-Ph-NN at 3711 cm ⁻¹	142
Figure 3.1: X-ray crystal structure of the oxidized CODH enzyme (PDB 1N5W). ¹¹⁷ ...	152
Figure 3.2: Active site geometry of oxidized CODH (PDB 1N5W). ¹¹⁷ Oxygen = red, carbon = cyan, sulfur = yellow, nitrogen = blue, phosphorus = bronze, molybdenum = orange, glutamate residue = purple.	153
Figure 3.3: Inhibitor-based mechanism for CODH.	154
Figure 3.4: Alternative mechanism for CODH.	155
Figure 3.5: CODH active site computational model with an equatorial hydroxo ligand. molybdenum (aqua), sulfur (yellow), copper (bronze), carbon (gray), oxygen (red), hydrogen (white).	164
Figure 3.6: Definition of the OMoOH dihedral angle in the CODH active site computational model.	168

Figure 3.7: Calculated g-values as a function of varying OMoOH dihedral angles (horizontal black lines mark the published experimental g-tensor for the enzyme) g_{\min} (black), g_{mid} (bronze), g_{\max} (gray).	169
Figure 3.8: Calculated isotropic hyperfine coupling constants as a function of varying OMoOH dihedral angles (the horizontal black line marks a value of zero for the calculated proton hyperfine). $A_{\text{iso}}(\text{H})$ blue, $A_{\text{iso}}(\text{Mo})$ red, $A_{\text{iso}}(\text{Cu})$ green.	170
Figure 3.9: Calculated proton hyperfine coupling constants as a function of varying OMoOH dihedral angles (isotropic: blue, and dipolar: black, red, lavender).....	170
Figure 3.10: Optimized geometries of the CODH active site with an equatorial oxo ligand with no CO bound (left) and upon CO binding at the Cu (right).....	173
Figure 3.11: CODH active site with an equatorial hydroxo ligand with no CO bound (left, I and III) and upon CO binding at the Cu (right, II and IV).	174
Figure 3.12: SOMO wavefunction of the CODH active site model with an equatorial hydroxy ligand.	178
Figure 3.13: Alternative modes of CO binding at the CODH active site.	179
Figure 3.14: CODH synthetic active site model compounds where Ar = Ph, 2s-Bu, 4s-Bu, 3t-Bu, or 2-tBu where the 2-position on Ar points in the opposite direction of the Mo- O_{axial} bond and the 5-position in the same direction as the Mo- O_{axial} bond.	182
Figure 3.15: $\text{Tp}^{\text{iPr}}\text{MoO}(\text{OPh})(\mu\text{-S})\text{Cu}(\text{Me}_3\text{tacn})$, optimized geometry (left) and α SOMO wavefunction (right). Hydrogens have been omitted for clarity. Molybdenum = turquoise, sulfur = yellow, copper = pink, carbon = gray, oxygen = red, nitrogen = blue.	184
Figure 3.16: VBCI description of the spin densities observed for Mo and Cu in CODH model compounds.	190
Figure 3.17: Q-band EPR spectrum of $\text{Tp}^{\text{iPr}}\text{MoO}(\text{OAr})(\mu\text{-S})\text{Cu}(\text{Me}_3\text{tacn})$ at ~80 K in butyronitrile.....	192
Figure 3.18: Calculated isotropic Cu hyperfine as a function of varying MoSCu bond angle: all data points calculated (right) and the linear region only (left).....	195
Figure 3.19: Mulliken reduced orbital spin populations on Cu as a function of MoSCu bond angles in $\text{Tp}^{\text{iPr}}\text{MoO}(\text{OPh})(\mu\text{-S})\text{Cu}(\text{Me}_3\text{tacn})$	196
Figure 3.20: Anaerobic (green) and aerobic (blue) room-temperature electronic absorption spectra of $\text{Tp}^{\text{iPr}}\text{MoO}(\text{OPh-3tBu})(\mu\text{-S})\text{Cu}(\text{Me}_3\text{tacn})$ (left) and $\text{Tp}^{\text{iPr}}\text{MoO}(\text{OAr})\text{S}$ (right).	197
Figure 3.21: Room temperature electronic absorption spectra of $\text{Tp}^{\text{iPr}}\text{MoO}(\text{OAr})(\mu\text{-S})\text{Cu}(\text{Me}_3\text{tacn})$, where Ar = Ph, 2s-Bu-Ph, 4s-Bu-Ph or 3t-Bu-Ph. Spectra are room temperature solutions in butyronitrile.....	199
Figure 3.22: DFT-calculated (black, using bandwidths of 3000 cm^{-1}) and experimental (red) electronic solution spectrum of $\text{Tp}^{\text{iPr}}\text{MoO}(\text{OPh})(\mu\text{-S})\text{Cu}(\text{Me}_3\text{tacn})$, as well as calculated oscillator strengths (orange bars).....	200
Figure 3.23: Variable-temperature-variable-magnetic-field MCD of the $\text{Tp}^{\text{iPr}}\text{Mo}(\text{OPh-4sBu})\text{SCu}(\text{Me}_3\text{tcn})$ model.	206
Figure 3.24: C-term MCD spectra of $\text{Tp}^{\text{iPr}}\text{MoO}(\text{OAr})(\mu\text{-S})\text{Cu}(\text{Me}_3\text{tacn})$, where Ar = Ph, 2s-Bu-Ph, 4s-Bu-Ph or 3t-Bu-Ph. Spectra are 5 K, 7 T – 0 T data, where the compounds were prepared as frozen solutions in butyronitrile.....	208

Figure 3.25: DFT-calculated (black, bandwidth 2500 cm^{-1}) and experimental (red) C-term MCD spectrum of $\text{Tp}^{\text{iPr}}\text{MoO}(\text{OPh})(\mu\text{-S})\text{Cu}(\text{Me}_3\text{tacn})$	209
Figure 3.26: Overlay of room-temperature electronic absorption and 5 K MCD for of $\text{Tp}^{\text{iPr}}\text{MoO}(\text{OAr})(\mu\text{-S})\text{Cu}(\text{Me}_3\text{tacn})$, where Ar = Ph, 2s-Bu-Ph, 4s-Bu-Ph or 3t-Bu-Ph..	211
Figure 4.1: GaussView rendition of $\text{Re}_2\text{X}_4(\text{PMe}_3)_4^+$: blue = Re, orange = P, gray = C, white = H, green = Cl, maroon = Br; left: $\text{Re}_2\text{X}_4(\text{PMe}_3)_4^+$ with primary coordination to Re only (methyl groups omitted for clarity), right: complete $\text{Re}_2\text{X}_4(\text{PMe}_3)_4^+$ compound ..	222
Figure 4.2: Electronic absorption spectra of $\text{Re}_2\text{Br}_4(\text{PMe}_3)_4\text{PF}_6$ at room temperature in acetonitrile (green, right y-axis) and butyronitrile (blue, left y-axis).....	232
Figure 4.3: Electronic absorption spectra of $\text{Re}_2\text{Cl}_4(\text{PMe}_3)_4\text{PF}_6$ (green, left y-axis) and $\text{Re}_2\text{Br}_4(\text{PMe}_3)_4\text{PF}_6$ (blue, right y-axis) at room temperature in acetonitrile.	233
Figure 4.4: Gaussian resolved room-temperature electron electronic absorption spectra of $\text{Re}_2\text{Cl}_4(\text{PMe}_3)_4\text{PF}_6$ (left) and $\text{Re}_2\text{Br}_4(\text{PMe}_3)_4\text{PF}_6$ (right).	234
Figure 4.5: Molecular orbital diagram showing the qualitative effect of halide substitution on ligand-to-metal charge transfer bands (energy levels are not drawn to scale).....	235
Figure 4.6: Variable temperature MCD of $\text{Re}_2\text{Cl}_4(\text{PMe}_3)_4\text{PF}_6$ (top) and $\text{Re}_2\text{Br}_4(\text{PMe}_3)_4\text{PF}_6$ (bottom) in a polystyrene film matrix. Spectra were taken at 7 T and are baseline-subtracted. 5 K (blue), 10 K (green), 20 K (red).....	241
Figure 4.7: Mechanisms for gaining C-term intensity: blue = transition dipole integrals, green = spin-orbit coupling integrals, after reference ¹⁴²	242
Figure 4.8: DFT-calculated MCD spectra of $\text{Re}_2\text{Cl}_4(\text{PMe}_3)_4\text{PF}_6$ (top) and $\text{Re}_2\text{Br}_4(\text{PMe}_3)_4\text{PF}_6$ (bottom) at various bandwidths: red 500 cm^{-1} , green 1000 cm^{-1} , blue 1500 cm^{-1}	245
Figure 4.9: Gaussian resolved 5 K, 7 T MCD spectra of $\text{Re}_2\text{Cl}_4(\text{PMe}_3)_4\text{PF}_6$ (top) and $\text{Re}_2\text{Br}_4(\text{PMe}_3)_4\text{PF}_6$ (bottom) in a polystyrene film matrix. Inset: zoom-out of the Gaussian resolved bands.....	247
Figure 4.10: DFT-calculated electronic absorption (green) and C-term MCD (blue) spectra plotted at a 1 cm^{-1} bandwidth for $\text{Re}_2\text{Cl}_4(\text{PMe}_3)_4\text{PF}_6$ (left) and $\text{Re}_2\text{Br}_4(\text{PMe}_3)_4\text{PF}_6$ (right).	250
Figure 4.11: Metal dimer d-orbitals.	252
Figure 4.12: Molecular orbitals and EDDMs (electron density difference maps) for $\text{Re}_2\text{Br}_4(\text{PMe}_3)_4^+$. Molecular orbitals that the transition is originating from is on the left of the arrow, the molecular orbital that the promotion is going into (δ^*) is on the right of the arrow, and the EDDM for that transition on top of the arrow (red is electron density loss, blue is gain). Isovalues are 0.03 for molecular orbitals, 0.001 for EDDM band 1, 0.003 for EDDM bands 4 and 5.....	255
Figure 4.13: Molecular orbitals and EDDMs (electron density difference maps) for $\text{Re}_2\text{Cl}_4(\text{PMe}_3)_4^+$. Molecular orbitals that the transition is originating from is on the left of the arrow, the molecular orbital that the promotion is going into (δ^*) is on the right of the arrow, and the EDDM for that transition on top of the arrow (red is electron density loss, blue is gain). Isovalues are 0.03 for molecular orbitals, 0.001 for EDDM band 1, 0.003 for EDDM bands 4 and 5.....	256
Figure 4.14: DFT-calculated (blue) and experimental (green) electronic absorption spectra of $\text{Re}_2\text{Cl}_4(\text{PMe}_3)_4\text{PF}_6$ (left) and $\text{Re}_2\text{Br}_4(\text{PMe}_3)_4\text{PF}_6$ (right).....	257

Figure 4.15: DFT-calculated (blue) and experimental (green) MCD spectra of $\text{Re}_2\text{Cl}_4(\text{PMe}_3)_4\text{PF}_6$ (left) and $\text{Re}_2\text{Br}_4(\text{PMe}_3)_4\text{PF}_6$ (right).	258
Figure 4.16: Molecular orbital diagram for $\text{Re}_2\text{X}_4(\text{PMe}_3)_4^+$ for the $\delta \rightarrow \delta^*$ band and LMCT bands (energy separations are not drawn to scale).	258
Figure 4.17: Gaussian resolved 5 K MCD $\delta \rightarrow \delta^*$ transition for $\text{Re}_2\text{Cl}_4(\text{PMe}_3)_4\text{PF}_6$ (top) and $\text{Re}_2\text{Br}_4(\text{PMe}_3)_4\text{PF}_6$ (bottom). Peaks belonging to the same progression are marked by the same letter (a, b, or c).	260
Figure 4.18: ORCA_ASA ¹⁷⁸ simulated intensity patterns of the vibronic progression overlaid on the experimental resolved vibronic progression.	262
Figure 4.19: Resonance Raman spectrum of $\text{Re}_2\text{Br}_4(\text{PMe}_3)_4\text{PF}_6$ in a NaCl/ Na_2SO_4 matrix at 458 nm excitation.	266
Figure 4.20: Resonance Raman spectrum of $\text{Re}_2\text{Br}_4(\text{PMe}_3)_4\text{PF}_6$ in a NaCl/ Na_2SO_4 matrix at 568 nm excitation.	267
Figure 4.21: Resonance Raman spectrum of $\text{Re}_2\text{Cl}_4(\text{PMe}_3)_4\text{PF}_6$ in a NaCl/ Na_2SO_4 matrix at 458 nm excitation.	269
Figure 4.22: Resonance Raman enhancement profiles for $\text{Re}_2\text{Cl}_4(\text{PMe}_3)_4\text{PF}_6$ (top) and $\text{Re}_2\text{Br}_4(\text{PMe}_3)_4\text{PF}_6$ (bottom).	271

LIST OF TABLES

Table	Page
Table 2.1: Experimental versus computational dihedral angles between ring moieties in phenyl-spaced DBA.	27
Table 2.2: DFT-calculated spin densities for [SQ-Ph-NN] ⁻	35
Table 2.3: Simulated isotropic nitrogen hyperfine coupling constants for molecules 1-6.	42
Table 2.4: Dihedral angles (°) from DFT-optimized geometries of molecules 1-6.....	43
Table 2.5: DFT band assignments for Tp ^{Cum,Me} Zn(SQ-Thp-NN).....	60
Table 2.6: Ring torsion angles of the DFT-optimized structures of Tp ^{Cum,Me} Zn(SQ-Thp ₂ -NN) (trans/cis) and Tp ^{Cum,Me} Zn(SQ-Ph ₂ -NN). Crystal structure data is a private communication with D. A. Shultz, North Carolina State University, unpublished (2012).	69
Table 2.7: DFT band assignments for Tp ^{Cum,Me} Zn(SQ-Thp ₂ -NN).	78
Table 2.8: DFT band assignments for Tp ^{Cum,Me} Zn(SQ-Ph ₂ -NN).....	80
Table 2.9: Theoretical Boltzmann populations of the singlet and triplet levels for Tp ^{Cum,Me} Zn(SQ-Ph ₂ -NN) and Tp ^{Cum,Me} Zn(SQ-Thp ₂ -NN) assuming 2J = +40 cm ⁻¹ and +80 cm ⁻¹ , respectively.	87
Table 2.10: Fit of the functional form of the nitrogen and bridging carbon spin populations of NN as the donor, acceptor, and bridge rings are rotated away from planarity. This is a fit of the data presented in Figure 2.8 (section 3.2.2), R ² values for all fits are 1.00.....	99
Table 2.11: Selected dihedral angles for sterically-hindered D-B-A biradicals.	102
Table 2.12: DFT-calculated spin populations in sterically-hindered DBA biradicals....	103
Table 2.13: DFT band assignments for Tp ^{Cum,Me} Zn(SQ-Xyl-NN).	106
Table 2.14: DFT band assignments for Tp ^{Cum,Me} Zn(SQ-PhMe-NN).....	109
Table 2.15: DFT band assignments for Tp ^{Cum,Me} Zn(SQ-MePh-NN).....	112
Table 2.16: DFT band assignments for Tp ^{Cum,Me} Zn(SQ-mPh-NN).....	126
Table 2.17: Selected dihedral angles and bond distances for fully optimized the NN-Ph-SQ/Cat-Co-SQ/Cat-Ph-NN.	140
Table 3.1: Calculated EPR parameters for the enzyme active site model featuring either an oxo or a hydroxy ligand as compared to published experimental ¹²⁵ enzyme EPR parameters.	165
Table 3.2: Isotropic and dipolar components of the Cu hyperfine tensor.....	167
Table 3.3: ENDOR parameters for CO reduced CODH. ^d	172
Table 3.4: DFT-calculated EPR parameters for the CODH active site with an equatorial oxo ligand.....	173
Table 3.5: DFT-calculated EPR parameters for the CODH active site with an equatorial hydroxo ligand, part 1.	174
Table 3.6: DFT-calculated EPR parameters for the CODH active site with an equatorial hydroxo ligand, part 2.	174

Table 3.7: DFT-calculated bond orders and atomic charges for CODH active site structures with an equatorial hydroxo ligand and CO bound at Cu.....	176
Table 3.8: DFT-calculated EPR parameters for alternative CO binding modes in the CODH active site.	179
Table 3.9: Calculated EPR parameters for the CODH active site with an equatorial bicarbonate ligand (all hyperfine coupling constants given in MHz).....	181
Table 3.10: Selected bond distances and angles of CODH models compounds Tp ^{iPr} MoO(OAr)(μ-S)Cu(Me ₃ tacn) and the oxidized enzyme active site.....	183
Table 3.11: DFT-calculated molecular orbital compositions of the SOMO, LUMO and LUMO+1 for Tp ^{iPr} MoO(OPh)(μ-S)Cu(Me ₃ tacn).	186
Table 3.12: DFT-calculated molecular orbital compositions of the HOMO and HOMO-n orbitals for Tp ^{iPr} MoO(OPh)(μ-S)Cu(Me ₃ tacn).	186
Table 3.13: DFT-calculated molecular orbital compositions of the α and β SOMO, and Mulliken spin populations for Tp ^{iPr} MoO(OPh)(μ-S)Cu(Me ₃ tacn).	189
Table 3.14: Simulated EPR parameters of Tp ^{iPr} MoO(OAr)(μ-S)Cu(Me ₃ tacn).	193
Table 3.15: DFT-calculated band assignments for Tp ^{iPr} MoO(OPh)(μ-S)Cu(Me ₃ tacn).	203
Table 3.16: Energies of Gaussian resolved electronic absorption bands of Tp ^{iPr} MoO(OAr)(μ-S)Cu(Me ₃ tacn).....	205
Table 3.17: Energies of Gaussian resolved MCD bands of Tp ^{iPr} MoO(OAr)(μ-S)Cu(Me ₃ tacn).	210
Table 4.1: Experimental absorption band energies and molar extinction coefficients, ε, and band assignments for Re ₂ Cl ₄ (PMe ₃) ₄ PF ₆ and Re ₂ Br ₄ (PMe ₃) ₄ PF ₆	237
Table 4.2: DFT-calculated band energies and oscillator strengths, and band assignments for Re ₂ Cl ₄ (PMe ₃) ₄ PF ₆ and Re ₂ Br ₄ (PMe ₃) ₄ PF ₆	238
Table 4.3: DFT-calculated contributions to C-term intensity for the δ → δ* transition.	243
Table 4.4: Band energies and heights of the Gaussian bands used to fit the 5 K MCD data from the Gaussian resolved MCD fit of Re ₂ Br ₄ (PMe ₃) ₄ PF ₆ and Re ₂ Cl ₄ (PMe ₃) ₄ PF ₆	248
Table 4.5: Selected bond lengths of DFT-optimized structures of Re ₂ Cl ₄ (PMe ₃) ₄ ⁺ and Re ₂ Br ₄ (PMe ₃) ₄ ⁺	251
Table 4.6: Composition of molecular orbitals for Re ₂ Cl ₄ (PMe ₃) ₄ ⁺ and Re ₂ Cl ₄ (PMe ₃) ₄ ⁺	253

CHAPTER 1

1. INTRODUCTORY REMARKS

In this dissertation the research results for three different molecular systems are presented, which exhibit different degrees of intramolecular electronic communication coupling between the Donor and Acceptor moieties. We have utilized a variety of spectroscopic and computational methods to develop a description of the electronic structure of each system. This work is organized as follows: the first chapter contains a brief introduction of the theoretical concepts used in the descriptions of molecular properties and molecular structure. Chapter 2 describes our studies of donor-bridge-acceptor biradicals, possess variable π conjugation. Chapter 3 details computational studies of the hetero-bimetallic enzyme active site of carbon monoxide dehydrogenase (CODH), as well as experimental and computational studies of synthetic model compounds of the CODH enzyme active site. Chapter 4 contains experimental and computational work on high-symmetry rhenium (Re) dimers. Chapter 5 provides a brief conclusion that summarizes significant results from chapters 2-4, and highlights some common themes encountered in the electronic structure descriptions and the research approaches used.

1.1 Valence Bond Configuration Interaction

The Valence Bond Configuration Interaction (VBCI) model¹ represents an alternative to the more familiar molecular orbital description of electronic structure. In the molecular orbital description, the wavefunction is a single determinant, When two

fragment orbitals (such as a metal and a ligand, or a donor ring fragment with an acceptor ring fragment, etc.) mix, a new wavefunction is formed that is a linear combination of the original fragment orbitals, and the relative magnitude of the mixing is reflected in the orbital coefficients of the new wavefunction.

In the VBCI model, the ground configuration mixes with excited configurations by configuration interaction. Excited configurations are formed from the ground configuration by one or more one-electron promotions. Typically, the excited configurations that interact with the ground configuration most strongly are those that are energetically close to the ground configuration (i.e. low energy excited states), and have the same spin multiplicity. A VBCI description can be a very useful tool in spectroscopic studies, since electronic transitions occur between states, and the VBCI model is expressed in terms of configurations, states and integrals that describe the interactions between various configurations. Tuzek and Solomon¹ reviewed several interesting examples of how the VBCI model has been used to understand various molecular systems, including how the most important excited state configurations and their corresponding interactions depend on the specific nature of the system. For example, VBCI descriptions for ligand bridged transition metal dimers can be expressed in terms of exchange integrals, Coulomb integrals, and either exchange- or Coulomb-mediated excitation transfer integrals. Additionally, multiple configurations or states can be considered, including ligand-metal charge transfer (LMCT) excited states or metal-metal charge transfer (MMCT) excited states, and the charge transfer and exchange integrals that describe the single-site orbital interactions pertaining to those excited states.

Importantly, the electronic coupling matrix element, H_{ab} , can be related to ground state covalency.

The use of the VBCI model can be illustrated using recent examples from Shultz and Kirk,²⁻⁴ where it was used to describe the electronic origin of the ferromagnetic exchange coupling between the nitronyl nitroxide (NN) acceptor and semiquinone (SQ) donor in donor-acceptor and donor-bridge-acceptor heterobiradicals as shown in Figure 1.1. In the ground state, one unpaired spin resides in the NN singly-occupied molecular orbital (SOMO), and the other unpaired spin in the SQ SOMO. The ground state can either be a spin singlet configuration, 1GC , or a spin triplet configuration, 3GC . Since there is no amplitude on the bridgehead carbon of the NN SOMO in $Tp^{Cum,Me}M(SQ-NN)$ that directly connects to the SQ SOMO, to a first approximation there is no orbital overlap between these two fragments. Thus the spins in the SQ and NN SOMOs do not interact, and the singlet- and triplet ground state configurations are degenerate. An intraligand donor \rightarrow acceptor charge transfer process can promote an electron from the SQ SOMO to the NN lowest unoccupied molecular orbital (LUMO) to create an excited state that can also be a triplet (3EC) or singlet (1EC). However, in the excited state, the NN LUMO and NN SOMO have considerable overlap densities, and the triplet configuration is stabilized over the singlet configuration via the single-site exchange interaction between the spin in the NN SOMO and the spin in the NN LUMO (Figure 1.1 (a)).

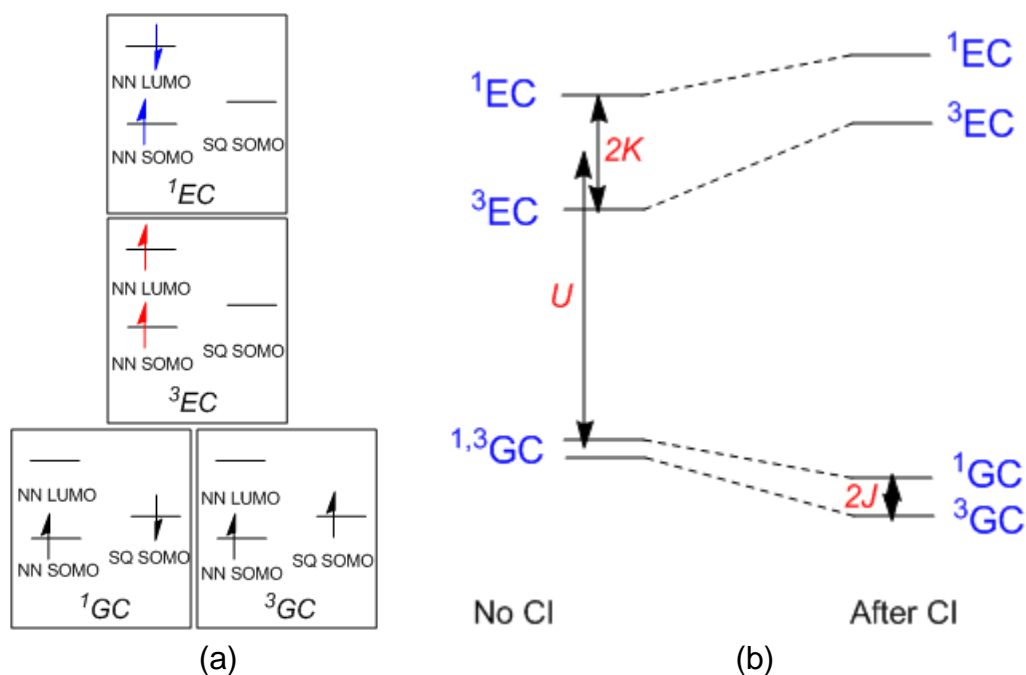


Figure 1.1: VBCI description of ferromagnetic coupling in [SQ-NN]⁻ biradicals. Adapted from reference ³.

Configuration interaction (CI) allows the singlet excited configurations (1EC) to admix with the singlet ground configuration (1GC), and likewise for the triplet excited- and ground configurations (3EC , 3GC). Since the 3EC s are energetically closer to the GC than the 1EC s, it is anticipated that the 3GC - 3EC mixing will be stronger, allowing the 3GC to be more stabilized than the 1GC (Figure 1.1 (b)). Thus the donor and acceptor spins in conjugated D-B-A biradical complexes are coupled ferromagnetically, as confirmed by magnetic susceptibility measurements, electron paramagnetic resonance (EPR) spectroscopy, and electronic absorption studies. An example is depicted in Figure 1.1 (b), where the energy differences between the four configurations correspond to experimental observables. Here, the 3GC - 1GC energy gap is parameterized by the ground state magnetic exchange parameter ($2J$), the gap 3EC - 1EC is the single-site exchange

integral $2K$, and the average charge transfer energy is U . Magnetic susceptibility measurements were used to determine $2J$, while U and K can be determined independently from variable-temperature electronic absorption measurements when both the 3GC and 1GC can be thermally populated.²⁻⁴

The value of the VBCI model lies not only in the fact that its parameters are related to experimental observables, but that it related excited state contributions to observed ground state properties. Additionally, the VBCI description allows one to more clearly separate what the contribution of each excited configuration should be to an observed ground state property, even if a specific contribution might be small.

In our research presented in this dissertation we use a variety of experimental techniques to access the ground- and excited state parameters of the VBCI models used to describe the molecules we study. Chapter Two utilizes a VBCI description for donor-bridge-acceptor biradicals that describes the ground state magnetic properties that derive from excited configuration interaction with the ground configuration. The ground state singlet-triplet gap, $2J$, is measured by magnetic susceptibility in the solid state and variable-temperature electronic absorption spectroscopy for polymer films of the D-B-A samples. Electronic absorption spectroscopy allows us to observe the donor \rightarrow acceptor charge transfer transition ($U-K$), which is energy separation of the triplet ground state and triplet excited configuration for the D-A CT excited state in ferromagnetically coupled biradicals. We can combine magnetic susceptibility measurements and variable-temperature absorption spectroscopy to separate the singlet and triplet components to the electronic absorption spectra, which allows us to observe $2K$, the single-site exchange

interaction that splits the singlet and triplet excited states. Using a variety of optical and magnetic techniques we can thus develop a detailed understanding of the electronic structure of the molecules within a VBCI framework.

In chapter Three we continue this strategy in the study of the covalency in the heterobimetallic active site of CODH, where a VBCI description of the enzyme active site and active site synthetic model compounds was developed based on the observed EPR of the molecules and active site. The VBCI model predicts the importance of MMCT states to the ground state properties of the molecules, and our electronic absorption and magnetic circular dichroism data provides experimental evidence for those MMCT contributions.

We also use DFT calculations to enhance our understanding of the electronic structure of the molecular systems we study. We correlate observed experimental data to DFT calculated parameters in order to ascertain if the DFT calculations accurately reflect the electronic structure of the molecule. Once DFT results have been thus spectroscopically calibrated, we use the additional details that DFT results provide to enhance and compliment our understanding of the experimental data. In chapter Two we use the correlation of nitrogen hyperfine coupling constants, which measure the unpaired spin on the nitrogen nuclei in an EPR experiment, to DFT-calculated spin populations on the nitrogen nuclei to validate the DFT description of our D-B-A biradicals. We then use our DFT-calculated results to aid in band assignments, in describing the excited state distortion of the bridge during the D-A CT transition, and in developing a detailed

description of ferromagnetic and antiferromagnetic exchange mechanism in our D-B-A biradicals.

1.2 Robin-Day Classification

In 1967 Robin and Day devised a classification for mixed-valent compounds, where they focused on mixed valency of transition metal ions in the presence of their ligand sets.⁵ This classification has been widely used, and we adapt here a graphical

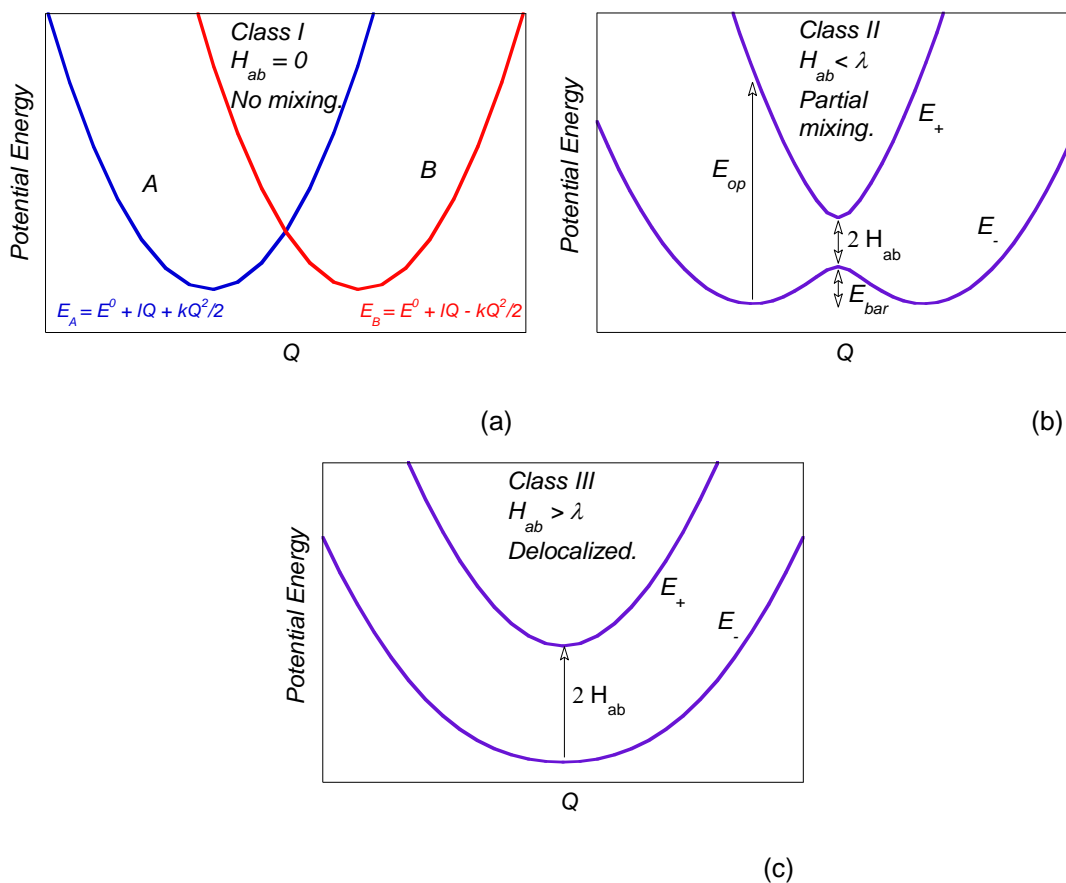


Figure 1.2: Potential energy surfaces of class I (a), II (b), and III (c) mixed-valent compounds in the Robin-Day classification, adapted from Kahn.⁶

description of mixed valent dimers published by Kahn⁶ (Figure 1.2). Figure 1.2 (a) illustrates a class I system, in which there is no orbital interaction between two mixed-valent metal ion sites A and B (Eq. 2). In chapter 4, we will describe mixed-valent compounds where A and B are rhenium ions of a metal dimer surrounded by trimethylphosphine and halide ligands, while in chapter 2 we describe a cobalt complex with mixed-valent ligands, where A and B are semiquinone- and catecholate ligands. Ψ_A is the unmixed electronic wavefunction of site A, and Ψ_B the unmixed electronic wavefunction of site B (Eq. 1).

$$\langle \Psi_A | \hat{H} | \Psi_A \rangle = \langle \Psi_B | \hat{H} | \Psi_B \rangle = E^0 \quad \text{Eq. 1}$$

$$\langle \Psi_A | \hat{H} | \Psi_B \rangle = 0 \quad \text{Eq. 2}$$

The potential energy surface of either site can be expressed as a quadratic equation in Q as shown in the panel, where Q is the vibrational coordinate that describes the electronic relaxation of bonds in response to the oxidation state of A or B. If the unpaired electron in the mixed-valent molecule resides in an antibonding orbital on A, the metal-ligand bonds around A are lengthened. In the same manner, when the excess electron resides on B the metal-ligand bonds of A contract and metal-ligand bonds on B expand. This leads to an antisymmetric breathing mode Q , with an associated force constant k , and a magnitude of the vibrational distortion, l .⁶ Energy minima of the potential energy surface for A and B occur at:

$$Q = \pm l/k. \quad \text{Eq. 3}$$

The energy for the transfer of the electron between A and B is the energy difference between surface A and B at *the same value of coordinate Q*, as shown in Eq. 4.

$$E_{op} = E_B(Q = -l/k) - E_A(Q = -l/k) = 2 l^2/k \quad \text{Eq. 4}$$

In a class II system (Figure 1.2 (b)), there is a non-zero orbital interaction between sites A and B, where H_{ab} is the transfer integral between A and B, also denoted as H_{ab} , and can be related to A-B covalency between A and B.

$$H_{ab} \equiv \langle \Psi_A | \hat{H} | \Psi_B \rangle . \quad \text{Eq. 5}$$

This non-zero off-diagonal matrix element, H_{ab} , results in a new set of equations describing A, B and the interaction between A and B. Here E_- describes the mixed A, B ground state surface and E_+ the excited state surface:

$$E_- = E^0 + \frac{kQ^2}{2} - \sqrt{l^2Q^2 + H_{ab}^2} \quad \text{and} \quad E_+ = E^0 + \frac{kQ^2}{2} + \sqrt{l^2Q^2 + H_{ab}^2} . \quad \text{Eq. 6}$$

Note that there is a non-zero energy barrier E_{bar} for electron transfer from A to B as a class II mixed-valent system has only partial orbital mixing between sites A and B (Figure 1.2 (b)).

A class III system (Figure 1.2 (c)) is one where the A-B mixing is large enough that the energy barrier has disappeared, and the system is said to be valence delocalized. The condition for the presence of an energy barrier between sites A and B depends on the magnitude of H_{ab} with respect to λ , the so-called vibronic coupling parameter:

$$\lambda \equiv l^2/k. \quad \text{Eq. 7}$$

The energy barrier (E_{bar}) vanishes when $H_{ab} \geq \lambda$ (Eq. 8), and the barrier-less ground state surface forms a new minimum at $Q = 0$, where a value of zero for the vibrational coordinate Q corresponds to equal geometric parameters (metal-ligand bond lengths, etc.) for sites A and B. A transition between the delocalized ground state potential energy surface to the excited surface has an energy of $2 H_{ab}$ in the class III limit.

$$E_{bar} = E_+(Q = 0) - E_{- \text{ at min}}, \text{ and thus } E_{bar} = \frac{l^2}{2k} + \frac{\beta^2 k}{2l^2} - |\beta| \quad \text{Eq. 8}$$

Valence delocalization within this description is thus a balance between the magnitude of the off-diagonal mixing element, H_{ab} , that when large favors delocalization, and the vibronic coupling parameter, λ , that when large favors a localization and geometric asymmetry between the two sites. Thus a completely-mixed class III valence delocalized system will possess a wavefunction with equal- or close-to-equal wavefunction coefficients for A and B, and indistinguishable sites A and B sites in terms of oxidation state and geometric parameters.

CHAPTER 2

2. SPECTROSCOPIC AND COMPUTATIONAL STUDIES OF DONOR-BRIDGE-ACCEPTOR BIRADICALS AND (EXTENDED) MOLECULAR ASSEMBLIES UTILIZING DONOR-BRIDGE-ACCEPTOR BIRADICALS

2.1 Introduction

A better understanding of donor-acceptor electronic communication across a molecular bridge, as well as magnetic exchange coupling over extended distances in molecular systems will be valuable in the rational design of future molecular electronic systems.^{7,8} A fundamental advantage of molecular electronics lies in the fact that molecules are generally easier to produce (i.e. synthesize) in a precise and uniform fashion at the nanoscale than semiconductor devices.⁹ In addition to challenges in device uniformity, the manufacturing process of microelectronic devices becomes increasingly more complicated as devices become smaller, and may be limited by dopant irregularities as well as by the limit to the speed at which the electrons can travel through a semiconductor material in the presence of lattice defects.

A prominent example of a molecular analogue to a microscale electronic device is an Aviram-Ratner diode.¹⁰ In an Aviram-Ratner diode, the p-n junction of a semiconductor device is replaced by a molecular construct where the ability to rectify current is designed into a molecule with an internal bias achieved by donor and acceptor moieties connected via a σ -bond “molecular barrier”. Other examples include molecular constructs that promote spin-polarized electron transport, where spin-dependent

intermolecular electron transfer is designed by the use of spin polarization within the molecules.¹¹

While researchers continue to explore, to understand, and to design molecules with specific conductive and magnetic functionalities,^{2-4,7,9-18} the connection of molecular electronic devices to bulk electrodes or surfaces while preserving the usefulness of the molecular “device” still presents a formidable challenge. For example, electron transport through delocalized states in molecular wires can be very fast, but is thought to be limited at the molecular-bulk interface.¹⁹ The interactions of bulk and molecular systems at the interface continue to be studied in both experimental conductance measurements²⁰⁻²⁹ and theoretical electron transport calculations.³⁰⁻⁴²

The nitronyl nitroxide radical is a well-known and stable molecular radical that has been used to construct heterospin biradical molecules (i.e. molecules containing two radical moieties that are not the same).^{2,3,16,43,44} These heterospin biradicals have been suggested to represent stable ground state analogues of radical pairs generated in photo-induced electron transfer processes,³ where $D^{\bullet}BA^{\bullet}$ is a ground state heterospin biradical, and $D^{+\bullet}BA^{-\bullet}$ is a excited state radical pair. Radical pairs generated by photo-induced electron transfer have short lifetimes, requiring using transient optical spectroscopies or time-resolved EPR experiments.^{18,45-57} Therefore, acquiring data on such species is inherently more difficult than for stable ground state biradicals.

Sugawara *et al.* have utilized the nitronyl nitroxide (NN) radical to construct heterobiradical molecules by binding the NN radical to benzoquinone and tetrathiafulvalene, and forming the biradical species in a redox process.⁵⁸ Both

antiferromagnetic and ferromagnetic exchange coupling was observed in these compounds, and the mechanism for ferromagnetic exchange is similar to that observed for the SQ-NN biradical ligand in $\text{Tp}^{\text{Cum,Me}}\text{Zn-SQ-NN}$. Namely, a large excited state exchange interaction between the unpaired spin in the NN SOMO and the unpaired spin in the SOMO of the benzoquinone moiety, which possesses partial NN LUMO character.

Heterospin biradicals that possess this type of ferromagnetic exchange coupling mechanism where the NN radical acts as an acceptor, and the semiquinone (SQ) radical acts as a donor, have been studied extensively by Kirk and Shultz.^{2-4,15,59-63} These biradical ligands are complexed to a divalent transition metal (M^{2+}), and form neutral complexes of the form $\text{Tp}^{\text{Cum,Me}}\text{M-SQ-NN}$ ($\text{Tp}^{\text{Cum,Me}}$ = hydro-tris(3-cumenyl-5-methylpyrazolyl)borate). In these complexes, the metal ion may also be paramagnetic. Here, it was observed that the intraligand exchange coupling is dominant, and variable metal-biradical exchange is observed dependent on the nature of the divalent metal.⁵⁹ When the metal ion is a spin singlet (i.e. Zn^{2+}), one can study the SQ-NN ligand exchange interaction directly. For this reason, the $\text{Tp}^{\text{Cum,Me}}\text{Zn(SQ-NN)}$ “parent” complex was chosen for detailed spectroscopic studies probing the electronic origin of the observed ferromagnetic exchange interaction. This has been expanded to include $\text{Tp}^{\text{Cum,Me}}\text{M(SQ-B-NN)}$ complexes where a bridge molecule is located between the donor and acceptor.^{3,4}

The $\text{Tp}^{\text{Cum,Me}}\text{Zn(SQ-NN)}$ donor-acceptor biradical exhibits a large ground state ferromagnetic coupling with $J \sim 550 \text{ cm}^{-1}$.^{3,59} A perturbative expression based on a VBCI description of the biradical was developed,³ and this expresses the donor-acceptor electronic coupling matrix element, H_{ab} , in terms of J, K, and U, which are all

experimental observables obtained from magnetic susceptibility measurements (J) and variable-temperature electronic absorption measurements.^{3,4,59} These are related as follows:

$$2J = \frac{2H_{ab}^2 K}{U^2 - K^2} \quad \text{Eq. 9}$$

Here, $(U-K)$ is the intraligand donor \rightarrow acceptor triplet charge transfer energy, and $(U+K)$ is the intraligand donor \rightarrow acceptor singlet charge transfer energy. In order to obtain values for both U and K independently, one needs to be able to observe both the triplet and singlet component of the intraligand $D \rightarrow A$ charge transfer band. This is not possible for the SQ-NN interaction in $\text{Tp}^{\text{Cum,Me}}\text{Zn}(\text{SQ-NN})$, since the singlet-triplet ground state gap is large ($\sim 1100 \text{ cm}^{-1}$).⁵⁹ This problem was overcome by using $\text{Tp}^{\text{Cum,Me}}\text{Ni}(\text{SQ-NN})$, where the nickel $S = 1$ ion can exchange couple with the spin triplet ground state of the radical to yield $S = 0, 1$, and 2 levels that are thermally accessible.³ Using the perturbative expression in Eq. 9, the H_{ab} calculated for $\text{Tp}^{\text{Cum,Me}}\text{Zn}(\text{SQ-NN})$ was $\sim 13500 \text{ cm}^{-1}$, and for $\text{Tp}^{\text{Cum,Me}}\text{Zn}(\text{SQ-Ph-NN})$ an attenuated value of $\sim 5700 \text{ cm}^{-1}$ was obtained.

Wasielewski and coworkers have dedicated themselves to the study of the charge separation and charge recombination processes in photo-generated radical pairs that exhibit very small exchange couplings on the order of 1 cm^{-1} or less.^{18,45-57} In order to generate the radical pair, the molecule chromophore is photoexcited with a laser pulse leading to charge separation followed by either direct charge recombination, or intersystem crossing followed by charge recombination (where the radical pair has

typical lifetimes of ~15 - 200 ns). These molecular systems are generally large organic ring systems where the donor, excitation chromophore, and acceptor rings are almost perpendicular (dihedral angles of 70-90°). Small exchange interactions are an integral part of the experimental strategy in these systems, where the presence of an external magnetic field enhances the charge recombination rate significantly when the microwave source during the EPR field sweep matches the triplet-singlet gap energy of 2J. The triplet yield of the radical pair is monitored by transient absorption spectroscopy, and the observation of an enhanced triplet yield at the 2J resonance allows for the small singlet-triplet splitting to be measured directly in the excited state.

Interestingly, the rate constant for charge recombination, k_{CR} , that is measured by transient absorption spectroscopy in an applied magnetic field, are related to the electronic coupling matrix element, H_{ab} , for the radical pair, and $FCWD$, the Franck-Condon weighted density of states⁵⁴:

$$k_{CR} = \frac{2\pi}{\hbar} |H_{ab(CR)}^2| (FCWD). \quad \text{Eq. 10}$$

Wasielewski *et al.*⁵⁴ have studied a variety of factors that influence charge recombination rates and mechanisms in these systems. This includes determining the effect of variations in molecular structure on charge recombination rates, where the charge recombination rates are proportional to H_{ab}^2 .⁵⁴ Another example involves a study by Weiss *et al.*⁵³ of the rates of charge recombination as a function of bridge distance, where it was found that the charge recombination mechanism switches from superexchange to charge hopping as the bridge gets longer. This switch was shown to be

due to (a) the superexchange decaying exponentially as measured by the exponential decay of k (Eq. 11) and (b) the charge hopping increasing for multiple para-phenylene bridge fragments ($n = 4, 5$) as the donor oxidized radical pair and bridge oxidized radical pair come into resonance. Equation 11¹⁷ describes the exponential decay of the electron transfer rate

$$k = k_0 e^{-\beta(r-r_0)} \quad \text{Eq. 11}$$

constant, k , where k_0 is the electron transfer rate constant at the van der Waals contact distance, r_0 is the van der Waals contact distance, and β is an exponential decay factor.¹⁷

Recently, there have been examples in the literature using cross-conjugated bridges to severely attenuate charge separation rates.¹⁷ Here, charge separation and recombination rates were measured experimentally for cross-conjugated, and linearly-conjugated bridges. It was observed that the cross-conjugated bridge had a charge separation rate that was ~30 times slower than that of the linearly-conjugated bridge. This result was correlated with the calculated transmission spectra for the compounds, and the authors concluded that quantum interference in the cross-conjugated system cuts off electron transport through the π electron system so that the observed rate corresponds to the much slower transport mediated by the σ system.

Bardeen *et al.* used transient absorption measurements to compare electron transfer rates in photo-generated donor-bridge-acceptor molecules, using a phenyl-acetylene bridge that was either para- or meta-conjugated to the donor and acceptor.⁶⁴ Time-resolved absorption spectroscopy measurements revealed similar forward electron

transfer rates but very different back electron transfer rates for meta- versus para-conjugation. The meta-conjugation enhances charge separation over charge recombination, and charge recombination is significantly slower for the meta-conjugated molecules (16.8 ns) compared to the para-conjugated molecule (1.8 ns).

Thus both experimental charge recombination rates and calculated transmission spectra reported in the literature indicate that the nature of the bridge conjugation in the molecular system has a large impact on electron transport behavior.^{17,64}

2.2 Experimental Details

2.2.1 Electronic Structure Calculations

Spin unrestricted gas-phase geometry optimizations for all compounds were performed at the density functional level of theory using the Gaussian03 program.⁶⁵ $\text{Tp}^{\text{Cum,Me}}\text{Zn}(\text{SQ-NN})$, $\text{Tp}^{\text{Cum,Me}}\text{Zn}(\text{SQ-Ph-NN})$, $\text{Tp}^{\text{Cum,Me}}\text{Zn}(\text{SQ-Thp-NN})$, $\text{Tp}^{\text{Cum,Me}}\text{Zn}(\text{SQ-Ph}_2\text{-NN})$, $\text{Tp}^{\text{Cum,Me}}\text{Zn}(\text{SQ-Thp}_2\text{-NN})$, $\text{Tp}^{\text{Cum,Me}}\text{Zn}(\text{SQ-Xyl-NN})$, $\text{Tp}^{\text{Cum,Me}}\text{Zn}(\text{SQ-MePh-NN})$, and $\text{Tp}^{\text{Cum,Me}}\text{Zn}(\text{SQ-PhMe-NN})$ have spin multiplicities of three, while NN-Ph and NN-Ph(OMe)₂ have spin multiplicities of two. All $\text{Tp}^{\text{Cum,Me}}\text{Zn}(\text{SQ-Bridge-NN})$ compounds are neutral, whereas [SQ-Bridge-NN]⁻ “ligands” are monoanions. All calculations employed the B3LYP hybrid exchange-correlation functional.^{66,67} A 6-31G(d,p) basis set, a split valence basis set with added polarization functions, was used for all atoms. For calculations on NN-Ph-SQCo^{III}(py)₂Cat-Ph-NN (multiplicity four, charge zero) a LANL2DZ basis set with effective core potentials⁶⁸⁻⁷⁰ was used for Co. Input files were prepared using the molecule builder function in the

Gaussview⁷¹ software package. Geometries with dihedral angles between zero and 180 degrees in steps of 15° between the nitronyl nitroxide and phenyl ring or the phenyl and semiquinone ring were constructed. With the two dihedral angles fixed, all remaining coordinates were allowed to optimize to the lowest energy geometry. Mulliken spin populations were extracted directly from the printed output of the Gaussian logfiles. DFT frequency calculations were done on the ligands, i.e. [SQ-NN]⁻, and [SQ-Bridge-NN]⁻. For time-dependent DFT⁷²⁻⁷⁵ calculations we found better agreement between computed and experimental band energies when using the full, neutral molecules.

Electron density difference maps (EDDMs) were constructed utilizing the “EDDM, Transition Density, and Orbital Generation for ADF and Gaussian 03” program written by Ben Stein at the UNM Department of Chemistry and Chemical Biology, 2011. SWizard^{76,77} was used to construct electronic absorption spectra from the Gaussian TD-DFT output file using Gaussian band shapes and half-bandwidths of 4000 cm⁻¹. The AOMix^{76,77} molecular orbital analysis program, version 6.51 was used to obtain compositions of molecular orbitals using a Mulliken population analysis, where overlap populations were split equally between two atoms, and the gross atomic population of an atom A, GP_A , is calculated as the summation where i runs over all molecular orbitals,

$$GP_A = \sum_i n_i \sum_{a \in A} \sum_k c_{ai} c_{ki} S_{ak} \quad \text{Eq. 12}$$

n_i is the number of electrons in a molecular orbital (0,1, or 2), k runs over all atomic orbitals of the molecules, a runs over all the atomic orbitals of atom A, S is the overlap integral, and c_{ai} and c_{ki} are the orbital coefficients of the atomic orbitals of atom A in

molecular orbital i and the atomic orbitals k of the molecule in molecular orbital i , respectively.

Complete-active space self-consistent field (CASSCF) calculations, which are based on a multiconfigurational approach,⁷⁸ were carried out for $\text{Tp}^{\text{Cum,Me}}\text{Zn}(\text{SQ-mPh-NN})$ using the ORCA SCF-MO program.^{79,80} CASSCF calculations employed a def2-TZVP triple zeta basis set with added polarization functions, and a convergence tolerance for the orbital gradient of $1\text{e-}4$. The energy was optimized for the singlet and triplet ground state with respect to the coefficients of the configurations that contribute to each state as well as the molecular orbital coefficients of the spin-restricted orbitals.

2.2.2 Electron Paramagnetic Resonance Spectroscopy (EPR)

EPR⁸¹ spectra were acquired on a Bruker model ESP 300 spectrometer with an X-band Bruker ER041XG microwave bridge (9.38 GHz) for $\text{Tp}^{\text{Cum,Me}}\text{Zn}(\text{SQ-Ph}_2\text{-NN})$. Simulations of the isotropic EPR spectra were carried out in the Bruker EPR simulation software XSophe.⁸² $\text{Tp}^{\text{Cum,Me}}\text{Zn}(\text{SQ-NN})$, $\text{Tp}^{\text{Cum,Me}}\text{Zn}(\text{SQ-Thp-NN})$, $\text{Tp}^{\text{Cum,Me}}\text{Zn}(\text{SQ-Ph-NN})$, and $\text{Tp}^{\text{Cum,Me}}\text{Zn}(\text{SQ-Xyl-NN})$ have a total spin of $S_T = 1$, while NN-Ph and NN-Ph(OMe)₂ have a total spin of $S_T = 0.5$. Hyperfine splitting by two equivalent $I = 1$ nitrogen nuclei was assumed. The isotropic hyperfine splitting and line widths were adjusted to fit the experimental spectra in the spectral simulation. Hyperfine values were simulated with a confidence of $0.5 \times 10^{-4} \text{cm}^{-1}$. These $S = 1$ systems have a Clebsch-Gordan coefficient of 0.5, and the spin 1 nucleus is treated in an uncoupled basis.

The EPR spectrum of $\text{Tp}^{\text{Cum,Me}}\text{Zn}(\text{SQ-Ph}_2\text{-NN})$ was simulated using the EasySpin 4.0.0 Toolbox⁸³⁻⁸⁷ run with MATLAB R2011b. The *pepper* spectral simulation for frozen

solution samples in the EasySpin program was used, and a hyperfine splitting of the electron by two equivalent $I = 1$ nuclei was assumed. As above, the $S = 1$ systems have a Clebsch-Gordan coefficient of 0.5, so that the observed (and simulated) hyperfine values must be multiplied by a factor 2 in order to obtain the intrinsic N hyperfine coupling constant.

2.2.3 Variable-Temperature Electronic Absorption

Low-temperature electronic absorption data can be acquired on either frozen solution samples or films samples. Frozen solution samples often have a higher scattering background and lower sample signals due to both scattering from the cracks in a frozen solution matrix and off of any condensation that may have collected on the windows of the sample during the mounting of the sample in the cryostat. It is thus preferable to make thin film samples, which is what we did for the variable-temperature electronic absorption measurements of the donor-bridge-acceptor molecules in this chapter. The state of the sample in a thin film is similar to that in a frozen solution matrix.

Polystyrene film samples were prepared by dissolving polystyrene beads ($M_w \sim 280,000$) in solvent in an approximate ratio of 1:3 (polystyrene beads:solvent) by volume. The polystyrene takes several hours to dissolve, and the final consistency of the dissolved polystyrene approximates the viscosity of corn syrup. Dichloromethane was used as the solvent because our D-B-A samples are both soluble and relatively stable in this solvent, and because dichloromethane dissolves polystyrene. While the samples are air-stable in the solid state and air-sensitive as solutions (as indicated by our collaborators, Prof. David A. Shultz and group, North Carolina State University), we

erred on the side of caution and undertook all sample preparations in the oxygen-free atmosphere of a glovebox. The dichloromethane solvent used was dried with Alfa Aesar molecular sieves, type 3A, -8+12 beads or by distillation, and then deoxygenated with repeated freeze-pump-thaw cycles. The samples were dissolved in dichloromethane separately from the polystyrene, and the concentration of sample in the solution is quite high (strongly colored) since the sample is later diluted by mixing with the dissolved polystyrene, and since the optical path length through the dried film is short (< 1 mm). The dissolved polystyrene and concentrated sample solution were mixed together by pouring and inverting rather than pipetting to avoid the formation of gas bubbles in the matrix. Since dichloromethane evaporates rather quickly, it is best to use enough solvent to achieve a viscosity between that of syrup and water, so that the film can be poured quickly. Films were poured onto a dry, flat, even surface, and covered immediately (within 10 seconds of being poured) with a watch glass. The addition of the watch glass slows the rate of solvent evaporation, and allows the polystyrene matrix to form a flat and even film. Films then dry for approximately two days.

Liquid nitrogen and liquid helium optical cryostats were used for low-temperature data collection. The liquid nitrogen cryostat can achieve temperatures as low as 75 K, while the liquid helium cryostat can achieve temperatures as low as 5 K. The liquid helium cryostat (Janis STVP-100) is a flow-through type cryostat in which the sample temperature is maintained by a continuous flow of cold helium gas over the sample surface. Our cryostat relies on the gas pressure in the liquid helium tank for positive pressure-flow, i.e. no pump is used. The flow rate is regulated by adjusting the pressure

in the liquid helium tank and/or by using the valve on the helium transfer line. A Lakeshore silicon diode (PT-470) was used to monitor the temperature in the sample space, and a separate heating unit can be used to stabilize the temperature before data acquisition. We used a relatively fast scan speed (300 nm/min in the UV/Vis and 750 nm/min in the NIR) in order to minimize temperature changes during the sample scan. The liquid nitrogen cryostat operates by thermal contact rather than gas flow, where a reservoir filled with liquid nitrogen coolant is connected to a brass sample holder, and a vacuum is applied to the sample space of the assembled cryostat. The vacuum minimizes the thermal losses and also prevents the condensation of moisture from the air onto the sample. Temperature control is achieved by the use of a heating unit close to the sample holder, and by a thermal attenuator within the liquid nitrogen reservoir that controls the size of the area of contact between the liquid nitrogen reservoir and the sample space. For the liquid nitrogen cryostat it is particularly important to allow the sample to thermally equilibrate at each temperature (5-10 minutes), though we also allowed samples to thermally equilibrate when using the flow-through liquid helium cryostat.

Low-temperature electronic absorption measurements were acquired on a Hitachi U-3501 spectrophotometer with the cuvette holder assembly removed to accommodate the cryostat in the sample chamber. The instrument was calibrated to the 656.1 nm deuterium line using the corresponding Hitachi software option, and spectra were resolved with Gaussian bands using Grams/AI, version 7.02 (Thermo Galactic, 1991-2002). Low-temperature electronic absorption spectra of frozen solutions or polystyrene films had a rising baseline due to scattering contributions, and a scattering correction was

applied to the spectra following the methodology of Bendit and Ross,⁸⁸ which uses the relationship of the absorbance due to scattering, A_{sca} , with the wavelength, λ , in a non-absorbing region of the spectrum:

$$A_{sca} = y\lambda^{-x}. \quad \text{Eq. 13}$$

2.2.4 Resonance Raman Spectroscopy

In a resonance Raman⁸⁹ enhancement profile the resonance Raman response of a mode of interest relative to the sulfate internal standard is plotted as a function of the excitation laser line energy. It is necessary to use the same sample (or a sample with the same concentration) for the entire experiment when obtaining a resonance Raman profile. Ideally, the available laser line energies (from the Ar⁺ laser: 458 nm, 488 nm, 514 nm; Kr⁺ laser: 407 nm, 568 nm, 614 nm) will encompass some lines that are on resonance with an absorption band of interest, and some lines that are off resonance with the absorption band, so that the enhancement of the Raman mode as a function of wavelength (energy) can be observed. The modes that will be enhanced under a particular absorption band are those that are coupled to the excited state distortion of the molecule (i.e. the change in the nuclear coordinates) that arises from the redistribution of the electron density in the excited state.

Resonance Raman samples were prepared in a solid state matrix and as solutions in CH₂Cl₂. The solid matrix consisted of finely ground NaCl/Na₂SO₄ in an approximate 10:1 ratio by weight, which was combined with sample powder and ground again to achieve a uniform, finely-ground resonance Raman sample. The resonance Raman samples were put into quartz capillary tubes, which were subsequently flame-sealed to

prevent sample from escaping the tube while the tube was spinning during measurements. Reference peaks for a solid resonance Raman sample are the nine sulfate peaks, and the Raman shifts (x-axis) of the spectra are calibrated to the largest sulfate peak at 992 cm^{-1} . Reference peaks for solution resonance Raman samples were dichloromethane peaks, where the most prominent peaks are at 283 cm^{-1} and 702 cm^{-1} . It is strongly recommended that one always acquire a reference spectrum of the specific solvent one plans to use to prepare the samples, as we have found that our dichloromethane resonance Raman spectrum differs from the published reference spectrum⁸⁹ both in the number of bands observed and in the relative intensities of the bands in the spectrum.

The resonance Raman configuration consists of a Coherent Innova I302C Ar^+ laser or alternatively a Kr^+ laser as the excitation source. The laser light is passed through Maxline laser line filters, which remove plasma lines from the laser output, and Razor Edge long pass filters, which cut off the Rayleigh scattering signal. These filters were obtained from Semrock. The incident laser power was measured at the sample. In order to avoid photobleaching or sample degradation we chose low laser powers ($\sim 15\text{ mW}$ for 407 nm , $\sim 20\text{ mW}$ for 458 nm and 488 nm , $\sim 25\text{ mW}$ for 514 nm , $\sim 35\text{ mW}$ for 568 nm , $\sim 50\text{ mW}$ for 647 nm) as well as short exposure times (ranging from three time exposures of 10 seconds each to 5 exposures of 1 minute each). The sample was also continually spun when exposed to the laser light in order to distribute the heat throughout the sample and minimize degradation. Scattered light at a 90° angle was focused by a series of lenses and directed to the input slit of a PI/Acton Spectrapro SP-2500i 500 mm focal length spectrograph with a triple-grating turret monochromator and finally to the liquid-nitrogen

cooled detector (PI/Acton Spec-10:100B back-illuminated 1340x100 pixel digit CCD camera).

Even using low laser powers and having the sample tube spin to distribute the heat more evenly, we observed degradation of the solution samples after we acquired a few resonance Raman spectra. This was evident by a color change or loss of color for the sample. This meant that solution samples could not be used to construct the resonance Raman profiles. Another problem we experienced when using solution samples was that a number of samples showed fluorescence emissions using selected laser lines, thus obscuring the resonance Raman signal. We therefore used solid state samples for the resonance Raman measurements used to construct the resonance Raman enhancement profiles presented in sections 2.4, 2.5, and 2.6.

2.3 Extending Previous Studies on $\text{Tp}^{\text{Cum,Me}}\text{Zn}(\text{SQ-Ph-NN})$

Previous work on $\text{Tp}^{\text{Cum,Me}}\text{Zn}(\text{SQ-Ph-NN})$ in the Kirk group was completed by Prof. Martin L. Kirk, Dr. Ezra C. Depperman (Depperman, E. C., PhD Thesis: Spectroscopic and Theoretical Characterization of Strong Ferromagnetic Interaction in Heterospin Biradicals, 2005), and by our collaborators in Prof. David A. Shultz's group (North Carolina State University). Prior data on $\text{Tp}^{\text{Cum,Me}}\text{Zn}(\text{SQ-Ph-NN})$ include resonance Raman spectroscopy, electronic absorption spectroscopy, EPR, and magnetic susceptibility measurements.^{4,90} Here, we describe the extension of the computational work started by Dr. Depperman on $\text{Tp}^{\text{Cum,Me}}\text{Zn}(\text{SQ-Ph-NN})$ to include additional detailed DFT electronic structure calculations. New ideas have evolved from these extended

computational studies as they relate to excited state contributions to the magnetic exchange.

2.3.1 Strong Acceptor-Bridge Interactions

Optimized geometries were calculated using DFT for both the biradical ligand, $[\text{SQ-Ph-NN}]^-$ and the full molecule $\text{Tp}^{\text{Cum,Me}}\text{Zn}(\text{SQ-Ph-NN})$, where NN is the nitronyl nitroxide acceptor radical, Ph is the phenyl bridge, SQ is the semiquinone donor radical, and $\text{Tp}^{\text{Cum,Me}}$ (= hydro-tris(3-cumenyl-5-methylpyrazolyl)borate) is a bulky substituted ligand, as shown in Figure 2.1.

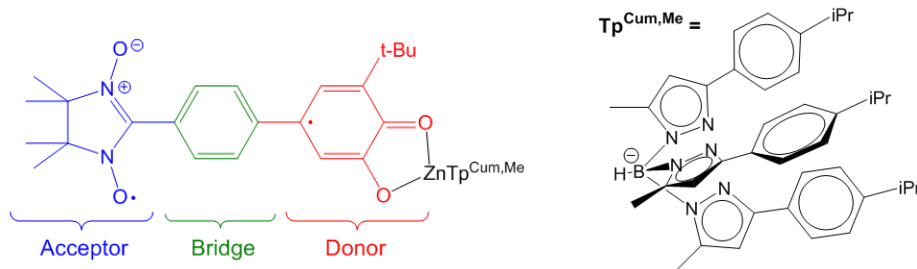


Figure 2.1: ChemDraw rendition of $\text{Tp}^{\text{Cum,Me}}\text{Zn}(\text{SQ-Ph-NN})$.

The optimized structure for $\text{Tp}^{\text{Cum,Me}}\text{Zn}(\text{SQ-Ph-NN})$ is shown in Figure 2.2. Notice that the t-Butyl (t-Bu) group on the semiquinone has been replaced by a methyl group. We found that the presence of the t-Butyl group does not affect the optimized geometry (i.e. specifically the dihedral angle between donor and bridge). However, it does add nine additional atoms to the calculation, and more importantly we found that the methyl groups on the t-Butyl substituent tend to have small rotational motions that make it difficult to achieve geometry convergence.

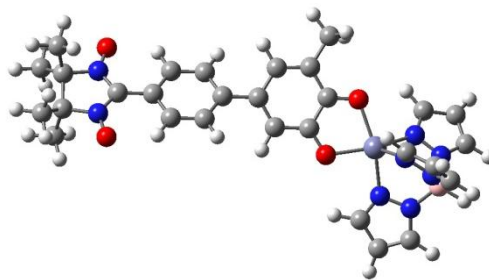


Figure 2.2: DFT-optimized structure of $\text{Tp}^{\text{Cum,Me}}\text{Zn}(\text{SQ-Ph-NN})$. Carbons are gray, nitrogens are blue, oxygens are red, hydrogens are white, boron is rose, and zinc is light-blue.

Another potential approximation to the computational structure is performing calculations only on the monoanionic ligand. Based on trial calculations we found that this gross truncation does not significantly affect the nature of the frontier and surrounding molecular orbitals or spin density distribution in the biradical ligand fragment of the molecule. For DFT frequency calculations, the full molecule is too large to handle, and therefore the $[\text{SQ-Ph-NN}]^-$ ligand was used. For time-dependent DFT calculations, it is preferable to use the full molecule since $\text{Tp}^{\text{Cum,Me}}\text{Zn}(\text{SQ-Ph-NN})$ is neutral, and the TD-DFT results are significantly closer to experimental absorption band energies when the calculations are performed on neutral molecules as opposed to the anions. As a comparison of the experimental and computational values for the dihedral

Table 2.1: Experimental versus computational dihedral angles between ring moieties in phenyl-spaced DBA.

Dihedral Angle	X-ray structure $\text{Tp}^{\text{Cum,Me}}\text{Zn}(\text{SQ-Ph-NN})$	DFT $\text{Tp}^{\text{Cum,Me}}\text{Zn}(\text{SQ-Ph-NN})$	DFT $[\text{SQ-Ph-NN}]^-$
NN-Ph	12.9	0.5-1	3-4
Ph-SQ	34.6	31-32	22

angles in the phenyl-spaced DBA (donor-bridge-acceptor biradical) in Table 2.1 shows, the DFT-calculated dihedral angles agree reasonably well with experimental values from X-ray crystallography, and as a function of computational model (full molecule versus [SQ-Ph-NN]⁻ ligand). The results show a small NN-Ph dihedral angle and larger (~30°)

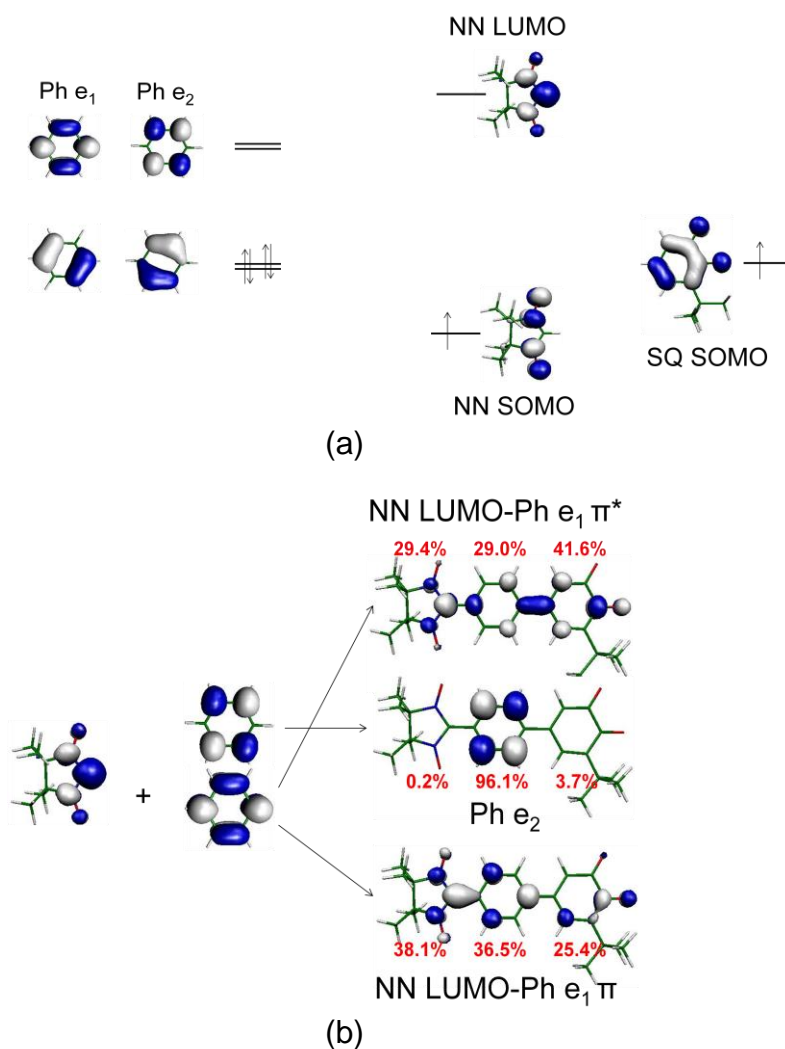


Figure 2.3: Fragment molecular orbitals of [SQ-Ph-NN]⁻, SOMO = singly occupied molecular orbital, LUMO = lowest unoccupied molecular orbital. Molecular orbitals are plotted at a contour isovalue of 0.05. Percentages are the molecular orbital contributions of each ring moiety to the total for each molecular orbital.

Ph-SQ dihedral angle indicating strong NN-Ph π -bonding. While the agreement between DFT-calculated and the X-ray crystal structure value for the NN-Ph dihedral is not quantitative, both methods do, however, indicated that the NN-Ph dihedral angle is small. We notice that dihedral angle values for the complete metallated molecules (in particular the Ph-SQ dihedral angle) are closest to experiment, and that DFT predicts a very planar NN-Ph structure. It is possible that the slight non-planarity of NN-Ph unit in the X-ray crystal structure is due to crystal packing forces, which are not present in the gas phase computations. In solution, the NN-Ph and Ph-SQ dihedral angles most likely fluctuate around an average value that is close to that of gas-phase DFT-calculated structures, and this is supported by results discussed in section 2.3.2.

Figure 2.3 illustrates the frontier fragment bridge, acceptor, and donor orbitals (Figure 2.3 (a)), and the [SQ-Ph-NN]⁻ molecular orbitals formed from the fragment orbitals (Figure 2.3 (b)). In Figure 2.3 (b) we see the result of the orbital mixing between the frontier fragment orbitals of the bridge with donor and/or acceptor frontier orbitals, and that is that the empty Ph e_1 bridge orbital mixes strongly with the NN LUMO to form a bonding (π) and antibonding (π^*) combination of the Ph e_1 and NN LUMO. The Ph e_1 orbital interacts very strongly with the NN LUMO yielding delocalized molecular orbitals with almost equal percent NN and Ph character. This is the case for both the bonding and antibonding combinations, and is indicative of the two fragment orbitals (NN LUMO and the Ph e_1 orbital) being very close in energy prior to their mixing.

Another indication that the NN LUMO and Ph e_1 orbitals are “in resonance” with one another is the fact that the new NN LUMO \pm Ph e_1 molecular orbitals are split in

energy around the non-bonding Ph e_2 orbital. The Ph e_2 orbital is degenerate with Ph e_1 in the isolated D_{4h} benzene molecule, and while the energies of both of these phenyl orbitals are close to the NN LUMO, the Ph e_2 has an orbital node along the NN-Ph bond (as well as the Ph-SQ bond), and therefore does not mix with the SQ or NN orbitals and is essentially non-bonding.

The formation of the NN-Ph delocalized acceptor orbital has a number of important consequences. Due to the energetic stabilization of the delocalized NN-Ph acceptor orbital when compared to the NN LUMO, the donor-acceptor charge transfer band is observed to occur at lower energy.⁴ It is also expected that K , the single-site exchange integral describing the exchange interaction between the (full) unpaired spin on the NN SOMO and the partial unpaired spin on the NN-Ph LUMO should decrease compared to the single-site exchange between electrons of the same spin in the NN SOMO and NN LUMO. The qualitative reason for this is that single-site exchange depends on the spatial overlap of the orbitals that the two spins occupy, and the NN-Ph LUMO is significantly (\sim factor of two) more delocalized than the NN LUMO, thus reducing the overlap density between an electron residing in the NN SOMO with that residing in the NN-Ph LUMO. The NN-Ph LUMO is in fact so delocalized over the NN and Ph e_1 orbitals that we have found it useful to treat the NN-Ph fragment as a single moiety interacting with the SQ, which is something we will do in section 2.3.3.

A new molecular orbital diagram can be constructed, which reflects the orbital interaction we have just discussed, and the DFT results for the full molecule are shown on the right of Figure 2.4. As for the $[\text{SQ-Ph-NN}]^-$ ligand, the full molecule shows that

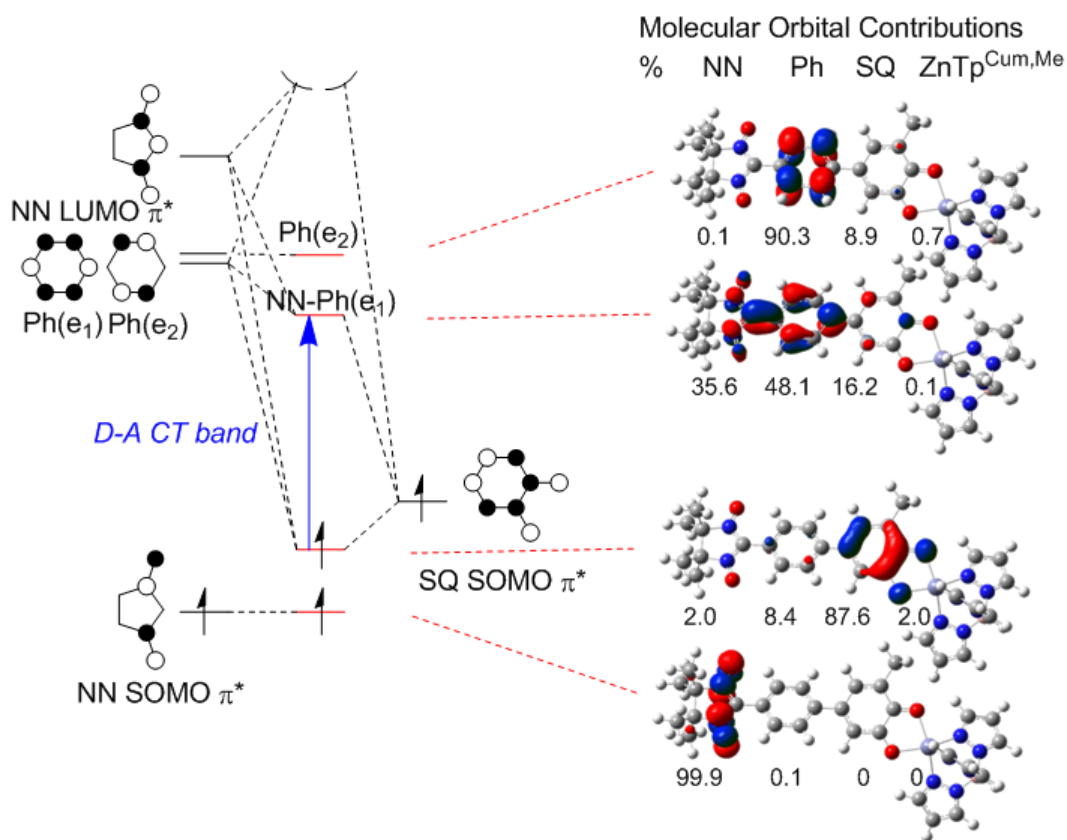


Figure 2.4: Molecular orbital diagram and DFT-calculated molecular orbitals and their compositions. Energies are not drawn to scale, orbitals are α orbitals and are displayed at a contour isovalue of 0.05.

orbitals with nodes on the atoms of connection, i.e. the NN SOMO and Ph e2 orbitals, do not mix with other fragment orbitals. The NN-Ph LUMO shows a large amount of delocalization over both the NN and Ph rings, while the SQ SOMO shows partial delocalization over the Ph ring (~8% of the total orbital character for that molecular orbital). While not discernible at the contour isovalue used in Figure 2.4, the SQ SOMO is admixed with some NN LUMO character. The Ph character in the SQ SOMO is not quite like any of the isolated Ph orbitals, but seems to have contributions from one member of the lower-lying filled e set of Ph orbitals.

2.3.2 Spin Polarization and Spin Delocalization

In this section we discuss the DFT-computed spin density distribution and relate this to experimentally measured quantities such as the isotropic nitrogen hyperfine coupling constants and the results of magnetic susceptibility measurements. The experimental spin density distribution of NN has been obtained by polarized neutron diffraction.⁹¹

2.3.2.1 Spin Polarization on Allyl- and the Nitronyl Nitroxide Radical

Spin polarization describes the interaction of an unpaired electron with α and β electrons in lower-lying, filled orbitals. This can be described using spin unrestricted orbitals, where the α and β electrons have different spatial characteristics and energies, or by using a spin restricted basis with configuration interaction. A well-known example of this phenomenon is observed in the allyl radical,⁶ which forms three π molecular orbitals, denoted as Φ_1 , Φ_2 , and Φ_3 , where Φ_1 is doubly-occupied with wavefunction amplitude on all three carbons, Φ_2 is singly-occupied with wavefunction amplitude on only the outer two carbons, and Φ_3 is unoccupied with wavefunction amplitude on all three carbons. In C_{2v} symmetry, Φ_1 and Φ_3 have the same symmetry and can mix. This results in the formation of new orbitals that are a weighted positive and negative linear combination of Φ_1 and Φ_3 . The ground state of the allyl radical would formally have no spin density on the central carbon, and positive spin density on the terminal carbons. What is observed, however, both computationally and experimentally, is a small amount on negative spin density on the central carbon atom. This derives from an excited state configuration

mixing into the ground state, where the excited configuration has one electron promoted into the LUMO that is Φ_3 admixed with Φ_1 . This excited configuration mixing with the ground configuration accounts for the nonzero spin density on the central carbon atom.

Spin polarization occurs in the nitronyl nitroxide radical via a similar mechanism that involves the NN highest occupied molecular orbital (HOMO), NN SOMO, and NN LUMO (Figure 2.5). We notice that much like for the allyl radical, the SOMO has nodal character on the bridgehead carbon. However, the inclusion of CI provides a mechanism for negative spin density on this carbon. The NN HOMO and NN LUMO have the appropriate symmetry to mix and form weighted positive and negative linear orbital combinations. NN HOMO \rightarrow NN LUMO excited state configurations 1 and 2 are shown

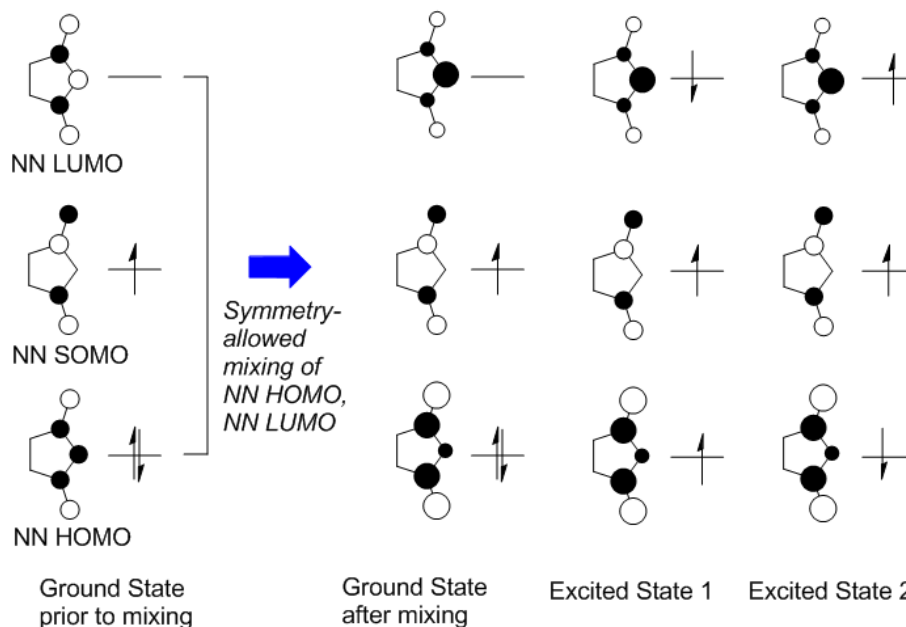


Figure 2.5: Spin polarization in the nitronyl nitroxide radical (energies and orbital coefficient not drawn to scale).

on the right, where excited state 1 is lower in energy due to the exchange interactions of the unpaired spins and analogous to the allyl radical. The NN HOMO \rightarrow NN LUMO excited state configurationally mixes into the ground state wavefunction, and this is what leads to the observed negative spin density on the NN bridging carbon.

2.3.2.2 Donor-Bridge-Acceptor Bond Torsions and the Resulting Spin Density Distributions

Figure 2.6 shows the spin density distribution for $\text{Tp}^{\text{Cum,Me}}\text{Zn}(\text{SQ-Ph-NN})$ obtained by density functional theory calculations. The net spin density on any given atom is the excess α minus β spin for positive spin density, or vice versa for net negative spin density. The molecule has two unpaired electrons that formally reside on the donor and acceptor, respectively. We observe the spin density to be distributed over the extended π network of donor, bridge and acceptor. The phenyl bridge, which formally has

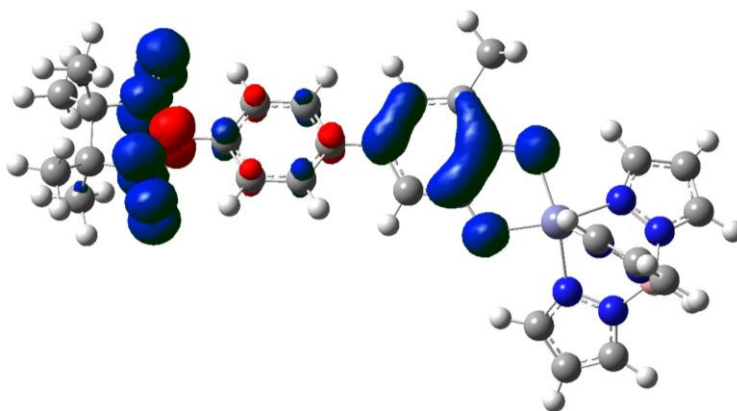

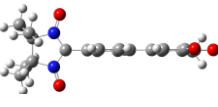
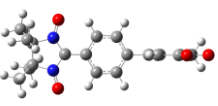



Figure 2.6: Spin density distribution of $\text{Tp}^{\text{Cum,Me}}\text{Zn}(\text{SQ-Ph-NN})$ (positive spin density blue, negative spin density red).

no unpaired spin, possesses both positive and negative spin density on alternate carbon atoms. It is instructive to look at how the spin density changes as a function of the dihedral angle and reduced π overlap between the rings in $\text{Tp}^{\text{Cum,Me}}\text{Zn}(\text{SQ-Ph-NN})$. The π overlap between the donor, bridge and acceptor can be disrupted computationally by constructing geometries with 90° dihedral angles between the respective rings. Table 2.2 shows the net spin densities on the donor, bridge and acceptor (summed over all atoms of the respective rings) as the dihedral angle is varied.

Table 2.2: DFT-calculated spin densities for [SQ-Ph-NN].

<i>Net DFT Spin Density for the moiety</i>			<i>Geometry</i>
<i>Nitronyl Nitroxide</i>	<i>Phenyl</i>	<i>Semiquinone</i>	
0.996	0.011	0.993	
0.998	0.093	0.909	
1.047	-0.041	0.994	
1.124	0.072	0.804	

When the bridge is perpendicular to both the donor and acceptor, we observe close to a net spin of one on both donor and acceptor with very little spin density on the bridge (line 1, Table 2.2). Restoring the overlap between donor and bridge while leaving

the acceptor ring perpendicular leads to a 10% decrease in spin density on the donor, which is effectively delocalized onto the bridge, giving the bridge a net positive spin density of 0.093 (line 2, Table 2.2). Interestingly, when we restore acceptor-bridge overlap while leaving the donor perpendicular to both acceptor and bridge, we observe an increase in net spin density on the acceptor, and a negative spin density on the bridge (line 3, Table 2.2). The acceptor thus delocalizes negative spin density from the bridging nitronyl nitroxide carbon, which carries a negative spin density due to a spin polarization mechanism on the nitronyl nitroxide, onto the bridge. This leads to an increase in the net positive spin density on the NN acceptor itself. Thus we realize that for the geometry in which all of the rings have maximal π overlap (i.e. 0° dihedrals between both the acceptor and bridge and the donor and bridge) the observed spin density is a sum of two contributions; a delocalization of positive spin from the donor onto the bridge and acceptor, as well as a delocalization, albeit smaller in magnitude, of negative spin density from the acceptor onto the bridge (line 4, Table 2.2). When all three rings are coplanar, 20% of the spin density of the SQ donor is delocalized onto the phenyl bridge and NN acceptor.

In order to better understand the delocalization of negative spin density from the NN to the bridge, we examined the spin population of the nitrogens and the bridging carbon on the NN fragment as a function of the dihedral angle between the semiquinone donor, the phenyl bridge and the nitronyl nitroxide acceptor. By changing the dihedral angle between the donor, bridge, and acceptor rings, one can computationally disrupt the π -type overlap between the donor, bridge and acceptor, and thus reducing the degree of

electronic communication between them. The nitronyl nitroxide bridging carbon has a net negative spin density due to the spin polarization mechanism occurring in the nitronyl nitroxide fragment. In the isolated nitronyl nitroxide fragment, the DFT-computed spin population on the bridging carbon is -0.238 . Notice that the isolated nitronyl nitroxide is

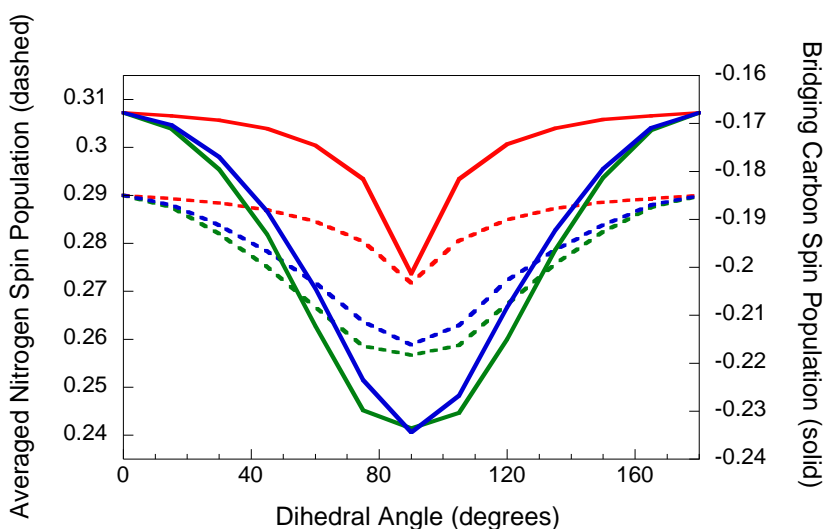


Figure 2.7: Calculated spin populations on the NN nitrogens (dashed lines) and bridging carbon (solid lines) of NN in [SQ-Ph-NN]⁻ in the triplet state as a function of rotating the donor (red), bridge (green), or acceptor (blue) individually away from a planar D-B-A geometry in 15° increments.

analogous to a 90° dihedral between the NN acceptor and the bridge (achieved by either rotation of the bridge 90° out of the plane of the donor and acceptor “bridge rotation”, green, or rotating the acceptor 90° out of the plane of the donor and bridge “acceptor rotation”, blue, Figure 2.7). In the planar geometry, with both donor-bridge and bridge-acceptor dihedrals at 0°, positive spin density is being delocalized to the acceptor from the donor via the bridge, causing spin populations on both the nitrogens and the bridging carbon to become more positive. This results in a decrease in the magnitude of the negative spin population on the bridging carbon, and an increase of the positive spin

population on the nitrogens. ^{13}C labeling of the bridging carbon should result in a decrease in the ^{13}C hyperfine coupling constant as the amount of spin donation from the donor to the acceptor increases, opposite to that observed for the nitrogen hyperfine coupling constant, which would increase. Figure 2.7 clearly shows the difference of disrupting acceptor-bridge overlap (green or blue curve, 90°) and bridge-donor overlap (red curve, 90°). When the Ph-SQ overlap is disrupted but the acceptor and bridge are coplanar (at the 90° geometry, red curve), spin populations on both the nitrogens and bridging carbon are less negative than for a 90° NN-Ph dihedral, due to the fact that the acceptor still has overlap with the bridge and thus can delocalize net negative spin density onto the bridge.

Previous studies by Aebersold *et al.*⁹² on a bimetallic Cu^{2+} system with bridging azido groups and a triplet ground state also demonstrated such combinations of spin delocalization and spin polarization. In this work, both polarized neutron diffraction data and density functional theory calculations revealed a spin density distribution that is explained as a combination of a spin delocalization and spin polarization, where spin is delocalized from Cu^{2+} to the azido bridging ligands. Spin polarization within the π orbitals of the azido ligands occurs via configuration interaction between the ground states and excited states of appropriate symmetry on the azido fragment leading to negative spin density on the central nitrogen of the azido.

We now revisit the spin density distribution of the fully optimized $\text{Tp}^{\text{Cum,Me}}\text{Zn}(\text{SQ-Ph-NN})$ shown in Figure 2.6. While the bridge possesses both negative and positive spin density on alternating carbon atoms of the phenyl ring, the net spin

density on the phenyl bridge is close to zero in the fully optimized geometry. At its optimized geometry $\text{Tp}^{\text{Cum,Me}}\text{Zn}(\text{SQ-Ph-NN})$ has a NN-Ph dihedral angle of 1° and a Ph-SQ dihedral angle of $32\text{-}33^\circ$, a net positive spin density of 1.063 on the NN, a net negative spin density of -0.003 on the Ph, and a net positive spin density of 0.932 on the SQ (also positive 0.008 on the $\text{Tp}^{\text{Cum,Me}}\text{Zn}$). This differs from the description detailed in Table 2.2, where all three rings are coplanar, and the bridge has a net positive spin density since the positive spin delocalization from the SQ to the Ph is larger than the delocalization of negative spin density from the NN to the Ph. However, at the optimized geometry the NN-Ph dihedral is close to zero, and negative spin density is delocalized from the NN to the Ph. At a Ph-SQ dihedral of 32° , the π overlap between donor and bridge is significantly reduced, and thus so is the spin delocalization from the donor to the bridge, where it happens to be that the optimized geometry is the geometry at which both positive and negative spin delocalizations onto the phenyl are about equal in magnitude. In conclusion, the magnitude of net spin density on the bridge is geometry-dependent.

We have ascertained that positive spin density on the NN acceptor fragment has two contributions, the delocalization of positive spin from the donor via the bridge to the acceptor, and the delocalization of negative spin from the acceptor onto the bridge. The magnitude of the single-site exchange, and thus the magnitude of the ferromagnetic exchange coupling between donor and acceptor, is proportional to the magnitude of unpaired spin localized on the NN portion of the NN-Ph LUMO. Thus the ferromagnetic donor-acceptor exchange coupling has **the same two** main contributions: the donor \rightarrow

acceptor charge transfer state, and a strong coupling of the bridge with the spin-polarized acceptor.

2.3.2.3 Correlation Between DFT Calculated Spin Densities, Experimental Nitrogen Hyperfine Coupling Constants, and Magnetic Susceptibility Data

Room temperature EPR spectra of various donor-acceptor, donor-bridge-acceptor, and acceptor-bridge molecules have been acquired by our collaborators, and simulated by us to extract isotropic nitrogen hyperfine coupling constants. Nitrogen hyperfine coupling constants have been calculated and measured previously for substituted NN-Ph radicals.⁹³ The chemical structure of the donor-acceptor, donor-bridge-acceptor, and acceptor-bridge

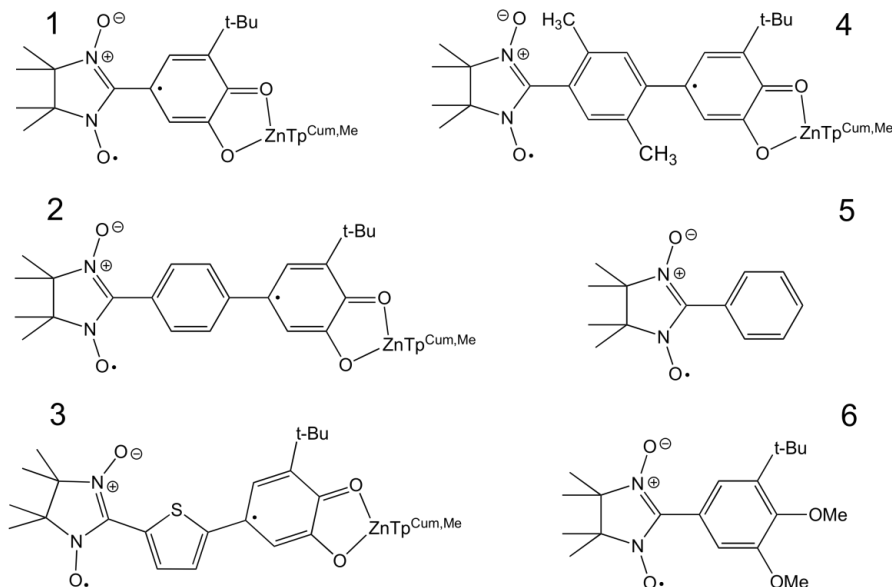


Figure 2.8: ChemDraw representations of the D-A, D-B-A, and B-A molecules.

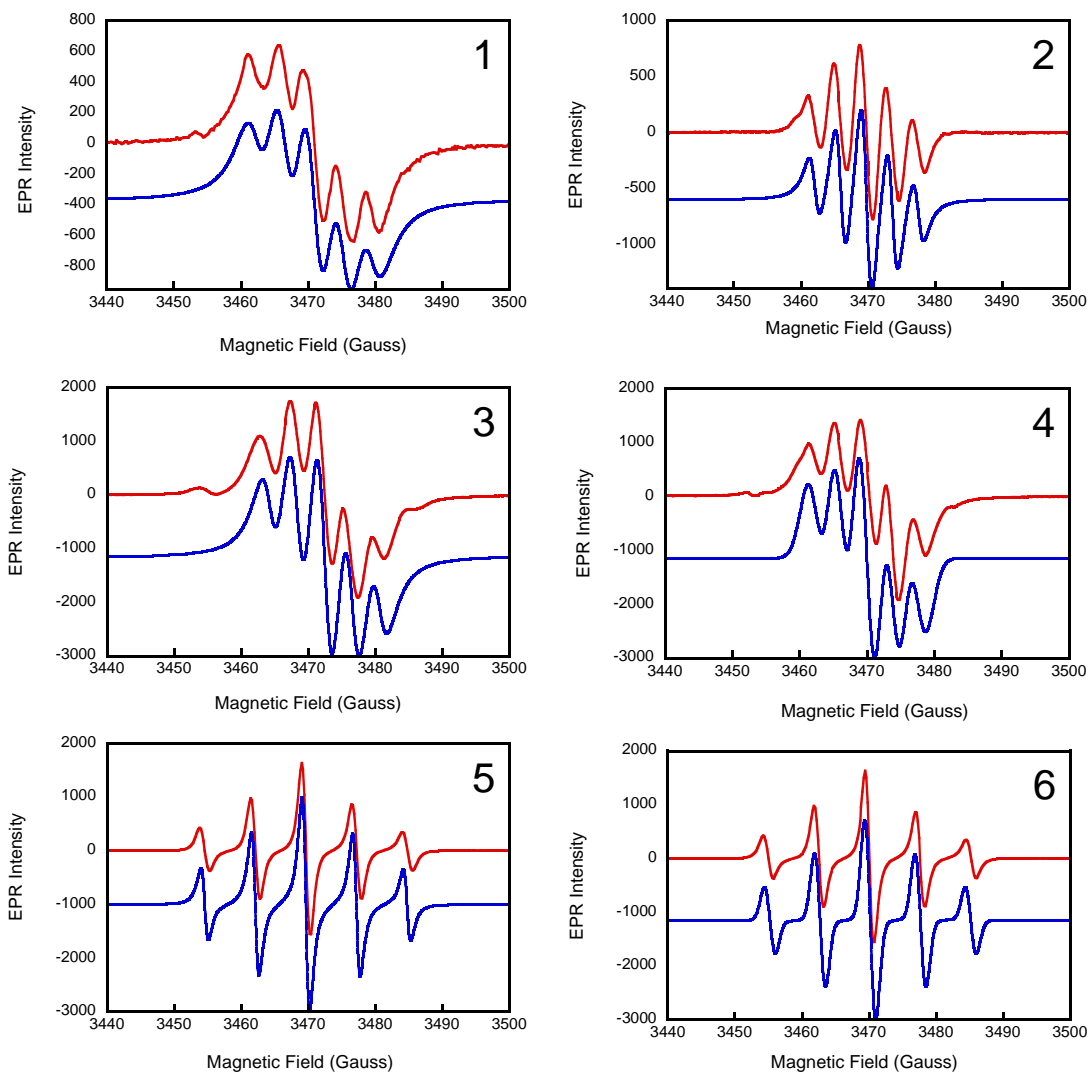


Figure 2.9: Room temperature EPR Spectra of $\text{Tp}^{\text{Cum,Me}}\text{Zn}(\text{SQ-NN})$ (1), $\text{Tp}^{\text{Cum,Me}}\text{Zn}(\text{SQ-Ph-NN})$ (2), $\text{Tp}^{\text{Cum,Me}}\text{Zn}(\text{SQ-Thp-NN})$ (3), $\text{Tp}^{\text{Cum,Me}}\text{Zn}(\text{SQ-Xyl-NN})$ (4), NN-Ph (5), and NN-Ph(OMe)₂ (6). Experimental data are in red and simulations in blue.

Table 2.3: Simulated isotropic nitrogen hyperfine coupling constants for molecules 1-6.

	$T_p^{\text{Cum,Me-Zn(SQ-NN)}}$	$T_p^{\text{Cum,Me-Zn(SQ-Ph-NN)}}$	$T_p^{\text{Cum,Me-Zn(SQ-Thp-NN)}}$	$T_p^{\text{Cum,Me-Zn(SQ-Xyl-NN)}}$	NN-Ph	NN-Ph(OMe) ₂
$A_{\text{iso, nitrogen in } 10^{-4} \text{ cm}^{-1}}$	7.60 +/-0.05	7.20 +/- 0.05	7.38 +/- 0.1	6.74 +/-0.05	7.06 +/- 0.05	7.07 +/-0.05
Line width in 10^{-4} cm^{-1}	2.1	1.1	1.9	1.7	0.9	0.9

$g \sim g_{\text{free electron}}$

molecules is shown in Figure 2.8, and their simulated EPR spectra are shown in Figure 2.9. A full analysis of this data has been published.¹⁵ The isotropic EPR spectra show a symmetric five-line pattern with intensity ratios of 1:2:3:2:1. This is consistent with the unpaired electron being split by two approximately equivalent $I = 1$ nitrogens. Molecule 1 is a D-A biradical, molecules 2-4 are D-B-A biradicals (where the bridge for 4 is 1,4-dimethylbenzene = xylene (Xyl)), and molecules 5-6 are B-A monoradicals.

The biradical, $S = 1$ systems have a Clebsch-Gordan coefficient of 0.5, so that the **observed** isotropic nitrogen hyperfine coupling constants are $\frac{1}{2}$ that of the monoradicals. As the EPR spectra are of organic radicals at room temperature, the isotropic g value is approximately that of a free electron. The magnitude of the isotropic hyperfine coupling constant and the line widths have been simulated, and are summarized in Table 2.3. The magnitude of the experimental isotropic nitrogen hyperfine coupling constants is proportional to the amount of unpaired spin density at the nitrogen nuclei,⁸¹ and thus EPR serves as a direct probe of the spin density on the NN nitrogens. We relate this experimental measure of spin density on the nitrogens to the nitrogen spin populations computed using density functional theory in Figure 2.10, and observe a linear relationship

with an excellent correlation ($R^2 = 0.98$). This follows the relationship $a_N \propto \rho_N$, which was previously observed by McConnell and coworkers.⁹⁴ Since the DFT-calculated spin populations are those of the gas-phase optimized geometries of the molecules, we believe that the DFT-optimized geometries represent the average solution structure of these molecules well.

Table 2.4: Dihedral angles ($^\circ$) from DFT-optimized geometries of molecules 1-6.

Dihedral angle ($^\circ$)	$\text{Tp}^{\text{Cum,Me}}\text{Zn}$ (SQ-NN)	$\text{Tp}^{\text{Cum,Me}}\text{Zn}$ (SQ-Ph-NN)	$\text{Tp}^{\text{Cum,Me}}\text{Zn}$ (SQ -Thp-NN)	$\text{Tp}^{\text{Cum,Me}}\text{Zn}$ (SQ-Xyl-NN)	NN-Ph	NN- Ph(OMe) ₂
Bridge-Acceptor	3*	1	0	46-51	6	6
Donor-Bridge	n/a	31-32	0	47-48	n/a	n/a

*donor-acceptor dihedral

Table 2.4 shows the dihedral angles between D, B, and A rings of the optimized structures of these molecules (coordinates of optimized geometries included in Appendix 6.1.2). Our DFT calculations predict a planar acceptor-bridge geometry, where the calculated NN-Ph dihedral is approximately equal to zero for all D-B-A biradicals in Table 2.4. The complex $\text{Tp}^{\text{Cum,Me}}\text{Zn}$ (SQ-NN) possesses no bridge and therefore has the largest spin density on the nitrogens. Inserting a bridge reduces the amount of spin donated from the donor to the acceptor, and computational and experimental data show that a thiophene bridge facilitates greater spin donation from the SQ donor to the NN acceptor than a phenyl bridge. Compared to $\text{Tp}^{\text{Cum,Me}}\text{Zn}$ (SQ-Ph-NN), the biphenylene bridged $\text{Tp}^{\text{Cum,Me}}\text{Zn}$ (SQ-(Ph)₂-NN) has a decreased donor \rightarrow acceptor spin delocalization, and this is expected to be related to both the increased donor-acceptor distance as well as the presence of Ph-Ph dihedral angle distortions that attenuate the π delocalized network.

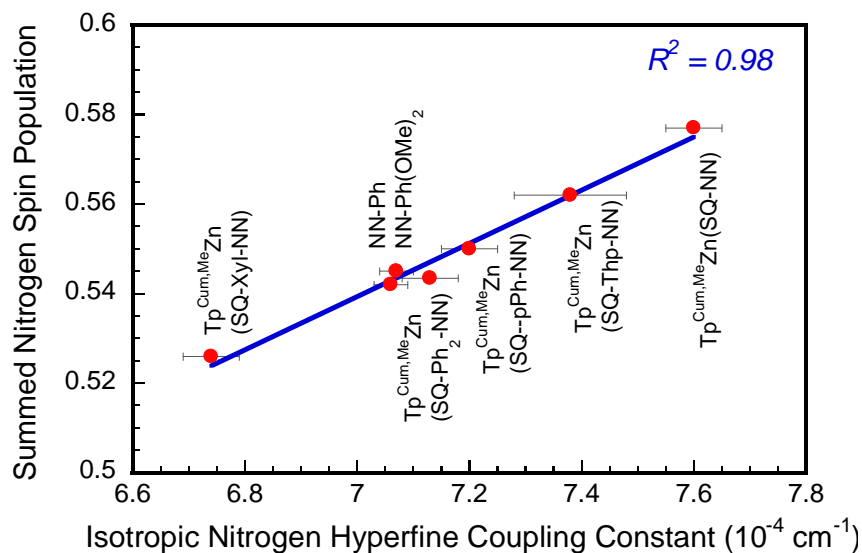


Figure 2.10: Correlation of experimental isotropic nitrogen hyperfine coupling constants and DFT-calculated nitrogen spin populations.

When no donor is present, as for NN-Ph and NN-Ph(OMe)₂, the spin density on the nitrogens is lowered even further. The data show no significant difference between the NN-Ph acceptor-bridge molecules and NN-Ph(OMe)₂, which possesses electron withdrawing groups on the phenyl group. Interestingly, the xylene-bridged D-B-A biradical has the lowest nitrogen spin density of all these molecules. This is explained by the fact that the bridge in the $\text{Tp}^{\text{Cum,Me}}\text{Zn}(\text{SQ-Xyl-NN})$ biradical is more sterically-hindered than an unsubstituted phenyl bridge, and this leads to large dihedral angles of $\sim 50^\circ$ between donor and bridge as well as between the bridge and the acceptor. In section 2.3.2 we showed that the NN delocalizes negative spin density onto the bridge. This increases the net positive spin density on the NN ring in general, and on the NN nitrogens in particular, which is disrupted as the acceptor-bridge planarity is compromised.

The strong agreement between our experimental and computational data in Figure 2.1 gives us confidence in the validity of using our computational results in the description of these D-B-A molecules. Furthermore the correlation between spin populations of gas-phased optimized structures and EPR solution measurements implies a structural similarity between DFT-optimized structures and solution structures, namely that the ring dihedral angles in solution do not rotate freely but instead favor specific non-zero dihedral angles analogous to the DFT-optimized structures. This can be understood as a constraint on NN-bridge and bridge-SQ dihedral angles via a resonance structure in which the (phenylene) bridge has quinoidal character, and the NN-bridge and bridge-SQ bonds have double-bond character. In section 2.3.3 we will encounter additional experimental evidence supporting this description.

2.3.3 Excited States and Excited State Distortions: TD-DFT Band Assignments, the Nature of the DA-CT Band and Bridge During the DA-CT Transition

In this section we will discuss the results of time-dependent DFT calculations for the electronic absorption spectrum of $\text{Tp}^{\text{Cum,Me}}\text{Zn}(\text{SQ-Ph-NN})$, and focus on the three lowest energy bands that are calculated with appreciable oscillator strengths. We will then correlate the electron density difference map (EDDM), and donor- and acceptor orbitals involved in the transition with the highest oscillator strength with experimental resonance Raman data and frequency calculations. Figure 2.11 shows the three lowest energy transitions that have appreciable oscillator strength for $\text{Tp}^{\text{Cum,Me}}\text{Zn}(\text{SQ-Ph-NN})$, and these are marked as bands 1, 2, and 3. Bands 1-3 are not the lowest DFT-calculated transitions, but bands between 1 & 2, and 2 & 3 have much lower oscillator strengths,

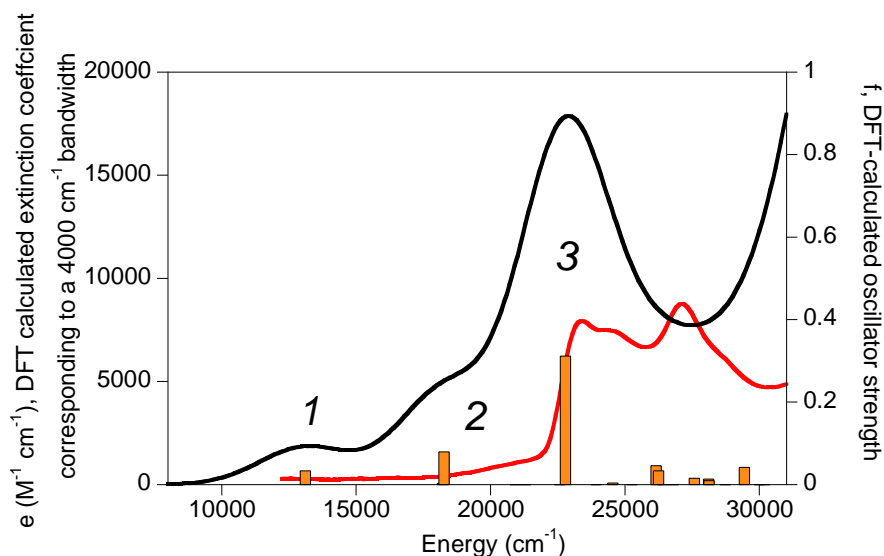


Figure 2.11: TD-DFT low-energy transitions for $\text{Tp}^{\text{Cum,Me}}\text{Zn}(\text{SQ-Ph-NN})$; bars are oscillator strengths, line spectra are calculated oscillator strengths widened into bands of 4000 cm^{-1} bandwidth (black). Experimental spectrum from reference^{4,90} (red).

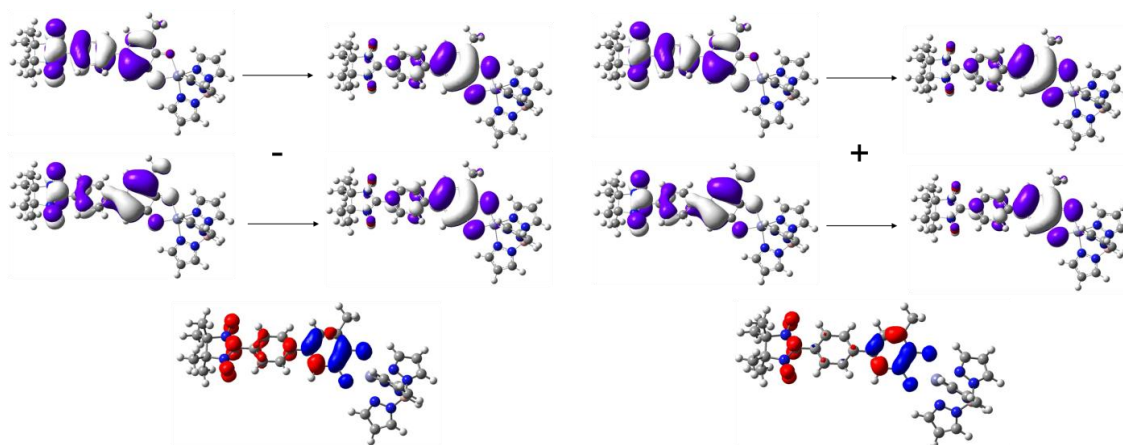


Figure 2.12: Orbital contributions (top, white/blue, first row: HOMO \rightarrow SQ SOMO, second row HOMO-1 \rightarrow SQ SOMO) and EDDMs (bottom, red = loss and blue = gain of electron density during the transition, contour isovalue is 0.002): Band 1 at the left, band 2 at the right.

resonance Raman data and frequency calculations. Figure 2.11 shows the three lowest energy transitions that have appreciable oscillator strength for $\text{Tp}^{\text{Cum,Me}}\text{Zn}(\text{SQ-Ph-NN})$, and these are marked as bands 1, 2, and 3. Bands 1-3 are not the lowest DFT-calculated

transitions, but bands between 1 & 2, and 2 & 3 have much lower oscillator strengths, and this can be seen in Figure 2.11 (bars represent DFT-calculated oscillator strength, and no bars have been omitted; i.e. bars for transitions between bands 1, 2, and 3 are present in the spectrum but are so small that they are not visible).

The TD-DFT spectrum in Figure 2.11 is in qualitative agreement with the published experimental spectrum. While the extinction coefficients are larger for the calculated spectrum than the experimental spectrum, computed transition energies agree well with experiment. Band 1 is calculated at $\sim 13100 \text{ cm}^{-1}$ and is observed experimentally as a broad, very weak band in the $12000 - 13000 \text{ cm}^{-1}$ region. Band 2 is calculated at $\sim 18200 \text{ cm}^{-1}$ and corresponds to a broad band observed experimentally at $\sim 19000 - 21000 \text{ cm}^{-1}$, and band 3 is calculated at $\sim 22800 \text{ cm}^{-1}$ and occurs at $\sim 22900 \text{ cm}^{-1}$ in the experimental absorption spectrum. Using the TD-DFT results to aid in the assignment of bands 1-3 is thus useful. Figure 2.12 shows the molecular orbitals for the largest contributing one-electron promotions to each calculated transition as well as the electron density difference maps (EDDM) for the transition. Band 1 is assigned as a [Ph-NN-SQ HOMO \rightarrow SQ SOMO - Ph-NN-SQ HOMO-1 \rightarrow SQ SOMO] transition, and band 2 is assigned as its higher energy counterpart, [Ph-NN-SQ HOMO \rightarrow SQ SOMO + Ph-NN-SQ HOMO-1 \rightarrow SQ SOMO]. The HOMO of this molecule refers to the highest *doubly* occupied molecular orbital and HOMO-n to the n^{th} orbital below the HOMO in energy. Both the HOMO and HOMO-1 are very delocalized orbitals having almost the same contribution from donor, bridge, and acceptor (i.e. the β HOMO is calculated to be 35% NN, 29% Ph, 36% SQ). The charge transfer nature of the transition

is seen in the EDDMs in the lower part of Figure 2.12, which indicate that band 1 has NN-Ph \rightarrow SQ charge transfer character whereas band 2 has NN \rightarrow SQ charge transfer character.

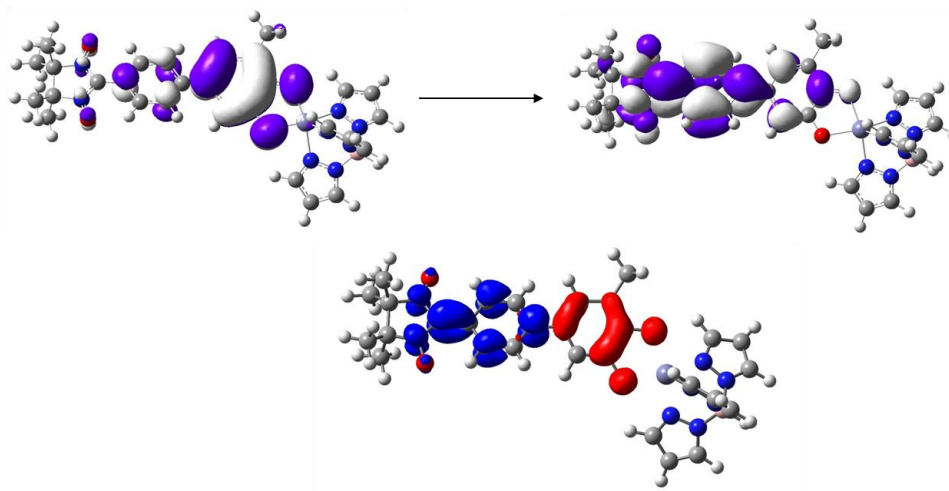


Figure 2.13: Orbital contributions (top, white/blue, contour isovalue 0.05) and EDDMs (bottom, red = loss of electron density during the transition, blue = gain of electron density during the transition, contour isovalue is 0.002) for band 3, the donor-acceptor charge transfer band.

Figure 2.13 shows the TD-DFT results of band 3, which is assigned as the donor-acceptor charge transfer transition from the SQ SOMO donor to the NN-Ph LUMO acceptor. The charge transfer character of this transition is donor \rightarrow acceptor, and can be seen clearly in the EDDM for band 3 in Figure 2.13. As previously reported for $\text{Tp}^{\text{Cum,Me}}\text{Zn}(\text{SQ-NN})$, this donor-acceptor charge transfer excited state is responsible for the strong donor-acceptor ferromagnetic coupling in $\text{Tp}^{\text{Cum,Me}}\text{Zn}(\text{SQ-NN})$ ($2J = 1100 \text{ cm}^{-1}$) and $\text{Tp}^{\text{Cum,Me}}\text{Zn}(\text{SQ-Ph-NN})$ ($2J = 200 \text{ cm}^{-1}$).^{2-4,59} Using a molecular orbital description, the SQ SOMO has partial NN-Ph LUMO character, and the unpaired electron residing in the SQ SOMO is partially delocalized onto the NN-Ph LUMO. Non-

zero overlap density between the NN-Ph LUMO and the NN SOMO dominantly contributes to the ground state exchange interaction and favors the triplet ground configuration over the singlet configuration by Hund's rule.^{2,3} Alternatively, we can understand origin of the ferromagnetic coupling using a VBCI model. The ground state is that which has one electron residing in the NN SOMO and one in the SQ SOMO, and the spins of those electrons can either be aligned parallel (a triplet state) or antiparallel (a singlet state). If we consider the fact that the NN SOMO has a node on the carbon atom connecting the NN to the bridge or SQ fragment, we can see that there is no electronic communication between the NN SOMO and the SQ SOMO fragment within the Hückel approximation, and the singlet and triplet states are therefore degenerate. The donor-acceptor charge transfer excited state has one unpaired electron in the NN SOMO and one in the NN LUMO. Due to the large single-site exchange of the two unpaired electrons in the same spatial region, the triplet excited states is energetically stabilized relative to the singlet excited state. The triplet excited state can interact with the triplet ground state, and the singlet excited state can interact with the singlet ground state, leading to a stabilization of the ground states and destabilization of the excited states in each case. Since the triplet excited state is closer than the singlet excited state in energy to the ground state, this will result in the triplet ground state being stabilized relative to the singlet ground state. These mechanisms for ferromagnetic coupling have been developed and published in previous works²⁻⁴ and are not new to this work, but have been mentioned here to underscore the importance of the strong donor-acceptor charge transfer transition to the strong ferromagnetic coupling in these molecules.

Resonance Raman spectroscopy can be used to probe how molecules distort in excited states relative to the ground state geometry. Thus, resonance Raman spectroscopy can be used to probe excited state distortions in D-A and D-B-A biradicals upon laser excitation in resonance with the D-A CT transition. This experimental data has been acquired and published by previous researchers (Depperman, E. C., PhD Thesis: Spectroscopic and Theoretical Characterization of Strong Ferromagnetic Interaction in Heterospin Biradicals, 2005).⁹⁰ Here we will use computational data from TD-DFT and frequency calculations to provide a description of how the phenyl bridge distorts in the excited state during the donor-acceptor charge transfer. Experimental resonance Raman data show an intense band at 1591 cm^{-1} , which is resonantly enhanced under the D→A CT band.⁴

Frequency calculations on $[\text{SQ-Ph-NN}]^-$ indicate vibrational modes at 1618 cm^{-1} and 1664 cm^{-1} , which possess a large amount of phenyl and SQ in-plane stretching character. For benzene we calculate a mode at 1642 cm^{-1} that is a totally symmetric ring stretch in the D_{2h} symmetry environment that the phenyl experiences in $[\text{SQ-Ph-NN}]^-$. In $[\text{SQ-Ph-NN}]^-$ this ring mode couples with a semiquinone in-plane ring stretch to form lower frequency in-phase (1618 cm^{-1}) and higher frequency out-of-phase (1664 cm^{-1}) linear combinations of phenyl and SQ vibrations (Figure 2.14). In order to determine which of these two vibrations corresponds to the resonantly-enhanced mode at 1591 cm^{-1} in the resonance Raman data, we examine the orbital character of the SQ SOMO, which contributes electron density, and the NN-Ph e_1 LUMO, which receives electron density

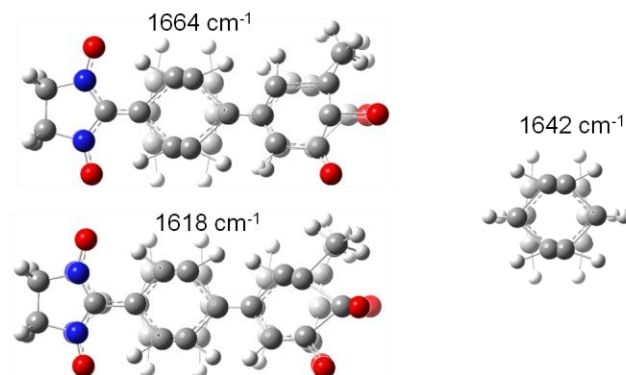


Figure 2.14: DFT-calculated vibrations and their frequencies. Left: [SQ-Ph-NN], right: benzene. Modes are shown as overlays of the extrema of the vibrational mode.

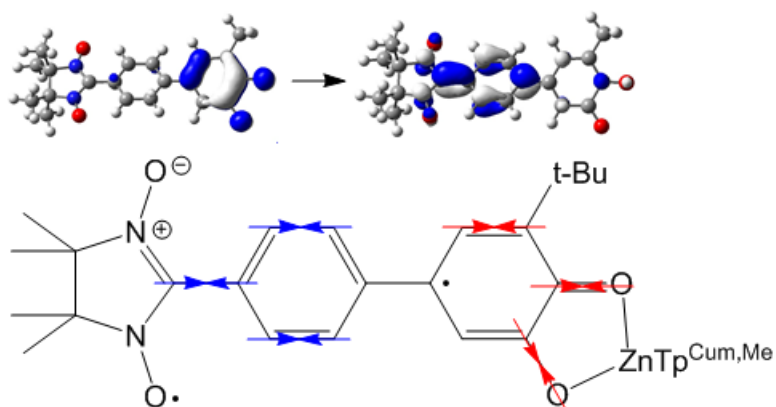


Figure 2.15: Top: SQ SOMO (left) and NN-Phe₁ LUMO (right) (Tp^{Cum,Me} and Zn were omitted for clarity, contour isovalue 0.05). Bottom: excited state distortion accompanying the removal of an electron from the SQ SOMO (red) and the addition of that electron to the NN-Phe₁ LUMO (blue), adapted from reference ⁴.

during the donor-acceptor charge transfer transition in Figure 2.15. The loss of electron density in the SQ SOMO should result in a contraction of the C-C and C-O bonds indicated in red at the bottom of Figure 2.15, since removal of electron density from an antibonding region causes bond contraction. Likewise, transfer of electron density into the NN-Ph LUMO should primarily cause a contraction of the C-C bonds indicated in

blue at the bottom of Figure 2.15, since the transfer of electron density to bonding regions also causes bond contraction. We notice that these bond distortions and their phases most closely mirror the 1618 cm^{-1} DFT-calculated vibrational mode. This distorting mode of the bridge in the D-A CT excited state is similar to the quinoidal resonance structure we evoked in section 2.3.2.3 to explain the structural correlation between solution geometries and DFT-optimized geometries.

Thus by combining electronic absorption and resonance Raman data with the DFT orbital description and DFT frequency calculations for $\text{Tp}^{\text{Cum,Me}}\text{Zn}(\text{SQ-Ph-NN})$ we see that the primary excited state distortion that accompanies the donor \rightarrow acceptor charge transfer involves a symmetric distortion of the phenylene bridge that is also delocalized over the SQ and NN units.

2.4 Changing the Electronic Nature of the Bridge: Replacing Phenylene with Thiophene

In $\text{Tp}^{\text{Cum,Me}}\text{Zn}(\text{SQ-Thp-NN})$, the phenyl bridge has been replaced by a thiophene bridge, and our interest lies in studying how this new bridge affects the electronic coupling between donor and acceptor. From section 3.2 we know that the dihedral angles between NN, thiophene, and SQ are zero, and all three rings are coplanar. Bridge substitution can have two effects: a structural perturbation since thiophene-SQ is more planar than Ph-SQ, and an electronic perturbation since thiophene is more electron-rich than phenyl. This is expected to result in an energy shift of the bridge orbital manifold, and lower thiophene energies compared to the orbital energies of a phenyl bridge. Equation 14 shows that the overall donor-acceptor electronic coupling, H_{ab} , depends on several factors. The intrinsic donor-acceptor coupling, H_{ab}^0 , depends on the chemical

nature of the donor, acceptor, and bridge. The second term in Eq. 14 is an exponential dampening factor that describes the decrease of donor-acceptor electronic communication as the donor-acceptor separation increases, while the last factor describes the π overlap between the ring moieties in the donor-acceptor path, and includes the effect of non-zero donor-bridge, bridge-bridge (for multi-ring bridges), as well as acceptor-bridge dihedral angles.

$$H_{ab}^2 = (H_{ab}^0)^2 e^{-\beta(r-r_0)} \cos^m \theta \quad \text{Eq. 14}$$

By changing the phenyl bridge to a thiophene, we are thus changing both H_{ab}^0 and the cosine term that describe π overlap between the ring moieties.

2.4.1 Frontier Molecular Orbitals, Spin Density Distribution, and the Molecular Orbital Diagram for $\text{Tp}^{\text{Cum,Me}}\text{Zn}(\text{SQ-Thp-NN})$

The optimized structure for $\text{Tp}^{\text{Cum,Me}}\text{Zn}(\text{SQ-Thp-NN})$ is remarkably planar with 0° dihedral angles for both NN-Thp and Thp-SQ. If we examine the frontier molecular orbitals in Figure 2.16, we see that the SQ SOMO has considerably more bridge character than in the phenyl case. The thiophene bridge orbital character in the SQ SOMO is that of a lower-lying, filled thiophene bridge orbital, which mixes with the SQ SOMO resulting in the filled thiophene bridge orbital acquiring some SQ SOMO character and being stabilized, while the SQ SOMO acquires some thiophene character and gets destabilized.

We may compare the relative energies of the frontier orbitals for a DBA biradical by normalizing the energies to the NN SOMO. In $\text{Tp}^{\text{Cum,Me}}\text{Zn}(\text{SQ-Ph-NN})$, the α orbital of the SQ SOMO lies 1097 cm^{-1} above the α orbital of the NN SOMO (from DFT). In

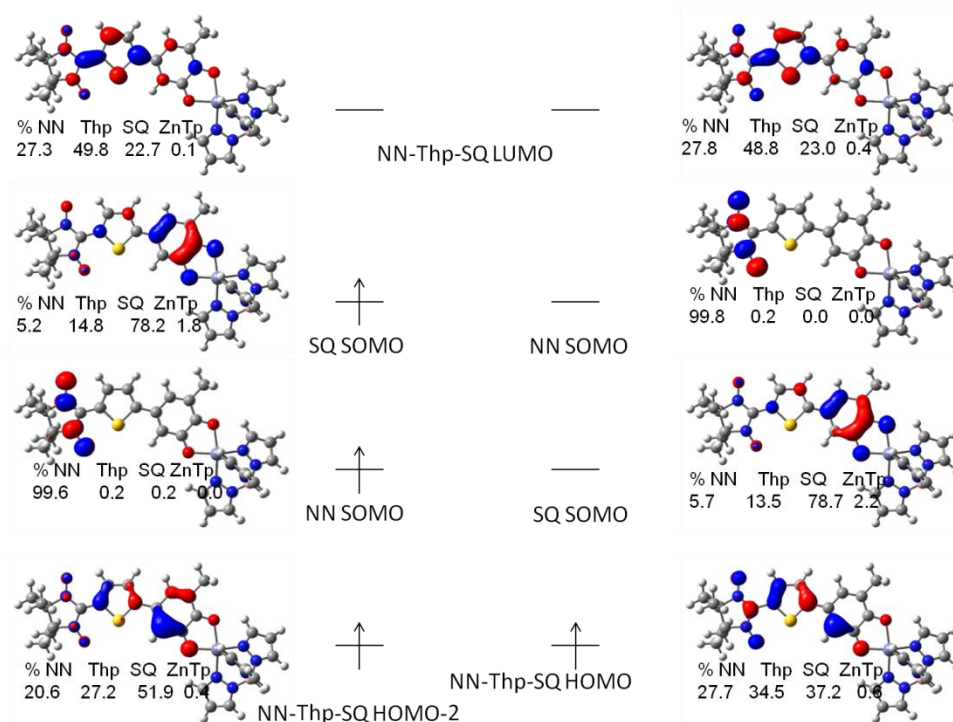


Figure 2.16: DFT frontier molecular orbitals and orbital compositions for $\text{Tp}^{\text{Cum,Me}}\text{Zn}(\text{SQ-Thp-NN})$. Note that no information about the relative energies of the orbitals with respect to each other is intended (i.e. α and β orbitals are not degenerate in the calculation). ZnTp denotes $\text{Tp}^{\text{Cum,Me}}\text{Zn}$ for space purposes in the diagram.

$\text{Tp}^{\text{Cum,Me}}\text{Zn}(\text{SQ-Thp-NN})$, the α orbital of the SQ SOMO lies 2853 cm^{-1} above the α orbital of the NN SOMO, which implies an energy destabilization of $\sim 1700 \text{ cm}^{-1}$ for the SQ SOMO of $\text{Tp}^{\text{Cum,Me}}\text{Zn}(\text{SQ-Thp-NN})$. The α orbital of the SQ SOMO for $\text{Tp}^{\text{Cum,Me}}\text{Zn}(\text{SQ-Thp-NN})$ has 14% thiophene character compared to only 8% phenyl character in the α orbital of the SQ SOMO for $\text{Tp}^{\text{Cum,Me}}\text{Zn}(\text{SQ-Ph-NN})$. The α orbital of the SQ SOMO for $\text{Tp}^{\text{Cum,Me}}\text{Zn}(\text{SQ-Thp-NN})$ also has a larger amount of NN character (5% compared to 2% when $B = \text{Ph}$). Here, the NN orbital character in the SQ SOMO is that of the SQ-Thp-NN LUMO. We expect the SQ SOMO to be energetically closer to the SQ-Thp-NN LUMO due to the SQ SOMO being energetically destabilized, and now

need to examine whether the SQ-Thp-NN LUMO is more energetically stabilized due to NN-thiophene orbital mixing compared to that of the NN-Ph LUMO due to NN-Ph orbital mixing. We consider the energy difference between the non-interacting “zero-point marker-orbital,” the NN SOMO α orbital, to the SQ-Thp-NN LUMO, where for $\text{Tp}^{\text{Cum,Me}}\text{Zn}(\text{SQ-Thp-NN})$ that DFT-calculated energy difference is $27,654 \text{ cm}^{-1}$ compared to $28,312 \text{ cm}^{-1}$ for $\text{Tp}^{\text{Cum,Me}}\text{Zn}(\text{SQ-Ph-NN})$. Thus the LUMO of the thiophene-bridged biradical is energetically more stabilized due to bridge mixing than the LUMO of the phenyl-bridged biradical. Both the lower energy LUMO and the higher energy SQ SOMO lead to an expected lowering of the energy of the donor-acceptor charge transfer band in $\text{Tp}^{\text{Cum,Me}}\text{Zn}(\text{SQ-Thp-NN})$. This is observed experimentally, where the donor-acceptor charge transfer band at $\sim 21050 \text{ cm}^{-1}$ is $\sim 1820 \text{ cm}^{-1}$ lower in energy for $\text{Tp}^{\text{Cum,Me}}\text{Zn}(\text{SQ-Thp-NN})$ compared to $\text{Tp}^{\text{Cum,Me}}\text{Zn}(\text{SQ-Ph-NN})$.

The qualitative molecular orbital diagram in Figure 2.17 helps us compare the NN LUMO-bridge mixing for $X = \text{Ph}$ and $X = \text{Thp}$. In section 2.3.1 we observed that the NN LUMO and Ph- e_1 orbital are energetically very close, and mix to give a highly delocalized NN-Ph e_1 LUMO that has very similar orbital contributions from the NN LUMO and Ph e_1 orbital (with respect to % contribution of the NN and Ph to the total wavefunction character of the LUMO). The corresponding thiophene orbital that mixes with the NN LUMO is lower in energy than the Ph e_1 is with respect to the NN LUMO, but still energetically close to the NN LUMO. Orbital mixing will lead to a stabilized molecular orbital and destabilized molecular orbital with more unequal NN and thiophene contributions. Thus the stabilized molecular orbital will have more thiophene

character than NN LUMO character, and the destabilized molecular orbital will have more NN LUMO character than thiophene character. The degree of stabilization and destabilization of the two orbitals that mix depends upon the overlap between those orbitals and their initial energy separation prior to mixing.

Since the energy separation between the NN LUMO and Ph e_1 orbital is smaller than the comparative energy gap between the NN LUMO and the thiophene bridge orbital, it might be expected that the NN LUMO-Ph e_1 bonding combination is stabilized by a greater amount (with respect to the energy of the isolated acceptor and bridge fragments) relative to the NN LUMO-Thp bonding combination. However, since the thiophene bridging orbital is at lower energy to begin with, the NN LUMO-thiophene bonding orbital ends up at lower energy than the NN LUMO-phenyl bonding orbital despite the smaller degree of orbital mixing.

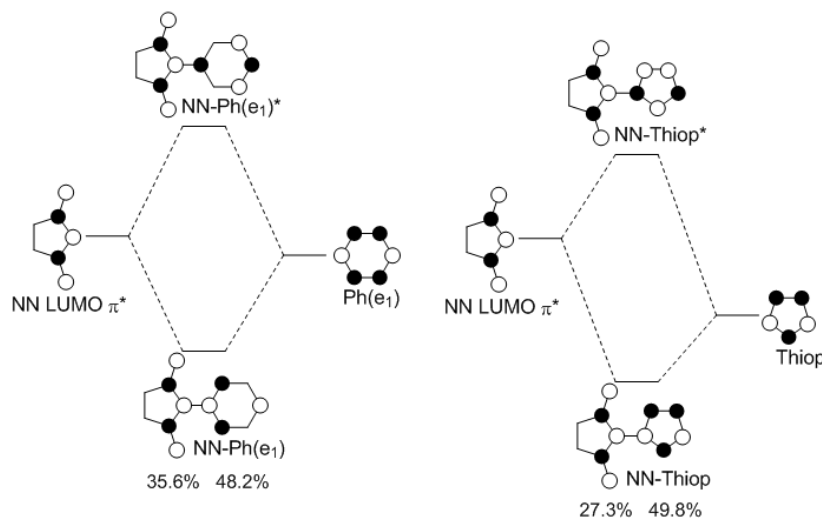


Figure 2.17: Molecular orbital diagram of NN-bridge mixing in $\text{Tp}^{\text{Cum,Me}}\text{Zn}(\text{SQ-Ph-NN})$ (left) and $\text{Tp}^{\text{Cum,Me}}\text{Zn}(\text{SQ-Thp-NN})$ (right). Energy levels are not drawn to scale. Percent contributions are obtained from the AOMix Mulliken Population Analysis of the DFT-calculated molecular orbitals of the full $\text{Tp}^{\text{Cum,Me}}\text{Zn}(\text{SQ-Bridge-NN})$ molecule.

Figure 2.18 shows the qualitative comparative molecular orbital diagram for the biradical component of $\text{Tp}^{\text{Cum,Me}}\text{Zn}(\text{SQ-Thp-NN})$. The energy gap between the delocalized SQ SOMO and the delocalized NN-Thp-SQ LUMO is smaller than the energy gap between the SQ SOMO and the delocalized NN-Ph-SQ LUMO in $\text{Tp}^{\text{Cum,Me}}\text{Zn}(\text{SQ-Ph-NN})$ due to the SQ SOMO being destabilized and the SQ-Thp-NN LUMO being stabilized. The donor-acceptor electronic communication is mediated by empty bridge orbitals for both $\text{X} = \text{Ph}$ and $\text{X} = \text{Thp}$.

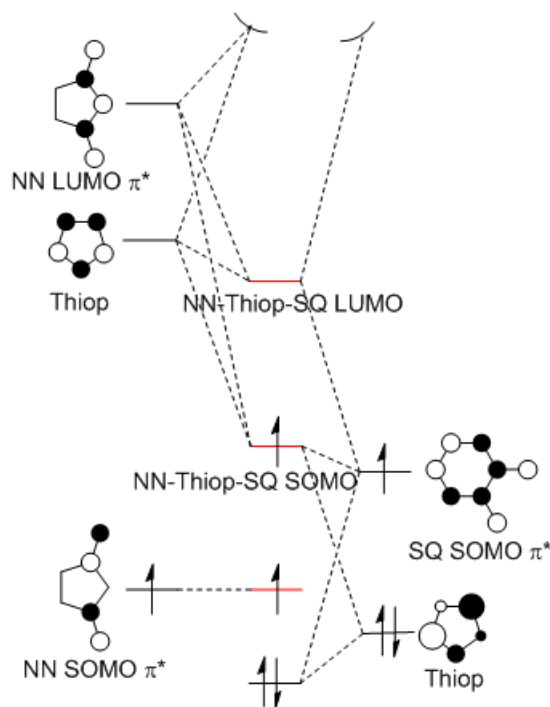


Figure 2.18: Molecular orbital diagram of $\text{Tp}^{\text{Cum,Me}}\text{Zn}(\text{SQ-Thp-NN})$. Energy levels are not drawn to scale. Thiophene sulfur points to the bottom.

The lower energy of the D-A charge transfer (CT) transition and more delocalized nature of the frontier orbitals both indicate that the amount of spin density that is delocalized from the SQ to NN is expected to be larger for $\text{Tp}^{\text{Cum,Me}}\text{Zn}(\text{SQ-Thp-NN})$ than for $\text{Tp}^{\text{Cum,Me}}\text{Zn}(\text{SQ-Ph-NN})$. This is observed both computationally and experimentally as the data in section 2.3.2.3 indicates. Figure 2.19 shows the spin density distribution for $\text{Tp}^{\text{Cum,Me}}\text{Zn}(\text{SQ-Thp-NN})$, and we observe both negative and positive spin population organized in an alternating pattern on the carbon atoms of the thiophene bridge. Interestingly, the sulfur has no net spin population. The summed Mulliken spin

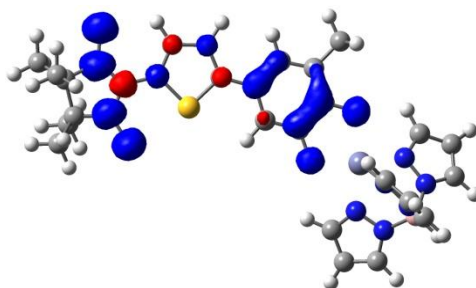


Figure 2.19: DFT-calculated spin density distribution for $\text{Tp}^{\text{Cum,Me}}\text{Zn}(\text{SQ-Thp-NN})$, where blue is positive spin density, red is negative spin density, and the contour isovalue is 0.004.

populations are: NN ring = 1.110, thiophene = 0.038, SQ = 0.845, and $\text{Tp}^{\text{Cum,Me}}\text{Zn} = 0.007$. This shows a larger spin delocalization from the donor to both the bridge and acceptor compared to $\text{Tp}^{\text{Cum,Me}}\text{Zn}(\text{SQ-Ph-NN})$ (NN: 1.063, Ph: -0.003, SQ: 0.932). Interestingly, the spin delocalization from the donor to both the bridge and acceptor is less than that for the *planar* $[\text{SQ-Ph-NN}]^-$ (NN: 1.124, Ph: 0.072, SQ: 0.804). Therefore the increased spin delocalization in $\text{Tp}^{\text{Cum,Me}}\text{Zn}(\text{SQ-Thp-NN})$ appears to have large a contribution from its more planar geometry. As the spin density distribution in Figure 2.19 indicates, there may be a spin delocalization of negative spin density from the NN

all the way onto the SQ donor, which would lead to a larger net positive spin density on the SQ.

2.4.2 Electronic Absorption Spectra and TD-DFT Band Assignments for $\text{Tp}^{\text{Cum,Me}}\text{Zn}(\text{SQ-Thp-NN})$

Room-temperature electronic absorption spectra for $\text{Tp}^{\text{Cum,Me}}\text{Zn}(\text{SQ-Thp-NN})$ were acquired by our collaborators in Prof. David A. Shultz's group (North Carolina State University) who possessed sufficient quantity of compound to accurately determine

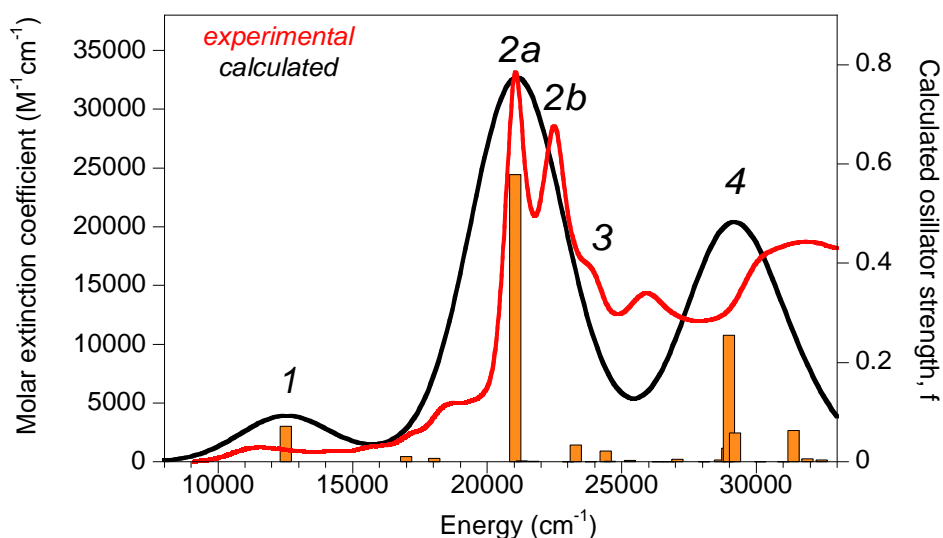


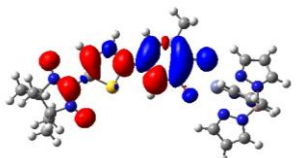
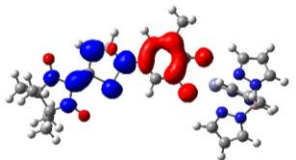
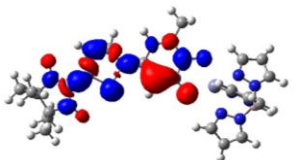
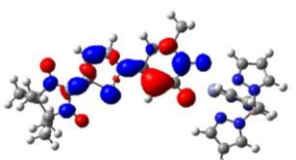
Figure 2.20: DFT-calculated (black) and experimental solution (red) spectra of $\text{Tp}^{\text{Cum,Me}}\text{Zn}(\text{SQ-Thp-NN})$. DFT bands were widened to 4000 cm^{-1} , bars represent calculated oscillator strengths.

extinction coefficients, while we prepared polymer film samples and acquired variable temperature electronic absorption spectra of the films.

Figure 2.20 shows the overlay of the experimental and TD-DFT-calculated electronic absorption of $\text{Tp}^{\text{Cum,Me}}\text{Zn}(\text{SQ-Thp-NN})$. Variable temperature electronic absorption data was acquired for $\text{Tp}^{\text{Cum,Me}}\text{Zn}(\text{SQ-Thp-NN})$, but no temperature dependent

spectral changes were observed consistent with a strong ferromagnetic exchange interaction. Table 2.5 and Figure 2.20 summarize the TD-DFT results for $\text{Tp}^{\text{Cum,Me}}\text{Zn}(\text{SQ-Thp-NN})$ allowing for comparison with the experimental solution electronic absorption spectrum of $\text{Tp}^{\text{Cum,Me}}\text{Zn}(\text{SQ-Thp-NN})$. Band 1 is assigned as a SQ-Thp-NN HOMO \rightarrow SQ SOMO transition, and is observed in the experimental spectrum

Table 2.5: DFT band assignments for $\text{Tp}^{\text{Cum,Me}}\text{Zn}(\text{SQ-Thp-NN})$.

Band	DFT		Assignment	Electron density difference map
	Energy (cm^{-1})	f		
1	12520	0.072	[SQ-Thp-NN HOMO \rightarrow SQ SOMO]	
2a 2b	21050	0.579	[SQ SOMO \rightarrow SQ-Thp-NN LUMO]; 0 \rightarrow 0' 0 \rightarrow 1' vibronic band built on 2a ΔE (3-2) = 1440 cm^{-1}	
3	23280	0.034	[SQ-Thp-NN HOMO \rightarrow SQ-Thp-NN LUMO] β - [SQ-Thp-NN HOMO \rightarrow SQ-Thp-NN LUMO] α	
4	28990	0.255	[SQ-Thp-NN HOMO \rightarrow SQ-Thp-NN LUMO] β + [SQ-Thp-NN HOMO \rightarrow SQ-Thp-NN LUMO] α	

at $\sim 11500\text{ cm}^{-1}$, which is at about 1000 cm^{-1} lower energy than calculated. Both calculated and experimental energies for band 1 occur at lower energy for $\text{Tp}^{\text{Cum,Me}}\text{Zn}(\text{SQ-Thp-NN})$ than for $\text{Tp}^{\text{Cum,Me}}\text{Zn}(\text{SQ-Ph-NN})$. Band 2 is the donor-acceptor charge transfer band, which also occurs at lower energy (2000 cm^{-1}) than the corresponding transition for $\text{Tp}^{\text{Cum,Me}}\text{Zn}(\text{SQ-Ph-NN})$ due to the reasons discussed in the previous section. The calculated and experimental band energies are in excellent agreement for band 2a, and the experimental data shows a second band (2b) at $\sim 1440\text{ cm}^{-1}$ higher energy than 2a, which is assigned as the $0 \rightarrow 1'$ vibronic band built on the $0 \rightarrow 0'$ origin (2a). Bands 2a and 2b occur at $\sim 21050\text{ cm}^{-1}$ and $\sim 22490\text{ cm}^{-1}$, respectively, in the experimental spectrum. Band 3 is calculated with a much lower oscillator strength than is observed experimentally, where the DFT calculations predict no bands of significant intensity between $\sim 21000\text{ cm}^{-1}$ and $\sim 29000\text{ cm}^{-1}$, while the experimental spectrum shows bands at $\sim 23700\text{ cm}^{-1}$ and $\sim 25900\text{ cm}^{-1}$. Band 3 is calculated as a negative linear combination of the $[\text{SQ-Thp-NN HOMO} \rightarrow \text{SQ-Thp-NN LUMO}]$ transition with contributions from both the α and β one-electron promotions, and may correspond to the absorption feature at $\sim 23700\text{ cm}^{-1}$. Band 4 is assigned as the positive linear combination counterpart to band 3, and may correspond to an intense, broad band at $\sim 31800\text{ cm}^{-1}$ in the experimental spectrum, where the experimental and calculated bands have similar extinction coefficients, but the experimental band is almost 2000 cm^{-1} higher in energy than the calculated band. Although the calculated bands 3 and 4 do not have the best agreement with experimental band energies, but we believe that the postulated assignments for bands 3 and 4 are reasonable in the context of the assignments for the

rest of the spectrum. The electronic absorption spectra, both calculated and experimental, confirm the picture for $\text{Tp}^{\text{Cum,Me}}\text{Zn}(\text{SQ-Thp-NN})$ that we have developed from the analysis of the DFT-calculated frontier molecular orbitals. Namely, there are significant differences in coupling of the bridge to donor and acceptor when the phenyl bridge is replaced by a thiophene bridge, and key thiophene orbitals couple more strongly to the donor than the phenyl orbitals leading to a lower energy donor-acceptor charge transfer transition.

2.4.3 Resonance Raman Spectra and DFT Frequency Calculations for $\text{Tp}^{\text{Cum,Me}}\text{Zn}(\text{SQ-Thp-NN})$

Resonance Raman spectra of $\text{Tp}^{\text{Cum,Me}}\text{Zn}(\text{SQ-Thp-NN})$ were acquired at excitation wavelengths from 407 nm to 647 nm in order to determine which vibrational modes may be enhanced when exciting into the donor-acceptor charge transfer band. In general, only totally symmetric vibrational modes have appreciable intensity in a resonance Raman experiment (A-term mechanism),^{89,95} and in particular the vibrational modes that will be most enhanced are those most strongly coupled to the geometric distortion that occurs during the electronic transition that is being excited by the laser. $\text{Tp}^{\text{Cum,Me}}\text{Zn}(\text{SQ-Thp-NN})$ has a lower effective symmetry than $\text{Tp}^{\text{Cum,Me}}\text{Zn}(\text{SQ-Ph-NN})$ due to the lower symmetry of thiophene compared to benzene. As a result of this, we might expect that $\text{Tp}^{\text{Cum,Me}}\text{Zn}(\text{SQ-Thp-NN})$ will possess a larger number of resonantly-enhanced modes compared to $\text{Tp}^{\text{Cum,Me}}\text{Zn}(\text{SQ-Ph-NN})$ when exciting into the donor-acceptor charge transfer band.

Figure 2.21 shows the resonance Raman spectrum of $\text{Tp}^{\text{Cum,Me}}\text{Zn}(\text{SQ-Thp-NN})$ using 458 nm laser excitation, where we observe the largest resonance enhancement. Resonance Raman spectra using additional laser lines are included in Appendix 6.1.1. We observe a large number of resonantly-enhanced modes over a large frequency range (600 – 1600 cm^{-1}), and the two most enhanced vibrations occur at 1399 cm^{-1} and 1424 cm^{-1} , followed in intensity by vibrational bands at 1521 cm^{-1} , 1499 cm^{-1} , 1290 cm^{-1} , 1055 cm^{-1} , and 627 cm^{-1} .

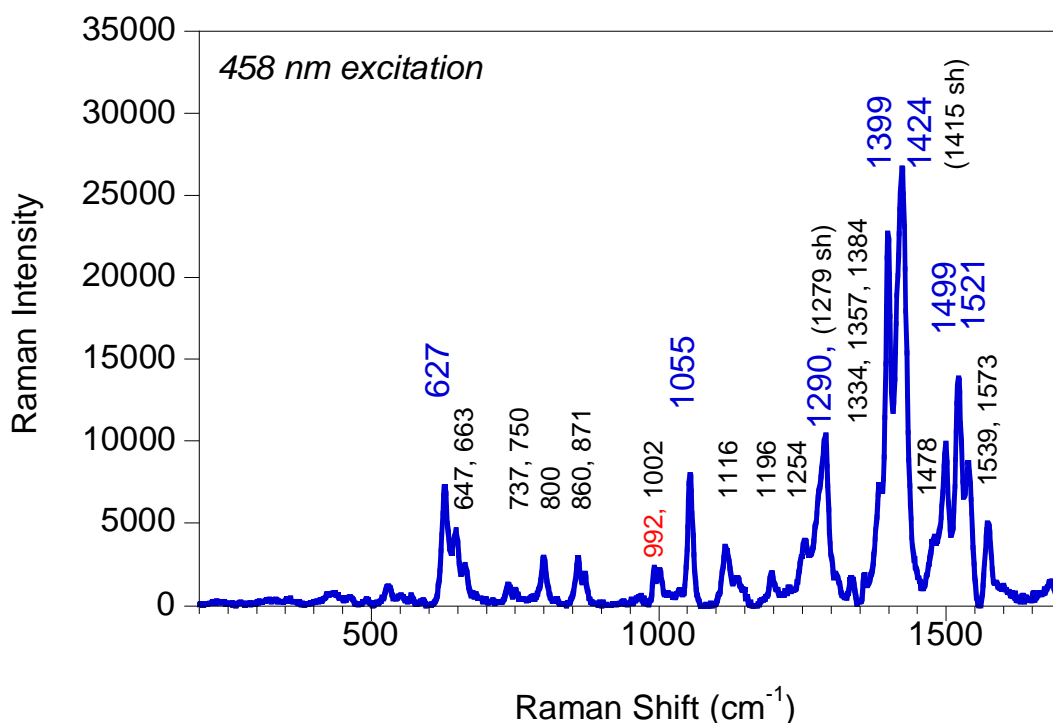


Figure 2.21: Resonance Raman spectrum of $\text{Tp}^{\text{Cum,Me}}\text{Zn}(\text{SQ-Thp-NN})$ in a $\text{NaCl}/\text{Na}_2\text{SO}_4$ matrix using a 458 nm excitation wavelength. Internal standard sulfate peak(s) are marked in red, and sample modes are marked in black and blue (most enhanced).

A resonance Raman enhancement profile (Figure 2.22) was constructed for the $\sim 1400\text{ cm}^{-1}$, $\sim 1420\text{ cm}^{-1}$, and $\sim 626\text{ cm}^{-1}$ vibrational modes. The mode at 626 cm^{-1} was chosen specifically since it is quite distinct for $\text{Tp}^{\text{Cum,Me}}\text{Zn}(\text{SQ-Thp-NN})$. The most enhanced modes for $\text{Tp}^{\text{Cum,Me}}\text{Zn}(\text{SQ-Ph-NN})$ occur in the $1100\text{-}1600\text{ cm}^{-1}$ range. Resonance Raman enhancement was calculated as the ratio of the area of the peak for a given vibrational mode to the area of the 992 cm^{-1} sulfate peak in each spectrum. We observe that all three modes are greatly resonantly enhanced under the D-A CT band.

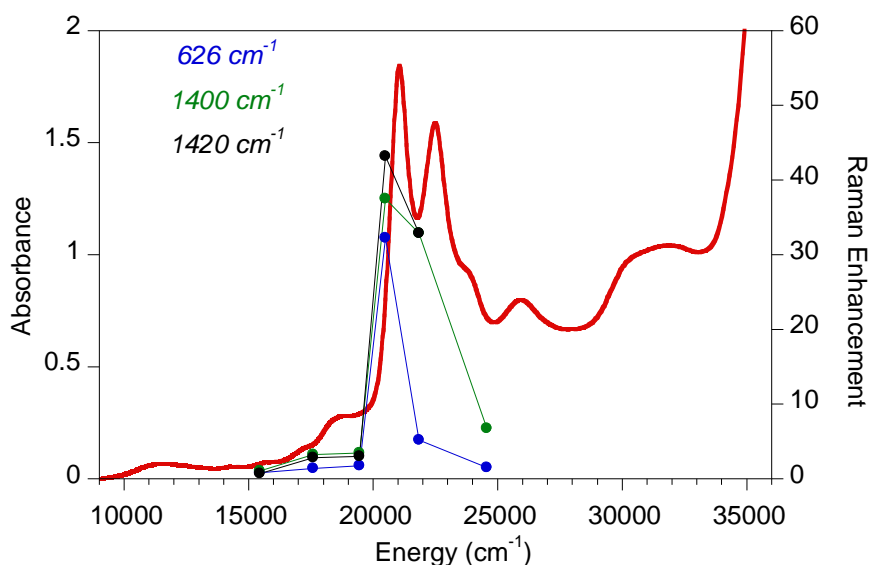


Figure 2.22: Resonance Raman enhancement profile for selected modes (blue 626 cm^{-1} , green 1400 cm^{-1} , black 1420 cm^{-1}) as a function of laser excitation energy and overlaid on the electronic absorption spectrum (red). The $\text{Tp}^{\text{Cum,Me}}\text{Zn}(\text{SQ-Thp-NN})$ sample was in the solid state in a $\text{NaCl}/\text{Na}_2\text{SO}_4$ matrix.

In order to better understand the origin of the resonantly-enhanced modes observed in Figure 2.21, we started by analyzing the Raman active modes of an isolated thiophene molecule. Figure 2.23 shows the five DFT-calculated modes that are expected to be the most Raman active. These vibrations are computed to occur at 610 cm^{-1} , 835

cm^{-1} , 1057 cm^{-1} , 1402 cm^{-1} , and 1468 cm^{-1} . The modes at 610 cm^{-1} and 835 cm^{-1} are predominantly ring breathing modes with a large C-S bond stretch component, while the modes at 1057 cm^{-1} , 1402 cm^{-1} , and 1468 cm^{-1} have more C-C stretching character in addition to the ring breathing. We notice that the frequencies of these thiophene modes correspond remarkably well to the general energy regions in Figure 2.21 where we see the resonantly enhanced modes for $\text{Tp}^{\text{Cum,Me}}\text{Zn}(\text{SQ-Thp-NN})$, and the most strongly

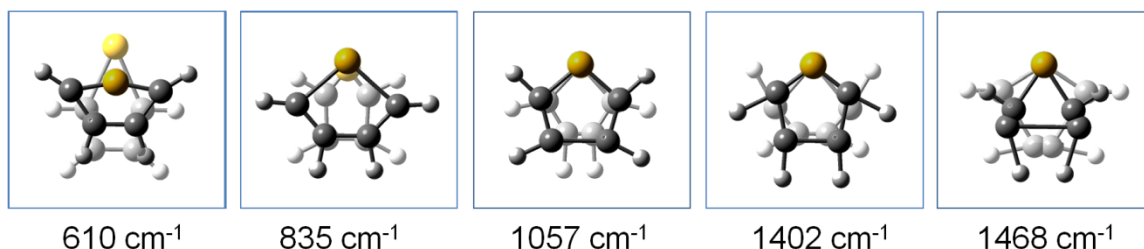


Figure 2.23: Raman active DFT-calculated vibrations of thiophene. Modes are shown as overlays of the extrema of the vibrational mode.

enhanced modes for $\text{Tp}^{\text{Cum,Me}}\text{Zn}(\text{SQ-Thp-NN})$ occur at 627 cm^{-1} , 1055 cm^{-1} , 1290 cm^{-1} , 1399 cm^{-1} , 1424 cm^{-1} , 1499 cm^{-1} , 1521 cm^{-1} .

Most of the enhanced modes fall into general regions: $600\text{-}700 \text{ cm}^{-1}$, $800\text{-}900 \text{ cm}^{-1}$, $1050\text{-}1060 \text{ cm}^{-1}$, $1200\text{-}1450 \text{ cm}^{-1}$ and $1470\text{-}1520 \text{ cm}^{-1}$. This similarity suggests that the resonance Raman spectrum of $\text{Tp}^{\text{Cum,Me}}\text{Zn}(\text{SQ-Thp-NN})$ is dominated by the vibrational modes of the thiophene bridge, and large geometric distortions of the thiophene bridge upon excitation into the D-A CT band. When we extend the DFT frequency calculations to the $[\text{SQ-Thp-SQ}]$ ligand, we observe that vibrational modes of the thiophene ring are coupled to the SQ and NN ring modes and occur at approximately

the same energies as calculated for the isolated thiophene molecule. Figure 2.24 shows a selection of such thiophene modes coupled to SQ and/or NN modes. Most of these modes predominantly involve either the thiophene and semiquinone with only a small stretching amplitude on the nitronyl nitroxide, or the thiophene and nitronyl nitroxide with a small degree of semiquinone distortion.

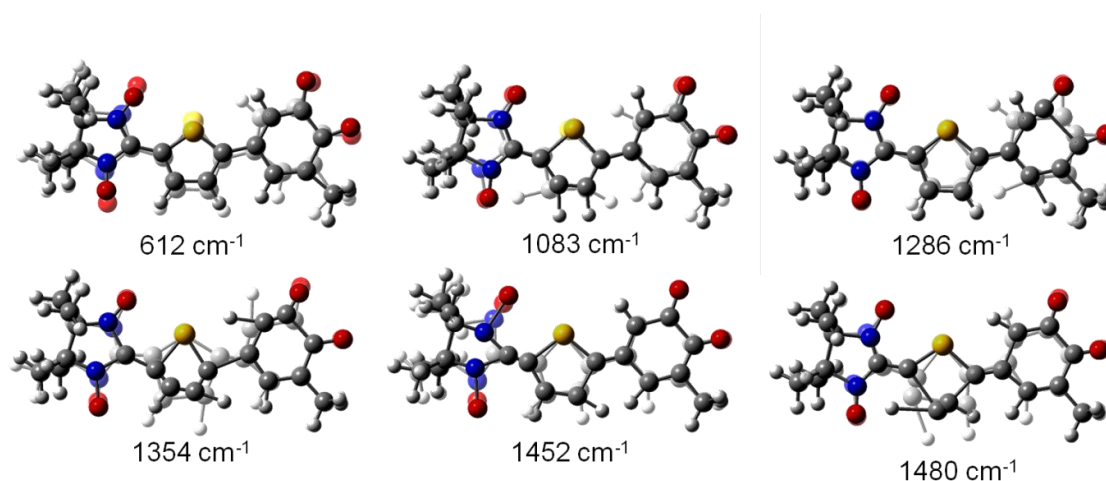


Figure 2.24: Selected DFT-calculated vibrations of [SQ-Thp-NN]. Modes are shown as overlays of the extrema of the vibrational mode.

When examining the orbital character of the thiophene bridge in the SQ-Thp-NN LUMO, which is the acceptor orbital in the D-A CT transition, we observe that an increase in electron density for this orbital is expected to lengthen both of the C-S bonds, as well as the C-C bonds adjacent to the C-S bonds of thiophene. Additionally, we expect a shortening of the C-C bond opposite the sulfur atom in thiophene. Such a distortion of the thiophene bridge is approximately observed in the calculated 1480 cm^{-1} mode shown in Figure 2.24, which is also a mode that displays some vibrational motion over all three constituent rings. The experimental mode that corresponds to this calculated mode may

be either the 1499 cm^{-1} mode or the 1521 cm^{-1} mode. While these are not the most enhanced modes in the resonance Raman spectrum, they are closer to 1480 cm^{-1} than the modes observed at 1400 cm^{-1} or 1420 cm^{-1} , and more importantly they are larger than the 1440 cm^{-1} excited state vibrational spacing observed in the electronic absorption spectrum of $\text{Tp}^{\text{Cum,Me}}\text{Zn}(\text{SQ-Thp-NN})$. Lower frequencies in the excited state are associated with the more antibonding nature of the occupied acceptor wavefunction in the excited state, and if we examine the SQ-Thp-NN LUMO, we note that the LUMO has more antibonding character within the thiophene ring than the SQ SOMO. However, the LUMO has more bonding character for the two bonds connecting the thiophene to the donor and acceptor than the SQ SOMO does. The mode at 1480 cm^{-1} has mostly stretching character within the thiophene ring, so that its corresponding excited state frequency would be expected to be at a lower frequency.

2.5 Extending the Length of the Bridge: Biphenyl and Bithiophene

2.5.1 Maintaining Ferromagnetic Coupling Over Longer Distances

Donor-bridge-acceptor biradicals with biphenyl and bithiophene bridges have been synthesized by the Shultz group at North Carolina State University. These bridges extend the length of the molecule (and the bridge) without losing the donor-acceptor ferromagnetic coupling. Having an extended two-ring (i.e. $\text{B} = \text{Ph}_2$ or $\text{B} = \text{Thiop}_2$) bridge not only changes the length of the donor-acceptor distance but also introduces an additional bridge-bridge dihedral angle to the DBA molecule, thus effecting both factors two and three (marked in red) of Eq. 15:

$$H_{ab}^2 = (H_{ab}^0)^2 e^{-\beta(r-r_0)} \cos^m \theta. \quad \text{Eq. 15}$$

Thus we expect both the exponential decay term and the cosine term of Eq. 15 to be affected. Assuming that the cosine overlap term is not significantly different from that in $\text{Tp}^{\text{Cum,Me}}\text{Zn}(\text{SQ-Ph-NN})$ and $\text{Tp}^{\text{Cum,Me}}\text{Zn}(\text{SQ-Thp-NN})$ (i.e. that the additional Ph-Ph or Thp-Thp dihedral angles are not very large), we can extract a value for β from the exponential decay term (Eq. 15). Here, β is related to how sensitive the donor-acceptor coupling is to an increase in the donor-acceptor distance. The Shultz group has obtained values for J from magnetic susceptibility measurements, and found that $J = +20 \text{ cm}^{-1}$ for $\text{Tp}^{\text{Cum,Me}}\text{Zn}(\text{SQ-Ph}_2\text{-NN})$, and $J = +40 \text{ cm}^{-1}$ for $\text{Tp}^{\text{Cum,Me}}\text{Zn}(\text{SQ-Thp}_2\text{-NN})$. This shows

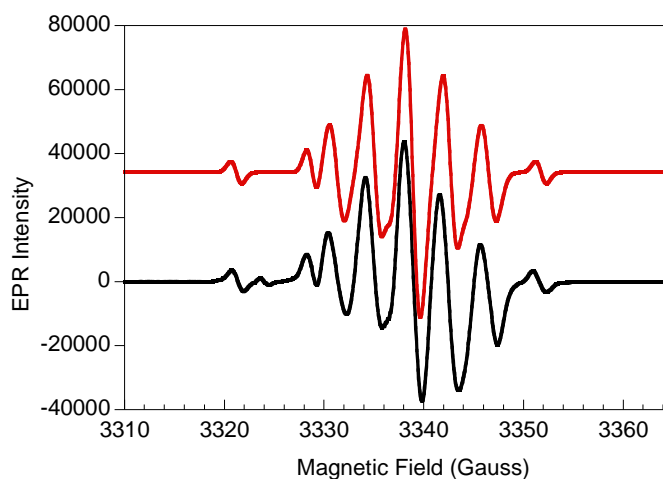


Figure 2.25: Room-temperature EPR of $\text{Tp}^{\text{Cum,Me}}\text{Zn}(\text{SQ-Ph}_2\text{-NN})$. Data (black), spectral simulation (red).

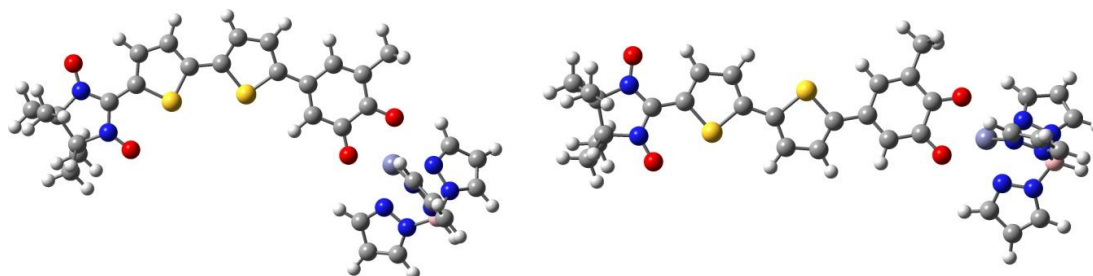


Figure 2.26: $\text{Tp}^{\text{Cum,Me}}\text{Zn}(\text{SQ-Thp}_2\text{-NN})$ in a cis-conformation (left) or trans-conformation (right).

Table 2.6: Ring torsion angles of the DFT-optimized structures of $\text{Tp}^{\text{Cum,Me}}\text{Zn}(\text{SQ-Thp}_2\text{-NN})$ (trans/cis) and $\text{Tp}^{\text{Cum,Me}}\text{Zn}(\text{SQ-Ph}_2\text{-NN})$. Crystal structure data is a private communication with D. A. Shultz, North Carolina State University, unpublished (2012).

	$\text{Tp}^{\text{Cum,Me}}\text{Zn}(\text{SQ-Thp}_2\text{-NN})$			$\text{Tp}^{\text{Cum,Me}}\text{Zn}(\text{SQ-Ph}_2\text{-NN})$		
Dihedral angle ($^\circ$)	NN-Thp	Thp-Thp	SQ-Thp	NN-Ph	Ph-Ph	SQ-Ph
DFT Optimized	1/1	7/11	9/13	3	35	33
Crystal Structure				35	38	25

that even at a separation of over 10 Å the donor and acceptor retain a relatively strong ferromagnetic coupling. Since J is proportional to H_{ab}^2 , plotting J as a function of donor-acceptor distance for the series of D-B-A biradicals allows one to determine that $\beta \sim 0.39^a$ which is comparable to values from the literature.¹⁸ We measured the isotropic room temperature EPR spectrum for $\text{Tp}^{\text{Cum,Me}}\text{Zn}(\text{SQ-Ph}_2\text{-NN})$, and simulated the spectrum with two equivalent $I = 1$ nitrogens and an isotropic nitrogen hyperfine coupling constant of $7.13 \text{ e-}4 \text{ cm}^{-1}$, Figure 2.25. The EPR spectrum also shows the presence of a paramagnetic impurity with $S = 1/2$, which is likely to be unreacted NN or SQ.

^a Private communication with D. A. Shultz, North Carolina State University, unpublished (2012).

Dihedral angles for the optimized structures of $\text{Tp}^{\text{Cum,Me}}\text{Zn}(\text{SQ-Thp}_2\text{-NN})$ and $\text{Tp}^{\text{Cum,Me}}\text{Zn}(\text{SQ-Ph}_2\text{-NN})$ are shown in Table 2.6. No crystal structure has been obtained yet for $\text{Tp}^{\text{Cum,Me}}\text{Zn}(\text{SQ-Thp}_2\text{-NN})$. $\text{Tp}^{\text{Cum,Me}}\text{Zn}(\text{SQ-Thp}_2\text{-NN})$ can adopt a cis- or trans-geometry with respect to the orientation of the thiophene rings, as shown in Figure 2.26. DFT calculations indicate that the trans-configuration is the lower energy structure, and we proceeded with the DFT analysis for $\text{Tp}^{\text{Cum,Me}}\text{Zn}(\text{SQ-Thp}_2\text{-NN})$ tentatively assuming that the molecule does indeed have the trans-geometry. Table 2.6 shows that the cis- and trans conformations do not differ significantly with respect to ring torsion angles, and, as observed for the monothiophene-bridged D-B-A complex, the optimized $\text{Tp}^{\text{Cum,Me}}\text{Zn}(\text{SQ-Thp}_2\text{-NN})$ structure is remarkably planar, with an NN-Thp dihedral angle of 1° , and Thp-Thp and SQ-Thp dihedrals of $\sim 10^\circ$. $\text{Tp}^{\text{Cum,Me}}\text{Zn}(\text{SQ-Ph}_2\text{-NN})$ has significantly larger ring-ring dihedral angles, and the NN-Ph and Ph-SQ dihedrals are as observed for the $\text{Tp}^{\text{Cum,Me}}\text{Zn}(\text{SQ-Ph-NN})$. The Ph-Ph dihedral is calculated to be 35° , and this is about the same value as the SQ-Ph dihedral. Crystal structure data^b show similar Ph-Ph and Ph-SQ dihedral angles and a large NN-Ph dihedral rather than the planar NN-bridge geometry that is usually observed in D-B-A biradicals. This could be due to the difference in the state of the sample, i.e. a solid crystal vs. a gas-phase calculated geometry, where it is conceivable that there are crystal packing forces that affect the fairly long $\text{Tp}^{\text{Cum,Me}}\text{Zn}(\text{SQ-Ph}_2\text{-NN})$ molecule. It is experimentally known that the molecular conductance of biphenyl molecules in a molecular junction between gold electrodes has a $\cos^2\theta$ dependence on the biphenyl ring torsion angle θ .²⁰

^b Private communication with D. A. Shultz, North Carolina State University, unpublished (2012).

In section 3.2.3 we showed that there was an excellent linear correlation between calculated nitrogen spin populations and isotropic nitrogen hyperfine coupling constants. We now have a small series of donor-acceptor/donor-bridge-acceptor biradicals consisting of $\text{Tp}^{\text{Cum,Me}}\text{Zn}(\text{SQ-NN})$, $\text{Tp}^{\text{Cum,Me}}\text{Zn}(\text{SQ-Ph-NN})$, and $\text{Tp}^{\text{Cum,Me}}\text{Zn}(\text{SQ-Ph}_2\text{-$

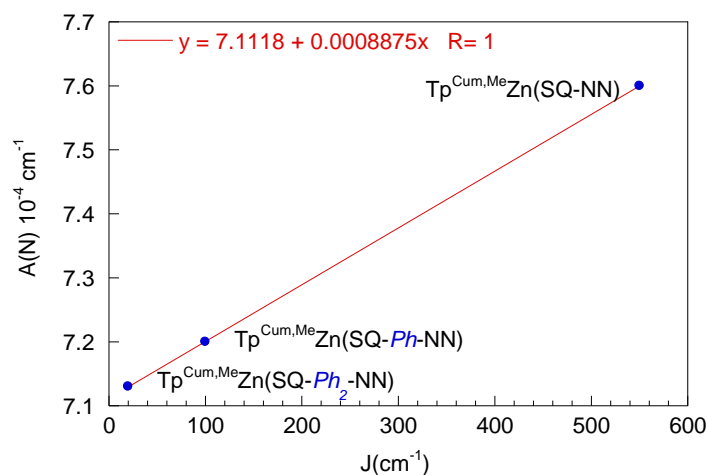


Figure 2.27: Experimental nitrogen hyperfine coupling constants as a function of J from experimental magnetic susceptibility measurements for $\text{Tp}^{\text{Cum,Me}}\text{Zn}(\text{SQ-Ph}_n\text{-NN})$, where $n = 0, 1$, and 2 .

NN) where $B = \text{Ph}_n$ and $n = 0, 1$, and 2 . Figure 2.27 shows the experimental nitrogen hyperfine coupling constants plotted as a function of the experimental J values, and we obtain an excellent linear correlation between those two experimental parameters. The correlation between J and A_N suggested previously as a means to estimate J from a known value for A_N .⁵⁹ It is remarkable to find such strong linear correlations between DFT-calculated parameters (spin populations) and between two sets of experimental observables from different experimental techniques (EPR and magnetic susceptibility data). We can further relate the experimental J values to H_{ab} , the donor-acceptor electronic coupling matrix element (Eq. 16 adapted from reference⁴):

$$\frac{J_{SQ-Ph_2-NN}}{J_{SQ-Ph-NN}} = \frac{H_{SQ-Ph_2-NN}^2}{H_{SQ-Ph-NN}^2}. \quad \text{Eq. 16}$$

Therefore, if we know the value of J for $\text{Tp}^{\text{Cum,Me}}\text{Zn}(\text{SQ-Ph}_2\text{-NN})$, we can use the known values of J and H_{ab}^2 for $\text{Tp}^{\text{Cum,Me}}\text{Zn}(\text{SQ-Ph-NN})$ to obtain H_{ab} values for unknown systems.^{4,59} Here, a five-fold reduction in J is expected to correspond to a factor of $\sqrt{5}$ (= 2.2) reduction in H_{ab} .

2.5.2 Frontier Molecular Orbitals and Orbital Compositions for $\text{Tp}^{\text{Cum,Me}}\text{Zn}(\text{SQ-Thp}_2\text{-NN})$ and $\text{Tp}^{\text{Cum,Me}}\text{Zn}(\text{SQ-Ph}_2\text{-NN})$

DFT-calculated frontier molecular orbitals were constructed and their orbital compositions have been analyzed by a Mulliken population analysis for $\text{Tp}^{\text{Cum,Me}}\text{Zn}(\text{SQ-Thp}_2\text{-NN})$ (Figure 2.28) and $\text{Tp}^{\text{Cum,Me}}\text{Zn}(\text{SQ-Ph}_2\text{-NN})$ (Figure 2.29). The frontier molecular orbitals of $\text{Tp}^{\text{Cum,Me}}\text{Zn}(\text{SQ-Thp}_2\text{-NN})$ show a large degree of delocalization over all four rings (NN, Thp, Thp, and SQ) of the D-B-A ligand, with the exception of the NN SOMO, which does not mix with any other molecular orbitals (MOs). The large degree of electron delocalization for $\text{Tp}^{\text{Cum,Me}}\text{Zn}(\text{SQ-Thp}_2\text{-NN})$ mirrors that observed in $\text{Tp}^{\text{Cum,Me}}\text{Zn}(\text{SQ-Thp-NN})$, and it is interesting to note that the two thiophene rings of the bridge have approximately equal contributions in most of the molecular orbitals.

This suggests that the fragment orbitals on each thiophene form positive and negative linear combinations with the thp-thp bonding combination being stabilized by the same degree as the thp-thp antibonding combination is destabilized for a given set of thiophene fragment orbitals. The orbital coefficients of both thiophene rings are

approximately equal in such a given set of orbitals. The bithiophene orbitals can interact further with various NN and SQ orbitals. When this occurs, the thiophene orbitals are no

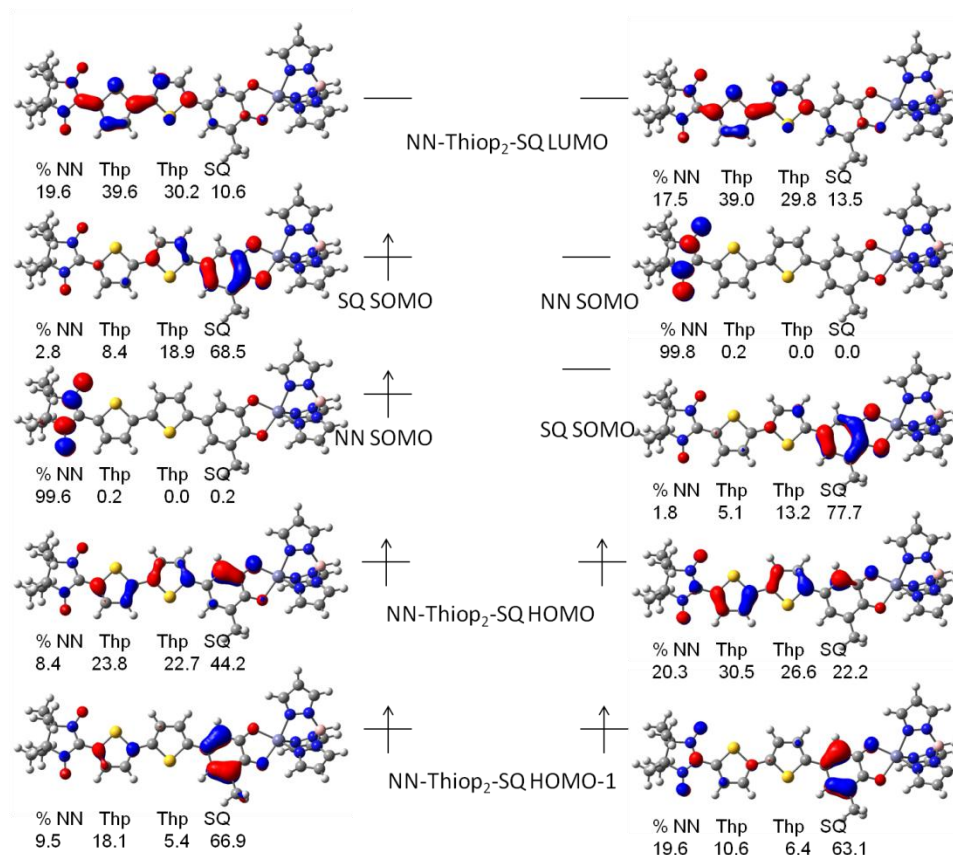


Figure 2.28: Frontier molecular orbitals and orbital composition for $\text{Tp}^{\text{Cum,Me}}\text{Zn}(\text{SQ-Thp}_2\text{-NN})$.

longer equivalent and their orbital coefficients no longer equal. Both the isosurfaces for the $\text{Tp}^{\text{Cum,Me}}\text{Zn}(\text{SQ-Thp}_2\text{-NN})$ molecular orbitals and their orbital compositions support this description. As a consequence of this, we expect molecular orbitals that use thp-thp bonding combinations to be shifted down in energy compared to the analogous orbital in a monothiophene-bridged molecule when normalized to the NN SOMO. The energy of

the NN SOMO is set to zero, as it does not mix with any other orbital and thus represents an internal zero-point. Similarly we expect molecular orbitals that use thp-thp antibonding combinations to be shifted to higher energy compared to the analogous orbital in a monothiophene-bridged molecule with respect to the NN SOMO. The α NN-Thiop₂-SQ LUMO has a thp-thp bonding combination, and its energy with respect to the α NN-SOMO in $\text{Tp}^{\text{Cum,Me}}\text{Zn}(\text{SQ-Thp}_2\text{-NN})$ is 25679 cm^{-1} , whereas in $\text{Tp}^{\text{Cum,Me}}\text{Zn}(\text{SQ-Thp-NN})$ the α NN-SOMO - α SQ-Thp-NN LUMO energy difference is 27654 cm^{-1} . The β NN-Thiop₂-SQ HOMO has a Thp-Thp antibonding combination, and its energy with respect to the α NN-SOMO in $\text{Tp}^{\text{Cum,Me}}\text{Zn}(\text{SQ-Thp}_2\text{-NN})$ is $+659\text{ cm}^{-1}$, whereas in $\text{Tp}^{\text{Cum,Me}}\text{Zn}(\text{SQ-Thp-NN})$ the energy of the β SQ-Thp-NN HOMO with respect to the α NN-SOMO is -1536 cm^{-1} . Thus the NN-Thiop₂-SQ LUMO is stabilized by $\sim 2000\text{ cm}^{-1}$ and the NN-Thiop₂-SQ HOMO destabilized by $\sim 2000\text{ cm}^{-1}$ compared to those orbitals in $\text{Tp}^{\text{Cum,Me}}\text{Zn}(\text{SQ-Thp-NN})$, which should lower both the energy of the donor-acceptor CT band and the low-energy HOMO to SQ SOMO transition, provided that the relative energy of the SQ SOMO itself has not changed much.

The frontier molecular orbitals of $\text{Tp}^{\text{Cum,Me}}\text{Zn}(\text{SQ-Ph}_2\text{-NN})$ (in Figure 2.29) show a lower degree of delocalization over the biphenyl bridge than we observed for the bithiophene bridged D-B-A biradical. This is particularly true for the LUMO, while the biphenyl bridge is fairly delocalized in the HOMO. Similar to $\text{Tp}^{\text{Cum,Me}}\text{Zn}(\text{SQ-Thp}_2\text{-NN})$, the NN-Ph LUMO in $\text{Tp}^{\text{Cum,Me}}\text{Zn}(\text{SQ-Ph}_2\text{-NN})$ has a Ph-Ph bonding combination and is anticipated to be energetically stabilized. The energy of the α NN-Ph LUMO in

$\text{Tp}^{\text{Cum,Me}}\text{Zn}(\text{SQ-Ph}_2\text{-NN})$ with respect to the α NN-SOMO in $\text{Tp}^{\text{Cum,Me}}\text{Zn}(\text{SQ-Ph}_2\text{-NN})$ is 27215 cm^{-1} , which is $\sim 1100 \text{ cm}^{-1}$ lower than the analogous energy difference in

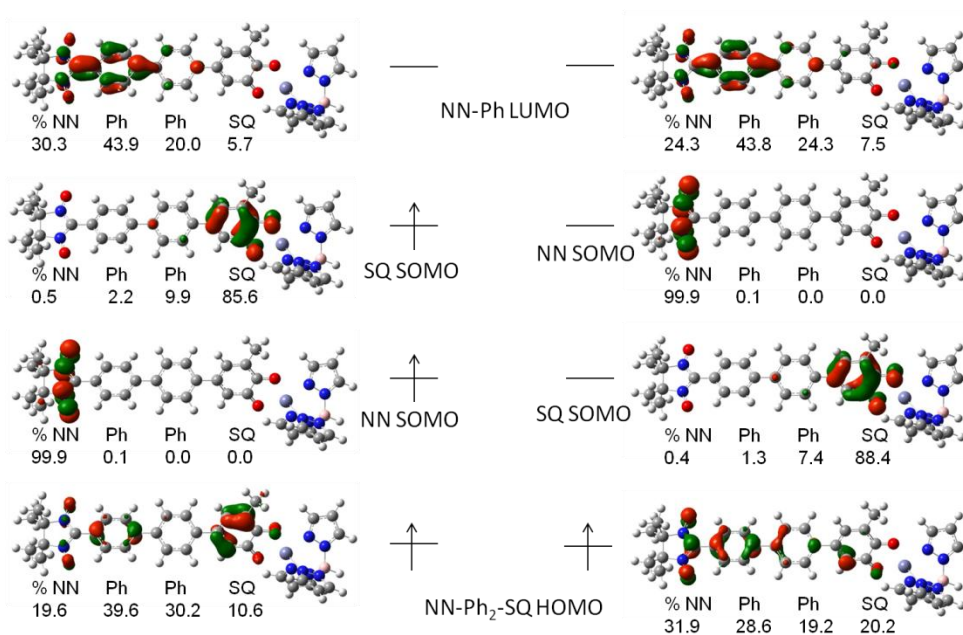


Figure 2.29: Frontier molecular orbitals and orbital composition for $\text{Tp}^{\text{Cum,Me}}\text{Zn}(\text{SQ-Ph}_2\text{-NN})$.

$\text{Tp}^{\text{Cum,Me}}\text{Zn}(\text{SQ-Ph-NN})$ (28312 cm^{-1}). Thus we would expect the D-A CT band to be at lower energy in $\text{Tp}^{\text{Cum,Me}}\text{Zn}(\text{SQ-Ph}_2\text{-NN})$ than in $\text{Tp}^{\text{Cum,Me}}\text{Zn}(\text{SQ-Ph-NN})$; although the D-A CT band in $\text{Tp}^{\text{Cum,Me}}\text{Zn}(\text{SQ-Ph}_2\text{-NN})$ is not expected to be lowered in energy as much as expected for $\text{Tp}^{\text{Cum,Me}}\text{Zn}(\text{SQ-Thp}_2\text{-NN})$. That the contributions from both phenyl rings of the bridge to the LUMO are not equal suggests that the Ph that is bonded to the NN mixes with the NN LUMO just as strongly, or maybe even more strongly, than it mixes with its neighboring phenyl. This is consistent with what we already know about the energetic similarity of the Ph e_1 orbital to the NN LUMO.

2.5.3 Room-Temperature Electronic Absorption Spectra, Time-Dependent DFT Results and Band Assignments for $\text{Tp}^{\text{Cum,Me}}\text{Zn}(\text{SQ-Thp}_2\text{-NN})$ and $\text{Tp}^{\text{Cum,Me}}\text{Zn}(\text{SQ-Ph}_2\text{-NN})$

Room-temperature solution spectra were acquired by the Shultz group at North Carolina State University in order to obtain molar extinction coefficients for $\text{Tp}^{\text{Cum,Me}}\text{Zn}(\text{SQ-Thp}_2\text{-NN})$ and $\text{Tp}^{\text{Cum,Me}}\text{Zn}(\text{SQ-Ph}_2\text{-NN})$. We obtained variable-temperature electronic absorption of $\text{Tp}^{\text{Cum,Me}}\text{Zn}(\text{SQ-Thp}_2\text{-NN})$ and $\text{Tp}^{\text{Cum,Me}}\text{Zn}(\text{SQ-Ph}_2\text{-NN})$ film samples, which were analyzed in detail as described below in section in 2.5.4. The film polymer film data is essentially identical to the room-temperature solution spectra. Figure 2.30 shows the experimental and DFT-calculated overlay of electronic absorption spectra for $\text{Tp}^{\text{Cum,Me}}\text{Zn}(\text{SQ-Thp}_2\text{-NN})$, where we included the calculated absorption trace for both the cis- and trans-isomers of $\text{Tp}^{\text{Cum,Me}}\text{Zn}(\text{SQ-Thp}_2\text{-NN})$. The calculated absorption bands for the cis- and trans isomers of $\text{Tp}^{\text{Cum,Me}}\text{Zn}(\text{SQ-Thp}_2\text{-NN})$ overlay one another except for a small energy shift of band 1, and differ mostly in the relative intensities of bands 2 and 3. We also notice that the calculated absorption spectra are shifted to lower energies by $\sim 1000 - 2000 \text{ cm}^{-1}$ compared to the experimentally observed bands. The calculated extinction coefficients were divided by 3 solely for the purpose of being able to plot the computed spectra on scale with the experimental data in Figure 2.30.

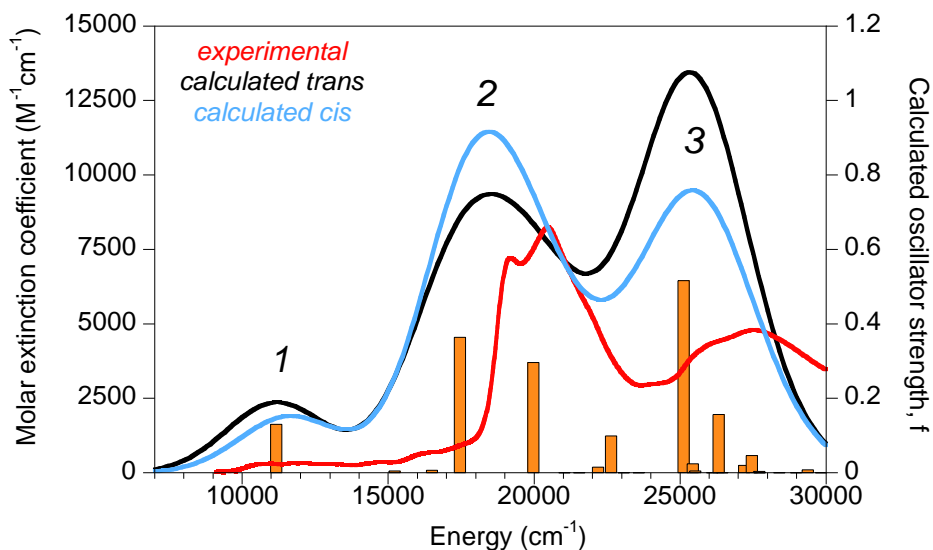
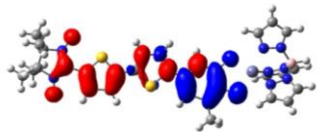
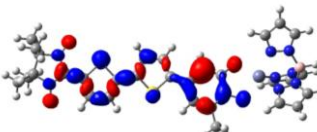
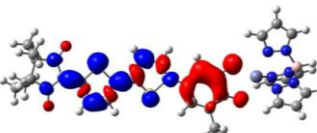
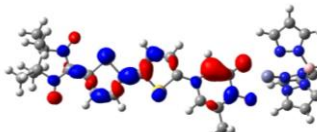
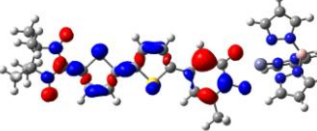


Figure 2.30: DFT-calculated (black for trans-, blue for cis-geometry) and experimental solution (red) spectra of $\text{Tp}^{\text{Cum,Me}}\text{Zn}(\text{SQ-Thp}_2\text{-NN})$. DFT bands were widened to 4000 cm^{-1} , bars represent calculated oscillator strengths for the trans -geometry. Calculated extinction coefficients were divided by 3 in order to be on scale with the experimental data.

Experimental band energies in the $\sim 11000 - 13000\text{ cm}^{-1}$ region correspond to the broad low-energy feature described as band 1. Experimental band energies at $\sim 19200\text{ cm}^{-1}$ and $\sim 20500\text{ cm}^{-1}$ correspond to band 2, those at $\sim 25800\text{ cm}^{-1}$ and $\sim 27600\text{ cm}^{-1}$ correspond to band 3. Experimentally, band 1 actually has distinct peaks at $\sim 10900\text{ cm}^{-1}$, $\sim 11930\text{ cm}^{-1}$, and $\sim 12960\text{ cm}^{-1}$ that are spaced in energy by about $1020\text{-}1040\text{ cm}^{-1}$. This may be a vibronic progression corresponding to the thiophene ring breathing mode with a large C-C stretch component as computed for the thiophene molecule. Table 2.7 shows the DFT derived band assignments for $\text{Tp}^{\text{Cum,Me}}\text{Zn}(\text{SQ-Thp}_2\text{-NN})$. Band 1 is assigned as a transition from the delocalized HOMO into the SQ SOMO, band 2 is the donor-acceptor charge transfer band, and is heavily mixed with $\text{HOMO-1} \rightarrow \text{SQ SOMO}$, $\text{HOMO} \rightarrow \text{SQ}$

SOMO, and HOMO \rightarrow LUMO one-electron promotions. Band 3 is assigned as HOMO \rightarrow LUMO transitions and HOMO-1 \rightarrow LUMO, amongst other contributions.

Table 2.7: DFT band assignments for $\text{Tp}^{\text{Cum,Me}}\text{Zn}(\text{SQ-Thp}_2\text{-NN})$.

Band	DFT-calculated Energy (cm^{-1}) f		Assignment	Electron density difference map
1	11170	0.130	[SQ-Thp ₂ -NN HOMO \rightarrow SQ SOMO]	
2	17450	0.364	[SQ-Thp ₂ -NN HOMO-1 \rightarrow SQ SOMO] -[SQ SOMO \rightarrow SQ-Thp ₂ -NN LUMO] [SQ-Thp ₂ -NN HOMO \rightarrow SQ-Thp ₂ -NN LUMO] -[SQ-Thp ₂ -NN HOMO \rightarrow SQ SOMO]	
	19960	0.297	[SQ SOMO \rightarrow SQ-Thp ₂ -NN LUMO] -[SQ-Thp ₂ -NN HOMO \rightarrow SQ-Thp ₂ -NN LUMO] +[SQ-Thp ₂ -NN HOMO \rightarrow SQ SOMO]	
3	25130	0.516	[SQ-Thp ₂ -NN HOMO \rightarrow SQ-Thp ₂ -NN LUMO] α , β	
	26320	0.157	[SQ-Thp ₂ -NN HOMO \rightarrow SQ-Thp ₂ -NN LUMO] α , β [SQ-Thp ₂ -NN HOMO-1 \rightarrow SQ-Thp ₂ -NN LUMO] etc.	

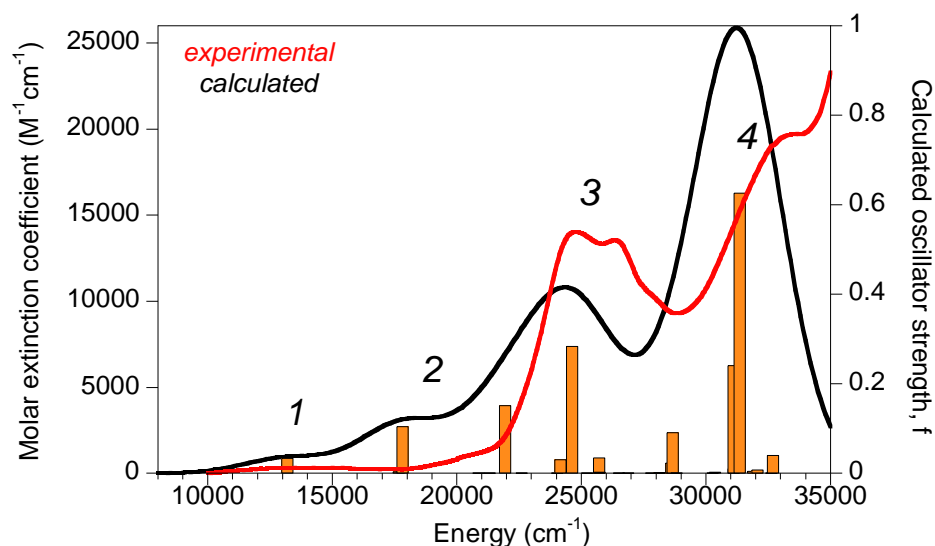


Figure 2.31: DFT-calculated (black) and experimental solution (red) spectra of $\text{Tp}^{\text{Cum,Me}}\text{Zn}(\text{SQ-Ph}_2\text{-NN})$. Computed bands have 4000 cm^{-1} bandwidth. Bars represent calculated oscillator strengths. Calculated extinction coefficients were divided by 2 in order to be on scale with the experimental data.

Figure 2.31 shows the overlay of the DFT-calculated and experimental absorption spectra for $\text{Tp}^{\text{Cum,Me}}\text{Zn}(\text{SQ-Ph}_2\text{-NN})$. As for $\text{Tp}^{\text{Cum,Me}}\text{Zn}(\text{SQ-Thp}_2\text{-NN})$ we notice that the calculated absorption spectrum is shifted $\sim 2000\text{ cm}^{-1}$ to lower energy than the experimental absorption spectrum, and the calculated extinction coefficients have been divided by 2 so that they are on scale with the experimental data. Experimental transitions are centered at $\sim 13800\text{ cm}^{-1}$ for the broad low-energy band 1, $\sim 20600\text{ cm}^{-1}$ for band 2, 24770 cm^{-1} and 26430 cm^{-1} for the band 3 region, and $\sim 33400\text{ cm}^{-1}$ for band 4.

Table 2.8: DFT band assignments for $\text{Tp}^{\text{Cum,Me}}\text{Zn}(\text{SQ-Ph}_2\text{-NN})$.

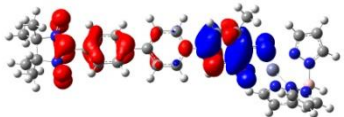
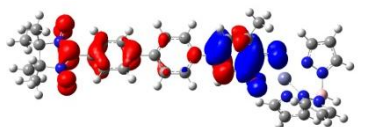
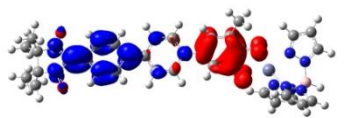
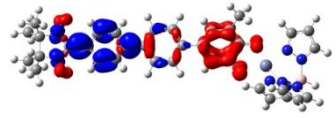
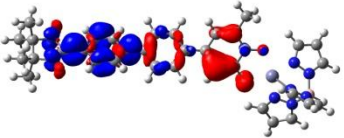
Band	DFT-calculated Energy (cm^{-1}) f		Assignment	Electron density difference map
1	~13200	0.033	[SQ-Ph ₂ -NN HOMO → SQ SOMO] + [SQ-Ph ₂ -NN HOMO-1 → SQ SOMO]	
2	~17800	0.104	[SQ-Ph ₂ -NN HOMO → SQ SOMO] - [SQ-Ph ₂ -NN HOMO-1 → SQ SOMO]	
3	~21900	0.151	SQ SOMO → NN-Ph LUMO - [SQ-Ph ₂ -NN HOMO → NN-Ph LUMO] etc.	
	~24600	0.284	SQ SOMO → NN-Ph LUMO + [SQ-Ph ₂ -NN HOMO → NN-Ph LUMO] etc.	
4	~31400	0.626	[SQ-Ph ₂ -NN HOMO → NN-Ph LUMO] α, β	

Table 2.8 summarizes the band assignments for $\text{Tp}^{\text{Cum,Me}}\text{Zn}(\text{SQ-Ph}_2\text{-NN})$. Bands 1 and 2 are assigned as positive and negative linear combinations of the transitions of the delocalized HOMO and HOMO-1 into the SQ SOMO. Both components contributing to band 3 are assigned as the DA CT transition mixed with the one-electron promotion from

the delocalized HOMO into the NN-Ph LUMO as well as additional one-electron promotions. Band 4 is assigned as the α and β one electron promotions from the delocalized HOMO into the NN-Ph LUMO. In contrast to our expectations, the experimental energy for the D-A CT band of $\text{Tp}^{\text{Cum,Me}}\text{Zn}(\text{SQ-Ph}_2\text{-NN})$ did not shift to lower energies when compared to $\text{Tp}^{\text{Cum,Me}}\text{Zn}(\text{SQ-Ph-NN})$.

2.5.4 Variable Temperature Electronic Absorption Experiments for $\text{Tp}^{\text{Cum,Me}}\text{Zn}(\text{SQ-Thp}_2\text{-NN})$ and $\text{Tp}^{\text{Cum,Me}}\text{Zn}(\text{SQ-Ph}_2\text{-NN})$

Since $\text{Tp}^{\text{Cum,Me}}\text{Zn}(\text{SQ-Thp}_2\text{-NN})$ and $\text{Tp}^{\text{Cum,Me}}\text{Zn}(\text{SQ-Ph}_2\text{-NN})$ have a much smaller singlet-triplet energy gap in the ground state than the corresponding mono-bridged biradicals, the spin singlet component of the electronic ground state is thermally accessible for $\text{Tp}^{\text{Cum,Me}}\text{Zn}(\text{SQ-Thp}_2\text{-NN})$ and $\text{Tp}^{\text{Cum,Me}}\text{Zn}(\text{SQ-Ph}_2\text{-NN})$. Therefore we observe temperature-dependent electronic absorption spectra for $\text{Tp}^{\text{Cum,Me}}\text{Zn}(\text{SQ-Thp}_2\text{-NN})$ and $\text{Tp}^{\text{Cum,Me}}\text{Zn}(\text{SQ-Ph}_2\text{-NN})$ (Figure 2.32 and Figure 2.33). As the thermal energy ($\sim 0.69 \text{ cm}^{-1}/\text{K}$) becomes comparable to the singlet-triplet ground state energy gap ($2J$, where $2J = +80 \text{ cm}^{-1}$ for $\text{Tp}^{\text{Cum,Me}}\text{Zn}(\text{SQ-Thp}_2\text{-NN})$ and $+40 \text{ cm}^{-1}$ for $\text{Tp}^{\text{Cum,Me}}\text{Zn}(\text{SQ-Ph}_2\text{-NN})$), the singlet ground state will become increasingly populated according to the Boltzmann distribution. Ferromagnetic exchange coupling (indicated by a positive value for J) corresponds to the triplet ground state being lower than the singlet ground state. Therefore, transitions originating from the triplet ground state should be most intense at low temperatures and lose intensity as the temperature increases. Conversely, transitions originating from the singlet ground state should gain intensity as the temperature increases and the singlet ground state becomes populated. In the variable-temperature

spectrum of $\text{Tp}^{\text{Cum,Me}}\text{Zn}(\text{SQ-Thp}_2\text{-NN})$ we observe significant changes in the absorption intensity as the temperature is increased from 5 K to 290 K. Specifically, the intensities of the two bands at $\sim 18800 \text{ cm}^{-1}$ and $\sim 19600 \text{ cm}^{-1}$ change dramatically as a function of temperature such that the relative intensity of the two bands switches between the lowest and highest temperatures. The inset in Figure 2.32 is an expanded view of the temperature-dependent spectra and shows that as the temperature changes the peak maxima of these two bands also shift.

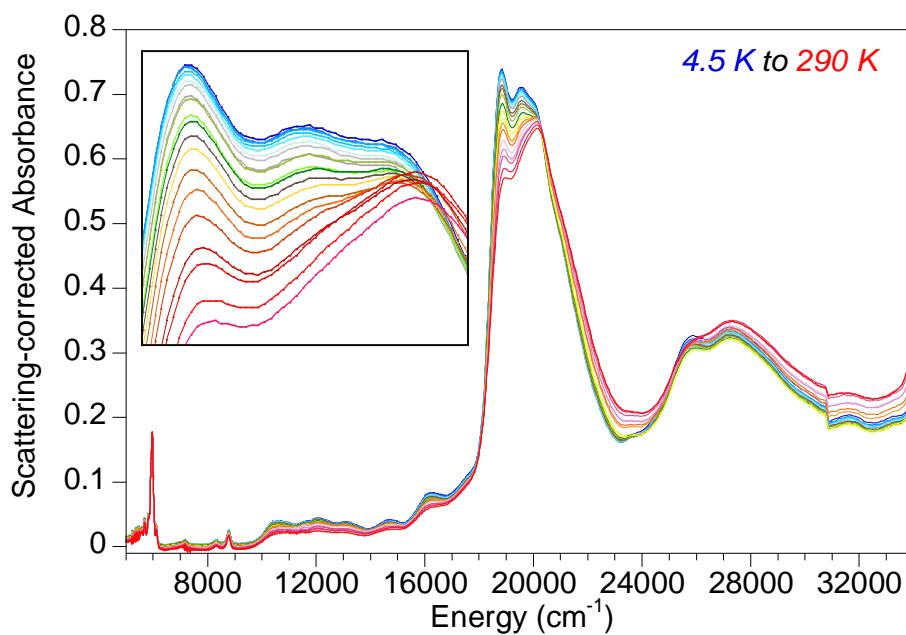


Figure 2.32: Variable-temperature electronic absorption spectra of $\text{Tp}^{\text{Cum,Me}}\text{Zn}(\text{SQ-Thp}_2\text{-NN})$ in a polystyrene film matrix. Temperatures from 5 K (blue) to 290 K (red). Expanded view of the temperature-dependent peaks from $\sim 18500 \text{ cm}^{-1}$ to $\sim 20500 \text{ cm}^{-1}$ (inset).

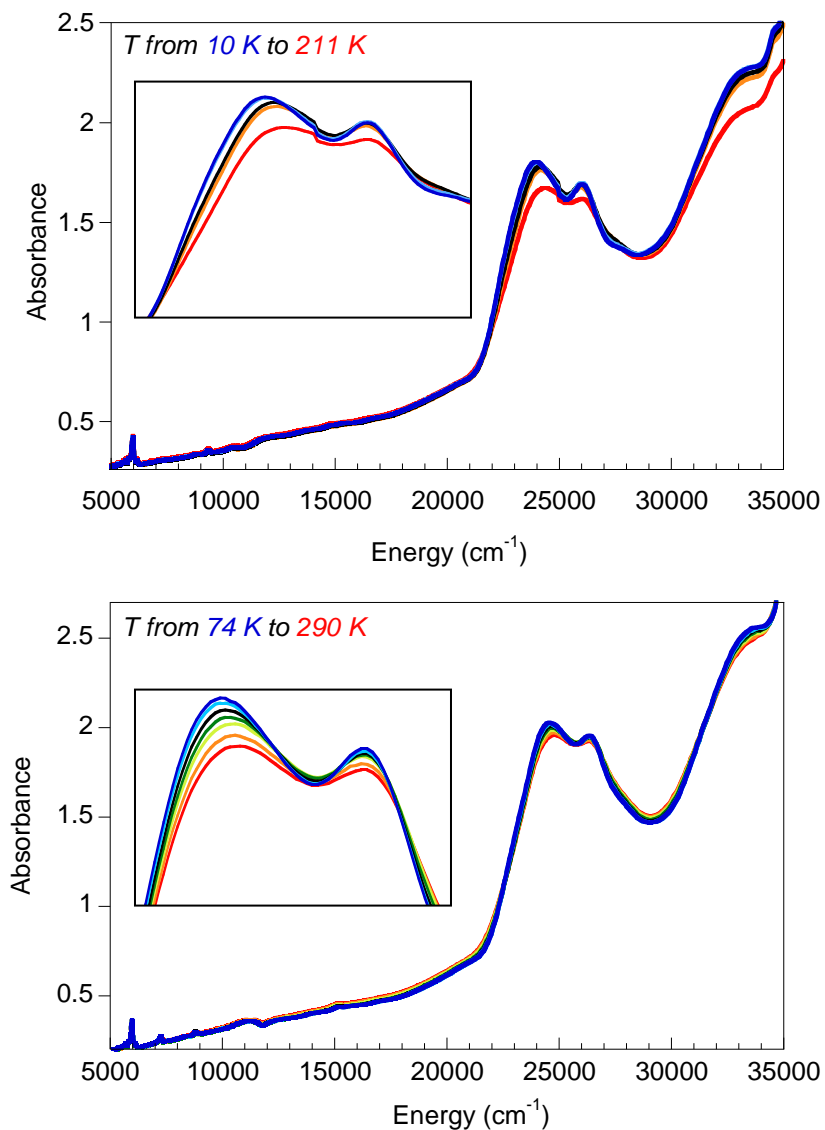


Figure 2.33: Variable-temperature electronic absorption spectra of $\text{Tp}^{\text{Cum,Me}}\text{Zn}(\text{SQ-Ph}_2\text{-NN})$ in a polystyrene film matrix. Top: using a liquid-helium cryostat, temperatures from 10 K (blue) to 211 K (red), inset: expanded view of the temperature-dependent peaks from $\sim 23500 \text{ cm}^{-1}$ to $\sim 27000 \text{ cm}^{-1}$; bottom: using a liquid-nitrogen cryostat, temperatures from 74 K (blue) to 290 K (red), inset: expanded view of the temperature-dependent peaks from $\sim 23000 \text{ cm}^{-1}$ to $\sim 27500 \text{ cm}^{-1}$.

An apparent shift in the band maximum as a function of temperature can be explained by having two (or more) unresolved Gaussian peaks contributing to the observed peak maximum. Specifically, when one peak increases in intensity relative to the other peak, the observed maximum of the band, which is the sum of the two contributing peaks, shifts toward the peak on increasing intensity. We observe such band shifts at several energies in the spectrum of $\text{Tp}^{\text{Cum,Me}}\text{Zn}(\text{SQ-Thp}_2\text{-NN})$, namely in the 25000 - 28000 cm^{-1} and 18000 - 21000 cm^{-1} regions. In addition to the temperature-dependence of absorption bands due to changes in the populations of energy levels, it is known that peak bandwidths generally decrease as the temperature decreases, and, since the integrated area of the peaks remains constant, peaks that decrease in bandwidth also slightly increase in intensity at low temperatures.

Figure 2.33 shows the variable temperature electronic absorption spectra of $\text{Tp}^{\text{Cum,Me}}\text{Zn}(\text{SQ-Ph}_2\text{-NN})$ for a data set using a liquid-helium cryostat in the temperature range of 10 K to 211 K, and a second data set using a liquid-nitrogen cryostat in the temperature range of 74 K to 290 K. We observe intensity changes for peaks in the ~24000 - 27000 cm^{-1} energy range as well as band shifts for the reasons outlined for $\text{Tp}^{\text{Cum,Me}}\text{Zn}(\text{SQ-Thp}_2\text{-NN})$.

For $\text{Tp}^{\text{Cum,Me}}\text{Zn}(\text{SQ-Thp}_2\text{-NN})$ the temperature-dependent changes in band intensities are large enough that we can extract an estimate of the singlet-triplet splitting for the ground state energy. We chose the peak with the largest temperature dependence, at 18832 cm^{-1} , and plotted its normalized intensity (red dots) as a function of temperature

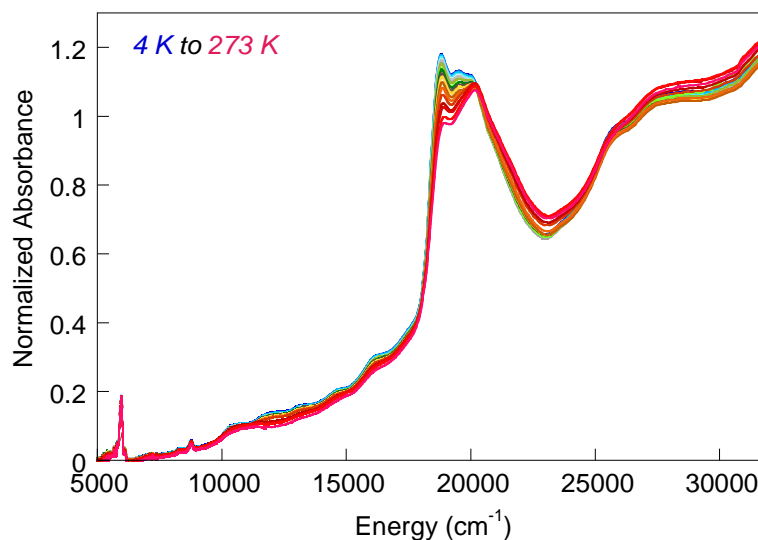


Figure 2.34: Variable-temperature electronic absorption spectra of $\text{Tp}^{\text{Cum,Me}_7}\text{Zn}(\text{SQ-Thp}_2\text{-NN})$ in a polystyrene film matrix. Temperatures from 5 K (blue) to 273 K (violet).

in Figure 2.35. In order to confirm our VT-derived value for the singlet-triplet ground state gap, we repeated the VT electronic absorption measurements, and the additional data set is shown in Figure 2.34. The fit of VT experimental band intensities to the Boltzmann-predicted depopulation of the triplet in Figure 2.35 is based on the experimental data shown in Figure 2.34. Theoretical Boltzmann populations for various singlet-triplet gap energies were plotted with the experimental data. We observe that small singlet-triplet energy gaps result in rapid intensity decreases at very low temperatures, and large singlet-triplet energy gaps result in more gradual intensity decreases that occur at higher temperatures. Comparison of the experimental and theoretical data yields a singlet-triplet ground state splitting of $\sim 100\text{-}160\text{ cm}^{-1}$, J of $\sim 50\text{-}80\text{ cm}^{-1}$. This value for J is larger than what was determined by magnetic susceptibility measurements. Magnetic susceptibility measurements are typically more accurate in

determining J values than variable-temperature (VT) electronic absorption measurements. However, the two techniques measure the sample in different physical states. Namely, magnetic susceptibility measurements were performed on powder samples while our VT electronic absorption measurements were performed on a polymer film solid solution.

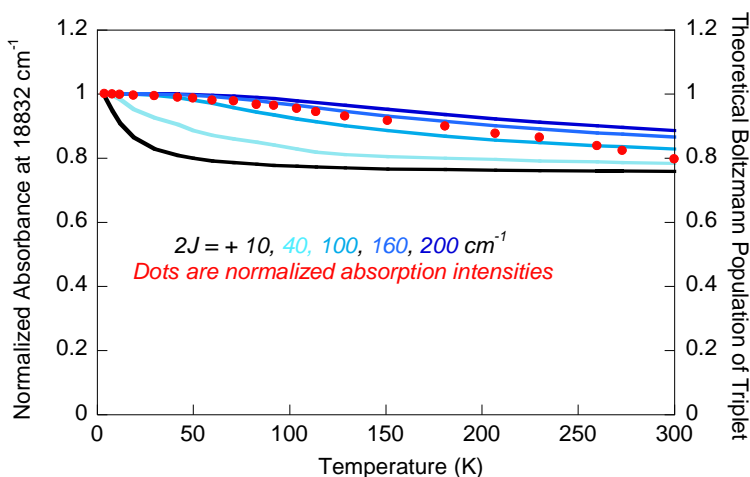


Figure 2.35: Theoretical Boltzmann populations (triplet state degeneracy of 3 and singlet state with degeneracy of 1) and an energy gap of 170 cm^{-1} between them. Lines are the Boltzmann-predicted depopulations of the triplet. Red dots are temperature-dependent electronic absorption intensities for the band at 18832 cm^{-1} .

We can use the value of J to deconvolute the triplet and singlet contributions to the observed electronic absorption spectrum, and since we have more confidence in the magnetic susceptibility measured value, we proceeded with the J values of $+20 \text{ cm}^{-1}$ for $\text{Tp}^{\text{Cum,Me}}\text{Zn}(\text{SQ-Ph}_2\text{-NN})$ and $+40 \text{ cm}^{-1}$ for $\text{Tp}^{\text{Cum,Me}}\text{Zn}(\text{SQ-Thp}_2\text{-NN})$, where the singlet-triplet gap equals $2J$. Table 2.9 summarizes the expected Boltzmann populations of the singlet and triplet levels for $\text{Tp}^{\text{Cum,Me}}\text{Zn}(\text{SQ-Ph}_2\text{-NN})$ and $\text{Tp}^{\text{Cum,Me}}\text{Zn}(\text{SQ-Thp}_2\text{-NN})$ at specific temperatures. We can use this information to construct two linearly-independent

Table 2.9: Theoretical Boltzmann populations of the singlet and triplet levels for $\text{Tp}^{\text{Cum,Me}}\text{Zn}(\text{SQ-Ph}_2\text{-NN})$ and $\text{Tp}^{\text{Cum,Me}}\text{Zn}(\text{SQ-Thp}_2\text{-NN})$ assuming $2J = +40 \text{ cm}^{-1}$ and $+80 \text{ cm}^{-1}$, respectively.

Theoretical Boltzmann distributions								
	$\text{Tp}^{\text{Cum,Me}}\text{Zn}(\text{SQ-Ph}_2\text{-NN})$ Data set 1		$\text{Tp}^{\text{Cum,Me}}\text{Zn}(\text{SQ-Ph}_2\text{-NN})$ Data set 2			$\text{Tp}^{\text{Cum,Me}}\text{Zn}(\text{SQ-Thp}_2\text{-NN})$		
T (K)	triplet	singlet	T (K)	triplet	singlet	T (K)	triplet	singlet
10	1.00	0.00	74	0.87	0.13	4	1.00	0.00
211	0.80	0.20	290	0.78	0.22	273	0.82	0.18

equations from the low temperature and high temperature measurements for each data set to solve for the pure singlet and pure triplet components of the absorption spectra. Figure 2.36 shows these singlet and triplet spectra for $\text{Tp}^{\text{Cum,Me}}\text{Zn}(\text{SQ-Ph}_2\text{-NN})$, where on the left are the deconvoluted spectra from one data set (liquid helium cryostat), and on the right from the second data set (liquid nitrogen cryostat).

We observe that the singlet transitions are shifted by $\sim 1000\text{-}1200 \text{ cm}^{-1}$ to higher energies than the corresponding triplet transitions. Apart from this shift, and the fact that the singlet spectrum has slightly lower band intensities than the triplet spectrum the

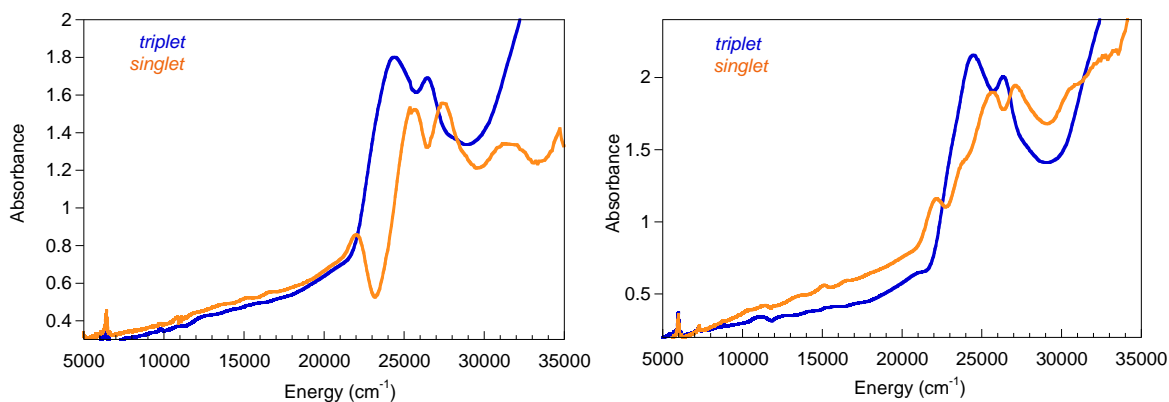


Figure 2.36: singlet (orange) and triplet (blue) electronic absorption spectra for $\text{Tp}^{\text{Cum,Me}}\text{Zn}(\text{SQ-Ph}_2\text{-NN})$. Left: data set from liquid helium cryostat, right: data set from liquid nitrogen cryostat.

singlet spectrum is very similar to the triplet spectrum. The singlet-triplet band shifts are a combination of the singlet-triplet splitting in the ground state ($2J$), and the more dominant singlet-triplet splitting in the excited state ($2K$). Since $2J$ at 40 cm^{-1} is much smaller than $2K$, the band shift of $\sim 1000\text{-}1200\text{ cm}^{-1}$ should be approximately equal to $2K$. We also notice that the band at $\sim 22000\text{ cm}^{-1}$ in the singlet spectrum, which appears to not have shifted to higher energies with the rest of the singlet spectrum, and thus is resolved, unlike in the triplet spectrum where it is a shoulder at the lower energy side of the DA CT band. If this interpretation is correct, one would expect the state at $\sim 22000\text{ cm}^{-1}$ to have a very small excited state exchange interaction. We know that single-site exchange between the unpaired electron in the NN SOMO and an unpaired electron in the NN LUMO is large.³ Considering which transitions lead to minimal single-site exchange interactions, we suggest that the 22000 cm^{-1} band may arise from a transition from a NN

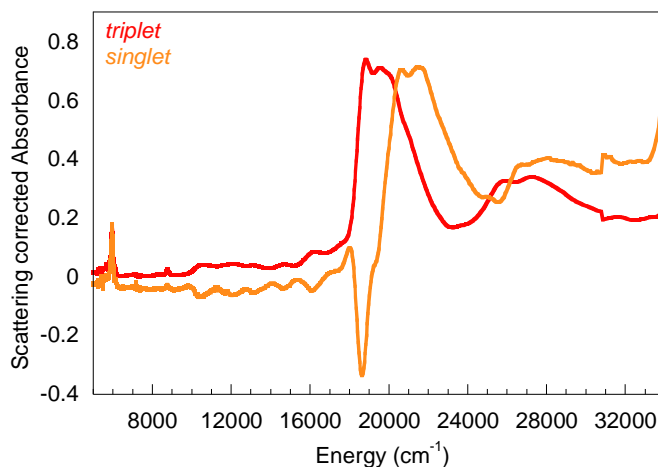


Figure 2.37: singlet (orange) and triplet (red) electronic absorption spectra for $\text{Tp}^{\text{Cum,Me}}\text{Zn}(\text{SQ-Thp}_2\text{-NN})$.

HOMO \rightarrow NN SOMO, or from a transition from a lower lying filled orbital with little NN character into the SQ SOMO.

Figure 2.37 shows the deconvoluted singlet and triplet absorption spectra for $\text{Tp}^{\text{Cum,Me}}\text{Zn}(\text{SQ-Thp}_2\text{-NN})$. As observed for $\text{Tp}^{\text{Cum,Me}}\text{Zn}(\text{SQ-Ph}_2\text{-NN})$, we see that the triplet spectrum is shifted to lower energy than the singlet spectrum by $\sim 1800\text{-}1900\text{ cm}^{-1}$ (i.e. $\sim 900\text{-}950\text{ cm}^{-1}$). Otherwise the singlet and triplet spectra are very similar. The deconvolution of the singlet and triplet absorption spectra for $\text{Tp}^{\text{Cum,Me}}\text{Zn}(\text{SQ-Thp}_2\text{-NN})$ was not as successful as for $\text{Tp}^{\text{Cum,Me}}\text{Zn}(\text{SQ-Ph}_2\text{-NN})$, since the singlet spectrum displays a negative feature. At $\sim 18000\text{ cm}^{-1}$ we observe a band in the singlet spectrum that does not appear to have shifted significantly compared to its position in the triplet spectrum, and we again speculate that it may correspond to a transition from a NN HOMO \rightarrow NN SOMO or to a transition from a lower lying filled orbital with little NN character into the SQ SOMO.

2.5.5 Resonance Raman Spectra and Frequency Calculations for $\text{Tp}^{\text{Cum,Me}}\text{Zn}(\text{SQ-Thp}_2\text{-NN})$ and $\text{Tp}^{\text{Cum,Me}}\text{Zn}(\text{SQ-Ph}_2\text{-NN})$

Resonance Raman spectra were acquired for $\text{Tp}^{\text{Cum,Me}}\text{Zn}(\text{SQ-Thp}_2\text{-NN})$ and $\text{Tp}^{\text{Cum,Me}}\text{Zn}(\text{SQ-Ph}_2\text{-NN})$ using laser excitation lines from 407 nm to 647 nm. Figure 2.38 shows the resonance Raman spectrum of $\text{Tp}^{\text{Cum,Me}}\text{Zn}(\text{SQ-Ph}_2\text{-NN})$ in a NaCl/Na₂SO₄ matrix at 407 nm, which is the laser excitation energy at which we observe the largest resonance enhancement. Resonance Raman spectra for the less enhanced laser lines are included in Appendix 6.1.1. The peaks of the sulfate internal standard are marked in red, while sample peaks are marked in black, and the most enhanced sample mode is marked

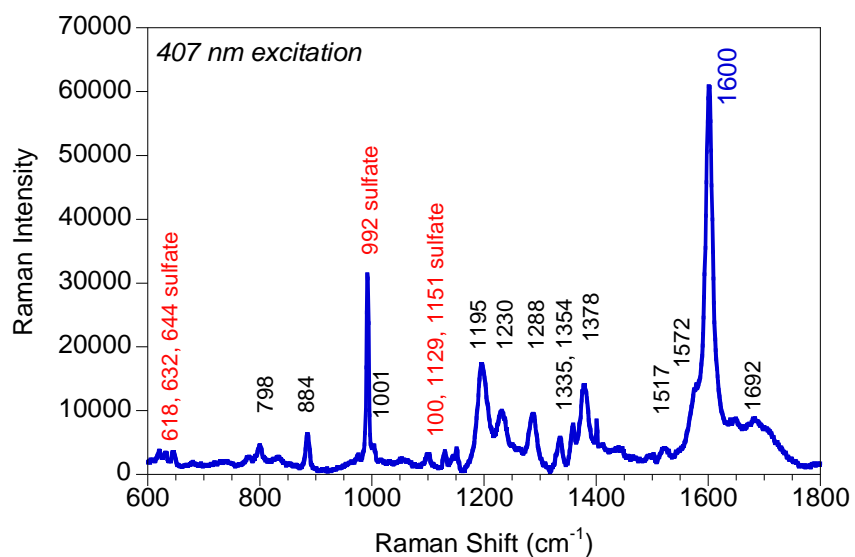


Figure 2.38: Resonance Raman spectrum of $\text{Tp}^{\text{Cum,Me}_7}\text{Zn}(\text{SQ-Ph}_2\text{-NN})$ in a $\text{NaCl}/\text{Na}_2\text{SO}_4$ matrix using a 407 nm excitation wavelength. Internal standard sulfate peak(s) are marked in red, and sample modes are marked in black and blue (most enhanced).

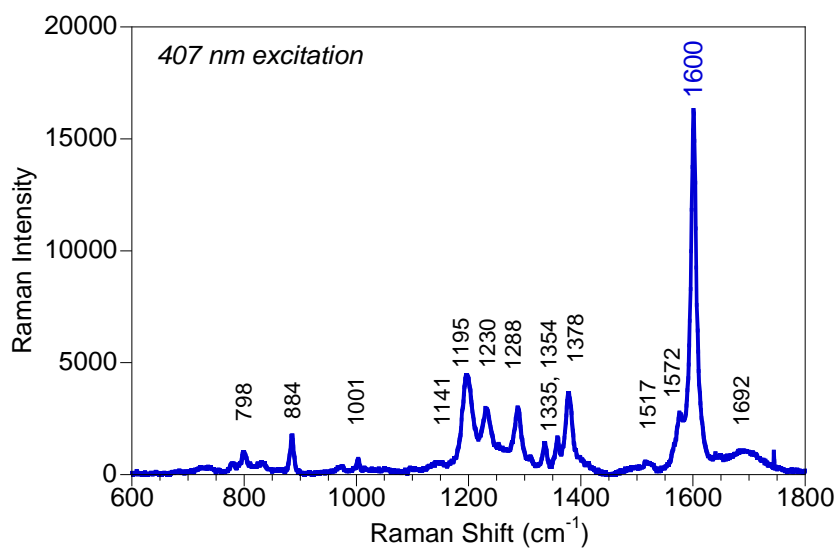


Figure 2.39: Resonance Raman spectrum of $\text{Tp}^{\text{Cum,Me}_7}\text{Zn}(\text{SQ-Ph}_2\text{-NN})$ in dichloromethane using a 407 nm excitation wavelength. Sample modes are marked in black and blue (most enhanced), and are labeled the same as for the solid state sample since shifts were within 1-2 cm^{-1} .

in blue. Figure 2.39 shows the resonance Raman spectrum of $\text{Tp}^{\text{Cum,Me}}\text{Zn}(\text{SQ-Ph}_2\text{-NN})$ at the same excitation wavelength of 407 nm in dichloromethane. The resonance Raman enhancement of the $\text{Tp}^{\text{Cum,Me}}\text{Zn}(\text{SQ-Ph}_2\text{-NN})$ modes at 407 nm is so large in the dichloromethane solution sample that the solvent peaks (the largest one is expected at 702 cm^{-1}) are no longer visible.

There are a number of enhanced vibrational modes in the $1200\text{-}1700\text{ cm}^{-1}$ range, and the most enhanced vibrational mode is observed at 1600 cm^{-1} . The solid and solution spectra show the same modes and the same relative intensities, and the observed vibrational modes in the solution spectrum have been labeled to correspond with the solid state sample, since observed spectral shifts were within $1\text{-}2\text{ cm}^{-1}$. We constructed a resonance Raman enhancement profile for the 1600 cm^{-1} vibration, and this is shown in Figure 2.40, for both the solid state and solution data set. We see that the 1600 cm^{-1} mode

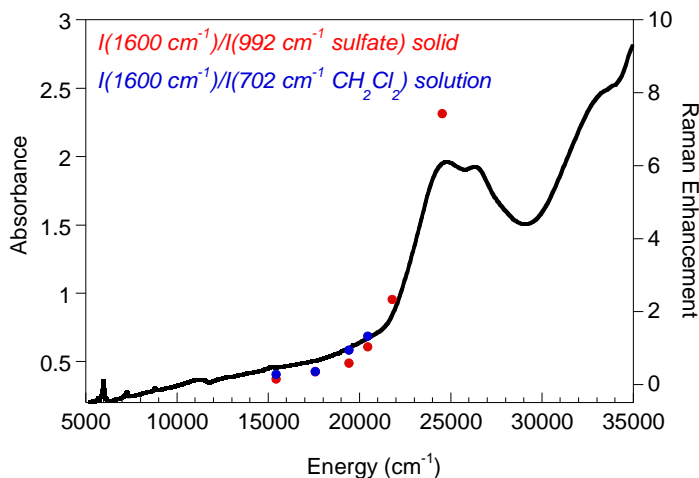


Figure 2.40: Resonance Raman enhancement profile for the 1600 cm^{-1} mode as a function of laser excitation energy and overlaid onto the electronic absorption spectrum (black). Red dots: resonance enhancement in a $\text{NaCl}/\text{Na}_2\text{SO}_4$ matrix, blue dots resonance enhancement in dichloromethane.

is clearly resonantly enhanced specifically under the DA CT band. The solution data set does not have data points for the 458 nm line and the 407 nm line because the solvent reference peak could not be observed (i.e. the sample modes were extremely resonantly enhanced).

DFT frequency calculations were used to assign the 1600 cm^{-1} mode, and the calculations predict a Raman active mode at 1613 cm^{-1} that is depicted graphically in Figure 2.41 as an overlay of the extrema of the computed vibration. This vibration is delocalized over all four of the constituent rings, but the amplitude of the vibration is smallest on the NN ring. The calculated mode is the positive linear combination of a symmetric ring stretch on SQ, Ph, and Ph, and is analogous to the mode calculated at 1618 cm^{-1} in $[\text{SQ-Ph-NN}]^-$. This is not surprising as the orbitals involved in the D-A CT

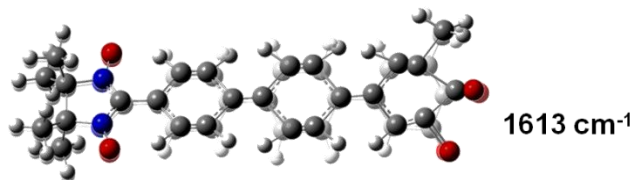


Figure 2.41: DFT-calculated vibration in $[\text{SQ-Ph}_2\text{-NN}]^-$. The mode is shown as overlays of the extrema of the vibrational mode.

transition for $\text{Tp}^{\text{Cum,Me}}\text{Zn}(\text{SQ-Ph}_2\text{-NN})$, i.e. the SQ SOMO and NN-Ph LUMO, are also analogous to those in $\text{Tp}^{\text{Cum,Me}}\text{Zn}(\text{SQ-Ph-NN})$. In comparison to the resonance Raman spectrum of $\text{Tp}^{\text{Cum,Me}}\text{Zn}(\text{SQ-Ph-NN})$, the $\text{Tp}^{\text{Cum,Me}}\text{Zn}(\text{SQ-Ph}_2\text{-NN})$ data shows a definite relative reduction in the intensity of vibrational modes in the $1400\text{-}1550\text{ cm}^{-1}$ region that

have previously been assigned as SQ-NN modes. Since resonance Raman intensities are relative rather than absolute, there is of course no reason to think that modes at 1400-1550 cm^{-1} are less resonantly enhanced for $\text{Tp}^{\text{Cum,Me}}\text{Zn}(\text{SQ-Ph}_2\text{-NN})$ than for $\text{Tp}^{\text{Cum,Me}}\text{Zn}(\text{SQ-Ph-NN})$, and it may be the modes at 1200-1400 cm^{-1} and at 1600 cm^{-1} are much more resonantly enhanced in $\text{Tp}^{\text{Cum,Me}}\text{Zn}(\text{SQ-Ph}_2\text{-NN})$ as to make the other modes appear smaller. Furthermore, frequency calculations indicate that it may be very difficult to associate a specific computed frequency with a specific ring mode as there are a large number of computed modes in the 1100-1600 cm^{-1} frequency range. We briefly list a few of the Raman active calculated modes, but this list is by no means complete and should not be regarded as constituting a definite assignment. In this notation the rings that have the greatest vibrational amplitude in that mode are in bold font, and the rings that have lower vibrational amplitudes are in regular font: **NNPhPhSQ**: 1418, 1447, 1507, 1540 cm^{-1} ; **NNPhPh**: 1175 cm^{-1} ; **Ph-Ph**: 1327 cm^{-1} ; **PhPhSQ**: 1216, 1224, 1230 cm^{-1} ; **SQPhPhNN**: 1076, 1268 cm^{-1} etc. We note that most of the calculated modes are delocalized over three to four of the constituent rings. Comparing these frequencies to the data we can make the general observation that most of the resonantly enhanced modes likely involve the SQ and Ph rings, whereas modes that have predominantly NN character are less resonantly enhanced.

Figure 2.42 shows the 514 nm resonance Raman spectrum of $\text{Tp}^{\text{Cum,Me}}\text{Zn}(\text{SQ-Thp}_2\text{-NN})$ in a $\text{NaCl}/\text{Na}_2\text{SO}_4$ matrix, which is the laser excitation energy at which we observe the largest resonance enhancements. Less resonantly enhanced Raman spectra are included in Appendix 6.1.1. The peaks of the sulfate internal standard are marked in

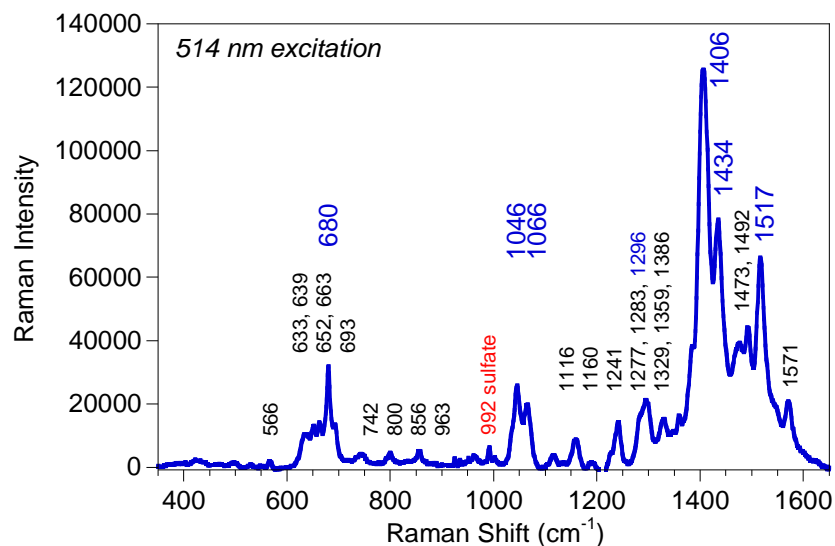


Figure 2.42: Resonance Raman spectrum of $\text{Tp}^{\text{Cum,Me}}_7\text{Zn}(\text{SQ-Thp}_2\text{-NN})$ in a $\text{NaCl}/\text{Na}_2\text{SO}_4$ matrix using a 514 nm excitation wavelength. Internal standard sulfate peak(s) are marked in red, and sample modes are marked in black and blue (most enhanced).

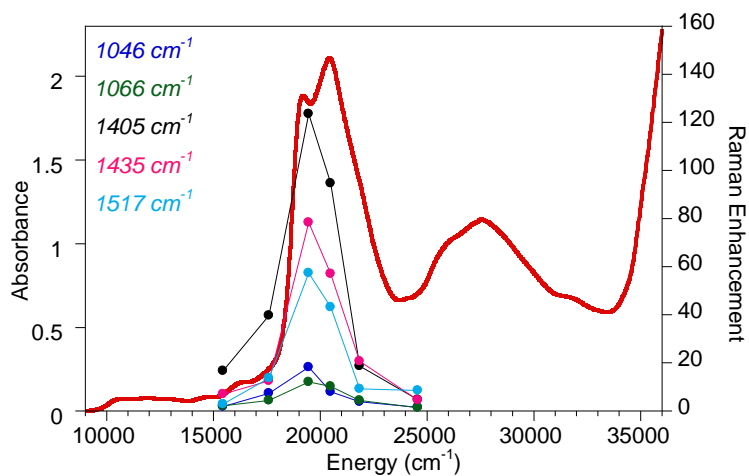


Figure 2.43: Resonance Raman enhancement profile for selected modes (blue 1046 cm^{-1} , green 1066 cm^{-1} , black 1405 cm^{-1} , pink 1435 cm^{-1} , light blue 1517 cm^{-1}) as a function of laser excitation energy and overlaid onto the electronic absorption spectrum (red). The $\text{Tp}^{\text{Cum,Me}}_7\text{Zn}(\text{SQ-Thp}_2\text{-NN})$ sample was in the solid state in a $\text{NaCl}/\text{Na}_2\text{SO}_4$ matrix.

red, while sample peaks are marked in black, and the most enhanced sample modes are marked in blue. Similar to what we observed for $\text{Tp}^{\text{Cum,Me}}\text{Zn}(\text{SQ-Thp-NN})$, we also observe a large number of enhanced vibrational modes throughout the entire spectrum. The most enhanced modes occur in the general regions of $600\text{-}700\text{ cm}^{-1}$, $1050\text{-}1060\text{ cm}^{-1}$, $1200\text{-}1450\text{ cm}^{-1}$, and $1470\text{-}1520\text{ cm}^{-1}$. The most enhanced modes are at 1406 and 1434 cm^{-1} , followed by 1517 cm^{-1} , 680 cm^{-1} , 1046 cm^{-1} , 1066 cm^{-1} and then other modes. The resonance Raman enhancement profile (Figure 2.43) confirms that the prominent modes at 1046 cm^{-1} , 1066 cm^{-1} , 1405 cm^{-1} , 1435 cm^{-1} , and 1517 cm^{-1} are indeed enhanced with optical excitation into the D-A CT band. The resonance Raman spectrum of $\text{Tp}^{\text{Cum,Me}}\text{Zn}(\text{SQ-Thp}_2\text{-NN})$ looks similar to $\text{Tp}^{\text{Cum,Me}}\text{Zn}(\text{SQ-Thp-NN})$, so much of interpretation for $\text{Tp}^{\text{Cum,Me}}\text{Zn}(\text{SQ-Thp-NN})$ transfers to $\text{Tp}^{\text{Cum,Me}}\text{Zn}(\text{SQ-Thp}_2\text{-NN})$. The most enhanced modes at 1406 cm^{-1} and 1434 cm^{-1} are 7 cm^{-1} higher than in $\text{Tp}^{\text{Cum,Me}}\text{Zn}(\text{SQ-Thp-NN})$, and some modes have “doubled,” where in the mono-thiophene bridged biradical there is one enhanced mode at 1055 cm^{-1} and in the bis-thiophene bridged biradical there are two modes of about equal intensity very close in energy (at 1046 cm^{-1} and 1055 cm^{-1}). Likewise in the $600\text{-}700\text{ cm}^{-1}$ range there is a greater number of similarly enhanced modes in $\text{Tp}^{\text{Cum,Me}}\text{Zn}(\text{SQ-Thp}_2\text{-NN})$ compared to $\text{Tp}^{\text{Cum,Me}}\text{Zn}(\text{SQ-Thp-NN})$.

This can be interpreted as arising from positive and negative linear combinations of the two thiophene rings forming in-phase and out-of-phase combinations of one thiophene with respect to the other thiophene. Figure 2.44 shows several of the more Raman active calculated vibrational modes for $[\text{SQ-Thp}_2\text{-NN}]^-$. Here we observe that the

vibrational modes at 1468 cm^{-1} and 1499 cm^{-1} form just such in-phase and out-of-phase combinations. The calculated mode at 1399 cm^{-1} is a delocalized mode with observed vibrational amplitude on both bridge rings, the SQ ring, and a small amplitude on the NN ring. We correlate this computed mode to the mode observed experimentally at 1406 cm^{-1} , which is the vibrational mode that is most resonantly enhanced when exciting into the D-A CT band. The mode calculated at 676 cm^{-1} is correlated with the mode observed experimentally at 680 cm^{-1} , and has vibrational amplitude on both bridge rings with a smaller vibrational amplitude on the SQ and NN rings.

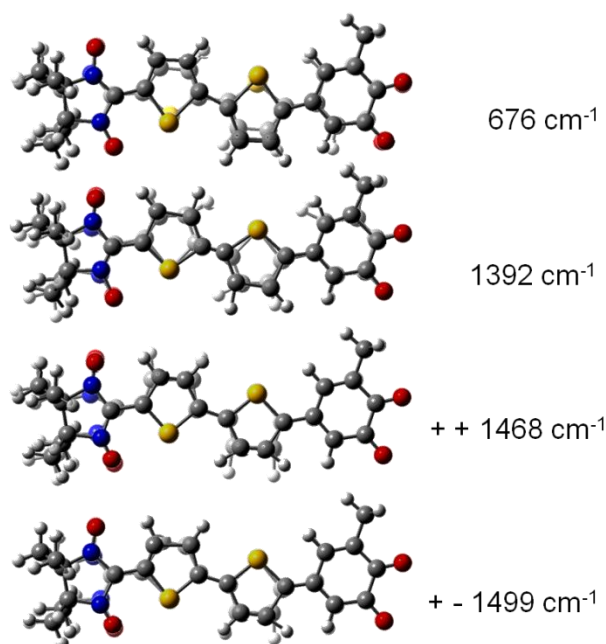


Figure 2.44: Selected DFT-calculated vibrations of [SQ-Thp₂-NN]. Modes are shown as overlays of the extrema of the vibrational mode.

We compared the calculated frequencies for both the cis- and trans-[SQ-Thp₂-NN] and found that vibrational modes were slightly shifted between the two isomers and

the computed frequencies were close to the observed experimental frequencies. In the 600-700 cm^{-1} range the computed 676 cm^{-1} vibration for the trans isomer is close to the experimentally most enhanced mode at 680 cm^{-1} and offers additional support for the trans isomer being more thermodynamically stable than the cis isomer.

2.6 Sterically-Hindered Bridges

2.6.1 Dependence of Overlap and Spin Populations as Functions of Donor, Bridge, and Acceptor Dihedral Angles

In this section we continue our discussion of factors that reduce donor-acceptor electronic communication in donor-bridge-acceptor biradicals. In previous sections we have examined how H_{ab}^0 , which is the intrinsic donor-acceptor coupling in a D-B-A biradical molecule, depends on the chemical nature of the donor, acceptor, and bridge. The substitution of a phenyl for a thiophene bridge results in a change of the value of H_{ab}^0 . The second term in Eq. 17 is an exponential dampening factor that describes the decrease of donor-acceptor electronic communication as the donor-acceptor separation increases. This can be explored by inserting multiple bridging units, such as in the bithiophene- and biphenyl-bridged D-B-A biradicals. The last factor (in red) describes the π overlap between the constituent rings in the donor-acceptor path, and includes the effect of non-zero donor-bridge, bridge-bridge (for multi-ring bridges), as well as acceptor-bridge dihedral angles.

$$H_{ab}^2 = (H_{ab}^0)^2 e^{-\beta(r-r_0)} \cos^m \theta \quad \text{Eq. 17}$$

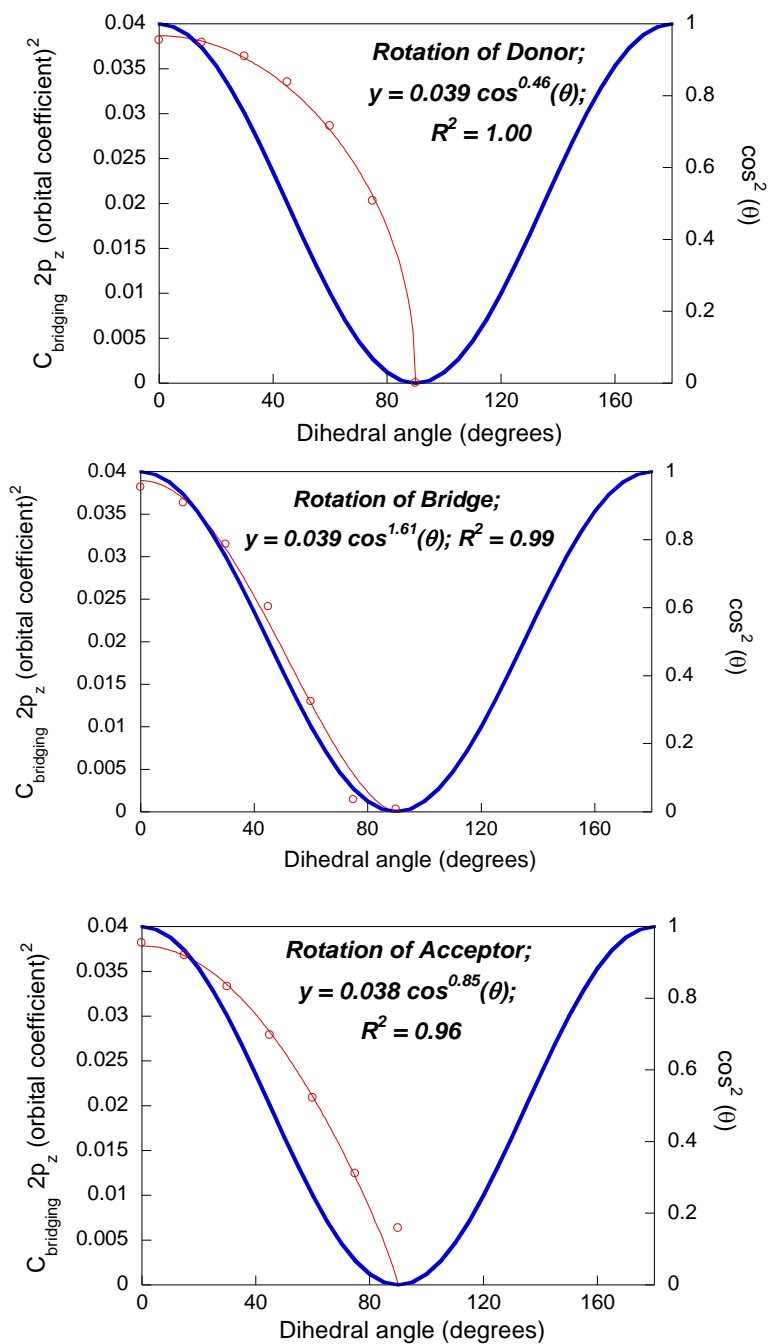


Figure 2.45: DFT-calculated correlation between ring torsion angles and the square of the $2p_z$ orbital coefficient for the NN-bridging carbon where in red are the data points and their fit and in blue is a $\cos^2\theta$ function for reference. Top: rotation of the SQ from planarity; middle: rotation of the Ph from planarity; bottom: rotation of the NN from planarity.

Table 2.10: Fit of the functional form of the nitrogen and bridging carbon spin populations of NN as the donor, acceptor, and bridge rings are rotated away from planarity. This is a fit of the data presented in Figure 2.7 (section 3.2.2), R^2 values for all fits are 1.00.

Spin population of	Rotation of	m for $y = a + b \cdot \cos^m x$
C	donor	0.373
C	acceptor	1.177
C	bridge	1.561
N	donor	0.529
N	acceptor	1.300
N	bridge	1.734

A cosine function is a logical choice for describing modulations in π overlap as a function of ring dihedral angles. The cosine function describes the projection of one vector onto another as the angle between the vectors changes. In this case the “vectors” would be the p_z orbitals of the atoms that are connection points of one ring with its neighbor. In order to extract a value for m in Eq. 17, we rotated the donor, acceptor, and bridge rings individually away from planarity in 15° increments and reoptimized the structures at each geometry with only the selected dihedral angle constrained. A similar study was done previously where the phenyl bridge was rotated away from the SQ and NN rings in [SQ-Ph-NN]⁻ without reoptimizing the geometry for each fixed value of the dihedral angle. In that study, the value obtained for m was $m \sim 4$,⁹⁰ which compares to the value of $m = 1.61$ obtained in the present study. Note that in Figure 2.45 we only show data points from 0° - 90° due to constraints imposed by the fitting routine used. Data points from 90° - 180° were indeed obtained and are close to symmetric to those from 0° - 90° .

We have considered the attenuation of both the π overlap (Figure 2.45) and the NN nitrogen and bridging carbon spin populations (Table 2.10) as a function of ring torsions. When comparing the value of m for these fits we notice that bridge rotations always have a much larger value of m than the donor or acceptor rotations, and the donor rotations have the smallest value of m . The values of m for donor only and acceptor only rotations do not always sum to equal the value of m for the bridge rotation in general though they may do so coincidentally as for rows 1-3. This is not unexpected since the wavefunction of the phenyl bridge, including both NN-Ph and Ph-SQ bond distances, change as the overlap changes when either donor or acceptor is perturbed. Both the attenuation of the π overlap (Figure 2.45) and of the nitrogen spin populations, which are directly related to the magnitude of the ferromagnetic D-A coupling, have merit as choices for obtaining m , and in fact give very similar results for the expected attenuation of H_{ab} .

As an example, we calculated the expected attenuation of H_{ab} for $\text{Tp}^{\text{Cum,Me}}\text{Zn}(\text{SQ-Xyl-NN})$ and $\text{Tp}^{\text{Cum,Me}}\text{Zn}(\text{SQ-Ph-NN})$. For $\text{Tp}^{\text{Cum,Me}}\text{Zn}(\text{SQ-Xyl-NN})$, the NN-B and B-SQ dihedral angles are both $\sim 50^\circ$ (corresponding to a bridge rotation), and $\cos^m\theta$ equals 0.49 and 0.46 for $m = 1.61$ and $m = 1.73$, respectively. For $\text{Tp}^{\text{Cum,Me}}\text{Zn}(\text{SQ-Ph-NN})$ the NN-B dihedral is approximately zero while the B-SQ dihedral is $\sim 32^\circ$ (corresponding to a donor only rotation), and $\cos^m\theta$ equals 0.87 and 0.92 for $m = 0.85$ and $m = 0.53$, respectively. Thus the xylene bridge is expected to reduce donor-acceptor coupling by a factor of $\sim 1/2$ with respect to a planar phenyl bridge. The actual optimized geometry (and crystal structure value) for the SQ-Ph dihedral in $\text{Tp}^{\text{Cum,Me}}\text{Zn}(\text{SQ-Ph-NN})$ is not zero,

however, so that the $\text{Tp}^{\text{Cum,Me}}\text{Zn}(\text{SQ-Ph-NN})$ structure itself does not have as large a donor-acceptor coupling as it could have if the molecule were planar. The computational data suggest that the attenuation of the donor-acceptor coupling as the donor rotates is described by a relatively flat curve, so that small to medium values of SQ-Ph bond torsion are not expected to attenuate the donor-acceptor coupling greatly. Specifically, the SQ-Ph dihedral of $\sim 32^\circ$ is calculated to have an attenuation of only $\sim 10\%$.

2.6.2 Optimized Geometries, DFT Spin Densities, and Frontier Molecular Orbitals

Three D-B-A biradicals with sterically-hindered bridges have been synthesized the Shultz group and are shown in Figure 2.46. Dihedral angles have been obtained both from X-ray crystallography measurements and DFT- optimized structures and are summarized in Table 2.11. Dihedral angles from DFT-optimized structures are in good agreement to the X-ray structure values. Para-xylene (1,4-dimethyl benzene) has two methyl substituents, one being close to the NN ring and the other close to the SQ ring. The other sterically-hindered bridges have only one methyl substituent on the phenyl bridge, either close to the NN ring ($\text{Tp}^{\text{Cum,Me}}\text{Zn}(\text{SQ-PhMe-NN})$) or the SQ ring ($\text{Tp}^{\text{Cum,Me}}\text{Zn}(\text{SQ-MePh-NN})$).

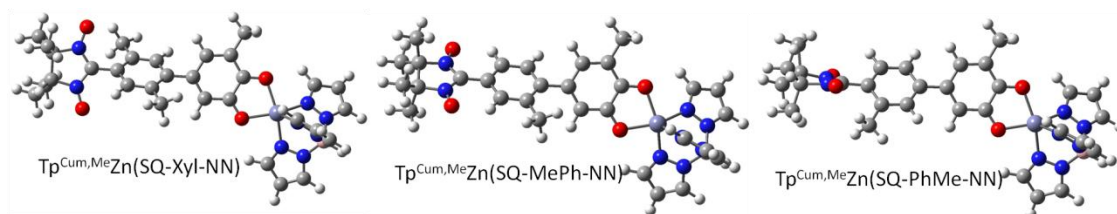


Figure 2.46: DFT-optimized structures of sterically-hindered D-B-A biradicals.

Table 2.11: Selected dihedral angles for sterically-hindered D-B-A biradicals.

Dihedral (°)	Tp ^{Cum,Me} Zn(SQ-PhMe-NN)	Tp ^{Cum,Me} Zn(SQ-MePh-NN)	Tp ^{Cum,Me} Zn(SQ*-MePh-NN)	Tp ^{Cum,Me} Zn(SQ-Xyl-NN)
NN-Ph DFT	51	5	2	51
Ph-SQ DFT	33	48	43	53
NN-Ph X-ray	45	13	13	62
Ph-SQ X-ray	30	49	49	46

*t-Bu group was included instead of Me on SQ

In order to make sure that representing the t-butyl group on SQ with a methyl group is a good approximation for a sterically-hindered bridge, we optimized the geometry of the full Tp^{Cum,Me}Zn(SQ*-MePh-NN) molecule, where * indicates that the full t-butyl group was included. Table 2.11 shows that including a t-butyl as opposed to a methyl group on the SQ did not cause any additional steric hindrance or result in larger dihedral angles. Based on this information, we decided to proceed with the structure that has a methyl group on the SQ for all further calculations. Comparing the computational data in Table 2.11 to experimental dihedral angles for Tp^{Cum,Me}Zn(SQ-Ph-NN) (X-ray structure: 13° NN-Ph, 35° Ph-SQ, DFT: 1° NN-Ph, 32° Ph-SQ), we notice that Tp^{Cum,Me}Zn(SQ-MePh-NN) is similar to Tp^{Cum,Me}Zn(SQ-Ph-NN) where the additional methyl group close to the SQ ring increases the SQ-Ph dihedral by ~15°. Tp^{Cum,Me}Zn(SQ-PhMe-NN) is more similar to Tp^{Cum,Me}Zn(SQ-Xyl-NN), since those molecules share the large NN-Ph dihedral, and differ by ~15-20° in the SQ-Ph dihedral. This similarity is also reflected in the absorption spectra of these compounds, (absorption data will be shown in the following section).

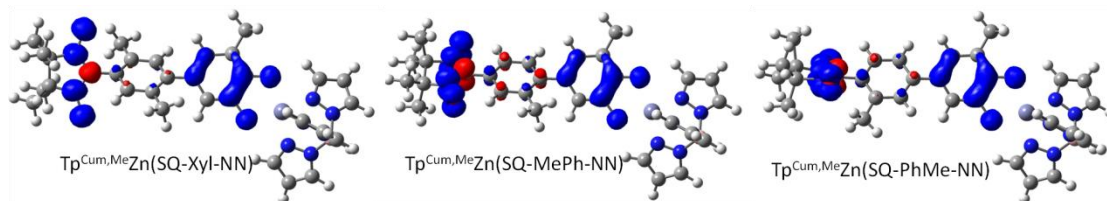


Figure 2.47: DFT-calculated spin density distributions of sterically-hindered DBA biradicals. Blue = positive spin density, red = negative spin density, contour isovalue = 0.004.

Table 2.12: DFT-calculated spin populations in sterically-hindered DBA biradicals.

Spin Populations	NN	Bridge	SQ	$\text{Tp}^{\text{Cum,Me}}\text{Zn}$
$\text{Tp}^{\text{Cum,Me}}\text{Zn}(\text{SQ-Xyl-NN})$	1.015	0.013	0.965	0.007
$\text{Tp}^{\text{Cum,Me}}\text{Zn}(\text{SQ-PhMe-NN})$	1.020	0.026	0.948	0.007
$\text{Tp}^{\text{Cum,Me}}\text{Zn}(\text{SQ-MePh-NN})$	1.054	-0.015	0.954	0.007
$\text{Tp}^{\text{Cum,Me}}\text{Zn}(\text{SQ-Ph-NN})$	1.063	-0.003	0.932	0.008

Figure 2.47 shows the spin density distributions and Table 2.12 summarizes the DFT-calculated spin populations for the optimized structures of these sterically-hindered D-B-A biradical molecules. The data in Table 2.12 is consistent with what we already know about spin delocalization in D-B-A molecules. Positive spin density gets delocalized from the SQ to the Ph if the SQ-Ph dihedral angle is small, reducing the amount of positive spin on the SQ. The spin density on SQ tracks with the SQ-bridge dihedral angle, $B = \text{Xyl} > \text{MePh} > \text{PhMe} \sim \text{Ph}$. The amount of positive spin density on NN is maximized when the NN-Ph dihedral angle is small, $\text{Ph} \sim \text{MePh} > \text{PhMe} \sim \text{Xyl}$. The spin density on the bridge depends on both dihedral angles, and for $B = \text{Xyl}$, there is little spin density on the bridge since the bridge overlap is reduced with both donor and acceptor rotations. In general we observe that the DBA biradicals with small NN-bridge

dihedrals have net negative spin density on the bridge, while those with larger NN-bridge dihedrals have net positive spin density on the bridge.

If we consider the spin populations on the NN ring and on the NN nitrogens to be an accurate proxy for the expected J values, we could the J value to decrease in the order of $\text{Tp}^{\text{Cum,Me}}\text{Zn}(\text{SQ-Ph-NN}) < \text{Tp}^{\text{Cum,Me}}\text{Zn}(\text{SQ-MePh-NN}) < \text{Tp}^{\text{Cum,Me}}\text{Zn}(\text{SQ-PhMe-NN}) <$ and $\text{Tp}^{\text{Cum,Me}}\text{Zn}(\text{SQ-Xyl-NN})$, with the first two compounds having the having the most positive J values and similar to one another, and the last two having the smallest J values and being similar to one another. An important point is that DFT-calculated spin densities and experimental nitrogen hyperfine coupling constants are both easier and faster to determine than J values from magnetic susceptibility measurements. Moreover, if one has not yet synthesized a particular DBA biradical, one might still use DFT-calculated values to estimate J. The caution to this statement, however, is that the DBA biradical should be of the same chemical nature as the previously studied D-B-A biradicals discussed here (see next section for a cross-conjugated bridge). The effect of large dihedral angles is seen in the nature of the wavefunctions for the frontier orbitals, where the NN SOMO and SQ SOMO behave as though they are uncoupled for $\text{Tp}^{\text{Cum,Me}}\text{Zn}(\text{SQ-Xyl-NN})$.

2.6.3 Electronic Absorption Spectra and Computational Studies of Sterically Hindered D-B-A Biradicals

Room-temperature electronic absorption spectra for the sterically-hindered DBA biradicals were acquired by the Shultz group, who possessed sufficient quantity of compound to accurately determine extinction coefficients, while we prepared thin film samples for variable temperature electronic absorption spectroscopy. The room-

temperature film and solution samples are essentially superimposable, but the solution sample spectra have been used here for comparison with the TD-DFT calculated spectra since this data has accurate molar extinction coefficients and less of a scattering background. We observe that the electronic absorption spectrum of $\text{Tp}^{\text{Cum,Me}}\text{Zn}(\text{SQ-PhMe-NN})$ is similar to $\text{Tp}^{\text{Cum,Me}}\text{Zn}(\text{SQ-Xyl-NN})$, and that of $\text{Tp}^{\text{Cum,Me}}\text{Zn}(\text{SQ-MePh-NN})$ is similar to $\text{Tp}^{\text{Cum,Me}}\text{Zn}(\text{SQ-Ph-NN})$, owing to the structural similarity of these compounds in terms of donor-bridge and bridge-acceptor dihedral angles.

Figure 2.48 shows an overlay of DFT-calculated (black) and experimental solution (red) spectra for $\text{Tp}^{\text{Cum,Me}}\text{Zn}(\text{SQ-Xyl-NN})$, where the bars are the calculated oscillator strengths. The spectra are marked with three broad bands, and it is assumed that

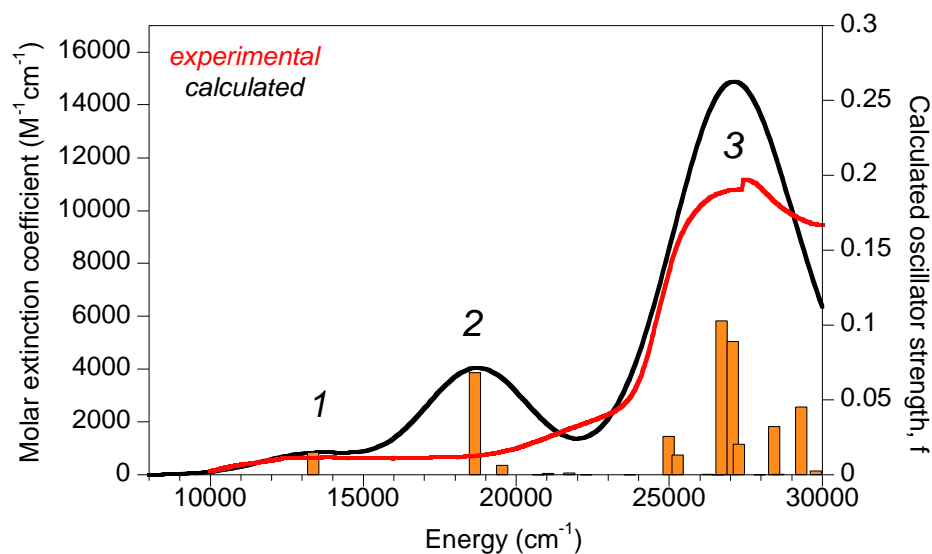
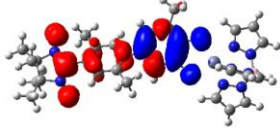
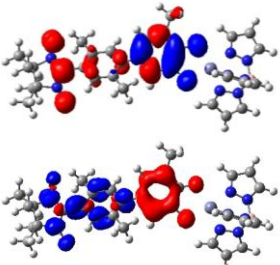
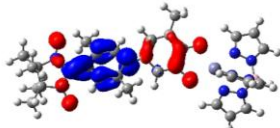
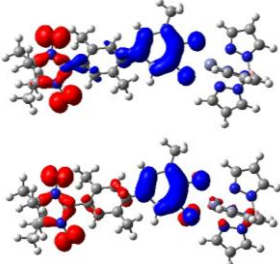


Figure 2.48: DFT-calculated (black) and experimental solution (red) spectra of $\text{Tp}^{\text{Cum,Me}}\text{Zn}(\text{SQ-Xyl-NN})$. DFT bands were widened to 4000 cm^{-1} , bars represent calculated oscillator strengths.

Table 2.13: DFT band assignments for $\text{Tp}^{\text{Cum,Me}}\text{Zn}(\text{SQ-Xyl-NN})$.

Band	DFT Energy (cm^{-1}) f		Assignment	Electron density difference map		
1	13370	0.015	[SQ-Ph-NN HOMO \rightarrow SQ SOMO] - [SQ-Ph-NN HOMO-1 \rightarrow SQ SOMO]			
			18520, 19530	0.068, 0.006	[SQ-Ph-NN HOMO \rightarrow SQ SOMO] + [SQ-Ph-NN HOMO-1 \rightarrow SQ SOMO] NN/SQ SOMO \rightarrow NN-Ph LUMO	
3	25000	0.026			NN/SQ SOMO \rightarrow NN-Ph LUMO	
			26740, 27100	0.103, 0.089	NN \rightarrow SQ SOMO	
					28410, 29330	0.032, 0.046

all of the bands, in particular band 3, are comprised of multiple one-electron promotion contributions. The spectra are marked with three broad bands, and it is assumed that all of the bands, in particular band 3, are comprised of multiple one-electron promotion contributions. There is a good agreement in band energy and extinction coefficients for bands 1 and 3, while band 2 is calculated to occur at lower energy (at $\sim 19000\text{ cm}^{-1}$) and may not correspond to the experimental band at $\sim 22000\text{ cm}^{-1}$.

Band assignments are shown in Table 2.13, and transitions below 20000 cm^{-1} are assigned as a NN-Ph-SQ HOMO \rightarrow SQ SOMO transitions. The donor-acceptor SQ SOMO \rightarrow NN-Ph LUMO transition has one of the lowest oscillator strengths and contributes to bands at $\sim 19500\text{ cm}^{-1}$ and $\sim 25000\text{ cm}^{-1}$ with $f = 0.006$ and 0.026 , respectively. The main component of band 3 is assigned as a transition from lower lying filled NN orbitals into the SQ SOMO with an oscillator strength that is approximately four times as large as the D-A CT band.

The variable-temperature electronic absorption spectrum of $\text{Tp}^{\text{Cum,Me}}\text{Zn}(\text{SQ-Xyl-NN})$ is shown in Figure 2.49. This temperature dependence is subtle, especially since the features in the spectrum are broad. We observe a decrease in band intensity at both $\sim 26000\text{ cm}^{-1}$ and $\sim 27500\text{ cm}^{-1}$, but the temperature-dependent changes in the spectra did not seem distinct enough to relate the temperature dependent data to singlet and triplet populations.

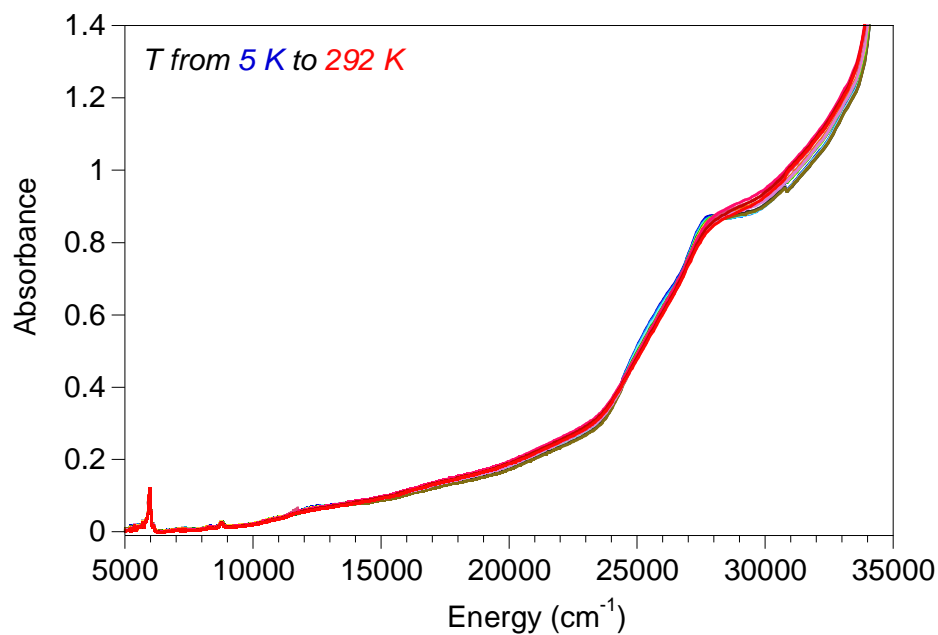


Figure 2.49: Variable-temperature electronic absorption spectra of $\text{Tp}^{\text{Cum,Me}}_2\text{Zn}(\text{SQ-Xyl-NN})$ in a polystyrene polymer matrix. Temperatures range from 5 K (dark blue) to 292 K (red), and data were baseline corrected to align with the temperature-independent polystyrene reference peak at $\sim 6000 \text{ cm}^{-1}$.

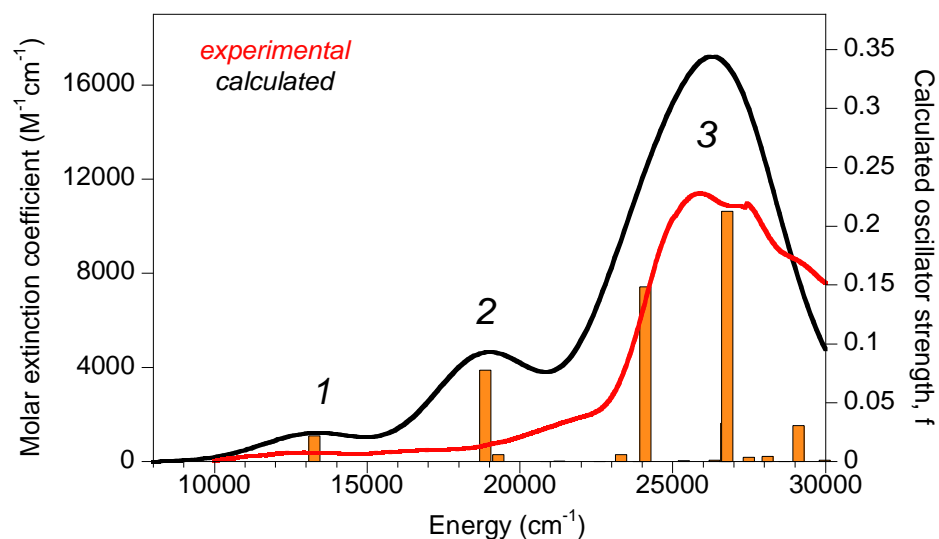


Figure 2.50: Computed (black) and experimental solution (red) spectra for $\text{Tp}^{\text{Cum,Me}}_2\text{Zn}(\text{SQ-PhMe-NN})$. Computed bands have bandwidths of 4000 cm^{-1} , and bars lengths represent calculated oscillator strengths.

Table 2.14: DFT band assignments for $\text{Tp}^{\text{Cum,Me}}\text{Zn}(\text{SQ-PhMe-NN})$.

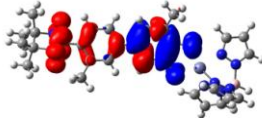
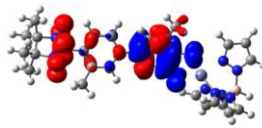
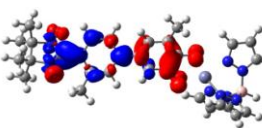
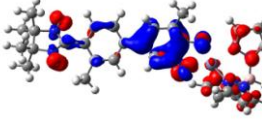
Band	DFT		Assignment	Electron density difference map
	Energy (cm^{-1})	f		
1	13280	0.022	[SQ-Ph-NN HOMO \rightarrow SQ SOMO]	
			+ [SQ-Ph-NN HOMO-1 \rightarrow SQ SOMO]	
2	18870	0.078	[SQ-Ph-NN HOMO-1 \rightarrow SQ SOMO]	
			- [SQ-Ph-NN HOMO \rightarrow SQ SOMO]	
3	24100	0.148	NN/SQ SOMO \rightarrow NN-Ph LUMO	
	26810	0.213	NN and Tp \rightarrow SQ SOMO	

Figure 2.50 and Table 2.14 show the calculated and room-temperature solution spectra for $\text{Tp}^{\text{Cum,Me}}\text{Zn}(\text{SQ-PhMe-NN})$. Bands 1 and 2 are assigned as delocalized HOMO \rightarrow SQ SOMO transitions. As was the case for $\text{Tp}^{\text{Cum,Me}}\text{Zn}(\text{SQ-Xyl-NN})$, we notice that the calculated energy of band 2 is lower than what is observed experimentally. The most significant difference with respect to the $\text{Tp}^{\text{Cum,Me}}\text{Zn}(\text{SQ-Xyl-NN})$ data is that the donor-acceptor charge transfer band, calculated to occur at $\sim 24100 \text{ cm}^{-1}$, has an increased oscillator strength that is about six times as large as when $B = \text{Xyl}$, even though it is still not the most intense transition in the spectrum.

Figure 2.51 shows the variable temperature electronic absorption spectra for $\text{Tp}^{\text{Cum,Me}}\text{Zn}(\text{SQ-PhMe-NN})$. For this compound, the temperature dependence is very weak. In general, biradicals with small (but nonzero) exchange couplings display temperature dependent absorption spectra since the energy gap between the triplet- and singlet ground states is small enough to allow thermal population of the spin singlet as the temperature is increased.

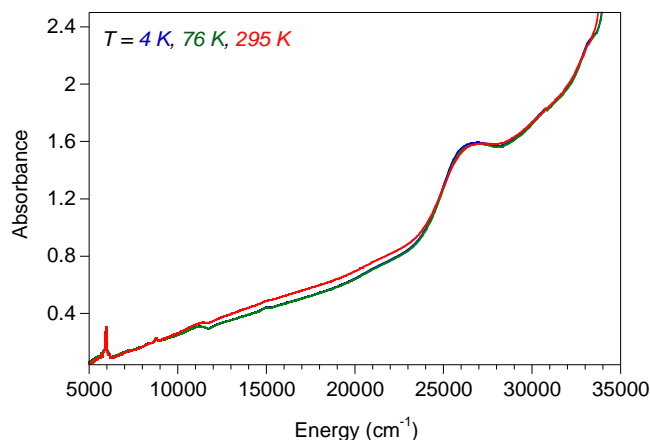


Figure 2.51: Variable-temperature electronic absorption spectra for $\text{Tp}^{\text{Cum,Me}}\text{Zn}(\text{SQ-PhMe-NN})$ in a polystyrene matrix. Temperatures are 4 K (blue), 76 K (green), and 295 K (red), and the data were baseline corrected to align the temperature-independent polystyrene reference peak at $\sim 6000 \text{ cm}^{-1}$.

Figure 2.52 and Table 2.15 display the results of calculated and room-temperature solution absorption spectra for $\text{Tp}^{\text{Cum,Me}}\text{Zn}(\text{SQ-MePh-NN})$. Bands 1 and 2 are assigned as delocalized HOMO \rightarrow SQ SOMO transitions, as observed for both $\text{Tp}^{\text{Cum,Me}}\text{Zn}(\text{SQ-Xyl-NN})$ and $\text{Tp}^{\text{Cum,Me}}\text{Zn}(\text{SQ-PhMe-NN})$. Band 3 occurs at much lower energy in $\text{Tp}^{\text{Cum,Me}}\text{Zn}(\text{SQ-MePh-NN})$ than it does for $\text{Tp}^{\text{Cum,Me}}\text{Zn}(\text{SQ-Xyl-NN})$ and $\text{Tp}^{\text{Cum,Me}}\text{Zn}(\text{SQ-PhMe-NN})$, but at a similar energy to that observed for $\text{Tp}^{\text{Cum,Me}}\text{Zn}(\text{SQ-Ph-NN})$. We assign this band as the D-A CT band. The D-A CT band is split into two

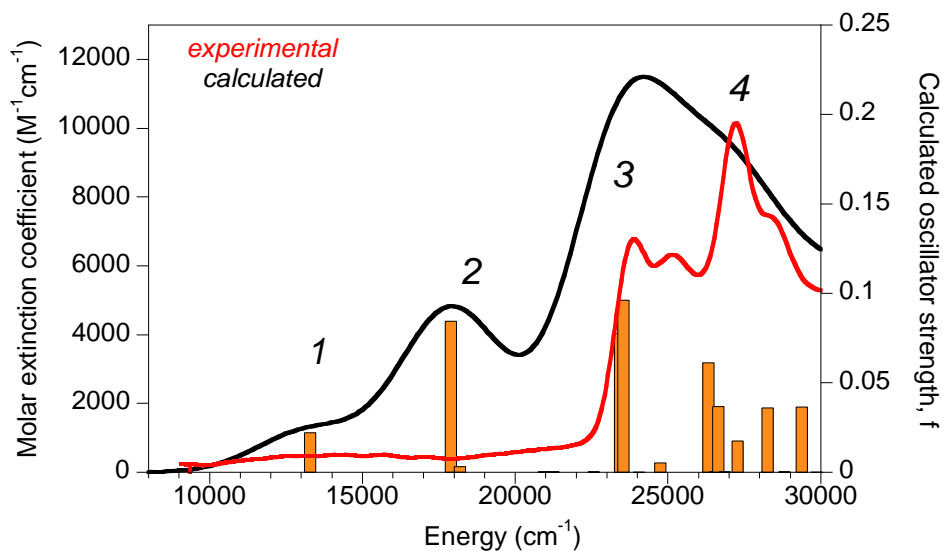
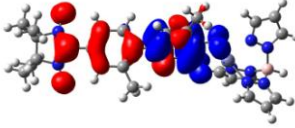
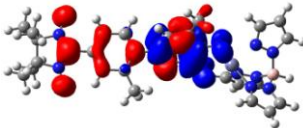
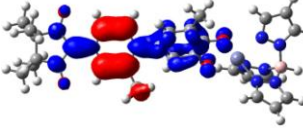
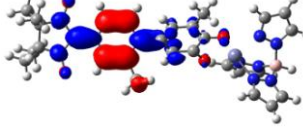
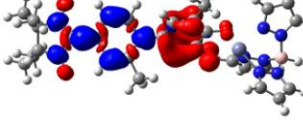
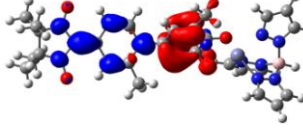


Figure 2.52: DFT-calculated (black) and experimental solution (red) spectra for $\text{Tp}^{\text{Cum,Me}}_2\text{Zn}(\text{SQ-MePh-NN})$. Computed transitions are shown with a 4000 cm^{-1} bandwidth, and bar heights represent calculated oscillator strengths.

components, a positive and negative linear combination of the SQ SOMO \rightarrow NN-Ph LUMO and Ph \rightarrow SQ SOMO one-electron promotions. This mixing of two one-electron promotions is not observed in the TD-DFT results for $\text{Tp}^{\text{Cum,Me}}_2\text{Zn}(\text{SQ-Ph-NN})$. The D-ACT band is the most intense calculated transition in the spectrum. Band 4 is assigned as transitions from the delocalized SQ-Ph-NN HOMO to the SQ SOMO, which was assigned as band 3 in $\text{Tp}^{\text{Cum,Me}}_2\text{Zn}(\text{SQ-Xyl-NN})$. The experimental and computed electronic absorption spectra show that sterically-hindered bridges in D-B-A biradical complexes result in increased NN-Ph dihedral angles with a concomitant reduction in intensity for the donor-acceptor charge transfer band.

Table 2.15: DFT band assignments for $\text{Tp}^{\text{Cum,Me}}\text{Zn}(\text{SQ-MePh-NN})$.

Band	DFT Energy (cm^{-1}) f		Assignment	Electron density difference map
1	13280	0.022	[SQ-Ph-NN HOMO \rightarrow SQ SOMO] -	
			[SQ-Ph-NN HOMO-1 \rightarrow SQ SOMO]	
2	17890	0.084	[SQ-Ph-NN HOMO-1 \rightarrow SQ SOMO] +	
			[SQ-Ph-NN HOMO \rightarrow SQ SOMO]	
3	23420	0.078	[SQ SOMO \rightarrow NN-Ph LUMO] -	
			[Ph \rightarrow SQ SOMO]	
3	23530	0.096	[SQ SOMO \rightarrow NN-Ph LUMO] +	
			[Ph \rightarrow SQ SOMO]	
4	28250	0.036	[SQ-Ph-NN HOMO \rightarrow NN-Ph LUMO] β -	
			[SQ-Ph-NN HOMO \rightarrow NN-Ph LUMO] α	
4	31750	0.066	[SQ-Ph-NN HOMO \rightarrow NN-Ph LUMO] α -	
			[SQ-Ph-NN HOMO \rightarrow NN-Ph LUMO] β	

We also acquired variable temperature electronic absorption data for $\text{Tp}^{\text{Cum,Me}}\text{Zn}(\text{SQ-MePh-NN})$ (Figure 2.53), and observe temperature-dependent bands at 23645 cm^{-1} , 25115 cm^{-1} , 26865 cm^{-1} and 28160 cm^{-1} . While the first three peaks decrease in intensity as the temperature increases, the last peak increases in intensity as the temperature increases. The energy separation between the peak at 23645 cm^{-1} and the peak at 25115 cm^{-1} is 1470 cm^{-1} .

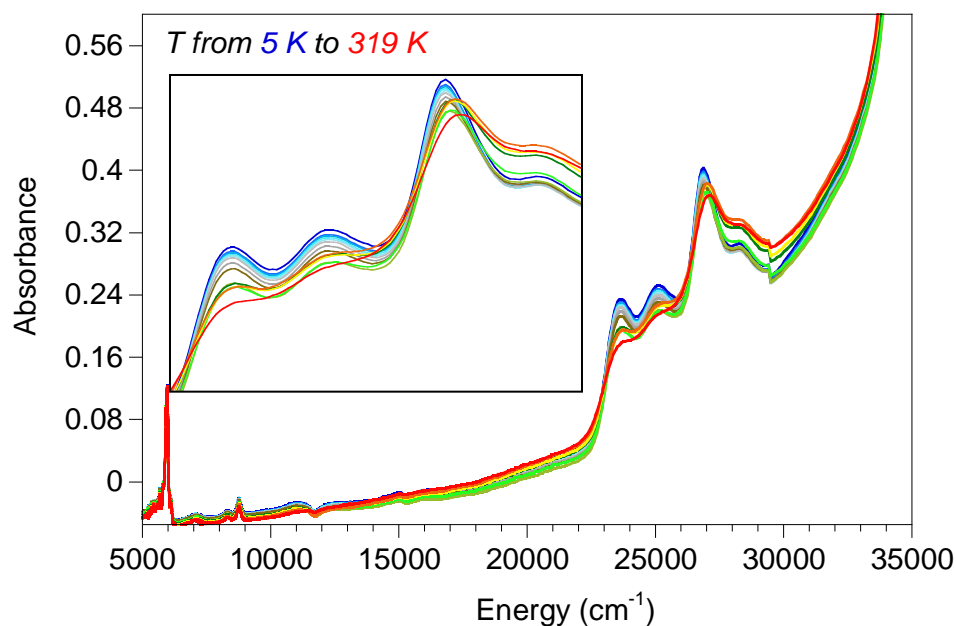


Figure 2.53: Variable-temperature electronic absorption spectra of $\text{Tp}^{\text{Cum,Me}}\text{Zn}(\text{SQ-MePh-NN})$ in a polystyrene polymer matrix. Temperatures range from 5 K (dark blue) to 319 K (red), and data were baseline corrected to align the temperature-independent polystyrene reference peak at $\sim 6000\text{ cm}^{-1}$.

We postulate that the 25115 cm^{-1} peak may be the $0 \rightarrow 1'$ vibronic transition built on the 23645 cm^{-1} $0 \rightarrow 0'$ origin. The 1470 cm^{-1} spacing is the excited state frequency associated with a vibration activated during the $\text{D} \rightarrow \text{A}$ CT transition and may correspond to the 1601 cm^{-1} vibration observed in the ground state Raman spectra of $\text{Tp}^{\text{Cum,Me}}\text{Zn}(\text{SQ-MePh-NN})$ (see next section).). If this is true, the excited state frequency is $\sim 8\%$ lower

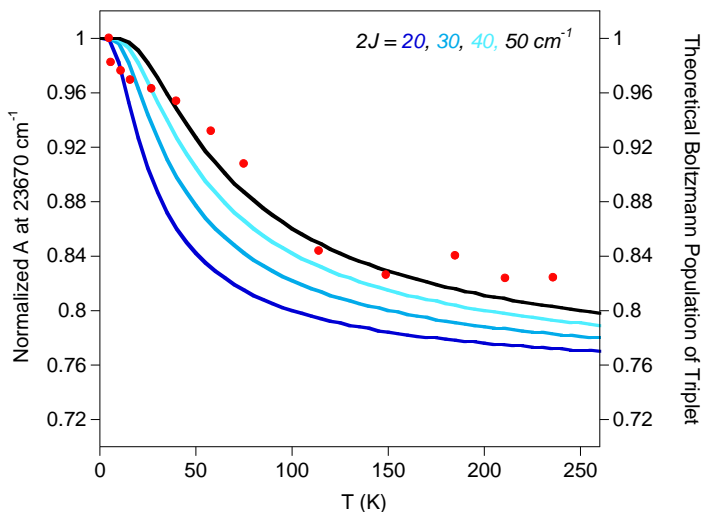


Figure 2.54: Absorbance at 23670 cm^{-1} for $\text{Tp}^{\text{Cum,Me}}\text{Zn}(\text{SQ-MePh-NN})$ as a function of temperature (red circles) and theoretical Boltzmann populations for ferromagnetic exchange couplings of $2J = 20\text{-}50\text{ cm}^{-1}$.

than the ground state frequency. This may be compared with $\text{Tp}^{\text{Cum,Me}}\text{Zn}(\text{SQ-Ph-NN})$, where the difference was $\sim 13\%$. The third temperature-dependent band is at 26865 cm^{-1} and is 1750 cm^{-1} higher in energy than the second band. Therefore, it most likely is not a vibronic component of the prior transition. The band at 28160 cm^{-1} may be the ${}^1\text{GC} \rightarrow {}^1\text{EC}$ D-A CT transition. For ferromagnetic exchange coupling we expect the triplet D-A CT band (i.e. ${}^3\text{GC} \rightarrow {}^3\text{EC}$) to be at lower energy and decrease in intensity as the temperature increases, while the singlet D-A CT band (${}^1\text{GC} \rightarrow {}^1\text{EC}$) should occur at higher energy and gain intensity as the temperature increases. The energy separation between the $0 \rightarrow 0'$ ${}^3\text{GC} \rightarrow {}^3\text{EC}$ D-A CT transition at 23645 cm^{-1} and the ${}^1\text{GC} \rightarrow {}^1\text{EC}$ transition at 28160 cm^{-1} is $\sim 4515\text{ cm}^{-1}$, yielding $K \sim 2255\text{ cm}^{-1}$ for this molecule.

The absorbance changes of a given band as a function of temperature depend on the singlet-triplet ground state energy gap, and in Figure 2.54 we attempt to describe the

temperature dependence of the $^3GC \rightarrow ^3EC$ DA CT transition using the theoretical Boltzmann populations for various values of the ground state singlet-triplet exchange ($2J$). The data does not fit any of the Boltzmann population curves very clearly, but appears to be considerably lower than $2J = 200 \text{ cm}^{-1}$ for $\text{Tp}^{\text{Cum,Me}}\text{Zn}(\text{SQ-Ph-NN})$.

2.6.4 Resonance Raman Spectra and DFT Frequency Calculations of Sterically Hindered DBA Biradicals

Resonance Raman data were acquired for $\text{Tp}^{\text{Cum,Me}}\text{Zn}(\text{SQ-Xyl-NN})$ and $\text{Tp}^{\text{Cum,Me}}\text{Zn}(\text{SQ-MePh-NN})$ in both a solid state sodium chloride matrix with a sodium sulfate internal standard, and as solutions of the compounds in dichloromethane. We noticed that solutions would change color or turn colorless a few hours into the Raman experiment indicating sample decomposition even at the lowest laser powers used. While the resonance Raman spectrum of a freshly prepared solution at a given laser line would produce acceptable data, acquiring a resonance Raman profile over the six laser lines we have available requires 1-2 days, and requires the same sample concentration/sample condition for all laser lines so that the peak intensities relative to the internal standard are comparable between all laser lines. We therefore focus on the solid state resonance Raman data we have acquired.

Figure 2.55 shows the resonance Raman spectra of $\text{Tp}^{\text{Cum,Me}}\text{Zn}(\text{SQ-Xyl-NN})$ and $\text{Tp}^{\text{Cum,Me}}\text{Zn}(\text{SQ-MePh-NN})$ using 407 nm excitation, which results in largest Raman enhancement for the sample peaks relative to the internal standard. In Figure 2.55 the sulfate peaks are marked in red, the most enhanced modes of the samples are marked in blue, and other peaks are marked in black. Resonance Raman spectra using other laser

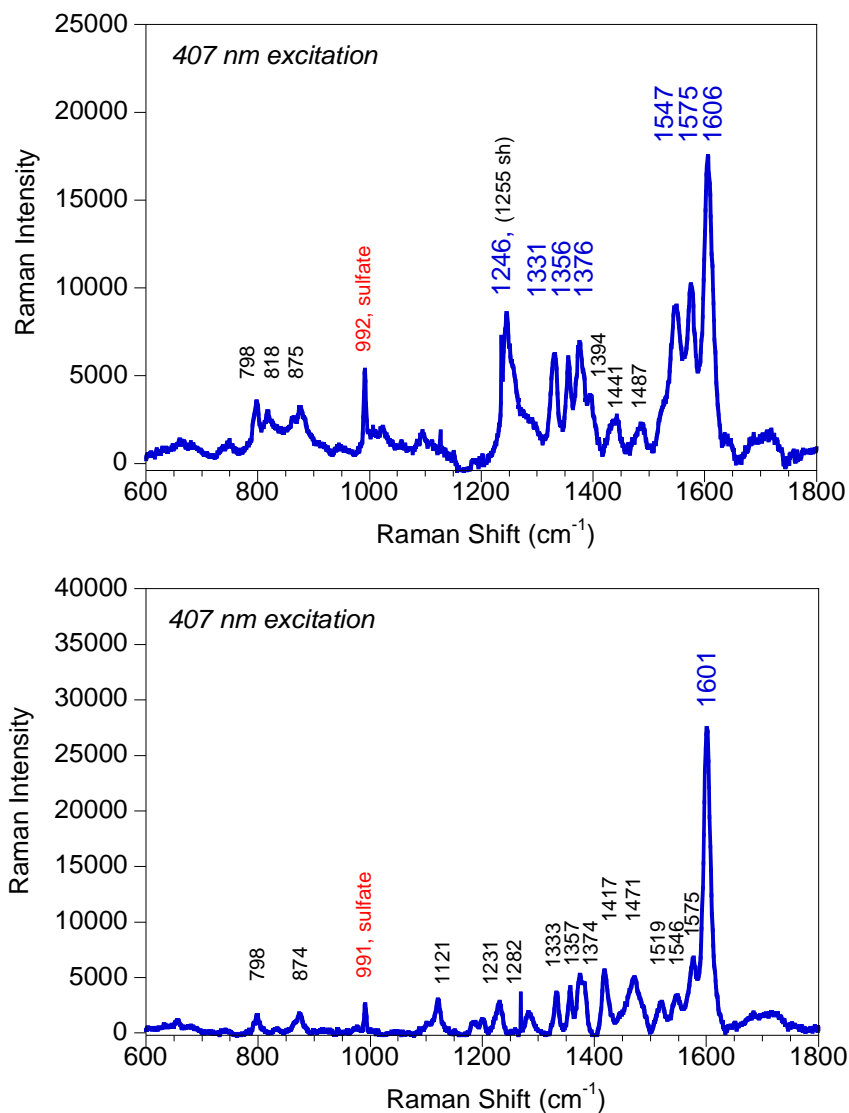


Figure 2.55: Resonance Raman data for Tp^{Cum,Me}Zn(SQ-Xyl-NN) (top) and Tp^{Cum,Me}Zn(SQ-MePh-NN) (bottom) in a solid state NaCl/Na₂SO₄ matrix using 407 nm excitation.

lines are included in Appendix 6.1.1. The data show Raman enhancement for a number of peaks in the 1200-1600 cm⁻¹ region where in-plane NN, Ph, and SQ ring modes are anticipated to occur. For Tp^{Cum,Me}Zn(SQ-Xyl-NN) we notice that the most enhanced

mode occurs at 1606 cm^{-1} , followed by modes at 1547, 1575, 1246, 1331, 1356, 1376 cm^{-1} . For $\text{Tp}^{\text{Cum,Me}}\text{Zn}(\text{SQ-MePh-NN})$, the most enhanced mode occurs at 1601 cm^{-1} .

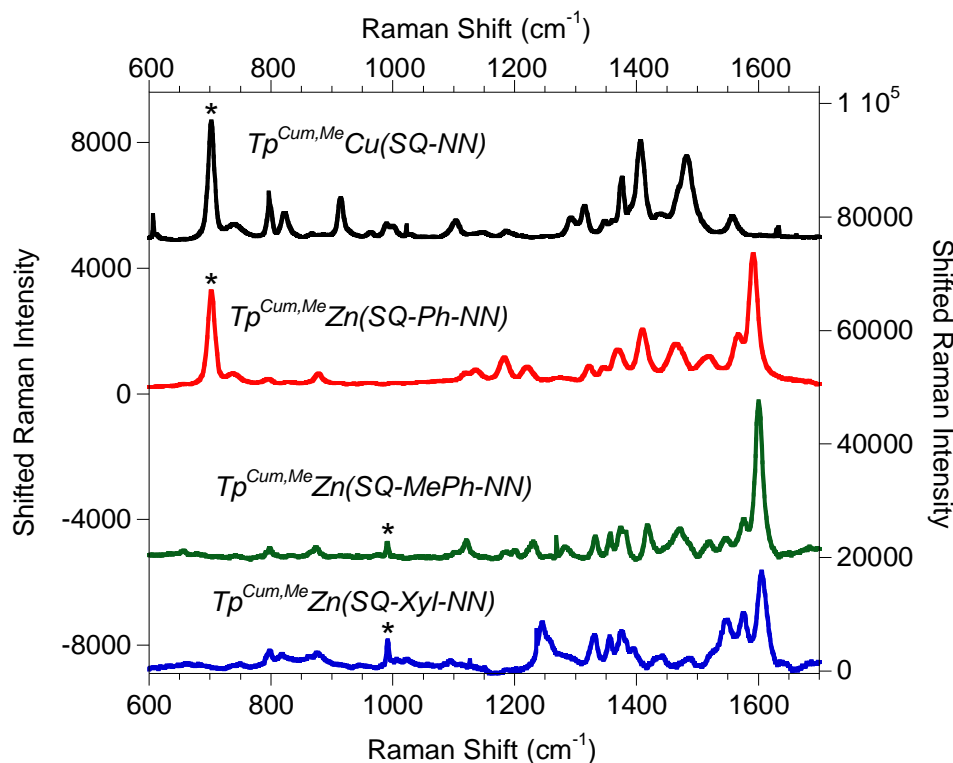


Figure 2.56: Overlay of Resonance Raman spectra for $\text{Tp}^{\text{Cum,Me}}\text{Cu}(\text{SQ-NN})$ (black, left y-axis, 413 nm excitation, in CH_2Cl_2)⁴, $\text{Tp}^{\text{Cum,Me}}\text{Zn}(\text{SQ-Ph-NN})$ (red, right y-axis, 413 nm excitation, in CH_2Cl_2)⁴, $\text{Tp}^{\text{Cum,Me}}\text{Zn}(\text{SQ-MePh-NN})$ (green, right y-axis, 407 nm excitation, in $\text{NaCl}/\text{Na}_2\text{SO}_4$), and $\text{Tp}^{\text{Cum,Me}}\text{Zn}(\text{SQ-Xyl-NN})$ (blue, right y-axis, 407 nm excitation, in $\text{NaCl}/\text{Na}_2\text{SO}_4$), solvent/sulfate peaks are marked with stars.

It is instructive to compare how the enhancement pattern of these modes changes compared to the earlier data for $\text{Tp}^{\text{Cum,Me}}\text{Cu}(\text{SQ-NN})$ and $\text{Tp}^{\text{Cum,Me}}\text{Zn}(\text{SQ-Ph-NN})$ acquired by Depperman.⁹⁰ This is shown in a stack plot with the $\text{Tp}^{\text{Cum,Me}}\text{Zn}(\text{SQ-Xyl-NN})$ and $\text{Tp}^{\text{Cum,Me}}\text{Zn}(\text{SQ-MePh-NN})$ spectra in Figure 2.56. We note that spectra for $\text{Tp}^{\text{Cum,Me}}\text{Cu}(\text{SQ-NN})$ and $\text{Tp}^{\text{Cum,Me}}\text{Zn}(\text{SQ-Ph-NN})$ were acquired in dichloromethane and thus show different internal standard (i.e. solvent) peaks than those acquired as solids

with a sulfate standard. From Figure 2.56 we notice that there are several differences between the resonance Raman spectra of $\text{Tp}^{\text{Cum,Me}}\text{Zn}(\text{SQ-Ph-NN})$ and $\text{Tp}^{\text{Cum,Me}}\text{Zn}(\text{SQ-Xyl-NN})$. The modes at 1547 cm^{-1} , 1575 cm^{-1} have increased in intensity relative to the 1606 cm^{-1} mode, or conversely the 1606 cm^{-1} mode is less enhanced than its counterpart at 1591 cm^{-1} in $\text{Tp}^{\text{Cum,Me}}\text{Zn}(\text{SQ-Ph-NN})$. The modes at 1547 cm^{-1} and 1246 cm^{-1} are new modes observed for $\text{Tp}^{\text{Cum,Me}}\text{Zn}(\text{SQ-Xyl-NN})$. The relative intensities of bands from $1300\text{-}1550\text{ cm}^{-1}$ change, and the bands found for $\text{Tp}^{\text{Cum,Me}}\text{Zn}(\text{SQ-Ph-NN})$ in the $1100\text{-}1250\text{ cm}^{-1}$ region are absent (or shifted) in $\text{Tp}^{\text{Cum,Me}}\text{Zn}(\text{SQ-Xyl-NN})$. The resonance Raman spectrum of $\text{Tp}^{\text{Cum,Me}}\text{Zn}(\text{SQ-MePh-NN})$ is very similar to $\text{Tp}^{\text{Cum,Me}}\text{Zn}(\text{SQ-Ph-NN})$, with only very minor differences in peak positions or relative intensities. Given that the two compounds have very similar ring dihedrals the resonance Raman band assignments for $\text{Tp}^{\text{Cum,Me}}\text{Zn}(\text{SQ-MePh-NN})$ are the same as for $\text{Tp}^{\text{Cum,Me}}\text{Zn}(\text{SQ-Ph-NN})$.

DFT frequency calculations for $\text{Tp}^{\text{Cum,Me}}\text{Zn}(\text{SQ-Xyl-NN})$ show that the modes at $\sim 1250\text{ cm}^{-1}$ phenyl ring breathing modes. Vibrational modes calculated at 1563 cm^{-1} , 1609 cm^{-1} , and 1652 cm^{-1} are in-plane phenyl stretches similar to the 1642 cm^{-1} vibration in benzene. For $\text{Tp}^{\text{Cum,Me}}\text{Zn}(\text{SQ-Ph-NN})$, this stretching motion occurs along the pseudo C_2 axis defined by the bonds that connect the phenylene to the NN and SQ rings. For $\text{Tp}^{\text{Cum,Me}}\text{Zn}(\text{SQ-Xyl-NN})$ the phenyl ring stretching motion also occurs along an axis defined by the methyl groups on xylene, and an axis defined by the hydrogens on xylene. The highest frequency stretch for $\text{Tp}^{\text{Cum,Me}}\text{Zn}(\text{SQ-Xyl-NN})$ (1652 cm^{-1}) is the one calculated to be along the NN-Ph-SQ axis of the xylene ring. There is no particular reason for a phenylene (or xylene) stretch that is not directed along the NN-Ph-SQ axis to

be resonantly enhanced during an electronic transition. Therefore we suggest that in the resonance Raman spectrum of $\text{Tp}^{\text{Cum,Me}}\text{Zn}(\text{SQ-Xyl-NN})$ the 1606 cm^{-1} vibration is has reduced enhancement compared to $\text{Tp}^{\text{Cum,Me}}\text{Zn}(\text{SQ-Ph-NN})$ due to the increased phenylene ring torsions relative to the SQ and NN brought about by the methyl substituents. This is consistent with the results of TD-DFT calculations where it is observed that the donor-acceptor charge transfer transitions in this spectral region are less intense for $\text{Tp}^{\text{Cum,Me}}\text{Zn}(\text{SQ-Xyl-NN})$ than for $\text{Tp}^{\text{Cum,Me}}\text{Zn}(\text{SQ-Ph-NN})$.

2.7 Computational and Experimental Studies of a Cross-Conjugated D-B-A Biradical: $\text{Tp}^{\text{Cum,Me}}\text{Zn}(\text{SQ-mPh-NN})$

2.7.1 $\text{Tp}^{\text{Cum,Me}}\text{Zn}(\text{SQ-mPh-NN})$ Shows Antiferromagnetic D-A Biradical Exchange Coupling

$\text{Tp}^{\text{Cum,Me}}\text{Zn}(\text{SQ-mPh-NN})$ was synthesized by the Shultz group and magnetic susceptibility measurements showed that, contrary to all previously studied D-B-A biradicals, this molecule has weak D-A antiferromagnetic exchange coupling ($J = -32\text{ cm}^{-1}$), and the ground state is a singlet. Figure 2.57 shows the $\text{Tp}^{\text{Cum,Me}}\text{Zn}(\text{SQ-mPh-NN})$ structure, where in the phenyl bridge is bound in a meta-configuration to the donor and acceptor and thus cross-conjugated. In all of the previously studied phenylene-bridged molecules, the phenylene was conjugated with the NN and SQ, while the phenylene bridge in $\text{Tp}^{\text{Cum,Me}}\text{Zn}(\text{SQ-mPh-NN})$ is cross-conjugated.. We are interested in understanding how the change in conjugation of the bridge relative to the donor and acceptor modifies the nature of the donor-acceptor coupling to change the nature of the

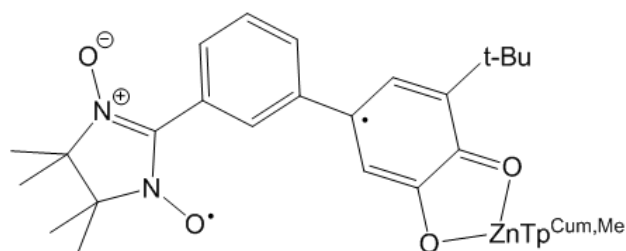


Figure 2.57: Chemical structure of $\text{Tp}^{\text{Cum,Me}}\text{Zn}(\text{SQ-mPh-NN})$.

D-A exchange coupling from strongly ferromagnetic with a triplet ground state to antiferromagnetic with a singlet ground state.

2.7.2 DFT Optimized Geometry and Frontier Molecular Orbitals of $\text{Tp}^{\text{Cum,Me}}\text{Zn}(\text{SQ-mPh-NN})$

The DFT-optimized structure of $\text{Tp}^{\text{Cum,Me}}\text{Zn}(\text{SQ-mPh-NN})$ calculated as both a broken-symmetry spin singlet and a spin triplet has ring torsion angles of 11° for the NN-Ph dihedral and 34° for the SQ-Ph dihedral. These dihedral angles are very similar to those observed for $\text{Tp}^{\text{Cum,Me}}\text{Zn}(\text{SQ-pPh-NN})$, and also comparable to crystallographically determined ring torsion angles of 6° for the NN-Ph dihedral and 24° for the SQPh dihedral in $\text{Tp}^{\text{Cum,Me}}\text{Zn}(\text{SQ-mPh-NN})$. Note that $\text{Tp}^{\text{Cum,Me}}\text{Zn}(\text{SQ-pPh-NN})$ refers to the same molecule as the previously used notation $\text{Tp}^{\text{Cum,Me}}\text{Zn}(\text{SQ-Ph-NN})$, but pPh = para-phenyl is used in this section to emphasize the distinction between meta- and para conjugation of the bridge in the D-B-A biradical. In the broken-symmetry singlet the spins are antiferromagnetically coupled making the molecule a net spin singlet, but the spins are located in different spatial orbitals (i.e. one on NN and the other on SQ) so that the molecule is still a biradical. DFT-calculated energies of the optimized triplet (trip)

and broken-symmetry singlet (bss) structures and the calculated expectation values of S^2 for the triplet and broken-symmetry singlet were used to obtain J for both the weak-coupling limit (Eq. 19)⁷⁹ and for an expression approximately valid for either strong or weak coupling (Eq. 18).⁷⁹ We obtained a value of J - 54.7 cm^{-1} in both cases.

$$J_{ab} = - \frac{\Delta E (\text{trip-bss})}{\langle S^2 \rangle_{\text{trip}} - \langle S^2 \rangle_{\text{bss}}} \quad \text{Eq. 18}$$

$$J_{ab} = - \frac{\Delta E (\text{trip-bss})}{(S_a + S_b)^2} \quad \text{Eq. 19}$$

Here J_{ab} is the exchange coupling between spins a and b in the Heisenberg-Dirac-van Vleck Hamiltonian:

$$H_{HDvV} = -2 J_{ab} \vec{S}_a \vec{S}_b \quad \text{Eq. 20}$$

We considered the frontier molecular orbitals for both the broken-symmetry singlet and triplet, shown in Figure 2.58 and 2.59, respectively. The SOMO, LUMO, and LUMO+1 orbitals are very similar for the $\text{Tp}^{\text{Cum,Me}}\text{Zn}(\text{SQ-mPh-NN})$ broken-symmetry singlet and triplet. However, the HOMO and HOMO-1 orbitals differ for the bss and triplet, since for the triplet the β HOMO and HOMO-1 orbitals are quite delocalized. Note that all HOMO \rightarrow SOMO transitions are β transitions since the α counterpart of the β SOMO is occupied.

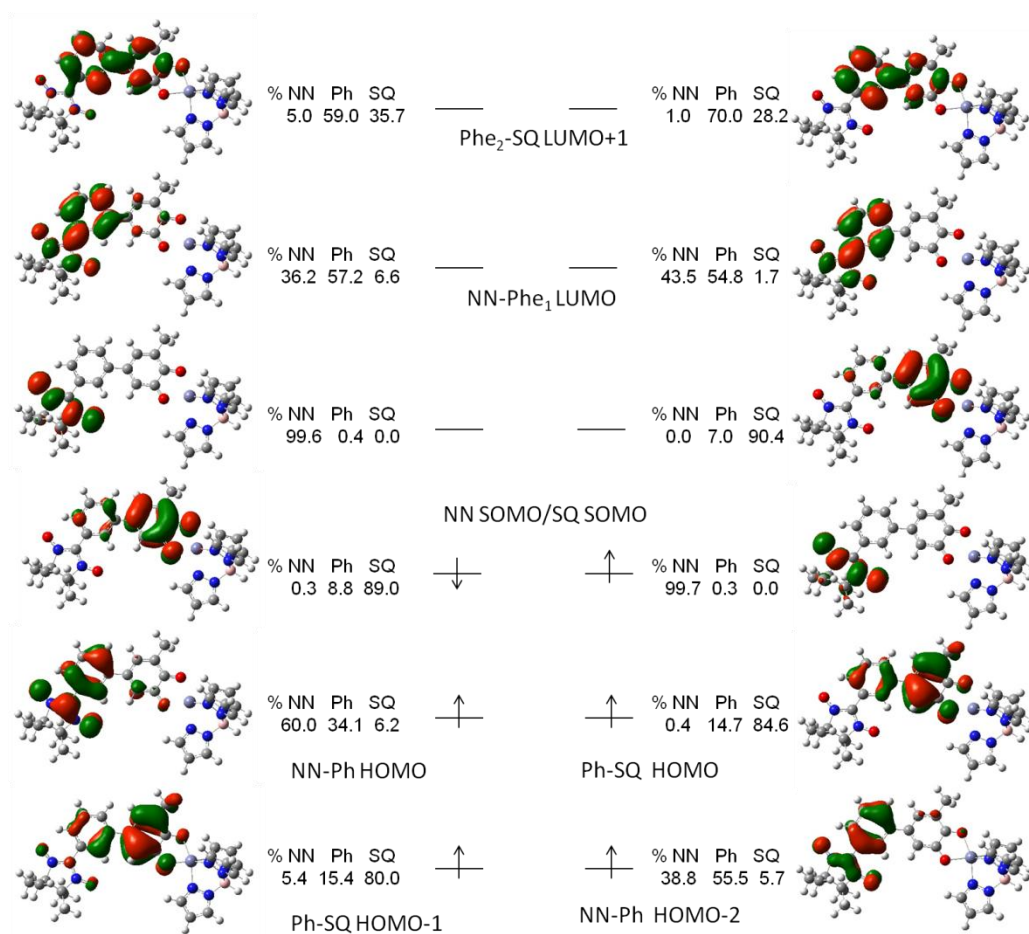


Figure 2.58: Frontier molecular orbitals and orbital compositions for $\text{Tp}^{\text{Cum,Me}}\text{Zn}(\text{SQ-mPh-NN})$ (broken-symmetry singlet).

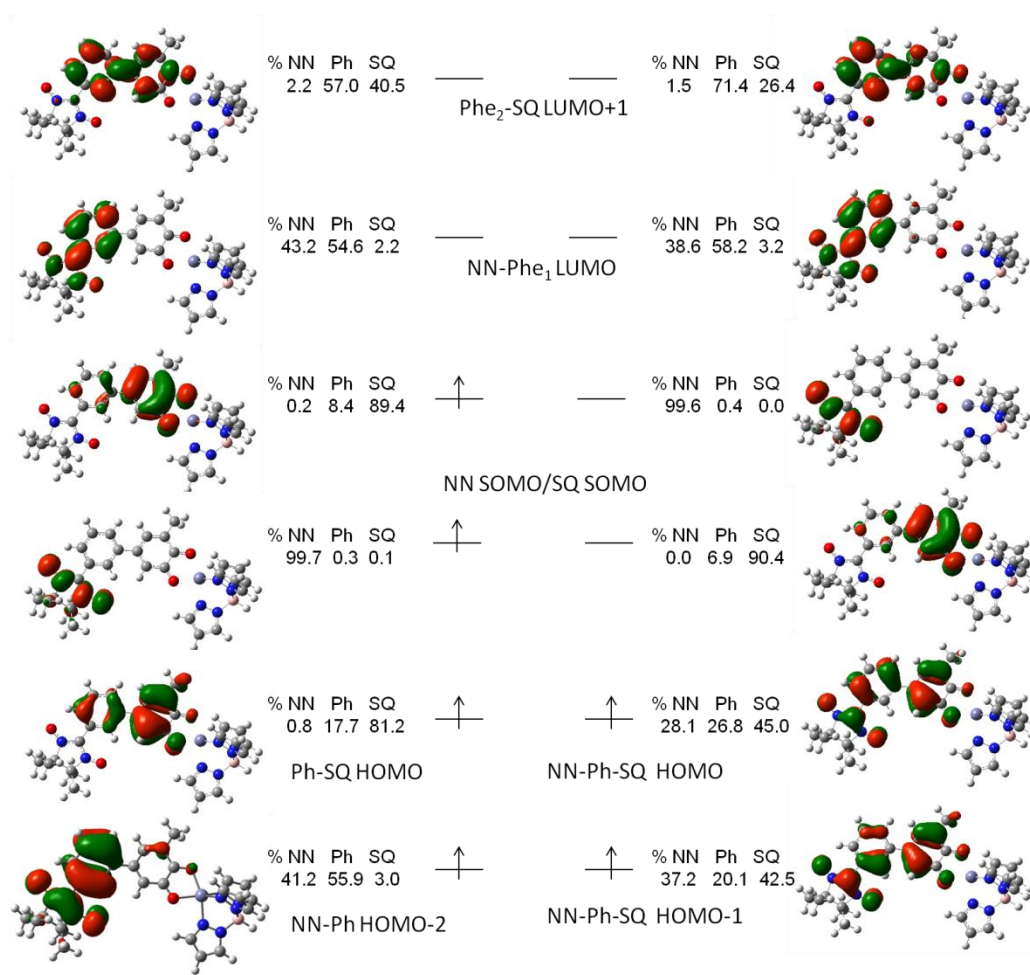


Figure 2.59: Frontier molecular orbitals and orbital compositions for $\text{Tp}^{\text{Cum,Me}}\text{Zn}(\text{SQ-mPh-NN})$ (triplet).

For the bss (and the α orbitals of the triplet), the HOMO and HOMO-1 orbitals are more localized and have the orbital character of either NN and Ph, or Ph and SQ, but are never delocalized over the entire SQ-Bridge-NN unit. We observe that the SOMO and LUMO compositions are very similar to those observed in $\text{Tp}^{\text{Cum,Me}}\text{Zn}(\text{SQ-pPh-NN})$. The

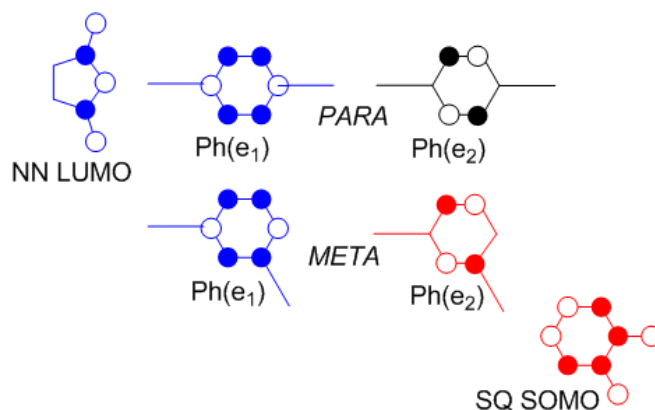


Figure 2.60: Orbital interactions in $\text{Tp}^{\text{Cum,Me}}_2\text{Zn}(\text{SQ-mPh-NN})$ versus $\text{Tp}^{\text{Cum,Me}}_2\text{Zn}(\text{SQ-pPh-NN})$.

LUMO+1 for $\text{Tp}^{\text{Cum,Me}}_2\text{Zn}(\text{SQ-mPh-NN})$ and $\text{Tp}^{\text{Cum,Me}}_2\text{Zn}(\text{SQ-pPh-NN})$ are very different. For the para isomer, the Ph e_2 orbital is nodal at the carbon atoms that connect to the donor and acceptor (Figure 2.60), while for the meta isomer the Ph e_2 orbital has a non-zero orbital coefficient on the phenyl ring carbon atom that is connected to the semiquinone. This allows the SQ SOMO to dominantly mix with the meta phenylene, leading to a LUMO+1 orbital that is delocalized over both the SQ and Ph rings.

2.7.3 Experimental and Calculated Electronic Absorption of $\text{Tp}^{\text{Cum,Me}}_2\text{Zn}(\text{SQ-mPh-NN})$ Compared to $\text{Tp}^{\text{Cum,Me}}_2\text{Zn}(\text{SQ-pPh-NN})$

The room temperature solution electronic absorption spectra were acquired by the Shultz group, and we collected the corresponding variable temperature electronic absorption data. Figure 2.61 shows the solution electronic absorption spectra for both $\text{Tp}^{\text{Cum,Me}}_2\text{Zn}(\text{SQ-mPh-NN})$

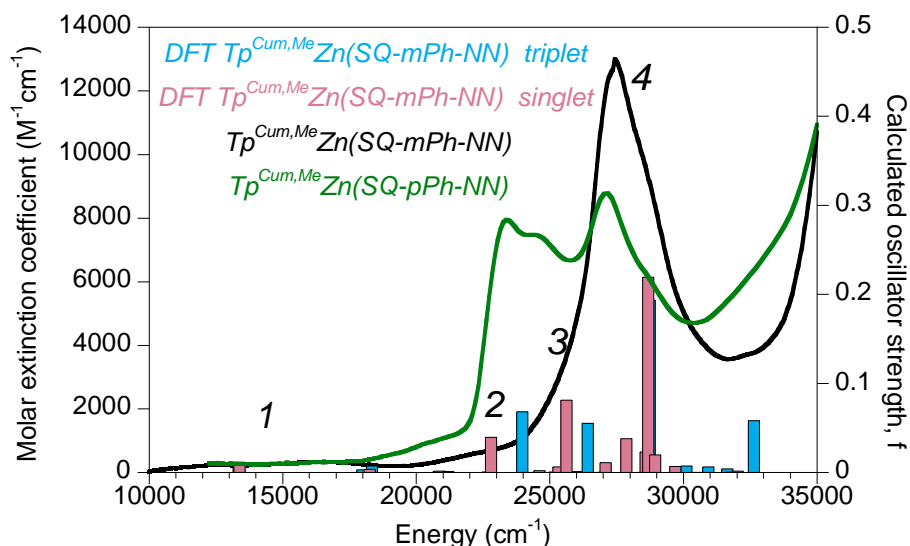
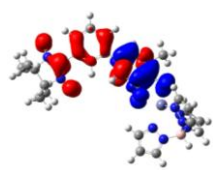

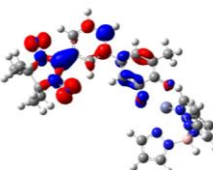
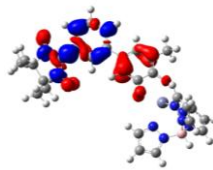
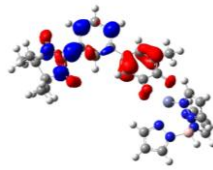
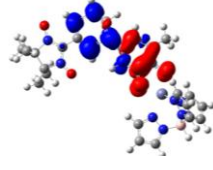


Figure 2.61: Overlay of room temperature electronic absorption spectra for $\text{Tp}^{\text{Cum,Me}}\text{Zn}(\text{SQ-mPh-NN})$ (black) and $\text{Tp}^{\text{Cum,Me}}\text{Zn}(\text{SQ-pPh-NN})$ (green) as well as DFT-calculated oscillator strengths (blue bars = triplet $\text{Tp}^{\text{Cum,Me}}\text{Zn}(\text{SQ-mPh-NN})$, pink bars = singlet $\text{Tp}^{\text{Cum,Me}}\text{Zn}(\text{SQ-mPh-NN})$).

(black) and $\text{Tp}^{\text{Cum,Me}}\text{Zn}(\text{SQ-pPh-NN})$ (green), as well as the DFT-calculated oscillator strengths for the $\text{Tp}^{\text{Cum,Me}}\text{Zn}(\text{SQ-mPh-NN})$ triplet (blue bars) and singlet (pink bars). We notice that the donor-acceptor charge transfer band seen in $\text{Tp}^{\text{Cum,Me}}\text{Zn}(\text{SQ-pPh-NN})$ at $\sim 23000 \text{ cm}^{-1}$ is absent in $\text{Tp}^{\text{Cum,Me}}\text{Zn}(\text{SQ-mPh-NN})$, and in fact there are no intense bands for $\text{Tp}^{\text{Cum,Me}}\text{Zn}(\text{SQ-mPh-NN})$ at energies below $\sim 26000 \text{ cm}^{-1}$. TDDFT calculations indicate that the donor-acceptor charge transfer band is still at the same energy as in $\text{Tp}^{\text{Cum,Me}}\text{Zn}(\text{SQ-pPh-NN})$, but with severely reduced oscillator strength. Table 2.16 summarizes the electronic absorption band assignments for $\text{Tp}^{\text{Cum,Me}}\text{Zn}(\text{SQ-mPh-NN})$, which are largely based on the triplet $\text{Tp}^{\text{Cum,Me}}\text{Zn}(\text{SQ-mPh-NN})$ DFT results since the room temperature absorption spectrum is dominated by the triplet spectrum.

Table 2.16: DFT band assignments for $\text{Tp}^{\text{Cum,Me}}\text{Zn}(\text{SQ-mPh-NN})$.

Band	DFT Energy (cm^{-1}) f		Assignment	Electron density difference map
1	~13400	0.010	[SQ-Ph-NN HOMO \rightarrow SQ SOMO] β + [SQ-Ph-NN HOMO-1 \rightarrow SQ SOMO] β	
	~18300	0.007	[SQ-Ph-NN HOMO-1 \rightarrow SQ SOMO] β - [SQ-Ph-NN HOMO \rightarrow SQ SOMO] β - [SQ-Ph-NN HOMO-1 \rightarrow NN SOMO] β	
2	~22800	0.040*	[NN-Ph, Ph \rightarrow SQ SOMO]	* from the singlet TDDFT
	~24000	0.068	[NN _{inplane} \rightarrow SQ SOMO] - [SQ SOMO \rightarrow NN-Ph LUMO]	
3	~26400	0.055	[NN-Ph HOMO \rightarrow NN-Ph LUMO] α - [SQ-Ph-NN HOMO-1 \rightarrow NN- Ph LUMO] β + [SQ-Ph-NN HOMO \rightarrow NN-Ph LUMO] β	
4	~28000	0.069	[NN SOMO \rightarrow NN-Ph LUMO] α + [SQ-Ph-NN HOMO-1 \rightarrow NN SOMO] β	
	~28700	0.193	[SQ SOMO \rightarrow Phe ₂ LUMO+1]	

Band 1 is a very broad, weak band at $\sim 11000 - \sim 16000 \text{ cm}^{-1}$, which clearly has more than one contributing transition. We assigned band 1 as the positive and negative linear combinations of a transition from the delocalized (β) SQ-Ph-NN HOMO and HOMO-1 to the SQ SOMO, mixed with a transition from the delocalized (β) SQ-Ph-NN HOMO-1 to the NN SOMO. Band 2 is also a weak band with a molar extinction coefficient of $\sim 700-800 \text{ M}^{-1}\text{cm}^{-1}$. This band occurs at the energy that the intense D-A CT band is observed for in $\text{Tp}^{\text{Cum,Me}}\text{Zn}(\text{SQ-pPh-NN})$. Band 2 has contributions from calculated transitions of both the singlet and triplet, namely NN-Ph \rightarrow SQ SOMO and Ph \rightarrow SQ SOMO promotions from the $\text{Tp}^{\text{Cum,Me}}\text{Zn}(\text{SQ-mPh-NN})$ singlet, and the D-A CT SQ SOMO \rightarrow NN-Ph LUMO and $\text{NN}_{\text{inplane}} \rightarrow$ SQ SOMO promotions from the $\text{Tp}^{\text{Cum,Me}}\text{Zn}(\text{SQ-mPh-NN})$ triplet. This mixed triplet transition that has both NN \rightarrow SQ and SQ \rightarrow NNPh charge transfer character leads to an overall transition with little net charge transfer character as the EDDM for band 2 in Table 2.16 shows. The computed oscillator strength for the meta-phenyl bridged DBA biradical DA CT band ($f = 0.068$) is less than a quarter of that in the para-phenyl bridged DBA biradical DA CT band ($f = 0.312$). Experimentally, the DA CT band is reduced by about a factor of 10 in $\text{Tp}^{\text{Cum,Me}}\text{Zn}(\text{SQ-mPh-NN})$ compared to $\text{Tp}^{\text{Cum,Me}}\text{Zn}(\text{SQ-pPh-NN})$. Band 3 is experimentally observed as an unresolved band in the $\sim 25000 - 26000 \text{ cm}^{-1}$ region, and is assigned as β type transitions from the SQ-Ph-NN HOMO and HOMO-1 to the NN-Ph LUMO, and as an α transition from the NN-Ph HOMO to the NN-Ph LUMO. Band 4 is a broad, intense band observed experimentally in the $\sim 26000 - 30000 \text{ cm}^{-1}$ region, and has several contributions to its intensity. The first transition contributing to band 4 is

calculated at $\sim 28000\text{ cm}^{-1}$ and has an EDDM that is very similar to band 3. Rather than a direct HOMO \rightarrow LUMO transition like band 3, the transition is described as a sum of NNPhSQ HOMO-1 \rightarrow NN SOMO and NN SOMO \rightarrow NNPh LUMO one-electron promotions, which effectively results in a NN-Ph-SQ HOMO-1 \rightarrow NN-Ph LUMO charge transfer description. The main component of band 4 is calculated at $\sim 28700\text{ cm}^{-1}$ with an oscillator strength of 0.193 and is assigned as a SQ SOMO \rightarrow Ph e_2 LUMO+1 **donor** \rightarrow **bridge** one-electron promotion.

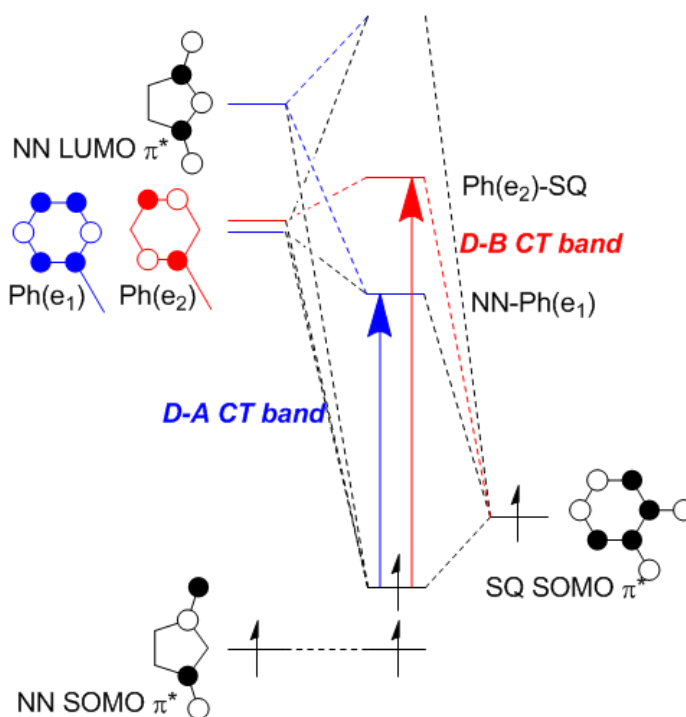


Figure 2.62: Molecular orbital diagram depicting electronic transitions in $\text{Tp}^{\text{Cum,Me}}_2\text{Zn}(\text{SQ-mPh-NN})$.

Thus, what we observe experimentally and computationally for $\text{Tp}^{\text{Cum,Me}}_2\text{Zn}(\text{SQ-mPh-NN})$ is a strong SQ SOMO \rightarrow Ph e_2 charge transfer band, which is made possible in

$\text{Tp}^{\text{Cum,Me}}\text{Zn}(\text{SQ-mPh-NN})$ due to the fact the semiquinone now attaches to the Ph e_2 orbital via a phenyl carbon atom that has a non-zero orbital coefficient (Figure 2.62). The band intensity for the SQ SOMO \rightarrow NN-Ph e_1 band in $\text{Tp}^{\text{Cum,Me}}\text{Zn}(\text{SQ-mPh-NN})$ is dramatically reduced, and all of the charge transfer character is of the SQ SOMO \rightarrow Ph e_2 variety.

2.7.4 Variable-Temperature Electronic Absorption of $\text{Tp}^{\text{Cum,Me}}\text{Zn}(\text{SQ-mPh-NN})$

Variable temperature electronic absorption data has been collected for $\text{Tp}^{\text{Cum,Me}}\text{Zn}(\text{SQ-mPh-NN})$ and is shown in Figure 2.63. The data shows very tight isosbestic points, which indicate the presence of only two interconverting species (i.e. the singlet and triplet ground states). We also notice that the temperature dependence of several bands is quite pronounced. This is due to both the small singlet-triplet gap ($2J = -64 \text{ cm}^{-1}$), as well as the fact that the state gaining population with increasing temperature is the triplet (and has three-fold degeneracy). The variable temperature spectrum shows that the band at 27550 cm^{-1} decreases in intensity, while bands at 24880 cm^{-1} and 31350 cm^{-1} gain intensity as the temperature increases.

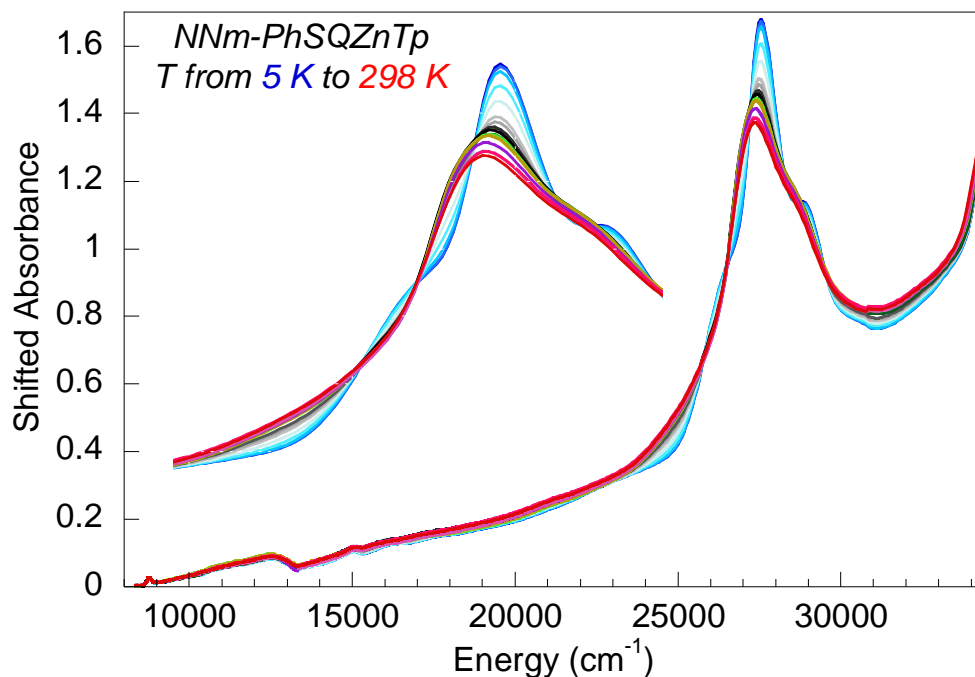


Figure 2.63: Variable-temperature electronic absorption of $\text{Tp}^{\text{Cum,Me}}\text{Zn}(\text{SQ-mPh-NN})$ as a film in a polystyrene matrix. Temperatures range from 5 K (blue) to 298 K (red), and spectra were normalized to a polystyrene reference peak at $\sim 6000 \text{ cm}^{-1}$.

We have plotted the intensities of these bands as a function of temperature and overlaid them on a plot with the expected Boltzmann populations for a singlet ground state with a 64 cm^{-1} singlet-triplet energy gap, show in Figure 2.64. The temperature-dependence of these absorption bands fits the expected temperature dependent of a singlet transition (27550 cm^{-1}) and triplet transition (24880 cm^{-1} , 31350 cm^{-1}) in $\text{Tp}^{\text{Cum,Me}}\text{Zn}(\text{SQ-mPh-NN})$ well, and confirms that the magnetic susceptibility data and solution absorption data are well-correlated.

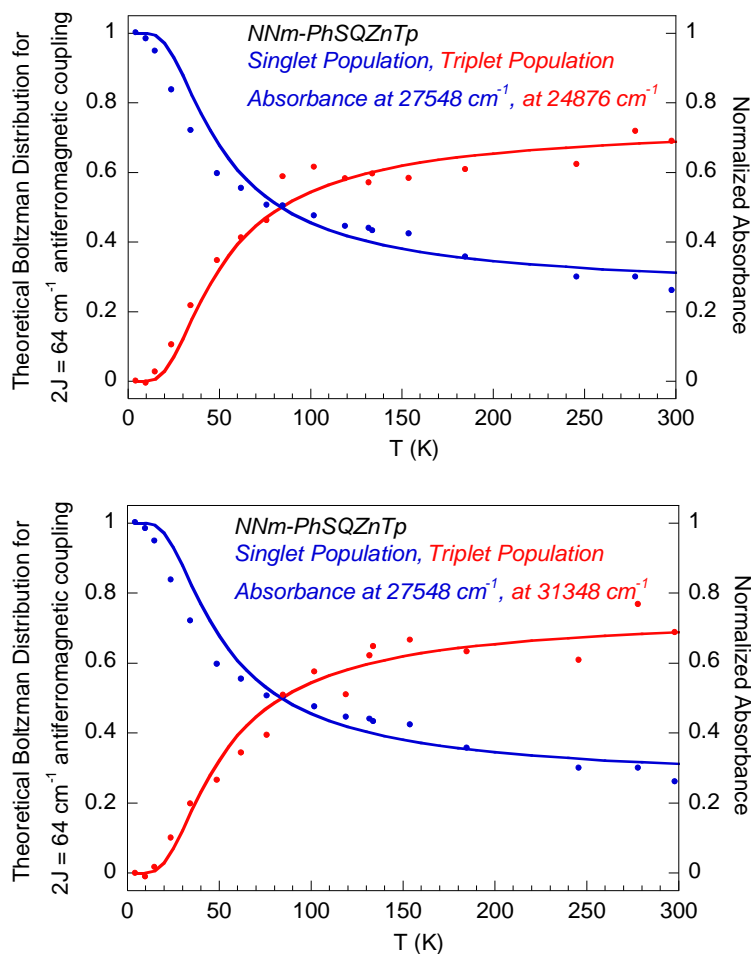


Figure 2.64: Theoretical Boltzmann populations and electronic absorption intensities as a function of temperature for $\text{Tp}^{\text{Cum,Me}}\text{Zn}(\text{SQ-mPh-NN})$.

The inset in Figure 2.63 expands on part of the temperature-dependent region of the spectrum to show that there are several additional features that gain and lose intensity as a function of temperature, and we can separate the singlet and triplet spectra as we have for the biphenyl- and bithiophene-bridged DBA biradicals. The resulting “pure” singlet and triplet spectra are shown in Figure 2.65. We notice that the singlet spectrum is very similar to the triplet spectrum, and that the triplet transitions in general occur at

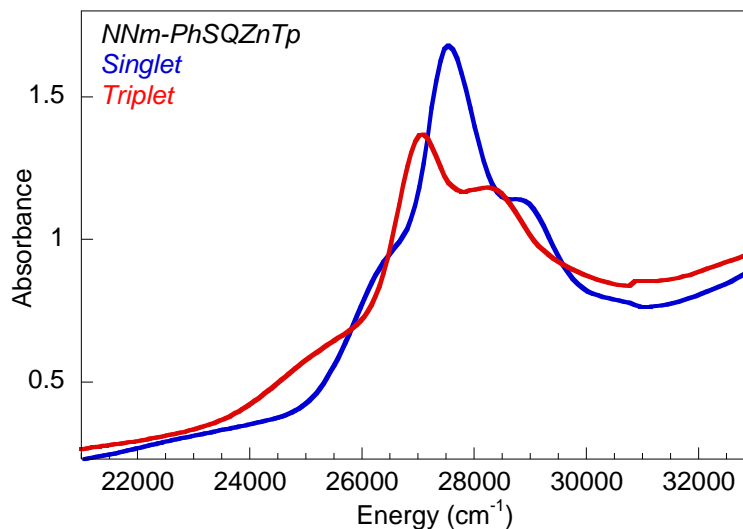


Figure 2.65: singlet (blue) and triplet (red) electronic absorption spectra for $\text{Tp}^{\text{Cum,Me}}\text{Zn}(\text{SQ-mPh-NN})$.

lower energies than the singlet transitions. The band shifts of the most intense peaks (~ 27500 and ~ 28700 cm^{-1}) for the singlet are shifted by $400\text{-}500$ cm^{-1} relative to the triplet (~ 27100 and ~ 28200 cm^{-1}). This is a considerably smaller shift than what was observed for the ferromagnetically coupled biphenyl ($\sim 1100\text{-}1200$ cm^{-1}) and bithiophene ($\sim 1800\text{-}1900$ cm^{-1}) DBA biradicals. Since the electronic absorption spectra indicate that most transitions are at lower energies for the triplet compared to the singlet in $\text{Tp}^{\text{Cum,Me}}\text{Zn}(\text{SQ-mPh-NN})$, we are left with the question of how it is that the biradical has a singlet ground state. In order to explore that issue, we consider the various lower energy excited states that may contribute to the ground state via configurational interaction.

2.7.5 Configuration Interaction States Contributing to the Antiferromagnetic Coupling in $\text{Tp}^{\text{Cum,Me}}\text{Zn}(\text{SQ-mPh-NN})$

Figure 2.66 shows the ground configuration and various low-energy excited configurations of singlet and triplet $\text{Tp}^{\text{Cum,Me}}\text{Zn}(\text{SQ-mPh-NN})$. In the ground

configuration, the unpaired electrons reside in the NN SOMO and SQ SOMO and can be aligned either parallel for the triplet or antiparallel for the singlet. Starting from those ground state configurations, we consider several one-electron promotions and their resultant excited configurations. An electron can be promoted from the HOMO to the NN SOMO (EC 1), the SQ SOMO (EC 2), or to the LUMO (ECs 3 and 4, depending on whether the α or β HOMO electron is promoted). The promotion of the electron from the SQ SOMO to the LUMO, i.e. the donor-acceptor charge transfer transition, EC 5.

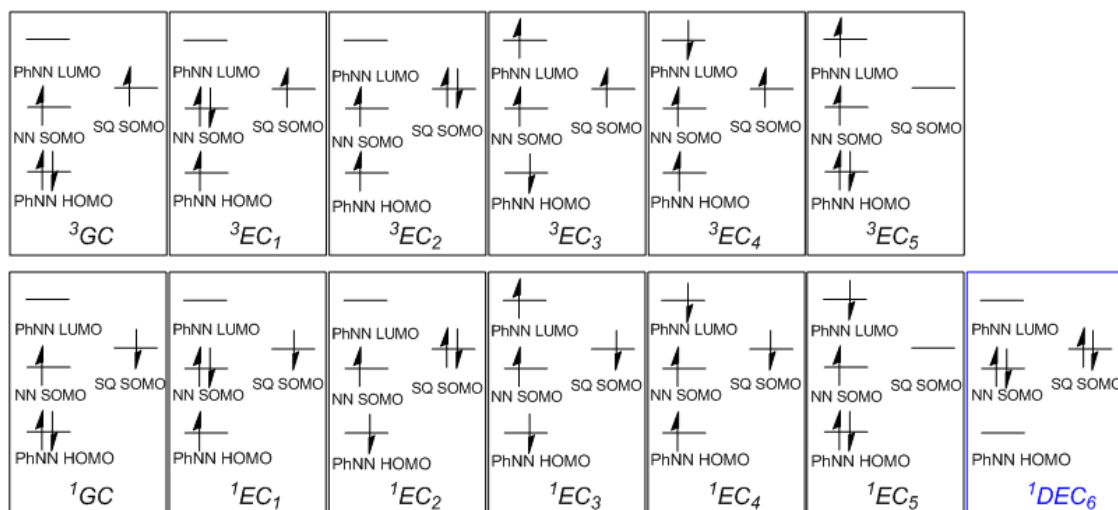


Figure 2.66: Various configurations for singlet and triplet $\text{Tp}^{\text{Cum,Me}_7}\text{Zn}(\text{SQ-mPh-NN})$.

Excited configuration 6 represents a double excitation from the HOMO into each of the SOMO orbitals, and is only accessible from the singlet ground state since the HOMO has one α and one β electron which cannot be promoted into two SOMOs that both have α electrons as is the case for the ground state triplet. The ${}^1\text{DEC}_6$ is thus unique to the ${}^1\text{GC}$, and CI mixing of this excited configuration into the ${}^1\text{GC}$ would preferentially stabilize the singlet ground state.

DFT calculations show evidence of a strong exchange splitting for the α and β components of the NN-Ph HOMO. For the NN-Ph HOMO the energy difference between the α and β orbitals are 4828 cm^{-1} for B = p-Ph (triplet), 6145 cm^{-1} for B = m-Ph (triplet and bss). We note that $\text{Tp}^{\text{Cum,Me}}\text{Zn}(\text{SQ-mPh-NN})$ has a more spin-polarized NN-Ph HOMO than $\text{Tp}^{\text{Cum,Me}}\text{Zn}(\text{SQ-pPh-NN})$. A large spin polarization in DFT-calculated spin-unrestricted molecular orbitals is indicative of that orbital possessing an unpaired spin, or, in the case of a doubly-occupied HOMO or unoccupied LUMO, of that orbital interacting strongly with an orbital that contains an unpaired electron. The spin-polarization in the DFT orbitals thus supports the idea that for the para-phenyl bridged D-B-A biradical promotions from the SQ SOMO to the NN-Ph LUMO are important, while for the meta-phenyl bridged D-B-A biradical transitions out of the NN-Ph HOMO are important.

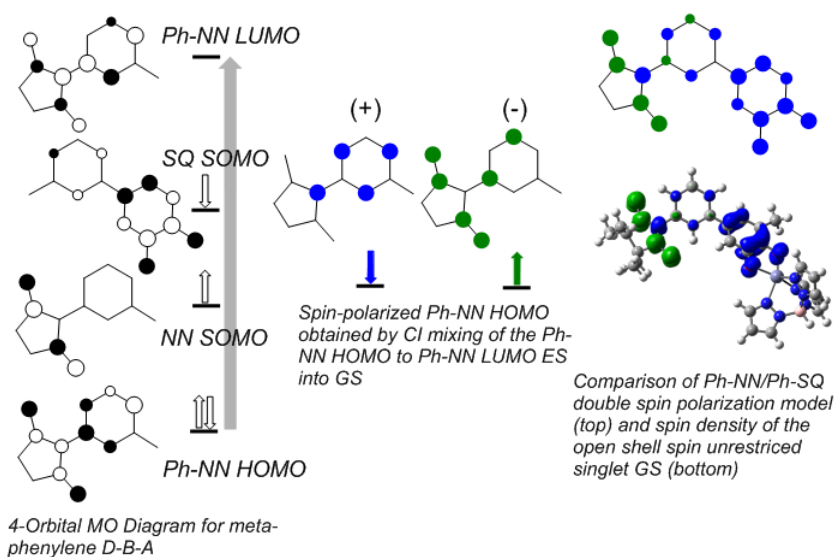


Figure 2.67: Spin polarization mechanism leads to antiferromagnetic coupling in $\text{Tp}^{\text{Cum,Me}}\text{Zn}(\text{SQ-mPh-NN})$

Complete-active space self-consistent field (CASSCF) calculations were carried out for $\text{Tp}^{\text{Cum.Me}}\text{Zn}(\text{SQ-mPh-NN})$, which treats this problem using a multiconfigurational approach. In CASSCF the spin restricted orbitals are used to build configurations, and the energies of the ground- and/or excited states of the molecule are optimized with respect to the coefficients of the configurations that contribute to each state as well as the molecular orbital coefficients of the spin restricted orbitals. When we consider an active space that includes only the NN SOMO and SQ SOMO the singlet-triplet energy splitting is calculated to be approximately zero (triplet stabilized by 0.4 cm^{-1}). However, if we increase the active space to include the NN-Ph HOMO and NN-Ph HOMO-1 (which are partitioned into an NN and a Ph orbital during the CASSCF calculation), the NN SOMO, SQ SOMO, NN-Phe₁ LUMO, and the Phe₂ LUMO+1, we obtain a singlet-triplet ground state splitting of 35 cm^{-1} with the singlet ground state at lower energy. The configurations that contribute to the singlet ground state (above the 1% cutoff) are 85% ^1GC , 7% $^3\text{EC}/^4\text{EC}$, and 3% of an excited configuration that is a double-excitation of both electrons from the NN-Ph HOMO to the NN-Ph LUMO.

Computational results thus point to the large spin polarization of the NN-Ph HOMO and contributions of the NN-Ph HOMO \rightarrow NN-Ph LUMO transition to the ground state. CI mixing of the NN-Ph HOMO \rightarrow NN-Ph LUMO excited state into the ground state leads to the observed spin polarization of the NN-Ph HOMO. Figure 2.67 describes how the spins in the NN-Ph HOMO are distributed into the two components of the spin polarized NN-Ph HOMO to minimize the energy due to exchange interactions of the two components of the spin-polarized NN-Ph HOMO in the NN-Ph fragment with the

NN SOMO in the NN-Ph fragment and SQ SOMO in the Ph-SQ fragment. This double spin polarization mechanism⁹⁶ accounts for the spin density distribution calculated for the open shell spin unrestricted singlet of $\text{Tp}^{\text{Cum,Me}}\text{Zn}(\text{SQ-mPh-NN})$ and for the antiferromagnetic coupling observed in the ground state of $\text{Tp}^{\text{Cum,Me}}\text{Zn}(\text{SQ-mPh-NN})$.

We can combine what we have learned thus far from the various experimental and computational methods used to determine the most important contributions to antiferromagnetic coupling in $\text{Tp}^{\text{Cum,Me}}\text{Zn}(\text{SQ-mPh-NN})$. We have learned from electronic absorption spectroscopy that most of the observed optical transitions are $\sim 500 \text{ cm}^{-1}$ lower in energy for the triplet than for the singlet. The excited state configurations corresponding to those transitions can mix with the respective singlet or triplet ground state configurations, where both the singlet and triplet ground states would be stabilized by the mixing. However, the triplet ground state will always be stabilized more since the triplet excited states are at lower energy. Figure 2.66 shows that there is one configuration, the double-excitation $^1\text{DEC}_6$, that can only be derived from a singlet ground state and has not counterpart in the triplet. This $^1\text{DEC}_6$ singlet excited state can configurationally mix with the ^1GC , thus stabilizing the singlet ground state. Beyond the contributions of any ^1DEC CI mixing into the ^1GC , for which no specific evidence, spin polarization of the NN-Ph HOMO and a double spin polarization mechanism of the components of the spin-polarized NN-Ph HOMO with the spins in both of the SOMOs accounts for the antiferromagnetic ground state of $\text{Tp}^{\text{Cum,Me}}\text{Zn}(\text{SQ-mPh-NN})$. CASSCF computations clearly indicate the importance of EC 3 and EC 4 to the observed ground state antiferromagnetic exchange interaction. Computational evidence from an

examination of the DFT-calculated α and β orbitals and CASSCF calculations thus support the importance of the double-spin polarization in the meta-conjugated D-B-A biradical.

2.8 Computational Studies of a Mixed-Valent Ligand Co Complex

2.8.1 Longe-Range Ferromagnetic Coupling in NN-Ph-SQCo^{III}(py)₂Cat-Ph-NN

Co-SQ/Cat-complexes have been studied previously in terms of their temperature-dependent Co^{II}(SQ)₂-Co^{III}(SQ-Cat) valence tautomerism and ligand valence delocalization.⁹⁷⁻¹⁰¹ Recently, symmetric Co^{II}(SQ)₂-Co^{III}(SQ-Cat), Co^{III}(NN-SQ,NN-Cat), and Co^{III}(NN-Ph-SQ,NN-Ph-Cat) complexes containing pendant NN radicals and axial pyridine ligands were synthesized.^{14,102} The [SQ-Ph-NN]⁻ ligand was used to construct the complex NN-Ph-SQCo^{III}(py)₂Cat-Ph-NN where Cat (catecholate) is the one-electron reduced form of SQ (semiquinone), and the axial ligands to Co are py = pyridine.¹⁴ This complex possesses mixed-valent ligands and is an organic analogue of the Creutz-Taube ion,¹⁰³ which features mixed valent metal ions. Our mixed-valent ligand complex could potentially exist as a class II valence delocalized compound (i.e. NN-Ph-SQCo^{III}(py)₂Cat-Ph-NN \leftrightarrow NN-Ph-CatCo^{III}(py)₂SQ-Ph-NN) with some energy barrier to interconvert the two forms.^{5,6} Alternatively, the energy barrier to interconversion could be zero, leading to a class III delocalized description.^{5,6} Figure 2.68 shows this SQ/Cat \leftrightarrow Cat/SQ delocalization. The green arrow represents the itinerant electron, which in the class III limit is delocalized between the SQ and Cat moieties.

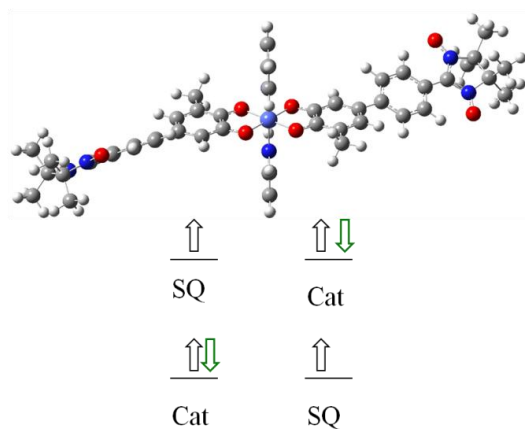


Figure 2.68: The SQ-Co^{III}-Cat core of NN-Ph-SQCo^{III}(py)₂Cat-Ph-NN.

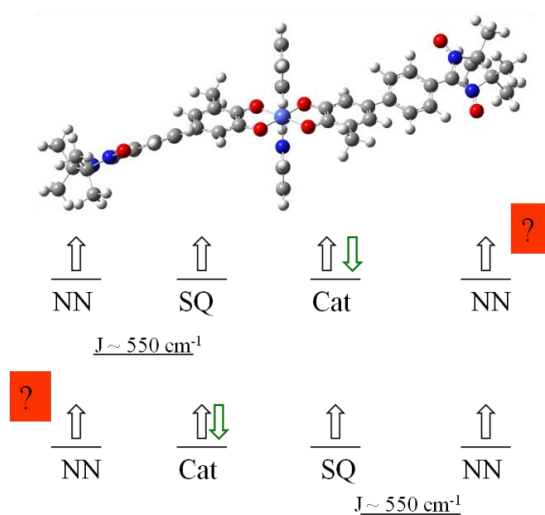


Figure 2.69: Stationary and itinerant electrons in NN-Ph-SQCo^{III}(py)₂Cat-Ph-NN.

If we extend our consideration beyond the SQ-Co^{III}-Cat core to the full [SQ-Ph-NN]⁻ ligand the electronic structure of NN-Ph-SQCo^{III}(py)₂Cat-Ph-NN becomes more complex. This results from the fact that the unpaired electron in the core can interact with the unpaired electrons on the nitronyl nitroxide radicals, as shown in Figure 2.69. From previous studies of the [SQ-Ph-NN]⁻ ligand, we know that the NN and SQ spins are

strongly ferromagnetically coupled with $J \sim 550 \text{ cm}^{-1}$. The NN spin of the $[\text{Cat-Ph-NN}]^{2-}$ ligand could be spin up and ferromagnetically coupled to the NN-SQ $S = 1$ unit leading to an $S = 3/2$ ground state for the molecule, or spin down and antiferromagnetically coupled to the NN-SQ $S = 1$ leading to an $S = 1/2$ ground state for the molecule, or uncoupled.

Experimental magnetic susceptibility measurements show that NN-Ph-SQCo^{III}(py)₂Cat-Ph-NN possesses an $S = 3/2$ ground state, indicating that the itinerant electron is delocalized over the core and thus polarizes both of the localized NN radicals spin up. This is remarkable since the $S = 3/2$ ferromagnetically coupled ground state of NN-Ph-SQCo^{III}(py)₂Cat-Ph-NN represents long-range spin coupling in a molecular system over a distance of 23 Å (when measured from the nitrogen of one NN to either nitrogen on the second NN). The experimental data supporting this ferromagnetic coupling, as well as a VBCI mechanism that uses excited state configurations to explain the ground state magnetic properties of NN-Ph-SQCo^{III}(py)₂Cat-Ph-NN have been published.¹⁴ Here we will describe the electronic structure of this molecule including the optimized geometry, spin density distribution, frontier molecular orbitals and calculated electronic transitions that support the interpretation of the experimental data and proposed VBCI mechanism for the $S = 3/2$ ground state.

2.8.2 Description of Delocalization in NN-Ph-SQCo^{III}(py)₂Cat-Ph-NN

The DFT-optimized geometry of $S = 3/2$ NN-Ph-SQCo^{III}(py)₂Cat-Ph-NN is shown in Figure 2.68 and Figure 2.69. While the optimized structure has C_2 symmetry, it approximates C_{2h} symmetry when considering the geometry of the planar SQ/Cat-Co-

SQ/Cat dioxolene core. If the NN-Ph and Ph-SQ dihedral angles are constrained to be planar, the molecule optimizes to C_{2h} structure that has an additional mirror plane containing the NN-Ph-SQ/Cat-Co-SQ/Cat-Ph-NN rings. Table 2.17 shows the dihedral angles and selected bond distances of the fully optimized structure of NN-Ph-SQCo^{III}(py)₂Cat-Ph-NN. These ring dihedral angles are nearly the same as in Tp^{Cum,Me}Zn(SQ-Ph-NN), where only the NN-Ph dihedral is slightly smaller.

Table 2.17: Selected dihedral angles and bond distances for fully optimized the NN-Ph-SQ/Cat-Co-SQ/Cat-Ph-NN.

	SQ/Cat-Ph-NN (a)	SQ/Cat-Ph-NN (b)
NN-Ph dihedral (°)	4.7	4.9
Ph-SQ/Cat dihedral (°)	32.2	32.3
O-Co bonds (Å)	1.896, 1.896	1.895, 1.893

Figure 2.70 shows the calculated spin density distribution for the quartet ground state at the DFT-optimized geometry of NN-Ph-SQCo^{III}(py)₂Cat-Ph-NN. We observe that the spin density is delocalized over the entire molecule. An unpaired spin is localized on each of the nitronyl nitroxide radicals while the third unpaired spin is delocalized over the

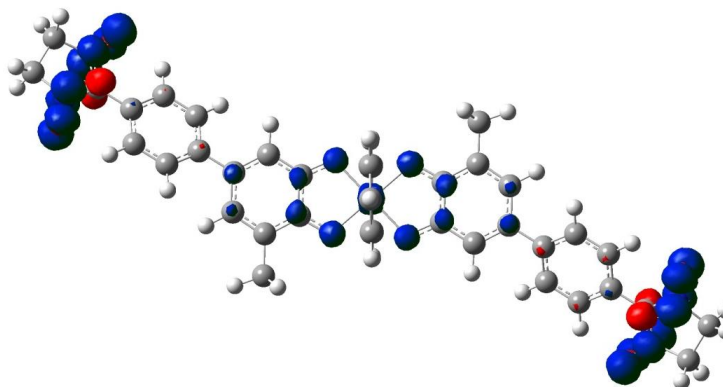


Figure 2.70: DFT-calculated spin density distribution of NN-Ph-SQCo^{III}(py)₂Cat-Ph-NN for an $S = 3/2$ ground state where blue represents positive spin density and red negative spin density at an contour isovalue of 0.005.

SQ-Co^{III}(pyr)₂-Cat dioxolene core. The summed spin population for SQ/Cat-Ph-NN(a) is 1.482, for SQ/Cat-Ph-NN (b) the summed spin populations are 1.444, and for the Co-dioxolene core the summed spin population is 0.074. Renormalizing so that the sum of the spin populations for both SQ/Cat-Ph-NN ligands sums to 100%, we obtain a spin distribution of 50.65% and 49.35% for the ligands. This delocalized spin density supports a class III valence delocalized system.

In the class III valence delocalized limit, the energy barrier between SQ ↔ Cat interconversion has disappeared, and the ligand wavefunctions combine as positive and negative linear combinations to form new delocalized wavefunctions akin to that of a homo-diatomic molecule. The normalized wavefunctions will be $\Psi_{bond} = \frac{1}{\sqrt{2}}(\Phi_a + \Phi_b)$ and $\Psi_{antibond} = \frac{1}{\sqrt{2}}(\Phi_a - \Phi_b)$ (Eq. 21),^{5,6,14} where in C_{2h} symmetry the bonding combination will be ‘ungerade’ with respect to inversion and the antibonding combination ‘gerade’ with respect to inversion. Thus, in place of a Cat → SQ IVCT (intervalence charge transfer) we expect to observe a $\Psi_u \rightarrow \Psi_g$ transition that is both spin- and dipole allowed. This transition is observed experimentally at 3500 cm⁻¹.¹⁴ Time-dependent DFT calculations confirm this assignment, where the lowest energy HOMO → LUMO transition for NN-Ph-SQCo^{III}(py)₂Cat-Ph-NN is calculated at 3711 cm⁻¹ with an oscillator strength of $f = 0.1659$ originating from a delocalized ‘ungerade’ bonding molecular orbital and going into the delocalized ‘gerade’ antibonding molecular orbital (Figure 2.71).

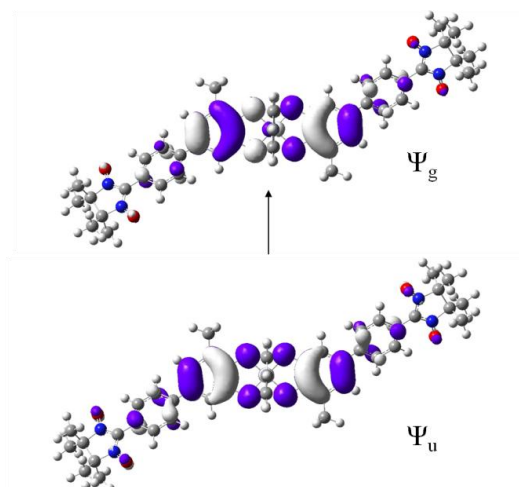


Figure 2.71: Lowest-energy TD-DFT-calculated transition of NN-Ph-SQCo^{III}(py)₂Cat-Ph-NN at 3711 cm⁻¹.

Figure 2.71 shows that the Ψ_u HOMO has no metal since none of the Co d-orbitals have the appropriate symmetry to mix with the dioxolene p orbitals. However, the Ψ_g LUMO wavefunction possesses ~3% Co d_{xz} character, where the xz plane is the plane perpendicular to the plane containing the pyridine rings and the plane containing the SQ/Cat-Co-Cat/SQ core. Thus the calculations indicate that the low-lying excited state accessed by the $\Psi_u \rightarrow \Psi_g$ transition, has both a small amount of metal character and a small amount unpaired spin density on the Co metal center.

2.9 Conclusions

The systematic computational and experimental studies of the D-B-A biradicals studied here have allowed us to extend our knowledge of the various factors that influence bridge-mediated donor-acceptor coupling in a molecular system. The fact that

NN-B-SQ are ground state biradicals allows for more a more detailed experimental investigation of donor-acceptor electronic communication than is possible for photogenerated radical pairs. We were thus able to obtain data from a variety of experimental techniques including electronic absorption spectroscopy (including variable-temperature electronic absorption), EPR spectroscopy, resonance Raman spectroscopy, and magnetic susceptibility measurements.

DFT bonding calculations indicate that the nitronyl nitroxide acceptor orbital mixes very strongly with an unoccupied phenyl bridge orbital forming a delocalized NN-Ph LUMO acceptor orbital with almost equal NN and Ph orbital character. The highly delocalized nature of the NN-Ph LUMO together with the near-planarity of the NN and Ph rings allows for strong acceptor-bridge interactions. A spin polarization mechanism on NN results negative spin density on the NN carbon atom that bonds directly to the Ph bridge, and this allows for the delocalization of negative spin density from the acceptor to the Ph bridge. The phenyl bridge thus carries both negative spin from the acceptor and positive spin from the donor, and the net spin on the bridge depends on both donor-bridge and acceptor-bridge dihedral angles.

We found that there are two mechanisms of increasing spin density on the NN acceptor in the DBA biradicals: delocalization of positive spin from the donor to the acceptor via the bridge, and delocalization of negative spin from the acceptor to the bridge. The delocalization of positive spin from the donor to the acceptor via the bridge is the result of an excited state configuration in which the electron from the donor SOMO is promoted to the acceptor LUMO, and is reflected experimentally in the donor \rightarrow acceptor

charge transfer band observed in the electronic absorption spectrum. The delocalization of negative spin from the acceptor to the bridge depends on both acceptor-bridge planarity, and the spin polarization within the NN acceptor. Spin polarization of the nitronyl nitroxide results from configurational mixing of a NN(Bridge) HOMO \rightarrow NN(Bridge) LUMO charge transfer state into the ground state. Regardless of how the net positive spin density is increased on the acceptor, a larger net positive spin density on the acceptor increases the single-site exchange with the unpaired spin in the SOMO of the acceptor and thus leads to a larger ferromagnetic donor-acceptor coupling. Thus the bridge not only serves as an extended π network used to delocalize spin from the donor to the acceptor, but also actively contributes to donor-acceptor ferromagnetic coupling via the acceptor-bridge interactions described above.

Both contributions to the positive spin density on the NN acceptor are reflected in the experimental isotropic nitrogen hyperfine coupling constants, as well as the computed Mulliken spin populations of the nitrogens on NN. Computed Mulliken spin populations of the nitronyl nitroxide nitrogens show an excellent linear correlation to both the experimentally measured isotropic nitrogen hyperfine coupling constants and experimental J values (where $2J$ is the singlet-triplet ground state gap energy). The high degree of correlation between computations and experimental data for a variety of donor-acceptor and donor-bridge-acceptor biradicals, as well bridge-acceptor radicals, validates the electronic structure description of these molecules.

In a linear correlation plot of computed and experimental spin density on the NN nitrogens (using computations and EPR data, respectively), we see that a thiophene

bridge is expected to promote stronger donor-acceptor ferromagnetic coupling than a phenyl bridge, and that the donor-acceptor coupling decreases as either the length of the bridge is extended or the π -overlap between donor, acceptor, and bridge is disrupted by increasing dihedral angles between the rings. Interestingly, a xylene-bridged DBA biradical that possesses large dihedral angles between donor and bridge as well as bridge and acceptor has smaller spin populations on the NN nitrogens than NN-bridge radicals that have no donor at all. This again underscores the non-trivial contribution of the acceptor-bridge interaction in these molecules.

In a systematic study of perturbations to donor-acceptor ferromagnetic coupling in the DBA biradicals, we extended previous studies of the $\text{Tp}^{\text{Cum,Me}}\text{Zn}(\text{SQ-NN})$ and $\text{Tp}^{\text{Cum,Me}}\text{Zn}(\text{SQ-Ph-NN})$ biradicals in terms of:

1. Changes in the electronic nature of the bridge from phenyl to thiophene,
2. Changes in the coupling distance between donor and acceptor by changing phenyl to biphenyl and thiophene to bithiophene
3. Changes in the π overlap between donor, bridge, and acceptor by introducing sterically-hindered phenyl-bridge analogues
4. Changes in the donor-bridge-acceptor conjugation by changing p-Ph to a m-Ph bridge

Electronic structure calculations indicated the ability of the thiophene bridge to promote stronger donor-acceptor ferromagnetic coupling has two contributions: a greater donor-bridge overlap, due to a small donor-bridge dihedral angle, and a more intense and lower energy donor-acceptor charge transfer band, due to a greater donor-bridge

delocalization in the SQ SOMO. In both phenyl- and thiophene-bridged biradicals an unoccupied bridge orbital strongly mixes with the NN LUMO acceptor orbital. In the thiophene-bridged D-B-A biradical the SQ SOMO also mixes significantly with a lower-lying occupied thiophene bridge orbital, increasing donor-bridge delocalization and bringing the donor orbital energetically closer to the NN-bridge acceptor orbital.

When the bridge length is extended, the donor-acceptor coupling is reduced exponentially, but due to the large donor-acceptor coupling in these D-B-A biradicals we still observe significant ferromagnetic donor-acceptor coupling for both the biphenyl- and bithiophene bridge. Singlet-triplet ground state energy gaps of that magnitude are thermally accessible by variable-temperature electronic absorption spectroscopy, and we observe temperature-dependent changes in the absorption spectra that correspond to temperature-dependent populations of the triplet and singlet ground states. With a known value for the gap energy ($2J$) from magnetic susceptibility measurements, we can calculate the expected Boltzmann populations of both the singlet and triplet ground states for any given temperature. This allows us to separate the singlet and triplet component spectra from the variable-temperature electronic absorption data. We observe that the singlet and triplet spectra are very similar, but the triplet spectra are shifted to lower energies with respect to the singlet spectra in D-B-A molecules with conjugated bridges. The combined analysis of magnetic susceptibility data and variable-temperature electronic absorption data thus allows us to obtain a measure of the energy splitting of the triplet and singlet excited states as well as the triplet and singlet ground states.

We examined the role of the bridge in donor-acceptor coupling in the excited state during the donor \rightarrow acceptor charge transfer using resonance Raman spectroscopy. We found that the bridge is directly involved in the donor \rightarrow acceptor charge transfer since specific bridge modes were the most resonantly-enhanced vibrations in the spectrum. The excited state distortions of the donor and bridge in the D-A CT state mirror those that are expected when electron density is removed from the SQ SOMO and added to the NN-Ph LUMO. For the biphenyl bridged D-B-A biradicals, we observe resonance enhancement of a similar symmetric bridge distortion along the direction of the donor-acceptor axis under the D-A CT band that is delocalized over the SQ donor and both phenyl rings. Resonance Raman data collected in resonance with the D-A CT bands for the thiophene- and bithiophene-bridged D-B-A biradicals show that the resonance Raman spectra are dominated by thiophene-bridge based vibrational modes.

Sterically-hindered bridges were studied, and we found that a phenyl bridge methylated close to the SQ donor is very similar to $\text{Tp}^{\text{Cum,Me}}\text{Zn}(\text{SQ-Ph-NN})$ in terms of the optimized geometry and electronic structure of the molecule. Methylation of a phenyl ring carbon that is close to the NN acceptor results in a disruption of NN-Ph π overlap, and consequently results in a reduction in the intensity for the D-A CT band. These molecules are expected to have reduced donor-acceptor ferromagnetic coupling.

When the conjugation of the phenyl bridge to the donor and acceptor is changed from para-Ph to meta-Ph, the ferromagnetic coupling is severely disrupted, and a small antiferromagnetic coupling between donor and acceptor is observed. The electronic absorption spectrum shows that the D-A CT band is greatly reduced in intensity, and a

higher energy band has been assigned as a donor-bridge CT band unique to the meta-conjugated phenyl bridge. Interestingly, the component singlet and triplet electronic absorption spectra obtained from the variable-temperature electronic absorption data show that the triplet transitions are at about 500 cm^{-1} lower in energy compared to the singlet transitions, and would thus be expected to stabilize the triplet ground state preferentially. We attribute antiferromagnetic coupling in the meta-bridged D-B-A biradical to a double-spin polarization mechanism between the SQ SOMO of the SQ-Ph fragment, the spin-polarized HOMO of the NN-Ph fragment, and the NN SOMO of the NN-Ph fragment. The spin-polarization in the NN-Ph HOMO arises from CI mixing of a NN-Ph HOMO \rightarrow NN-Ph LUMO excited state into the ground state, which is supported computationally by the DFT-calculated molecular orbital description of $\text{Tp}^{\text{Cum,Me}}\text{Zn}(\text{SQ-mPh-NN})$ and CASSCF calculation for $\text{Tp}^{\text{Cum,Me}}\text{Zn}(\text{SQ-mPh-NN})$. The antiferromagnetic coupling observed in $\text{Tp}^{\text{Cum,Me}}\text{Zn}(\text{SQ-mPh-NN})$ is thus the result of a balance between the attenuation of the SQ SOMO \rightarrow NN-Ph LUMO donor-acceptor charge transfer contribution in favor of a SQ SOMO \rightarrow Phe₂ LUMO+1 donor-bridge charge transfer contribution, and the presence of the double-excitation $^1\text{DEC}_6$ state exclusive to the singlet.

Long-range exchange coupling was achieved by using the strongly ferromagnetically coupled $[\text{SQ-Ph-NN}]^-$ ligand in the construction of a symmetric mixed-valent ligand Co complex. The mixed-valent ligands are the $[\text{SQ-Ph-NN}]^-$ biradical ligand and its one-electron reduced catecholate form. The mixed valent ligands in this complex appear to be class III valence delocalized. The itinerant electron has been shown

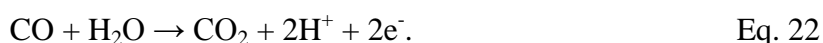
to spin polarize the NN spins on each sides of the molecule resulting in NN-NN coupling over a 23 Å range.

CHAPTER 3

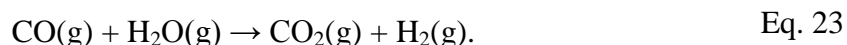
3. SPECTROSCOPIC AND COMPUTATIONAL STUDIES OF THE
BIMETALLIC ENZYME ACTIVE SITE OF CARBON MONOXIDE
DEHYDROGENASE AND A SERIES OF ACTIVE SITE MODELS THAT
ARE ELECTRONIC STRUCTURE AND GEOMETRY MIMICS OF THE
ACTIVE SITE

3.1 Introduction

Carbon Monoxide Dehydrogenase (CODH) is an enzyme involved in the aerobic metabolism of the soil-bacterium *Oligotropha carboxidovorans*, and is the first metalloenzyme with a heterobimetallic active site containing Mo and Cu.¹⁰⁴⁻¹⁰⁶ CODH catalyzes the oxidation of carbon monoxide to carbon dioxide¹⁰⁷ (Eq. 22):



This enzyme-catalyzed reaction is very similar to the exothermic water gas-shift reaction, used in industrial processes at high temperatures in the production of hydrogen, which in turn is needed to produce ammonia.¹⁰⁸ The use of transition metal catalysts, such as Cu, allows the reaction to proceed at lower temperatures of 175-300 °C¹⁰⁹ :



The CO concentration in the atmosphere is the result of a balance between various natural and anthropogenic sources and sinks. It has been estimated in the 1970's that

contributions from natural processes that contribute to the balance of the CO concentration in the atmosphere are at least an order of magnitude larger than anthropogenic sources of CO.^{110,111} More recently, estimates of anthropogenic contribution to annual global CO emissions have been much higher at 60% versus emissions from natural processes of 40% of the annual total.¹¹² Amongst the natural sources of CO are the world's oceans as well as the oxidation of methane by hydroxyl radicals in the troposphere. Oxidation of CO by hydroxyl radicals to CO₂ in the troposphere, diffusion into the stratosphere, as well as the biological activity of the soil are also major sinks of CO in the atmosphere. Various literature reports point to the importance of CO removal from the atmosphere by biological activity in the soil, where one estimate for the amount of CO removed from the surface of the soil in the U.S. is 569 million metric tons per year.¹¹⁰ More recently the contribution of the soil as a CO sink has been estimated as 10% of the global total of 2600 ± 600 million tons per year.¹¹² While the literature reflects uncertainty in the contribution of each factor, and many processes can act simultaneously as sources and sinks depending on the geographic location and thus environmental conditions,¹¹²⁻¹¹⁴ the biological activity of the soil contributes to the changing global CO balance. Understanding the metabolic processes of such soil bacteria is therefore of relevance, both in terms of the environment and human health. CO toxicity is attributed to the fact that CO binds tightly to the metal ion centers in various physiological enzymes including hemoglobin and cytochrome oxidase.^{115,116}

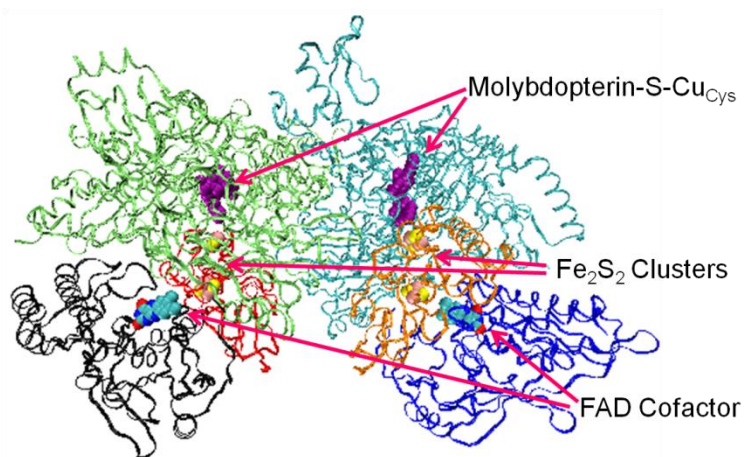


Figure 3.1: X-ray crystal structure of the oxidized CODH enzyme (PDB 1N5W).¹¹⁷

CODH is a 277 kDa dimer of heterotrimers, where each heterotrimer consists of a small (18 kDa, red & orange), medium (30 kDa, blue & black), and large (89 kDa, green & cyan) subunit¹⁰⁶ (Figure 3.1). The large subunit holds the [MoSCu] active site, which resides in the interior of the protein and is accessible to CO via a hydrophobic substrate access channel. As carbon monoxide gets oxidized at the active site, the enzyme active site is reduced by two electrons, and the electrons are channeled through the protein to its surface via two iron-sulfur clusters (small subunit) and a flavin adenine dinucleotide (FAD, medium subunit).

CODH is classified in the xanthine oxidase family as a molybdenum hydroxylase,^{118,119} and has an active-site [MoSCu] unit that is unique in biology since it is the first known heterobimetallic enzyme active site to feature Mo and Cu.¹⁰⁴⁻¹⁰⁶ The active site of CODH (Figure 3.2) has an approximately square pyramidal geometry, where the molybdenum ion is coordinated by a pyranopterin via its dithiolene group. The molybdenum is further coordinated by axial oxo group, an equatorial oxo- or hydroxyl

ligand, and a sulfido ligand bridging to a Cu ion. The Cu is coordinated to a cysteine residue of the protein chain itself.

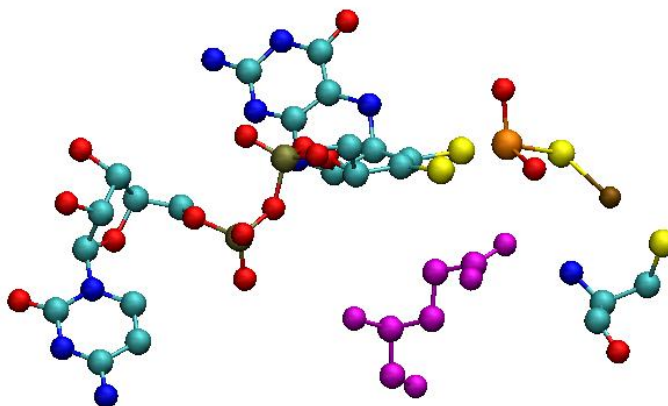


Figure 3.2: Active site geometry of oxidized CODH (PDB 1N5W).¹¹⁷ Oxygen = red, carbon = cyan, sulfur = yellow, nitrogen = blue, phosphorus = bronze, molybdenum = orange, glutamate residue = purple.

Structural determinations of CODH have been made via X-ray absorption (Mo and Cu K-edge) spectroscopy¹⁰⁵ and X-ray diffraction methods.¹¹⁷ The equatorial oxygen ligand is modeled as an oxo-ligand by X-ray absorption methods (1.74 Å bond length) and as a hydroxy-ligand by X-ray diffraction methods (1.87 Å). Structural data also shows a glutamate residue, which could act as a general base, in close proximity to the molybdenum center and the hydroxyl-ligand (where the glutamate-equatorial oxygen distance in the oxidized enzyme is 2.99 Å). An inhibitor-bound (n-butyl isocyanide) structure has been obtained, showing that the inhibitor inserts itself into the sulfur-copper bond, where the Mo to Cu distance becomes 5.07 Å.¹¹⁷ The hetero bi-metallic [MoSCu] unit, the electronic communication between the molybdenum and the copper ions, and its

relevance to the catalytic mechanism of CO oxidation form the focus of our interest in CODH.

The mechanism for CO oxidation in the CODH active site is still under debate. Two very different mechanisms have been proposed^{104,117,120} for substrate oxidation, and are shown in Figure 3.3 and Figure 3.4. The mechanism in Figure 3.3 is based on the inhibitor-bound structure that has been obtained,¹¹⁷ and postulates the insertion of the substrate into the S-Cu bond. Following electron transfer from the substrate to the active site the product is formed, followed by the reformation of the S-Cu bond. Note that this mechanism requires various bond breaking and bond formation steps, including the breaking of the S-Cu bond for substrate insertion, and more importantly, the breaking of a S-C bond for product release and the restoration of the active site geometry. This mechanism was supported computationally by Siegbahn *et al.*¹²⁰

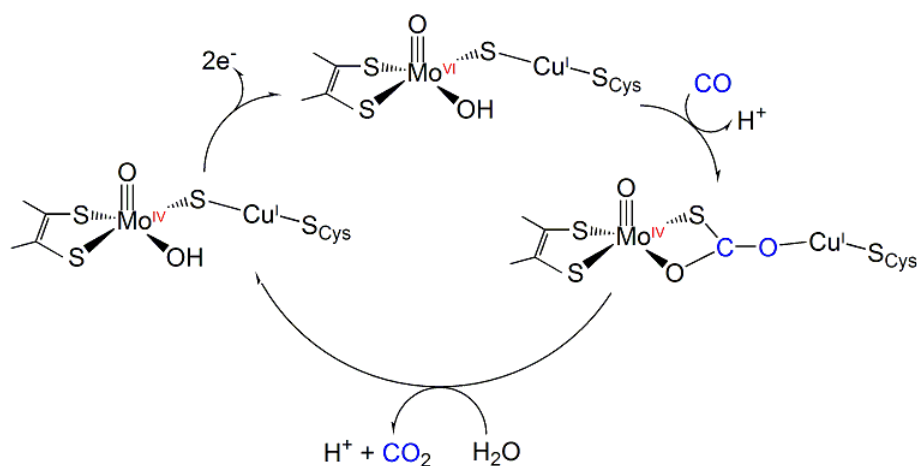


Figure 3.3: Inhibitor-based mechanism for CODH.

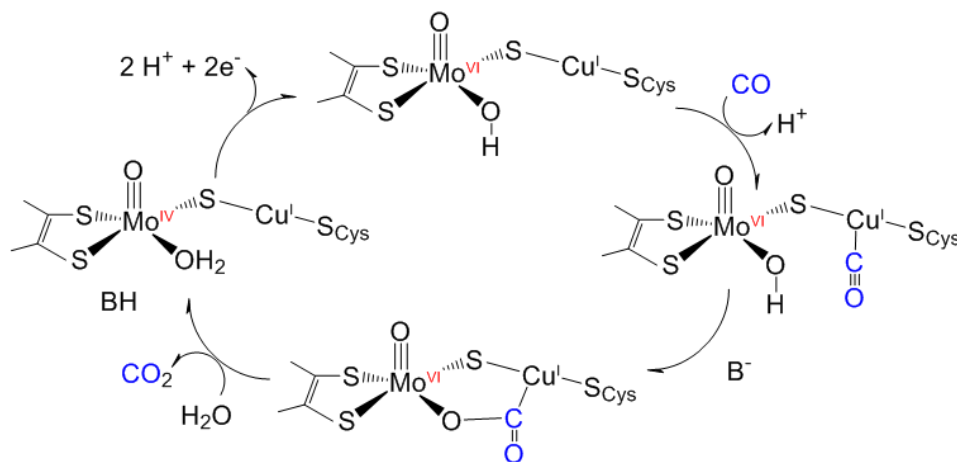


Figure 3.4: Alternative mechanism for CODH.

In an alternative mechanism proposed by Hofmann *et al.*¹⁰⁴ (Figure 3.4) the [MoSCu] unit is preserved during catalysis. Upon substrate binding to the Cu, nucleophilic attack on the carbonyl carbon occurs by the deprotonated hydroxyl ligand, followed by electron transfer through the [MoSCu] unit to the molybdenum center, and release of the CO₂ product. The equatorial coordination of molybdenum can be filled by a water ligand, which is subsequently deprotonated to a hydroxyl ligand. Thus the two proposed mechanisms differ significantly in the role of the [MoSCu] unit for catalysis, and we propose that the covalency of the [MoSCu] unit in the active site supports electron transfer from the substrate to the molybdenum via the Cu and μ -sulfido.

Studies of enzymatic activity confirm the catalytic importance of the [MoSCu] unit where activity assays of CODH show that an intact Mo-S-Cu unit is absolutely necessary for activity. When the oxidized active enzyme is treated with KCN, sulfur and

copper are lost with a simultaneous loss of enzyme activity. To recover activity, both the bridging sulfur and the copper have to be restored.¹²¹

An analysis of bond distances, bond energies, stretching frequencies and theoretical calculations of M-CO bonding in the literature focuses on Cu(I) and Ag(I) carbonyls,¹²² and notes that both Cu(I) and Ag(I) carbonyls have relatively little CO π backbonding. While Ag has little M to CO π backbonding due to the weak and long Ag-C bonds it forms that reduce the π overlap, Cu is in the regime of having just enough M to CO π backbonding to bind CO but bind it reversibly.¹²² This balance can presumably be exploited and modulated by the enzyme active site for both substrate binding and product release. Recently substitution of the copper at the active site by silver has been shown to lead to a functional form of the enzyme, albeit with a five-fold slower rate.¹²³

The presence of the two Fe₂S₂ cluster cofactors in the enzyme makes the CODH active site difficult to access by electronic absorption spectroscopy, as the spectrum is dominated by Fe₂S₂ absorption. Thus experimental techniques that target the paramagnetic metals of the active, such as electron paramagnetic resonance spectroscopy (EPR) and magnetic circular dichroism (MCD) spectroscopy, are useful tools for probing the active site directly and understanding its electronic structure. A paramagnetic form of the enzyme has been observed by EPR, and the EPR spectrum reveals that the unpaired spin resides on the molybdenum but is significantly delocalized onto the copper as evidenced by the large observed Cu-hyperfine.^{116,124,125} Recent published work reports g-values of 2.001, 1.960, and 1.955, as well as a Cu hyperfine of 117, 164, and 133 MHz, where the enzyme was reduced with either sodium dithionite, or by incubation with CO.

When ^{13}C O was used to reduce the enzyme, a broadening of the Cu hyperfine lines was observed indicating that the labeled carbon is associated with the signal-giving reduced enzyme active site.¹²⁵ Tris- D_2O buffer was used to check for proton hyperfine and thus elucidate the nature of the equatorial ligand. No line broadening was observed, so that the authors concluded that the equatorial ligand may be an oxo rather than hydroxy ligand. At the modulation amplitude of 5 Gauss, which was used for the data acquisition, and considering the linewidths of the experimental hyperfine signal, it is not likely that proton hyperfine of a smaller magnitude (~ 10 MHz or less) would be observed even if it were present.

Paramagnetic model compounds that replicate the $\text{O}_{\text{ax}}\text{MoSCu}$ structure found in the enzyme active site have been synthesized (Figure 3.14).¹²⁶ These CODH active site models produce an EPR signal that is very similar to that of the enzyme, and are thus thought to mimic the electronic structure of the enzyme active site in addition to its geometry.¹²⁶ The study of these CODH active site model compounds allows us to study the electronic structure of the active site via electronic absorption spectroscopy (in addition to paramagnetic methods such as EPR and MCD) since the synthetic models lack the spectroscopic interference of the iron-sulfur clusters. Synthetic models are also useful tools for investigating how small perturbations to the active site effect the observed electronic structure of the active site and the covalency across the $[\text{MoSCu}]$ unit. Other efforts towards synthetic model compounds for the CODH active site have been made,^{127,128} including a $[(\text{dithiolate})\text{Mo}^{\text{VI}}\text{OS}_2\text{CuAr}]^{2-}$ model compound, in which

Mo and Cu are bridge by two sulfido bridges. There are, however, no other CODH models that preserve the [MoSCu] unit of the active site.

3.2 Experimental Details

3.2.1 Sample Handling

In order to avoid exposing the samples to higher temperatures, which cause sample degradation over time, samples were refrigerated at 4° C sealed in a vial with inert atmosphere until the day of the EPR experiment. All sample preparation was done in an anaerobic environment in a glove box. Butyronitrile (BuCN) was chosen as the solvent, since the samples were stable and soluble in butyronitrile, and the solvent forms a good glass at $T < 95\text{K}$ for low temperature EPR experiments. Butyronitrile was fractionally distilled with KOH to remove any moisture, and freeze/pump/thawed repeatedly to remove oxygen. Samples dissolved in BuCN to give a clear golden-brown solution.

3.2.2 Multifrequency Electron Paramagnetic Resonance Spectroscopy (EPR)

EPR spectra were acquired on a Bruker model ESP 300 spectrometer with an X-band Bruker ER041XG microwave bridge (9.38 GHz) and a Q-band Bruker ER051QG microwave bridge (34 GHz) microwave source. Frozen glass spectra were acquired at 20K for X-band and 80K for Q-band in a liquid helium flow Oxford ESR 910 cryostat. The model compounds very found to be extremely sensitive to moisture and air (oxygen), so that EPR samples in closed tubes were frozen immediately after removal from the glove box. Spectral simulations were carried out using the EasySpin⁸³⁻⁸⁷ spectral simulation software.

3.2.3 Density Functional Calculations

Spin unrestricted gas-phase geometry optimizations for all compounds were performed at the density functional level of theory using the Amsterdam Density Functional suite (ADF 2012.01)¹²⁹⁻¹³⁴ and the ORCA software package (An ab initio, DFT and semiempirical SCF-MO package, Version 2.8-20 September 2010).^{79,135} Input files were prepared using the molecule builder function in the Gaussview⁷¹ software package. DFT bonding calculations and EPR calculations carried out in ORCA employed a B3LYP^{66,67} hybrid exchange-correlation functional and a TZVP basis sets for all atoms. Scalar relativistic all-electron calculations used the zeroth order regular approximation (ZORA),¹³⁶ and radial integration accuracies for Mo and Cu were increased as recommended for heavy atoms. Calculations of the electronic structure and absorption and MCD spectra of the CODH synthetic models in ADF used a ZORA scalar relativistic Hamiltonian, triple-zeta polarized basis with small core, and PBE¹³⁷ generalized-gradient approximation functional. The 100 lowest energy singlet electronic transitions and the 50 lowest energy C-term MCD transitions¹³²⁻¹³⁴ were calculated. While we used the B3LYP functional, which is a well-established functional for molecular calculations, for most our calculations, the functionality for calculating MCD transitions available in ADF had not yet been extensively tested for the B3LYP functional at the time we started our calculations.^c The results of spectral calculations with the PBE functional showed that for both the heterobimetallic enzyme active site studied in chapter Three and the rhenium dimers studied in chapter Four, the ADF calculations using the PBE functional provided

^c Private communication: B. Stein, University of New Mexico, with ADF staff.

very good agreement with experimental absorption and MCD spectra. Other researchers have reported good performance for the calculated geometries of 1st, 2nd, and 3rd row transition metal complexes for the PBE functional in particular.¹³⁸

The synthetic models were represented completely as shown in Figure 3.14 (neutral with one unpaired electron), whereas the enzyme active site was represented by a Mo(V) with an axial oxo ligand and equatorial ene-1,2-dithiolate ligand, equatorial oxo or hydroxy ligand, and equatorial sulfido bridging to Cu-SCH₃ to represent the Cu-S_{Cys} of the active site (variable negative charge, one unpaired electron). For investigations of the effect of the OMoOH dihedral angle select bond and dihedral angles were constrained to crystal structure values (oxidized enzyme) in the geometry optimization in order to observe the effect of the OMoOH clearly.

3.2.4 Electronic Absorption Spectroscopy

Butyronitrile solvent was dried carefully by refluxing the solvent over K₂CO₃ for several hours, followed by a fractional distillation and anaerobic collection of the solvent using a small vacuum. The butyronitrile was freeze-pump-thawed for a minimum of five cycles to remove oxygen, and then transferred into the anaerobic glovebox, where sample preparation took place. Electronic absorption spectra of the compounds were acquired anaerobically as butyronitrile room-temperature solutions on a U-4100 Hitachi spectrophotometer with a measureable wavelength range of 185-3300 nm using a deuterium lamp (for the UV wavelength range) and a 50 W tungsten-halogen lamp (for the NIR/Vis wavelength range) as the light sources. A photomultiplier tube (for the

UV/Vis wavelength range) and a cooled type PbS detector (for the NIR wavelength range) were used as detectors. Scan speeds were 120 nm/min in the UV/Vis and 300 nm/min in the NIR, the detector switch was at 850 nm, lamp switch at 325 nm, slit-width was 2 nm in the UV/Vis, variable in the NIR. A baseline was acquired with the same cuvette using butyronitrile. The cuvettes used for measurements were masked quartz cells manufactured by Starna Cells featuring a screw cap top with a silicone rubber septum. Both electronic absorption and MCD spectra were resolved with Gaussian bands using Grams/AI, version 7.02 (Thermo Galactic, 1991-2002).

3.2.5 MCD Spectroscopy

Frozen solution samples used for magnetic circular dichroism spectroscopy were prepared in as anaerobic a fashion as possible. Samples were dissolved in the dry, deoxygenated solvent in the glove box and drawn up into a syringe. The syringe was inverted and additional nitrogen gas was pulled up into the syringe to provide an “anaerobic blanket.” The syringe needled was then sealed within a thick rubber septum before removal from the glove box. In a nitrogen-purged glovebag a dewar filled with liquid nitrogen was set-up, and the assembled MCD cell (see Appendix 6.2.5 for additional details) was precooled for ~20-30 seconds in liquid nitrogen (a strategy suggested by Dr. Regina Peter Mtei in the Kirk research group). The pre-cooling of the MCD sample cell prior to injection of the sample solution proved necessary as the viscosity of the BuCN solvent is such that the sample will just simply flow out of the assembled MCD cell as it is being injected when the cell is not pre-cooled. After the cell was pre-cooled, the rubber seal from the syringe holding the sample solution was

removed, and the sample was injected quickly into the cell. It is necessary to inject the sample quickly in order to prevent the syringe needle from getting frozen stuck into the injection port of the sample cell. The sample cell was lowered into the liquid nitrogen immediately after sample injection, and maintained frozen and submersed in liquid nitrogen even during the mounting of the sample cell onto the MCD sample rod.

This caution in sample preparation and in maintaining sample integrity was motivated by the fact that we knew the samples to be extremely air-sensitive, and further by the fact that while for EPR sample degradation was immediately apparent by the loss/degradation of the Cu hyperfine signal, such a corresponding “tell” in the MCD spectrum was unknown to us. This motivated us to check the state of the sample after the MCD experiment by electronic absorption spectroscopy. By comparing strictly anaerobic solution electronic absorption spectra with aerobic spectra of the model compound solutions, we noticed several key shifts in absorption peaks. Upon removal of the frozen solution sample from the MCD cryostat, it was immediately submersed into liquid nitrogen and maintained frozen during the mounting onto the electronic absorption liquid nitrogen cryostat. Electronic absorption spectra of the post-MCD frozen solution samples were thus obtained and compared to the anaerobic solution spectra of the compounds.

The MCD system includes two JASCO spectropolarimeters; JASCO J-810 for the UV/Vis wavelength range (165 nm - 900 nm), and JASCO J-730 for the NIR range (800 nm – 2000 nm). The J-810 unit utilizes a 150 W xenon lamp as a light source and a head-on photomultiplier tube as a detector. The J-730 unit utilizes a 150 W halogen lamp as a light source and a liquid-nitrogen cooled InSb detector (Infrared Associates, IS-2.0

series). The Oxford superconducting magnet and cryostat unit have a magnetic field range of 0-7 T, and a temperature range of the cryostat is 1.5 – 300 K. Spectra were acquired at 5 K, 10 K and 20 K and magnetic fields of 0 T (baseline) and 7 T. The depolarization of the circularly polarized light was quantified using a nickel tartrate standard solution before acquisition of the data. The depolarization of the nickel tartrate CD signal due to the presence of the sample is calculated by calculating the CD intensity range at a maximum (371 nm) and minimum (400 nm) with the nickel tartrate located before and after the sample with respect to the light source. Depolarizations ranged from 1-7% (Ar = OPh 3%, Ph-3tBu 4%, Ph-2sBu 7%, and Ph-4sBu 1%), and are very acceptable for the frozen solution samples.

3.3 Computational Studies of the Enzyme Active Site

3.3.1 Equatorial Oxo Ligand vs. Equatorial Hydroxy Ligand

As discussed above, the nature of the equatorial ligand remains disputed in the literature, and has been proposed to be either an oxo or hydroxyl ligand. We have explored this question computationally by computing the EPR parameters of the enzyme active site for both choices of equatorial ligand. We model the active site as shown in Figure 3.5, where the cysteine that coordinates Cu is modeled by $[\text{SCH}_3]^-$, and the pyranopterin by an ene-1,2-dithiolene. This computational model of the CODH enzyme active site preserves the chemical nature of the metal coordination up to and including the second coordination sphere for both Mo and Cu. We were not interested in calculating the energy or vibrational modes of this molecule, for which the full pyranopterin ligand

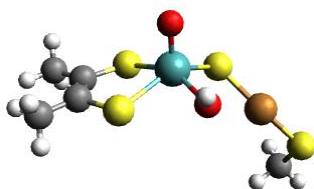


Figure 3.5: CODH active site computational model with an equatorial hydroxo ligand. molybdenum (aqua), sulfur (yellow), copper (bronze), carbon (gray), oxygen (red), hydrogen (white).

should be included. Our interest lies in calculating the EPR parameters and SOMO wavefunction, and thus leaving the non-spin bearing parts of the extended ligand off is reasonable. The SOMO wavefunction is not expected to change significantly between a model with a methylated ene-1,2-dithiolene and a model with a full pyranopterin ligand.^d

Computed and experimental EPR parameters are presented in Table 3.1, and show that an equatorial oxo ligand has g -values that are quite inconsistent with the observed experimental g -values for the reduced CODH. Calculations show that g_{\min} for the equatorial-oxo enzyme active site is **much** lower than experimentally observed. Such low values of g_{\min} have been reported previously for $\text{cis-}[\text{Mo}^{\text{V}}\text{O}_2]^+$ compounds,¹³⁹ and can be explained by the energetic proximity of the spin bearing Mo d-orbital to the other empty Mo d-orbitals in $\text{cis-}[\text{Mo}^{\text{V}}\text{O}_2]^+$ systems.

To confirm that the values of the g -tensor for the dioxo enzyme active site model are not an artifact of the high charge on the molecule (-3), we replaced methyl groups with ammonia groups in the DFT calculation leading to a neutral species. The g -tensor for this neutral dioxo enzyme active site model was calculated as $g_{\min} = 1.908$, $g_{\text{mid}} = 1.986$, g_{\max}

^d Private communication with Dr. Yang, University of New Mexico, 2013.

= 1.999^e indicating that the very low g -values for g_{\min} are associated with the equatorial oxo ligand and not the charge on the molecule. Values for g_{mid} and g_{max} are in reasonable agreement with experimental value for both an equatorial oxo and hydroxy ligand.

Table 3.1: Calculated EPR parameters for the enzyme active site model featuring either an oxo or a hydroxy ligand as compared to published experimental¹²⁵ enzyme EPR parameters.

	g_{\min}	g_{mid}	g_{max}	$A_{\text{iso}}(\text{Cu})$ in MHz
Experiment: reduced CODH	1.955	1.960	2.001	138
DFT: equat. oxo	1.901	1.951	1.997	209
DFT: equat. hydroxy*	[1.950, 1.964]	[1.955, 1.968]	[2.006, 2.019]	[188, 246]
DFT: equat. hydroxyl OMoOH 30°	1.954	1.959	2.012	228

* calculated EPR parameters vary depending on the value of the OMoOH dihedral angle; values in parentheses are the range of values for all values of the OMoOH dihedral angle

The Hamiltonian describing the unpaired electron in the SOMO wavefunction of the CODH active site and the resulting EPR parameters has at its simplest form three terms⁸¹:

$$\hat{H} = g_e \beta_e H \cdot \hat{S} + a \cdot \hat{I} \cdot \hat{S} + \frac{\mu_n \mu_e}{r^3}, \quad \text{Eq. 24}$$

where the first term describes the interaction of the magnetic dipole of the spin = 1/2 electron with the external magnetic field H , and terms describing the interaction of the nuclear spin (I , where $I \neq 0$) with the electron spin (S) in the presence of a magnetic field.⁸¹ The interaction of the nuclear spin with the electron spin has two main components, an isotropic term (the second term of Eq. 24), and a dipolar term (the third

^e The Lande g -factor is a unitless quantity.

term of Eq. 24). The isotropic term depends on the magnetic parameters of the nucleus and is proportional to the electron density directly at the nucleus ($\Psi(0)$).⁸¹

$$a \propto \frac{\mu_I}{I} |\Psi(0)|^2 \quad \text{Eq. 25}$$

The isotropic nuclear-electron spin interaction is described by the isotropic hyperfine coupling constant (A_{iso}) of the unpaired spin with a given $I \neq 0$ nucleus and reflects the amount of electron density in an s-orbital of the nucleus in the SOMO wavefunction. The dipolar term (the third term of Eq. 24) describes the distance dependence ($\frac{1}{r^3}$) of the electron- and nuclear dipoles in the SOMO wavefunction, and thus carries information about the shape of the spin-bearing metal orbital (i.e. d-orbital).

The value of the isotropic Cu hyperfine coupling constant is overestimated in the DFT calculations for both ligands, and there are no significant differences between the isotropic Cu hyperfine between an equatorial oxo or hydroxy ligand. It is perhaps not surprising that the magnitudes of the DFT-calculated isotropic Cu hyperfine coupling constants are not accurate, as Cu has a very large intrinsic isotropic hyperfine coupling constant, and thus the Cu hyperfine coupling constants are exquisitely sensitive to even small differences in the s-orbital character in the SOMO wavefunction. Specifically, the Cu hyperfine coupling for a full unpaired electron in an s-orbital is ~5995 MHz.⁹⁵

Table 3.2 shows that the Cu hyperfine tensor is very isotropic, both experimentally and in the DFT calculations of the enzyme active site. This has been shown to be due to the Cu-s orbital character in the SOMO wavefunction of the enzyme active site, where DFT calculations revealed a strong π^* interaction between Mo and S in the SOMO, and a

pseudo- σ^* interaction between S and Cu in the SOMO. The Cu d-orbital character in the SOMO was shown computationally to be predominantly d_{xz} and d_{z^2} in character, where the importance of the d_{z^2} orbital character for Cu in the SOMO wavefunction lies in the fact that in the effective $C_{\sigma v}$ symmetry around Cu d_{z^2} and s-orbital mixing is symmetry allowed. The Cu character d_{z^2} in the SOMO wavefunction thus contributes to the large observed isotropic Cu hyperfine coupling via symmetry-allowed and s-orbital mixing.¹²⁶

Table 3.2 shows that while the magnitude of the isotropic Cu hyperfine differs between calculation and experiment, the nature of the hyperfine tensor, i.e. a large isotropic component with a small orthorhombic dipolar component, is the same between experiment and calculation, and between the calculation with an equatorial oxo ligand and an equatorial hydroxo ligand. The isotropic hyperfine coupling constant is calculated as $A_{iso} = \frac{1}{3} (A_1 + A_2 + A_3)$, and the dipolar contribution to the hyperfine as $A_{1,dip} = A_1 - A_{iso}$.⁸¹

Table 3.2: Isotropic and dipolar components of the Cu hyperfine tensor.

Cu hyperfine coupling constants (MHz)	A_1, A_2, A_3	A_{iso}	$A_{dip1}, A_{dip2}, A_{dip3}$
Experiment: reduced CODH ¹²⁵	117, 164, 132	138	+21, -26, +6
DFT: equat. oxo	206, 208, 212	209	+3, +1, -3
DFT: equat. hydroxyl OMoOH 30°	219, 224, 240	228	+9, +4, -12

For a hydroxo ligand all three g-values are in agreement between theory and the observed enzyme experimental parameters, though g_{max} is calculated to be somewhat larger than observed experimentally. One of the reasons why researchers have proposed

that the equatorial ligand is an oxo rather than hydroxy is that in the EPR data of the reduced enzyme no proton hyperfine structure is resolved. Hille *et al.*¹²⁵ observed no line broadening in the hyperfine peaks of the reduced enzyme when using D₂O rather than H₂O solvent. We have simulated the experimental X-band^f reduced CODH enzyme EPR spectrum using the experimental microwave frequency, g-tensor, Cu hyperfine tensor, and Euler angles published by Hille *et al.*¹²⁵ and a linewidth of 0.4 mT to produce a best possible match to the published spectra. Our spectral simulations show that for small proton hyperfines of 10 MHz or less there are is no noticeable change in the features or even linewidths of the spectrum given the linewidth of the Cu hyperfine the published experimental data has.

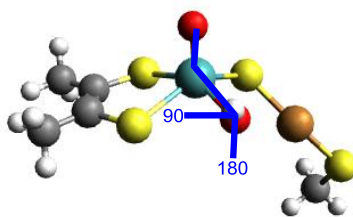


Figure 3.6: Definition of the OMoOH dihedral angle in the CODH active site computational model.

We investigated the dependency of the proton hyperfine and of the EPR parameters in general on the OMoOH dihedral angle (defined in Figure 3.6) by computationally constraining the OMoOH dihedral angle in 15° increments, optimizing the structure with the constrained in place, and calculating EPR parameters. Bond angles and dihedral

^f X-band EPR uses microwave radiation of a frequency of about 9.4 GHz.

angles along the Mo-S-Cu-S-C chain were constrained to the values found in the X-ray crystal structure of the oxidized active site, since we found that when those dihedral angles were unconstrained there would be large deviations in the position of the atoms along the S-Cu-S-C chain dependent on the choice for the OMoOH dihedral angle. This is not only unreasonable for direct comparisons of calculated parameters as a function of the OMoOH dihedral, but we also believe large changes in the positions of the S-Cu-S-C atoms to be unreasonable in light of the fact that in the enzyme the cysteine residue that coordinates the Cu is unlikely to undergo such large motions. The cysteine thus providing an anchor point for the Cu that is absent in the computational model.

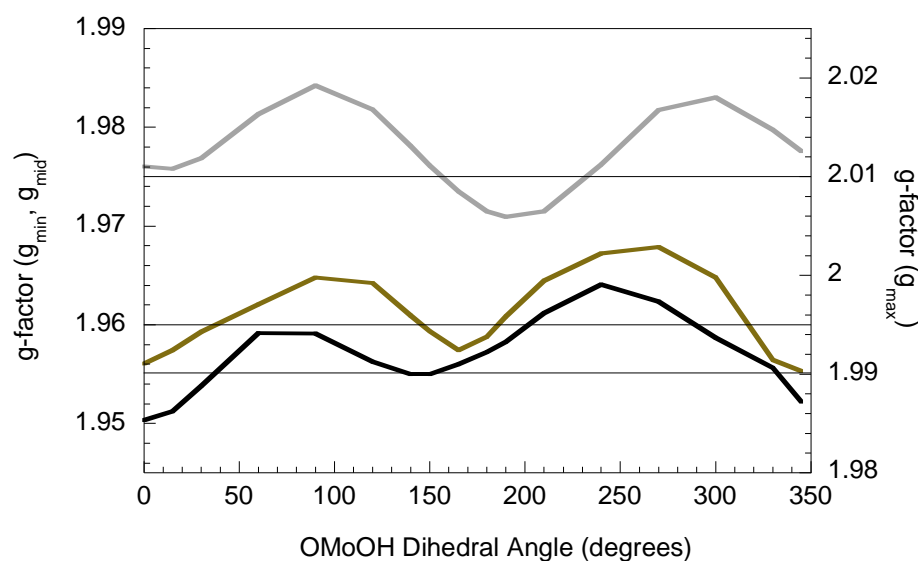


Figure 3.7: Calculated g-values as a function of varying OMoOH dihedral angles (horizontal black lines mark the published experimental g-tensor for the enzyme) g_{\min} (black), g_{mid} (bronze), g_{\max} (gray).

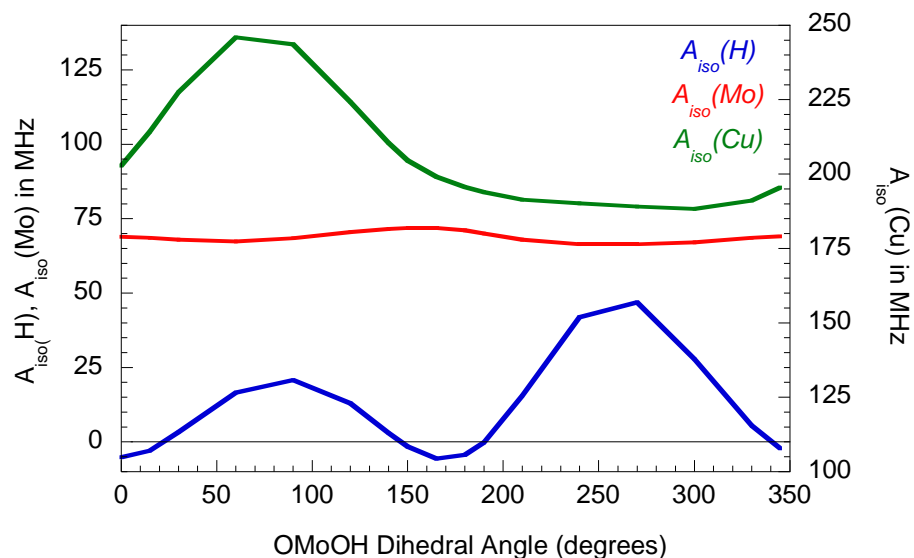


Figure 3.8: Calculated isotropic hyperfine coupling constants as a function of varying OMoOH dihedral angles (the horizontal black line marks a value of zero for the calculated proton hyperfine). $A_{iso}(H)$ blue, $A_{iso}(Mo)$ red, $A_{iso}(Cu)$ green.

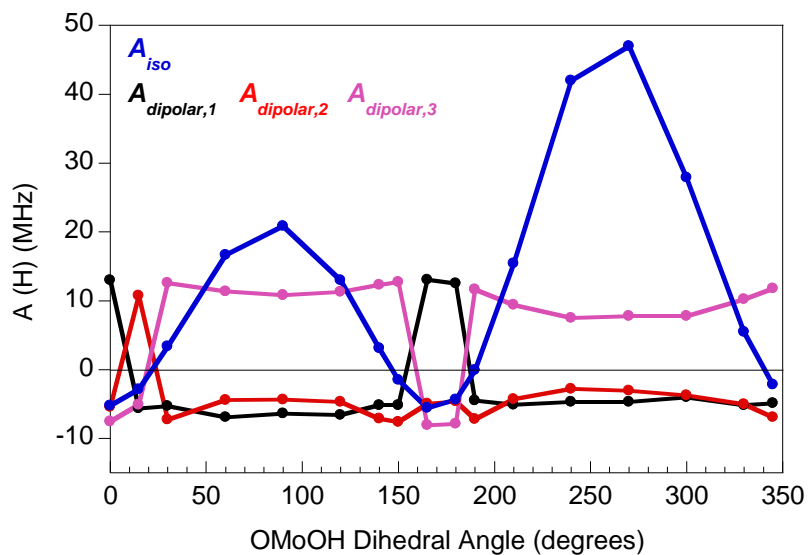


Figure 3.9: Calculated proton hyperfine coupling constants as a function of varying OMoOH dihedral angles (isotropic: blue, and dipolar: black, red, lavender).

The results of this computational study of the dependence of the OMoOH dihedral angle on EPR parameters of the active site are shown in Figure 3.7 for the dependence of g-values on the OMoOH dihedral angle, Figure 3.8 for the dependence of isotropic hyperfine coupling constants on the OMoOH dihedral angle, and Figure 3.9 for the dependence of dipolar components of the proton hyperfine coupling constants on the OMoOH dihedral angle. We can clearly see that all EPR parameters depend on the OMoOH dihedral angle. Proton hyperfine values can vary from -6 to +47 MHz, and becomes zero at several values of the OMoOH dihedral angles, at which the dipolar components of the proton hyperfine become small. This suggests that even though proton hyperfine is not observed experimentally, the equatorial ligand may be a hydroxyl. In fact, whenever computed g-values approach the experimental g-values, the proton hyperfine and its dipolar components get small as well (i.e. at OMoOH angles of 30-40°, 150-160° and 190°), and best agreement of theory and experiment suggests a OMoOH dihedral of about 30° or 150-160°. The average isotropic proton hyperfine corresponding to a free rotation of the hydroxyl proton was obtained as 10 MHz by averaging the 15° increment-value for the isotropic proton hyperfine coupling constant.

By comparing experimental EPR parameters for the reduced CODH enzyme to computational EPR parameters for a model with either an equatorial oxo or and equatorial hydroxo ligand we see that the equatorial oxo is strongly inconsistent with experimental g-values, while the equatorial hydroxo ligand has g-values that are consistent with experiment. We also observed that the proton hyperfine depends strongly on the OMoOH dihedral angle, and is close to zero at several values of the OMoOH

dihedral angle. Isotropic calculated Cu hyperfine is overestimated computationally, but the nature of the Cu hyperfine tensor of a large isotropic and small orthorhombic dipolar component agrees between experiment and calculations for both the equatorial oxo- or hydroxy ligand.

3.3.2 Geometry Changes at the Cu Site upon CO Binding

Recent unpublished results from ENDOR measurements on the CO reduced enzyme active site provide experimental hyperfine coupling constants for Cu similar to those obtained by EPR, as well as ^{13}C hyperfine coupling constants for the CO carbon[§] (Table 3.3). Both the Cu and ^{13}C hyperfine have a large isotropic component and small dipolar component.

Table 3.3: ENDOR parameters for CO reduced CODH. ^d

			Cu hyperfine (MHz)				^{13}C hyperfine (MHz)			
g_{min}	g_{mid}	g_{max}	$A_{1,\text{dip}}$	$A_{2,\text{dip}}$	$A_{3,\text{dip}}$	A_{iso}	$A_{1,\text{dip}}$	$A_{2,\text{dip}}$	$A_{3,\text{dip}}$	A_{iso}
1.955	1.960	2.001	-7	-7	+14	137	-0.7	-0.7	1.4	17.4

When we bind CO at the Cu in the computational CODH active site with the equatorial oxo ligand, we observe that the Cu hyperfine decreases ~20%, and that the geometry of Cu changes from nearly linear to nearly trigonal (Figure 3.10). The calculated ^{13}C hyperfine (Table 3.4) is not in good agreement with experimental values for either the dipolar or isotropic contribution. More importantly, however, the dioxo

[§] Private communication with B. M. Hoffman, University of California, Riverside, unpublished (2013).

enzyme active site g-tensor is still inconsistent with experimental data as g_{\min} is much too low, both with and without CO bound.

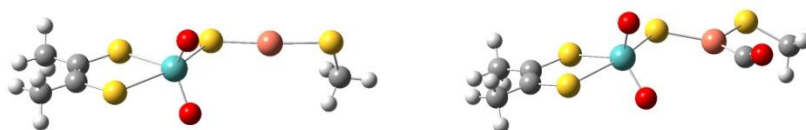


Figure 3.10: Optimized geometries of the CODH active site with an equatorial oxo ligand with no CO bound (left) and upon CO binding at the Cu (right).

Table 3.4: DFT-calculated EPR parameters for the CODH active site with an equatorial oxo ligand.

CO bound	Net charge				Cu hyperfine (MHz)				^{13}C hyperfine (MHz)			
		g_{\min}	g_{mid}	g_{\max}	$A_{1,\text{dip}}$	$A_{2,\text{dip}}$	$A_{3,\text{dip}}$	A_{iso}	$A_{1,\text{dip}}$	$A_{2,\text{dip}}$	$A_{3,\text{dip}}$	A_{iso}
No	-3	1.902	1.951	1.997	3	1	-3	209	--	--	--	--
Yes	-3	1.911	1.950	1.996	13	-2	-11	167	4	5	-10	4

We have used the CODH enzyme active site computational model with the equatorial hydroxy ligand to explore the effect of CO binding upon the EPR parameters in more detail, since it has EPR parameters that are much more consistent with the experimental EPR of the reduced CODH enzyme. In the absence of bound substrate the oxidized CODH active site crystal structure reveals a near-linear Cu geometry (SCuS angle 156° , Figure 3.11). Upon CO binding calculations show that the Cu will adopt a trigonal conformation, where the SCuS angle optimizes to 120° (Figure 3.11). In order to separate the effects of the geometry change induced by CO binding on the EPR parameters from the effects of the Cu-CO bonding interaction on the EPR parameters, we also considered a CO bound Cu center held fixed at the crystal structure SCuS bond angle of 156° and a Cu with no CO bound but a SCuS bond angle of 120° (Figure 3.11).

Table 3.5: DFT-calculated EPR parameters for the CODH active site with an equatorial hydroxo ligand, part 1.

	CO bound	SCuS angle	Net charge				Cu hyperfine (MHz)			
				g_{\min}	g_{mid}	g_{\max}	$A_{1,\text{dip}}$	$A_{2,\text{dip}}$	$A_{3,\text{dip}}$	A_{iso}
I	No	156 °	-2	1.954	1.959	2.012	9	4	-12	228
II	Yes	156 °	-2	1.953	1.962	2.010	11	8	18	191
III	No	120 °	-2	1.956	1.961	2.016	19	2	-20	237
IV	Yes	120 °	-2	1.954	1.958	2.015	13	8	-21	90

Table 3.6: DFT-calculated EPR parameters for the CODH active site with an equatorial hydroxo ligand, part 2.

	CO bound	SCuS angle	^{13}C hyperfine (MHz)				OH Proton hyperfine (MHz)			
			$A_{1,\text{dip}}$	$A_{2,\text{dip}}$	$A_{3,\text{dip}}$	A_{iso}	$A_{1,\text{dip}}$	$A_{2,\text{dip}}$	$A_{3,\text{dip}}$	A_{iso}
I	No	156 °	--	--	--	--	5.3	7.2	-12.6	3.3
II	Yes	156 °	4.2	2.0	-6.1	32.5	4.9	6.9	-11.9	3.4
III	No	120 °	--	--	--	--	4.7	6.7	-11.5	1.6
IV	Yes	120 °	2.6	1.7	-4.4	15.8	4.6	6.6	-11.1	3.8

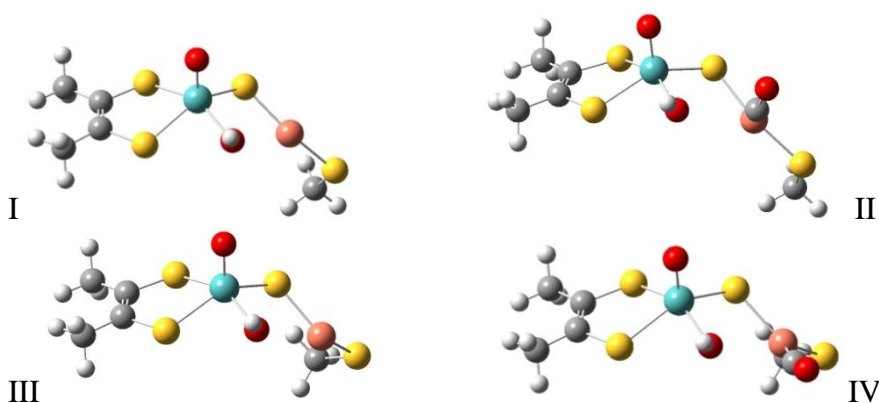


Figure 3.11: CODH active site with an equatorial hydroxo ligand with no CO bound (left, I and III) and upon CO binding at the Cu (right, II and IV).

In order to focus on the effects of CO binding and geometry changes at the SCuS bond angle only, the OMoOH dihedral angle was chosen as 30° for structures I-IV, and bond angles and dihedrals were constrained to crystal structure values along the MoSCuSC chain as described previously with the exception of the SCuS bond angle which was either allowed to optimize upon CO binding or constrained as described above. The EPR parameters calculated for I-IV are summarized in Table 3.5 and Table 3.6. Structures I-IV with an equatorial hydroxo ligand all have reasonable g -values, though g_{\max} is consistently somewhat larger calculated than experimentally. The calculated Cu and ^{13}C hyperfine tensors are rhombic for all four structures (no ^{13}C hyperfine without CO) with large isotropic contributions and small dipolar contributions. The dipolar components are quite comparable to the experimental values for both the Cu and ^{13}C hyperfine tensors.

When CO binds, the Cu hyperfine decreases $\sim 16\%$, even when no change in the SCuS bond angle is allowed to occur. Upon CO binding **accompanied by** Cu becoming trigonal, however, Cu hyperfine is reduced two-threefold. Removing the CO from a trigonal Cu site (so that the SCuS bond angle is 120° but there is no third ligand present) does not lead to a reduction in Cu hyperfine. The computed ^{13}C hyperfine is closest to experimental values both in terms of the isotropic and dipolar contributions for structure IV, the equatorial hydroxy ligand enzyme active site with CO bound and an optimized trigonal Cu site. Structure IV (trigonal Cu) is calculated to be 2.97 kcal/mol (1040 cm^{-1}) lower in energy than structure II (SCuS angle 156°). We should consider, however, that

there may or may not be any constraints on the Cu geometry upon CO binding in the enzyme, where the Cu is coordinated by a cysteine residue.

We found that varying the SCuS bond angle computationally allowed us to match the experimental $A_{\text{iso}}(\text{Cu})$, where at a SCuS bond angle of 139° the hyperfine is computed to be 136 MHz. As previously mentioned, we believe that the magnitude of the computed isotropic Cu hyperfine is very sensitive to the exact s-orbital character in the SOMO wavefunction, and even small changes of only 1% difference in the s-orbital character correspond to large Cu hyperfine changes of 60 MHz. Therefore, we concede that it is

Table 3.7: DFT-calculated bond orders and atomic charges for CODH active site structures with an equatorial hydroxo ligand and CO bound at Cu.

<i>Feature</i>	<i>Structure II</i>	<i>Structure IV</i>
SCuS angle $^\circ$	156	120
Mulliken atomic charge Cu	0.012	-0.018
Mulliken atomic charge C	0.221	0.286
Mulliken atomic charge O	-0.172	-0.203
Mayer bond order $S_{\mu}\text{Cu}$, $S_{\text{cys}}\text{Cu}$	0.72, 0.73	0.66, 0.72
Mayer bond order CuC	0.63	1.00
Mayer bond order CO	2.15	2.12
Total C p-orbital character in molecular orbitals with $\text{Cu}_{\text{occ}}\text{-C } \pi$	1.1 α 1.1 β	2.4 α 2.5 β
CuCO angle $^\circ$	146	169

likely not a good idea to match the magnitude of the calculated and experimental isotropic Cu hyperfine. It is useful to illustrate, however, that the Cu hyperfine is sensitive to both structural perturbations and to a smaller degree also the perturbation of the CO binding independent of the accompanying geometric change. DFT calculations confirm that a trigonal Cu site has different CO bonding interactions than a Cu with a more linear SCuS bond angle. Table 3.7 summarizes the Mulliken atomic charges and Mayer bond orders of selected atoms at the Cu site. We observed that structure IV (trigonal Cu) forms a weaker bond to the bridging sulfido and a stronger bond to the CO carbon than structure II. The Cu-C bond has contributions from both σ donation from a lone pair-type carbon orbital to Cu and π backbonding from filled Cu d-orbitals into a CO π^* orbital, where both the Cu-C σ and Cu-C π bonding interactions strengthen the Cu-C bond, but the Cu-C π backbonding also weakens the C-O bond of CO. The Mulliken charges of the trigonal Cu site reflect both the stronger Cu-C σ and Cu-C π back bonding interactions with a more negative Cu, a more positive C and a more negative O. A stronger metal-carbonyl interaction in the trigonal Cu site polarizes the CO bond more, making the C more electropositive and thus more susceptible to nucleophilic attack.

We recalculated EPR parameters of the CODH active site with the equatorial hydroxyl ligand for CO bound and no CO bound, removing the bond angle constraints and leaving in place the constraints for dihedral angles along the MoSCuSC chain as well as OMoOH only. For the CO bound structure we found that none of the bond angles changed significantly from the calculation with the crystal structure constraints: notation (constrained angle \rightarrow optimized angle), MoSCu ($113^\circ \rightarrow 114^\circ$) and CuSC ($109^\circ \rightarrow$

102°), and SCuS 120° for both. Calculated EPR parameters are hence did not change either between the structure with and without the bond angle constraints, where the largest change was a decrease of 2 MHz in the isotropic Cu hyperfine for the calculation without bond angle constraints.

For the enzyme active site without CO bound MoSCu (113° → 115°) and CuSC (109° → 102°) bond angles did not change significantly upon removing the constraint, while the SCuS (156° → 172°) bond became significantly more linear than found in the X-ray structure of oxidized CODH. Interestingly, the more linear SCuS angle corresponds to a lower isotropic Cu hyperfine of 206 MHz, compared to 228 MHz when SCuS is 156°.

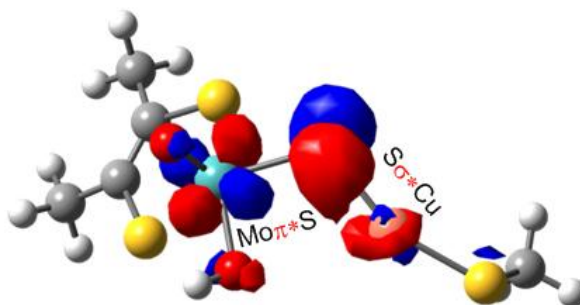


Figure 3.12: SOMO wavefunction of the CODH active site model with an equatorial hydroxy ligand.

In the SOMO wavefunction of the CODH active site computational model, the d_{22} -type orbital on Cu points directly at one of the lobes of the sulfur p-orbital for maximum σ^* overlap (Figure 3.12 and reference ¹²⁶). The lower value for the isotropic Cu hyperfine for the more linear SCuS bond angle of 172° implies that maximum σ^* overlap occurs at a SCuS bond angle closer to 156° than to 172°.

3.3.3 Alternative Geometries for CO Binding

We considered a few additional possibilities of how CO might be bound at the enzyme active site and calculated EPR parameters for each. Structures a-c in Figure 3.12 show CO bound at Cu forming a ring structure with the equatorial ligand, which is either a deprotonated hydroxyl (a), a hydroxyl whose proton has migrated to the CO oxygen (b), or an equatorial site that has no ligand but a direct bond to the CO carbon (c).

Table 3.8: DFT-calculated EPR parameters for alternative CO binding modes in the CODH active site.

	Net charge	Cu hyperfine (MHz)				¹³ C hyperfine (MHz)						
		g_{\min}	g_{mid}	g_{\max}	$A_{1,\text{dip}}$	$A_{2,\text{dip}}$	$A_{3,\text{dip}}$	A_{iso}	$A_{1,\text{dip}}$	$A_{2,\text{dip}}$	$A_{3,\text{dip}}$	A_{iso}
a	-3	1.955	1.982	2.024	-9	114	-95	10	9	9	-19	54
b	-2	1.961	1.967	2.034	-44	-8	53	-35	4	2	-6	9
c	-1	1.989	1.997	2.042	84	-7	-77	149	6	2	-8	32

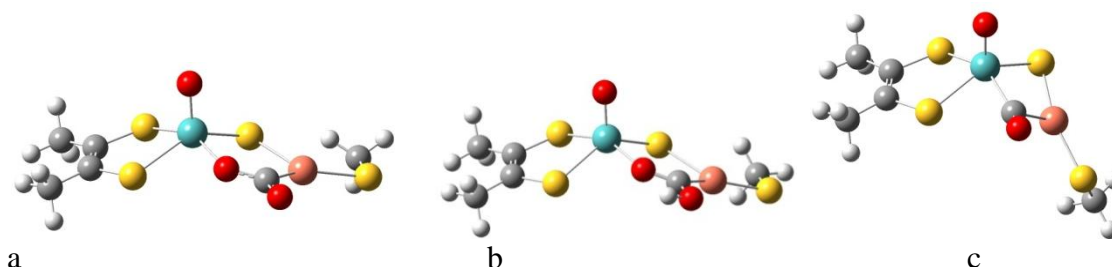


Figure 3.13: Alternative modes of CO binding at the CODH active site.

Since the charges of -2 and -3 are high, additional calculations were performed with the conductor like screening model (COSMO),¹⁴⁰ which models the solvent as a dielectric polarizable continuum that interacts with the molecular charge density to partially screen the charges. Results did not differ significantly from calculations without solvent (same qualitative result, 10-20% change in hyperfine values); therefore all calculations reported here are without solvent. Structure c is not consistent with

experimental g-values, and structure b is also not a very good match to experimental g-values. All three structures can be eliminated more clearly, however, on the basis of having a **much** too large dipolar component to the Cu hyperfine. The closed ring (MoSCuCO or MoSCuC) geometries of these structures significantly change the position of the Cu with respect to the Mo-dithiolene plane, where the OMoSCu dihedral angle either becomes smaller (structure a,b) or larger (structure c) than observed in the crystal structure of the oxidized enzyme. The formation of a cyclic structure involving Cu and CO at the active site thus reorients the d-orbitals of Cu with respect to the S_{μ} -Cu bond, resulting in the marked differences in anisotropy of the Cu hyperfine tensor.

We considered active site structure where CO has inserted into the S_{μ} -Cu bond (akin to step 2 in Figure 3.3), but found that they did not optimize to a stable structure and resulted in the detachment of Cu-S-CH₃ from the rest of the molecule. We suspect that even if such a geometry could have optimized successfully, the Cu hyperfine would have been quite reduced. We also considered a neutral ligand such as water as the equatorial Mo ligand, but observed that g_{mid} was shifted to 1.98 and g_{max} to 2.03, both higher values than observed experimentally.

3.3.4 Bicarbonate as the Equatorial Ligand

A final possibility we considered is that the equatorial ligand may not be a hydroxyl ligand in the signal-giving species for the EPR spectra of CODH, but rather a bicarbonate ligand, which may be formed by the addition of the carbon dioxide product and water in the active site. Having an equatorial bicarbonate ligand reconciles the lack of observed proton hyperfine in the experimental EPR data (and also the lack of observed

proton hyperfine in unpublished ENDOR data). Calculated EPR parameters for the equatorial bicarbonate (i.e. HCO_3^-) ligand are summarized in Table 3.9.

Table 3.9: Calculated EPR parameters for the CODH active site with an equatorial bicarbonate ligand (all hyperfine coupling constants given in MHz).

	g_{min}	g_{mid}	g_{max}	Cu A_{iso}	Cu A_{dip}	C A_{iso}	C A_{dip}	H A_{iso}	H A_{dip}
I	1.949	1.967	2.022	281	-17, -7, 24	18.6	-1.0, -1.0, 2.0	3	-1, -1, 2
II	1.955	1.965	2.020	236	-11, -8, 19	7.2	-1.2, -0.9, 2.1	0	-1, -1, 2

Structures I and II in Table 3.9 differ in the orientation bicarbonate at the active site, where in I bicarbonate is in-plane (the plane of the dithiolene sulfurs and the bridging sulfido), and in II bicarbonate is tilted out of the plane of the sulfurs. Both structures have EPR parameters that are close to the experimental values in terms of g -values, a large isotropic Cu hyperfine, the magnitude of the dipolar Cu hyperfine, as well as the magnitude of the ^{13}C hyperfine. Also notice that the proton hyperfine of the HCO_3^- proton is zero (or close to zero). While the magnitude of the isotropic and anisotropic carbon hyperfine for I is virtually identical to the observed experimental values for reduced CODH, the magnitude of the isotropic and anisotropic carbon hyperfine for II is the same as in HMP-very rapid XO (where XO = xanthine oxidase, HMP = 2-hydroxy-6-methylpurine), which also features an out-of-plane orientation for the HMP substrate.¹⁴¹

3.4 Computational and Experimental Studies of the Active Site Model Compounds

Paramagnetic CODH active site model compounds that replicate the $[\text{O}_{\text{ax}}\text{MoSCu}]$ unit of the CODH enzyme active site have been synthesized¹²⁶ by our collaborators from

Prof. Young's group, at the University of Melbourne, Australia. The molecular structure is represented in Figure 3.14, where in addition to the $[O_{ax}MoSCu]$ "core", the Cu is coordinated by a (Me_3tacn) ligand ($Me_3tacn = 1,4,7$ -trimethyl-1,4,7-triazacyclononane), and Mo by a trispyrazolyl borate ligand ($Tp^{iPr} =$ hydrotris(3-isopropylpyrazol-1-yl)borate) as well as a phenolate ligand (OAr). The phenolate ligand represents the equatorial hydroxy ligand, and various substitutions on OAr were synthesized including Ar = Ph, 2s-Bu, 4s-Bu, 3t-Bu and 2-tBu. Work on these model compounds was started by Dr. Sushilla Knottenbelt and Dr. Nick Rubie in the Kirk research group, including the first EPR and electronic absorption & MCD spectral assignments for the model compound where Ar = Ph-4Ph.¹²⁶ Here we present the results for the models where Ar = Ph, 2s-Bu, 4s-Bu, and 3t-Bu, as well as electronic structure calculations used to understand and assign the experimental EPR, electronic absorption, and MCD data.

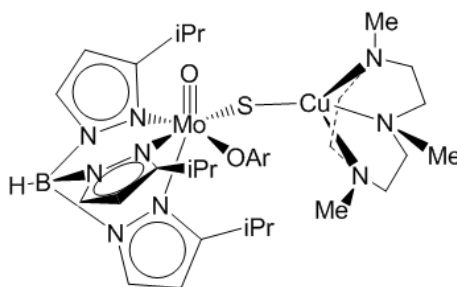


Figure 3.14: CODH synthetic active site model compounds where Ar = Ph, 2s-Bu, 4s-Bu, 3t-Bu, or 2-tBu where the 2-position on Ar points in the opposite direction of the Mo-O_{axial} bond and the 5-position in the same direction as the Mo-O_{axial} bond.

Table 3.10: Selected bond distances and angles of CODH models compounds $\text{Tp}^{\text{iPr}}\text{MoO}(\text{OAr})(\mu\text{-S})\text{Cu}(\text{Me}_3\text{tacn})$ and the oxidized enzyme active site.

	CODH model compounds	CODH enzyme active site, oxidized ¹¹⁷
Mo-S _μ bond (Å)	2.27-2.30	2.32
Cu-S _μ bond (Å)	2.10-2.13	2.18
Mo-Cu distance (Å)	3.75-4.04	3.74
MoSCu bond angle (°)	116-134	113

As observed in the published work on the Ar = Ph-4Ph model, these CODH model compound are both good structural and good electronic structure mimics of the CODH enzyme active site. Table 3.10 shows that distances and angles in the [MoSCu] unit of the CODH model compounds are similar to those of the enzyme active site, where the range of values given for the model compounds refers to models with different phenolate substitutions. The oxidation state of molybdenum in these paramagnetic model compounds is +5, which represents the oxidation state of Mo during the transfer of electrons from the substrate to the Mo center. The similarity of the EPR spectrum of the model compounds and enzyme¹²⁶ indicates that the models likely capture the electronic structure of the enzyme active site as well.

3.4.1 Frontier Orbitals and Electronic Structure of CODH Model Compounds

The frontier molecular orbitals of the CODH model compounds were generated from the DFT-optimized structure of the $\text{Tp}^{\text{iPr}}\text{MoO}(\text{OPh})(\mu\text{-S})\text{Cu}(\text{Me}_3\text{tacn})$ model compound, and the SOMO wavefunction of the models are similar to that of the CODH enzyme active site model. We considered a few different model compound calculations,

using either the Gaussian suite or ADF program for DFT electronic structure calculations, as well as choices of MoSCu bond angles between $110^\circ - 134^\circ$ to reflect the range observed in both the model compounds and the enzyme active site itself. The specific numerical values quoted in this section refer to the ADF optimized structure of $\text{Tp}^{\text{iPr}}\text{MoO}(\text{OPh})(\mu\text{-S})\text{Cu}(\text{Me}_3\text{tacn})$, which without any bond angle constraints optimizes to a MoSCu bond angle of 110° . This value for the MoSCu bond angle is smaller than what is observed in the X-ray crystal structure for $\text{Ar} = \text{Ph}$, but the calculated electronic absorption and MCD spectra for this lower-value MoSCu bond angle are in much closer agreement to the experimentally observed spectra than spectra calculated for larger MoSCu bond angles. The observations on the frontier orbitals made in this section, however, are true for other values of MoSCu bond angles and Gaussian calculated structures as well.

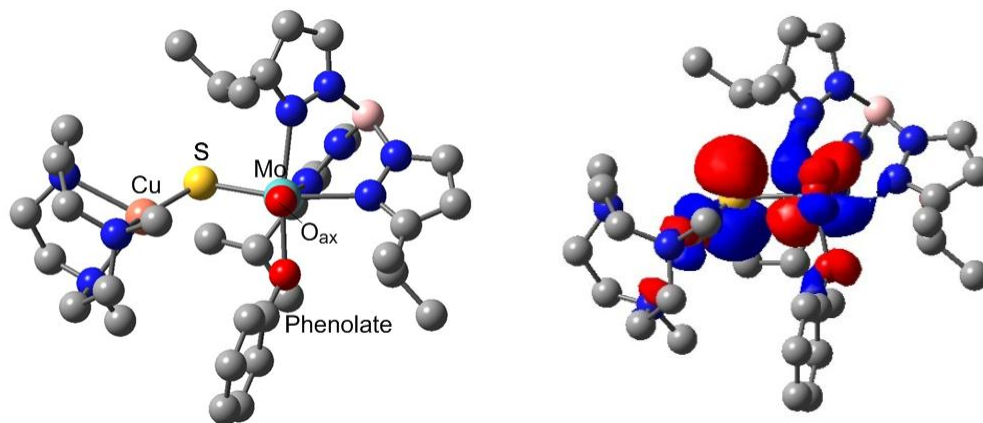


Figure 3.15: $\text{Tp}^{\text{iPr}}\text{MoO}(\text{OPh})(\mu\text{-S})\text{Cu}(\text{Me}_3\text{tacn})$, optimized geometry (left) and α SOMO wavefunction (right). Hydrogens have been omitted for clarity. Molybdenum = turquoise, sulfur = yellow, copper = pink, carbon = gray, oxygen = red, nitrogen = blue.

The α SOMO wavefunction (Figure 3.15, right) is highly covalent and delocalized across the [MoSCu] unit, where molybdenum contributes ~40% to the wavefunction, sulfur ~25%, and copper ~15%. As observed previously for the SOMO wavefunction of the computational model of the CODH enzyme active site, molybdenum and sulfur have a π^* interaction, while copper and sulfur have a pseudo- σ^* interaction, where one lobe of the Cu d-orbital points directly at only one lobe of the sulfur p-orbital. Both metals thus have overlap with the bridging sulfido ligand, which forms a connection between the two metal centers in terms of orbital covalency. The orbital covalency in the SOMO is important since the SOMO of the Mo^V model compounds is the model compound analogue of the orbital involved in electron transfer from the substrate to the Mo center in the CODH enzyme active site. Thus a large orbital covalency across the [MoSCu] unit in the α SOMO supports the idea of electron transfer from the substrate to the Mo via the Cu and S in the active site of the enzyme.

This delocalization is particular to the SOMO wavefunction, where Table 3.11 shows that the unoccupied Mo-d orbitals, which lie directly above the SOMO in energy, are noticeably more localized on the molybdenum and axial oxo, which have a π^* interaction. If we define the bond of molybdenum to the axial oxo ligand as the z-axis, the the bond of molybdenum to the equatorial phenolate ligand as the y-axis, and the bond of molybdenum to bridging sulfido ligand as approximately along the x-axis, we can describe the Mo d-orbital character in the SOMO as d_{xy} , in the LUMO as d_{yz} , and in the LUMO+1 as d_{xz} . The Mo d-orbitals that have $d_{x^2-y^2}$ and d_{z^2} character are much higher

Table 3.11: DFT-calculated molecular orbital compositions of the SOMO, LUMO and LUMO+1 for $\text{Tp}^{\text{iPr}}\text{MoO}(\text{OPh})(\mu\text{-S})\text{Cu}(\text{Me}_3\text{tacen})$.

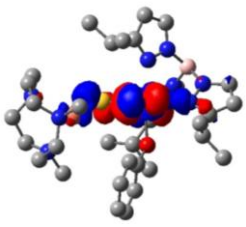
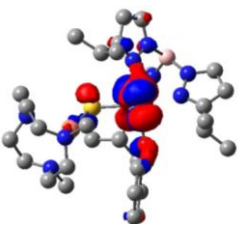
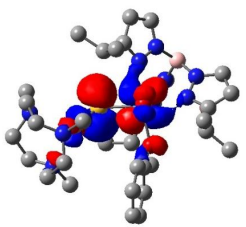
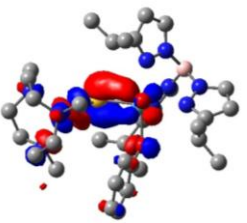
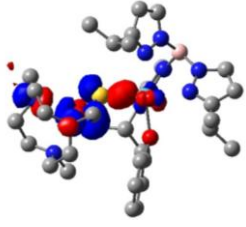
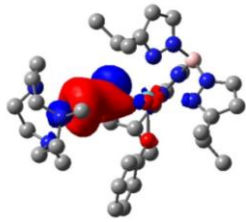
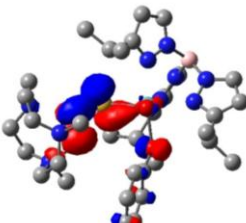
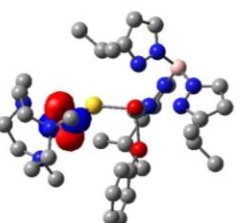
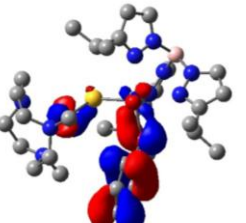
Molecular orbital Composition (%)	Mo	S	Cu	Molecular orbital, isovalue 0.03
α LUMO+1 (unoccupied)	54.6 (& 12.2 axial oxo)	4.3	2.2	
α LUMO (unoccupied)	56.7 (& 16.9 axial oxo)	4.2	1.2	
α SOMO (occupied)	39.4	24.8	15.1	

Table 3.12: DFT-calculated molecular orbital compositions of the HOMO and HOMO-n orbitals for $\text{Tp}^{\text{iPr}}\text{MoO}(\text{OPh})(\mu\text{-S})\text{Cu}(\text{Me}_3\text{tacen})$.

β Molecular Orbital	Orbital composition %			Molecular orbital, isovalue 0.03	(Anti)bonding Interactions
	Mo	S	Cu		
HOMO	9.5	12.0	51.0		Mo-S π Cu-S π^*

H-1 (HOMO-1)	2.0	4.7	69.1		Mo-S pseudo- σ Cu-S π^*
H-2	1.9	19.6	67.3		Cu-S pseudo- σ^*
H-3	1.0	11.5	69.7		Cu-S pseudo- σ
H-4	0	0	96.7		N/A
H-5	Mo: 2.2, S: 1.4 <u>Phenolate:</u> 57.7		21.2		Mo-Phenolate π

in energy, and will not play a role in the discussion of the electronic absorption and MCD spectra in the upcoming sections.

Directly below the delocalized SOMO (in energy) lie mixed Cu/S orbitals of predominant Cu d-character and lesser S p-character, and followed below in energy by phenolate-based orbitals. Table 3.12 summarizes the orbital character of those HOMO-n orbitals, which are also the orbitals that are the involved in the calculated electronic transitions from 7000 – 25000 cm^{-1} discussed in section 3.4.4. These HOMO-n orbitals have a small amount Mo of Mo-d character, with the HOMO having 9.5% and the orbitals below the HOMO having 2% or less Mo character. With the exception of H-4, these orbitals are delocalized over both Cu and S, or Cu/S/phenolates (H-5).

If we examine the orbital composition of the α and β SOMO of $\text{Tp}^{\text{iPr}}\text{MoO}(\text{OPh})(\mu\text{-S})\text{Cu}(\text{Me}_3\text{tacn})$ cluster (Table 3.13), we notice a difference in the orbital composition between the α and β SOMO, which indicates that spin polarization plays a role in the electronic structure of the model compound. The β SOMO composition approaches the Mulliken spin populations more closely than the α SOMO, but we observe a marked difference between the spin populations and the orbital compositions of both the α and β SOMO.

Table 3.13: DFT-calculated molecular orbital compositions of the α and β SOMO, and Mulliken spin populations for $\text{Tp}^{\text{iPr}}\text{MoO}(\text{OPh})(\mu\text{-S})\text{Cu}(\text{Me}_3\text{tacn})$.

Molecular orbital composition	Mo	S	Cu
α SOMO (occupied)	39.4%	24.8%	15.1%
β SOMO (unoccupied)	57.7%	19.1%	10.2%
Mulliken spin population	0.778	0.171	0.053

Specifically, we notice that molybdenum has a much larger positive spin population than expected from the Mo character in the α SOMO wavefunction, while sulfur and copper have smaller positive spin populations than expected from their orbital character in the α SOMO wavefunction.

3.4.2 Covalency versus Spin Density Distribution Across the [MoSCu] Unit

The discrepancy between the orbital character of the SOMO wavefunction and the spin density distribution across the [MoSCu] unit discussed in section 3.4.1 can be explained using a valence bond configuration interaction (VBCI) model as shown in Figure 3.16. In a VBCI description, the ground state provides α -spin density on the Mo, while a metal-to-metal (Cu \rightarrow Mo) charge transfer (MMCT) excited state that promotes an electron from Cu d-orbitals into the Mo d_{xy} SOMO provides α -spin density on the Cu. MMCT transitions into higher lying Mo d orbitals can be considered, where the excited state that forms a local triplet state on the molybdenum center (${}^1\text{EC}_b$) is lower in energy due to the single-site exchange interaction of two spins occupying the same spatial region than the excited state that generates a local singlet state on Mo (${}^1\text{EC}_c$).

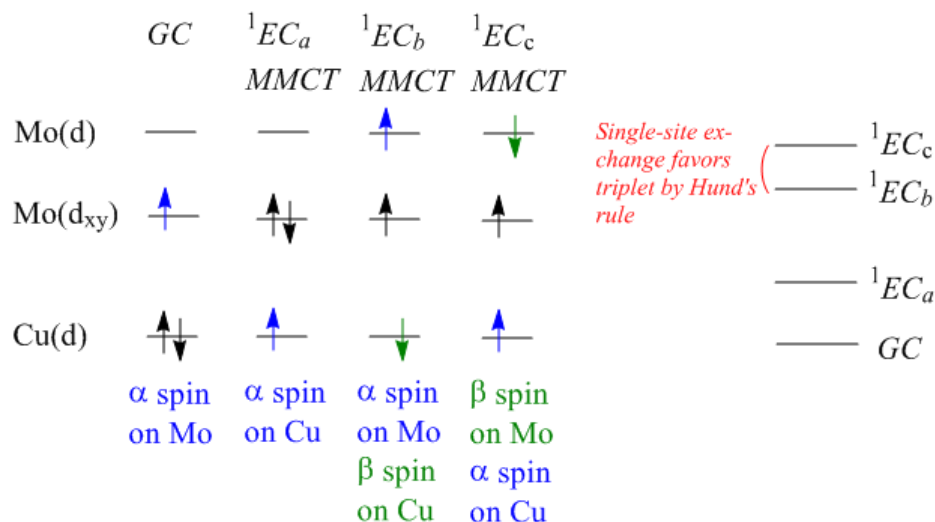


Figure 3.16: VBCI description of the spin densities observed for Mo and Cu in CODH model compounds.

While both 1EC_b and 1EC_c will configurationally interact with the ground state, 1EC_b interacts more strongly with the ground state due to being energetically closer. The **net** effect of both 1EC_b and 1EC_c mixing with the ground state is an increase in the α -spin density on the Mo and decrease in α -spin density on Cu. This effect is magnified by the fact that there are several such MMCT excited states corresponding to promotions into different empty Mo d-orbitals or out of different Cu d-orbitals, each adding a small net increase of positive spin on Mo and decrease of positive spin on Cu. The importance of the MMCT states is confirmed by electronic absorption and MCD spectroscopy, where the electronic absorption and MCD spectra of the model compounds show intense MMCT and LMCT bands at low energies (15,000-24,000 cm^{-1}). We also note that the MMCT transitions originate from orbitals of mixed Cu/S character, so that the CT is Cu

and S → Mo, which leads to a net reduction of positive spin on the bridging sulfido just like for Cu.

3.4.3 Electron Paramagnetic Resonance Spectroscopy of CODH Model Compounds

The paramagnetic model compounds were characterized by EPR spectroscopy, at both X-band (9.4 GHz) and Q-band (34 GHz). The low-temperature Q-band EPR data and spectral simulations of the CODH model compounds are shown in Figure 3.17. Q-band EPR data was very valuable for the spectral simulations, since the larger frequency of microwave radiation used in Q-band causes the g-values to be separated enough in the magnetic field axis so that all hyperfine lines are clearly visible and do not overlay one another. We observe twelve hyperfine lines, four associated with each g-value, which we assign as Cu hyperfine, where $^{63,65}\text{Cu}$ is a 100% abundant $I = 3/2$ nucleus. Mo hyperfine lines are noticeably less intense than Cu hyperfine line due to the fact that $^{95,97}\text{Mo}$ $I = 5/2$ is only 25.5% abundant and is split into a 6 line pattern. Thus we were only able to observe the outer two of six Mo hyperfine lines on g_{\min} and g_{\max} , where $A(\text{Mo})$ on g_{\min} is ~175 MHz and $A(\text{Mo})$ on g_{\max} as ~130 MHz.

Table 3.14 shows the EPR parameters obtained by spectral simulation of the Q-band EPR data. X-band EPR spectra were simulated well with the same EPR parameters that were determined from the Q-band simulations, and are shown in Appendix 6.2.3. We observe a rhombic g-tensor for all model compounds, where g-values do not vary as a function of phenolate substitution. The g_{average} is 1.94, where $1.94 < 2.00$, which confirms that the unpaired electron resides in a less-than-half-filled d-orbital shell,⁸¹ consistent

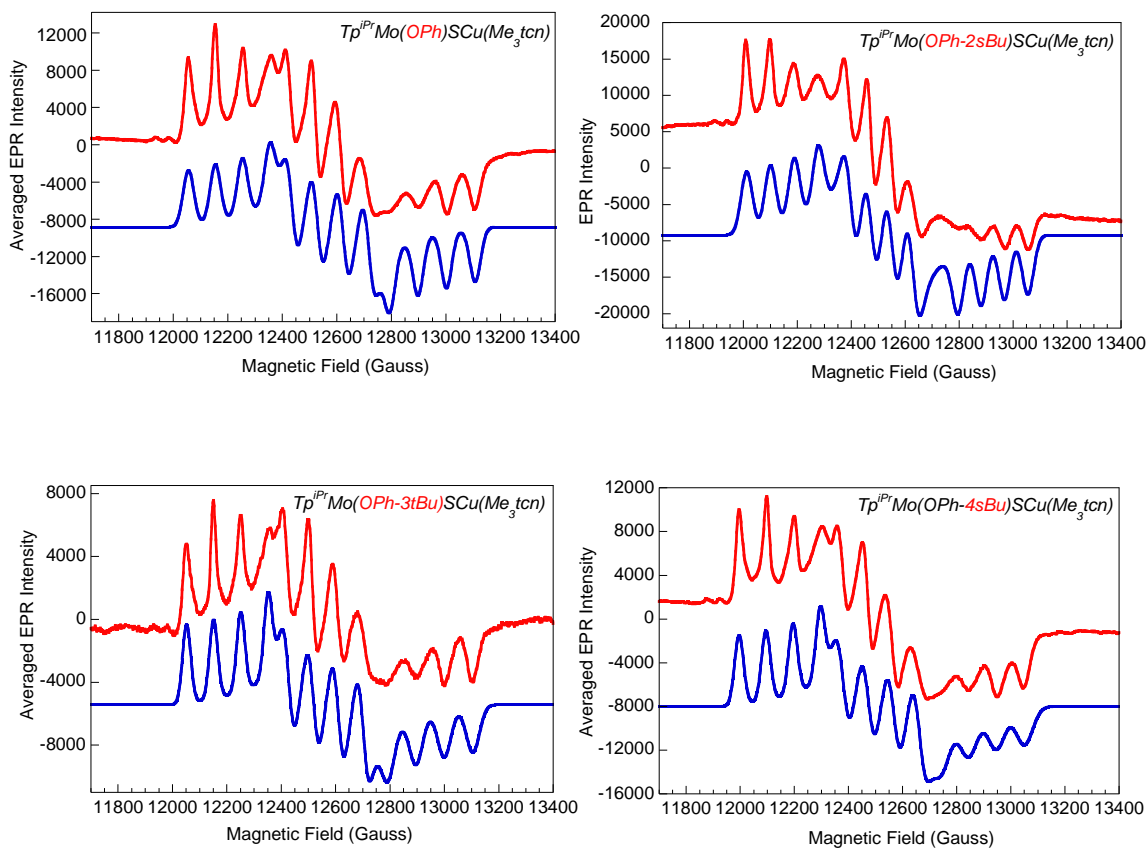


Figure 3.17: Q-band EPR spectrum of $Tp^{iPr}MoO(OAr)(\mu-S)Cu(Me_3tcn)$ at ~ 80 K in butyronitrile.

with the oxidation states of the metals being Mo^V (d^1) and Cu^I (d^{10}) as opposed to Mo^{IV} (d^2) and Cu^{II} (d^9). It is noteworthy that Cu^I with a completely filled d-shell is diamagnetic, and thus no Cu hyperfine is expected to be observed **in the ground state**. The observed Cu hyperfine is thus an excited state contribution to experimental observables measure in the ground state, and reflects the MMCT excited state configurations mixing into the ground state configuration.

Table 3.14: Simulated EPR parameters of $\text{Tp}^{\text{iPr}}\text{MoO}(\text{OAr})(\mu\text{-S})\text{Cu}(\text{Me}_3\text{tacn})$.

				Cu hyperfine (MHz)*			
Ar =	g_{min}	g_{mid}	g_{max}	A_{iso}	$A_{1,\text{dip}}$	$A_{2,\text{dip}}$	$A_{3,\text{dip}}$
Ph	1.88	1.94	2.00	264	-5	14	-8
Ph-4sBu	1.88	1.94	2.00	268	-2	13	-12
Ph-3tBu	1.89	1.94	2.00	268	-7	18	-12
Ph-2sBu	1.88	1.94	2.00	224	-1	19	-19

*Uncertainty of simulated Cu hyperfine is within 5 MHz

Alike to what is observed in the reduced CODH enzyme, the observed Cu hyperfine of the model compounds has a very large isotropic components and a small dipolar contribution. While the magnitude of the isotropic Cu hyperfine for the models is larger than in the reduced enzyme, the dipolar component of the Cu hyperfine is very similar for the model compounds and the enzyme. Spectral simulations of the Cu hyperfine have an error bar of ~5 MHz, and Tabel 3.14 shows that within those error bars there is no real differences in EPR parameters for the models with Ar = Ph, Ph-4sBu, and Ph-3tBu. The model with the 2sBu substitution on the phenolate ligand shows a decrease in Cu hyperfine of ~8% compared to the other model compounds. Our collaborators, Prof. Young and group at the University of Melbourne, also synthesized CODH model compounds with a 2-tBu phenolate substitution, and observed a Cu hyperfine value of ~ $\frac{1}{2}$ that of the other model compounds. Unfortunately, $\text{Tp}^{\text{iPr}}\text{MoO}(\text{O-2tBu})(\mu\text{-S})\text{Cu}(\text{Me}_3\text{tacn})$ is very unstable, and despite our best effort we were never able to obtain an EPR spectrum of the compound in our lab without it being decomposed as evidenced by the loss of Cu hyperfine in the EPR spectrum.

The X-ray crystal structure of the 2*t*-Bu substituted model compound reveals a MoSCu bond angle of 116°. X-ray structures for OAr = 2*s*Bu-Ph show a MoSCu bond angle of 127°, while those for OAr = Ph and Ph-4Ph (previously published) show MoSCu bond angles of 134°. We do not have structures for the 3*t*Bu-Ph and 4*s*Bu-Ph substituted model compounds, though from the structural data that is available it appears that a substitution in the 2-position leads to a larger perturbation in the MoSCu bond angle than a substitution in the 4-position (i.e. para to the O-Ph bond). The decrease in Cu hyperfine for models with smaller MoSCu bond angles combined with the clear dependence of the computed Cu hyperfine on the SCuS bond angle in the enzyme active site computational model suggests that the Cu hyperfine also has a dependence on the MoSCu bond angle. As we noted before in our discussion of the EPR of the reduced CODH enzyme, the large isotropic Cu hyperfine depends on the amount of d_{z^2} -*s* orbital mixing on Cu, and the d_{z^2} -type orbital on Cu in the SOMO wavefunction points directly at one of the lobes of the sulfur *p* orbital. Thus a change in the MoSCu bond angle will have a similar effect than changes in the SCuS bond angle in that they will modulate the overlap between the sulfur and Cu d_{z^2} -type orbital.

DFT calculations of EPR parameters of the model compounds were carried out to investigate the dependence of the Cu hyperfine on the MoSCu bond angle. $\text{Tp}^{\text{iPr}}\text{MoO}(\text{OAr})(\mu\text{-S})\text{Cu}(\text{Me}_3\text{tacn})$ with Ar = Ph was used for a series of EPR calculations in which the MoSCu bond angle was varied from 110° to 140°, values that were chosen to bracket crystal structure MoSCu angles of the model compounds.

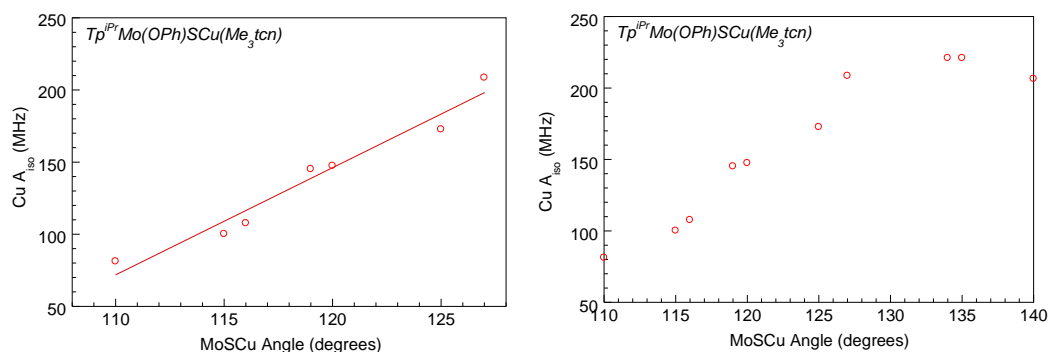


Figure 3.18: Calculated isotropic Cu hyperfine as a function of varying MoSCu bond angle: all data points calculated (right) and the linear region only (left).

DFT-calculated g -tensors range from 1.88-1.89 for g_{min} , 1.94-1.95 for g_{mid} , and 2.01-2.03 for g_{max} over the range of MoSCu bond angles and are in good agreement with the observed experimental values, though as observed for the CODH enzyme active site model calculations, g_{max} is calculated somewhat larger than the experimental value. Figure 3.18 shows the isotropic Cu hyperfine as a function of MoSCu bond angle, and on the left panel we see that the DFT-calculated Cu hyperfine increases linearly from 110° to 130° . The dependence of the isotropic hyperfine on the MoSCu bond angle is significant as the hyperfine changes by almost a factor of three over the 20° range on the left. At $\sim 130^\circ$, the hyperfine stops increasing and decreases at $\sim 140^\circ$, which indicates that the maximum amount of spin in a Cu s -orbital occurs at a MoSCu bond angle of $\sim 130^\circ - 135^\circ$.

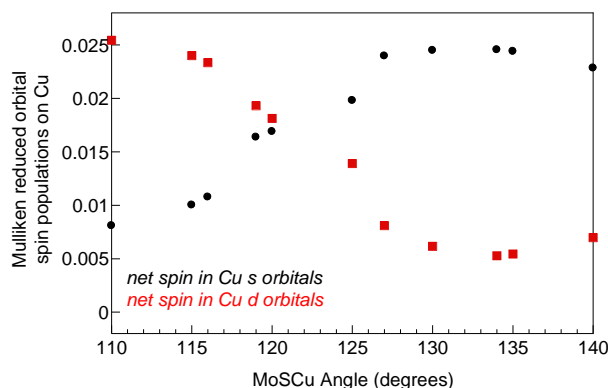


Figure 3.19: Mulliken reduced orbital spin populations on Cu as a function of MoSCu bond angles in $\text{Tp}^{\text{iPr}}\text{MoO}(\text{OPh})(\mu\text{-S})\text{Cu}(\text{Me}_3\text{tacn})$.

Figure 3.19 confirms that in fact net spin populations in Cu s-orbitals reach a maximum at a MoSCu bond angle of $\sim 130^\circ - 135^\circ$, at an expense of net spin in Cu d-orbitals. The sum of the spin populations in s and d orbitals stays relatively constant over the bond angle range, which suggests that the changes in Cu hyperfine are likely not a matter of sulfur-copper orbital overlap in general, but rather of which d-orbital it is that interacts with the sulfur p orbital in the SOMO wavefunction. In the CODH model compounds the effective symmetry of Cu is $\sim C_{3v}$, where d_{z^2} -s orbital mixing is symmetry allowed, so that spin density that delocalizes into a d_{z^2} -type orbital on Cu can be mixed into the Cu 5s orbital.

3.4.4 Electronic Absorption and Magnetic Circular Dichroism of CODH Model Compounds

Electronic absorption spectra were acquired under both anaerobic and aerobic conditions. Figure 3.20 shows the overlay of the electronic absorption spectra of the

anaerobic room-temperature solutions prepared in the glovebox and the aerobic spectra of the very same solutions after air exposure, where following the anaerobic scan the cuvette was opened and exposed to atmosphere for ~10-15 minutes and the aerobic scan was then obtained. The right panel of Figure 3.20 shows the electronic absorption spectra for $\text{Tp}^{\text{iPr}}\text{MoO}(\text{OAr})\text{S}$, which differs from the model compounds in that it has a terminal rather than bridging sulfido ligand coordinated to Mo and is thus missing the $\text{Cu}(\text{Me}_3\text{tacn})$ part. We can see that the aerobic and anaerobic spectra of $\text{Tp}^{\text{iPr}}\text{MoO}(\text{OAr})\text{S}$ overlay one another perfectly.

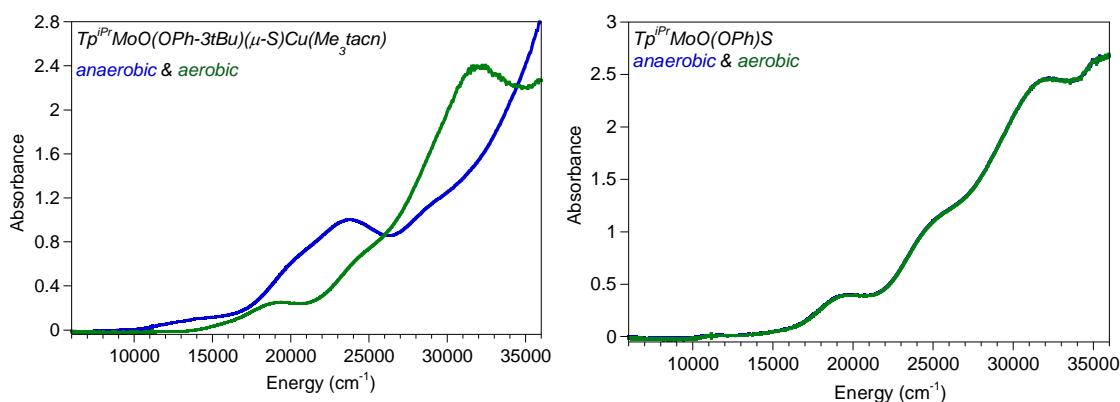


Figure 3.20: Anaerobic (green) and aerobic (blue) room-temperature electronic absorption spectra of $\text{Tp}^{\text{iPr}}\text{MoO}(\text{OPh-3tBu})(\mu\text{-S})\text{Cu}(\text{Me}_3\text{tacn})$ (left) and $\text{Tp}^{\text{iPr}}\text{MoO}(\text{OPh})\text{S}$ (right).

In the left panel of Figure 3.20 are the anaerobic and aerobic electronic absorption spectra of $\text{Tp}^{\text{iPr}}\text{MoO}(\text{OPh-3tBu})(\mu\text{-S})\text{Cu}(\text{Me}_3\text{tacn})$, and we observe significant differences in the electronic absorption spectrum upon air exposure. In fact, the aerobic spectra of all models strongly resemble that of the $\text{Tp}^{\text{Pr}}\text{MoOS}(\text{OPh})$ compound, which suggests that the $\text{Tp}^{\text{Pr}}\text{MoOS}(\text{OPhX})(\mu\text{-S})\text{Cu}(\text{Me}_3\text{tacn})$ models lose the $\text{Cu}(\text{Me}_3\text{tacn})$ unit. The aerobic and anaerobic electronic absorption spectra of the other model compounds

show the same changes as for Ar = Ph-3tBu (and are included in Appendix 6.2.4), though the spectral changes upon oxidation were most pronounced for Ar = Ph-3tBu, perhaps due to a slightly longer air exposure and more complete oxidation of the Ar = Ph-3tBu model than for the other model compounds. We observe that the bulk of the low-energy bands from $\sim 10000\text{ cm}^{-1}$ to $\sim 25000\text{ cm}^{-1}$ are lost in the electronic absorption spectra of the CODH models upon loss of the Cu(Me₃tacn), which suggests that those transitions are transitions involving Cu(Me₃tacn). As we know from section 3.4.2, the filled Cu d-orbital manifold mixed with sulfido character lies just below the empty Mo d-orbital manifold, so that the Cu specific transitions from 10000 cm^{-1} to 25000 cm^{-1} can be reasonably assigned as Cu (or Cu/S) \rightarrow Mo charge transfer bands by comparison of the spectra in Figure 3.20. Continuing that line of reasoning, the band observed for Tp^{iPr}MoO(OAr)S at $\sim 18000\text{ cm}^{-1}$ to 19000 cm^{-1} may be a S \rightarrow Mo charge transfer band, where in the absence of the Cu center the spectra may show LMCT bands from the sulfido ligand manifold to the lowest lying Mo d-orbital(s). We next used the DFT-calculated electronic structure and calculated electronic absorption spectra to further explore the band assignments of the lower energy part of the observed experimental absorption spectra of the model compounds, where calculated results also assign low-energy bands as MMCT bands in agreement to what is deduced by consideration of the experimental data alone.

The electronic absorption data for the CODH models is shown in Figure 3.21, and we observe that the spectra of the model compounds are very similar to one another with only small band shifts for the various models (OAr = Ph, Ph-2sBu, Ph-4sBu, and Ph-

3tBu). The largest difference is observed for the OAr = Ph-4sBu model, where the bands appear at the same energies as for the other model compounds but at different relative intensities, specifically, bands at $\sim 11000\text{ cm}^{-1}$ to $\sim 24000\text{ cm}^{-1}$ have a lower intensity relative to the higher energy bands at $\sim 28000\text{ cm}^{-1}$ +.

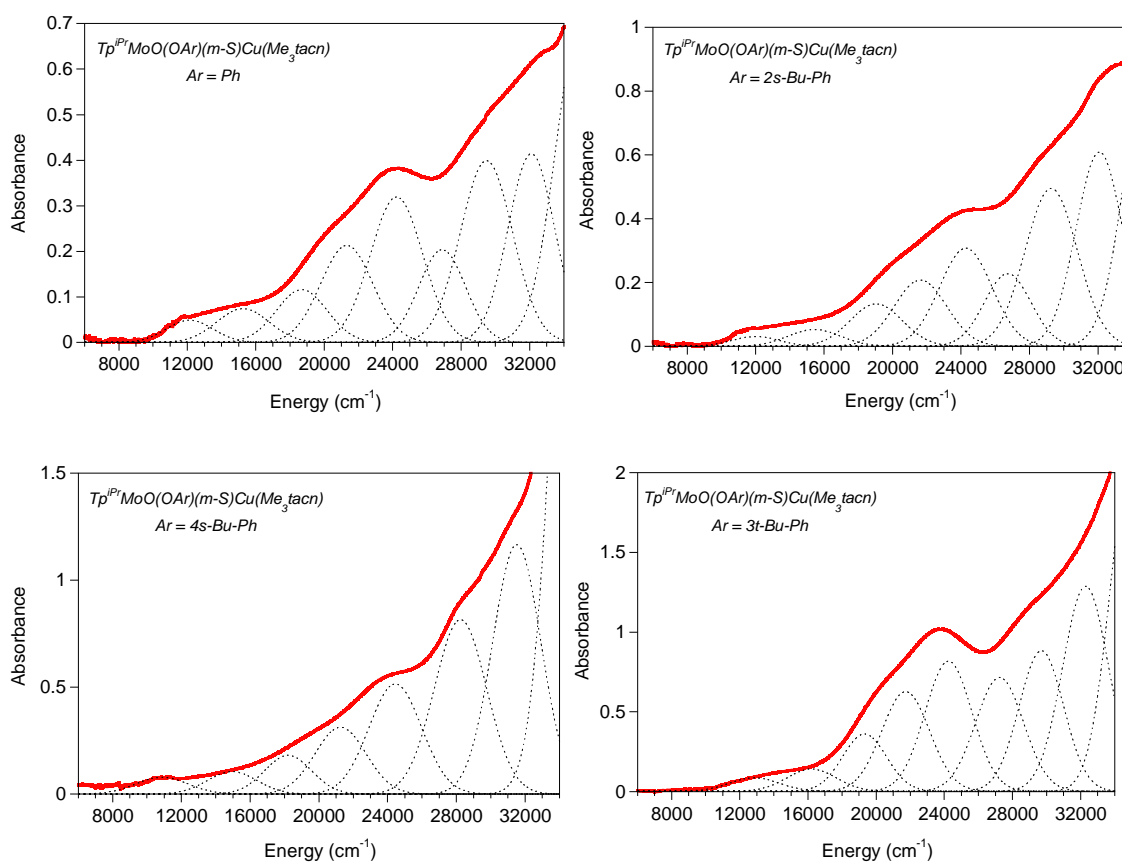


Figure 3.21: Room temperature electronic absorption spectra of $\text{Tp}^{\text{iPr}}\text{MoO}(\text{OAr})(\mu\text{-S})\text{Cu}(\text{Me}_3\text{tacn})$, where Ar = Ph, 2s-Bu-Ph, 4s-Bu-Ph or 3t-Bu-Ph. Spectra are room temperature solutions in butyronitrile.

Figure 3.22 shows an overlay of the DFT-calculated (black) and experimental (red) electronic solution spectrum of $\text{Tp}^{\text{iPr}}\text{MoO}(\text{OPh})(\mu\text{-S})\text{Cu}(\text{Me}_3\text{tacn})$, as well as calculated oscillator strengths (orange bars). The DFT-calculated spectrum agrees well

with the experimental data but is shifted to $\sim 2000\text{ cm}^{-1}$ lower energy than the experimental spectrum.

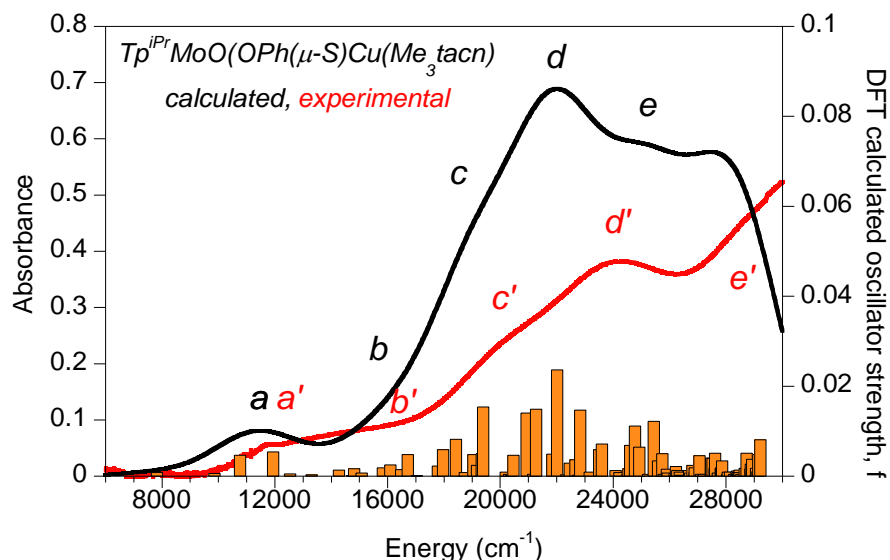


Figure 3.22: DFT-calculated (black, using bandwidths of 3000 cm^{-1}) and experimental (red) electronic solution spectrum of $\text{Tp}^{\text{iPr}}\text{MoO}(\text{OPh})(\mu\text{-S})\text{Cu}(\text{Me}_3\text{tacn})$, as well as calculated oscillator strengths (orange bars).

If we examine the calculated oscillator strengths (orange bars) we notice that there are a number of calculated transitions with about equal oscillator strengths contributing to the observed absorption bands throughout the spectrum, rather than a few intense transitions dominating. The distribution of oscillator strengths across the spectrum is related to the MoSCu bond angle of the $\text{Tp}^{\text{iPr}}\text{MoO}(\text{OPh})(\mu\text{-S})\text{Cu}(\text{Me}_3\text{tacn})$ model compound in the calculation, where changes in the MoSCu bond angle change the position of the sulfido ligand with respect to the Mo equatorial plane (a plane defined by the phenolate oxygen atom and the two nitrogen atoms of the Tp ligand bonded to Mo and cis to the axial oxo group). Narrower MoSCu bond angles move the sulfur below the equatorial plane of Mo (where “above” refers to the same side as the axial oxo and

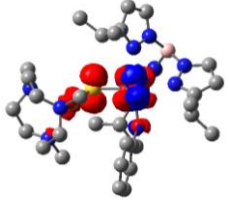
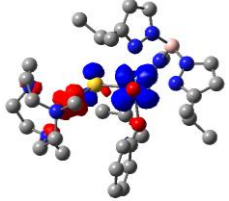
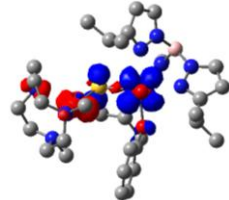

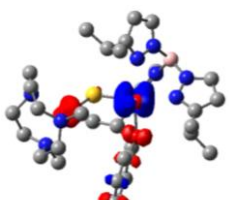
“below” to the opposite side of the axial oxo). The position of the sulfido ligand in turn orients the *Mo-d orbitals in the Cu/S based HOMO-n orbitals* with respect to the equatorial plane or the axial planes (where axial planes are along the xz and yz axis defined in section 3.4.1). A larger MoSCu bond angle brings the sulfido ligand closer to the equatorial Mo plane, and Mo d-orbitals in the Cu/S based HOMO-n orbitals are aligned either to the equatorial plane or the axial plane. A small MoSCu bond angle (such as the 110 ° angle for which the calculation results are shown in Figure 3.22) moves the sulfido ligand further below the equatorial plane, and the Mo d-orbitals in the Cu/S based HOMO-n orbitals are then tilted out of either plane to an orientation in-between the axial and equatorial plane. The orbital overlap of a Cu/S based HOMO-n orbital with the SOMO, LUMO, or LUMO+1 orbital that the charge transfer transition goes into is proportional to the oscillator strength expected for the transition.

Since the SOMO, LUMO, and LUMO+1 Mo d-orbitals are oriented either in the equatorial plane or axial planes, overlap of those acceptor orbitals with the Cu/S based HOMO-n orbitals will be either small or large when the Mo-d orbitals in the Cu/S based HOMO-n orbitals are also oriented with respect to the equatorial or axial planes, as is the case for larger values of the MoSCu bond angle. The calculated absorption spectrum then shows transitions of high oscillator strength (good overlap) and low oscillator strength (poor overlap). In contrast, for a small MoSCu bond angle such as 110°, overlap between the SOMO, LUMO, and LUMO+1 Mo d-orbitals and the Cu/S based HOMO-n orbitals will be intermediate for almost all MMCT transitions, leading to an absorption spectrum where the oscillator strength is distributed more equally over the MMCT transitions

throughout the spectrum. This is the case for the experimentally observed spectrum as well as the calculated spectrum shown in Figure 3.22. Thus the MoSCu bond angle influences the relative intensities of the MMCT bands throughout the absorption spectrum.

Table 3.15 shows the band assignments for the most intense low-energy calculated transitions of $\text{Tp}^{\text{iPr}}\text{MoO}(\text{OPh})(\mu\text{-S})\text{Cu}(\text{Me}_3\text{tacn})$. The electron-density-difference maps (EDDMs) for the transitions are shown in the far right column and represent the change of electron density during the transition, where regions of loss are red, and regions of gain are blue. The most intense calculated transitions are all charge transfer transitions, and their charge transfer character is listed in the table but also clearly visible from the EDDMs. The first transition in Table 3.15, calculated at $\sim 7800\text{ cm}^{-1}$, is a Mo d-d transition from the SOMO to the HOMO, but has considerable Cu/S to Mo/ O_{ax} charge transfer character also, since the SOMO Mo d-orbital is delocalized over the Cu and S also while the HOMO is localized on the Mo and axial oxo ligand. The following transitions 2-10 calculated at $\sim 10800 - 24800\text{ cm}^{-1}$ are all MMCT transitions from Cu to Mo with LMCT character from either sulfido or phenolate to Mo mixed in. Cu/S to Mo charge transfer character is predominant at lower energies ($\sim 10800 - \sim 18400\text{ cm}^{-1}$), while at higher energies ($\sim 19400 - \sim 24800\text{ cm}^{-1}$) both Cu/S to Mo CT and Cu/Phenolate to Mo CT transitions occur. Transition 11 calculated at $\sim 25400\text{ cm}^{-1}$ is a

Table 3.15: DFT-calculated band assignments for $\text{Tp}^{\text{iPr}}\text{MoO}(\text{OPh})(\mu\text{-S})\text{Cu}(\text{Me}_3\text{tacn})$.

	Transition energy (cm^{-1})	Calculated oscillator strength, f	Largest contribution to the transition	Charge transfer character	Electron density difference map, isovalue 0.002
1	~7800	0.0009	α SOMO-LUMO	Cu/S/Mo \rightarrow Mo/ O_{ax} (Mo d-d)	
2	~10800	0.0047	β HOMO-SOMO	Cu \rightarrow Mo/S	
3	~11900	0.0055	β (H-1)-SOMO	Cu \rightarrow Mo/S	
4	~18000, ~18400	0.0060 + 0.0083	β (H-2)-LUMO	Cu/S \rightarrow Mo/ O_{ax}	
5	19.4	0.0154	β (H-5)-SOMO	Cu/Phenolate \rightarrow Mo	

6	20.9	0.0141	β (H-2)-(L+1)	Cu/S \rightarrow Mo/O _{ax}	
7	21.3	0.0149	α (H-5)-LUMO	Cu/Phenolate \rightarrow Mo/O _{ax}	
8	22.0	0.0236	β (H-3)-LUMO	Cu/S \rightarrow Mo/O _{ax}	
9	22.8	0.0147	β (H-4)-(L+1) β (H-5)-LUMO	Cu/Phenolate \rightarrow Mo/O _{ax}	
10	24.8	0.0112	β (H-5)-LUMO	Cu/Phenolate \rightarrow Mo/O _{ax}	
11	25.4	0.0122	α SOMO- (L+10)	Cu/S/Mo \rightarrow Tp/Mo	

charge transfer transition from the delocalized SOMO to a higher-lying Mo/Tp orbital, and marks the energy in the calculated absorption spectrum at which transitions involving other ligands (Tp, tacn) start occurring.

Based on the band assignments of the calculated spectrum, a band assignment for the experimental electronic absorption spectrum has been proposed in Table 3.16. We notice that the first calculated transition (SOMO→LUMO, at $\sim 7800\text{ cm}^{-1}$) is too weak to be observed in either the calculated or experimental absorption spectrum. While it is hard to assign specific bands in a one-to-one correlation between experiment and calculation when there are a number of bands close to each other in energy, we can divide the

Table 3.16: Energies of Gaussian resolved electronic absorption bands of $\text{Tp}^{\text{iPr}}\text{MoO}(\text{OAr})(\mu\text{-S})\text{Cu}(\text{Me}_3\text{tacn})$.

EA peaks	Ar =				Region	Assignment
	Ph	2s-Bu-Ph	4s-Bu-Ph	3t-Bu-Ph		
Energy (cm^{-1})	12133	11991	10870	12865	a'	MMCT: HOMO, H-1 → SOMO
	15250	15489	14960	16214	b'	lower intensity MMCT bands
	18685	19044	18207	19318	c'	Cu/S → Mo CT
	21315	21626	21259	21734	c'	Cu/phenolate → Mo CT
	24226	24275	24446	24247	d'	MMCT, possibly (H-4 → SOMO)
	26887	26724	28239	27241	e'	Cu/phenolate → Mo MMCT & Cu/S → Tp/Mo CT

calculated and experimental spectra into regions (marked a-e and a'-e' in Figure 3.22), and transfer the computational band assignments per region to the experimental spectrum. The results of this are shown in Table 3.16, where even for the experimental band at $\sim 24200 - 24400 \text{ cm}^{-1}$, which is the most transition of the spectrum below $\sim 28000 \text{ cm}^{-1}$ both calculated and experimentally, we cannot say with complete certainty that the Cu to Mo CT band originates from the HOMO-4 orbital, though we can say that this intense band is a Cu to Mo MMCT band originating from one of the lower Cu d-orbitals.

MCD spectra were acquired as anaerobic frozen butyronitrile solutions. As a control the variable-temperature-variable-field (VTVH) MCD of $\text{Tp}^{\text{iPr}}\text{Mo}(\text{OPh-4sBu})\text{SCu}(\text{Me}_3\text{tcn})$ model was acquired on the same sample as the MCD spectrum of $\text{Tp}^{\text{iPr}}\text{Mo}(\text{OPh-4sBu})\text{SCu}(\text{Me}_3\text{tcn})$ in Figure 3.24. The concern lies in that these MoSCu model compounds are very air-sensitive, and we wanted to make sure that the MCD sample was not decomposed or anything besides $\text{Tp}^{\text{iPr}}\text{Mo}^{\text{V}}(\text{OPh-4sBu})\text{SCu}(\text{Me}_3\text{tcn})$.

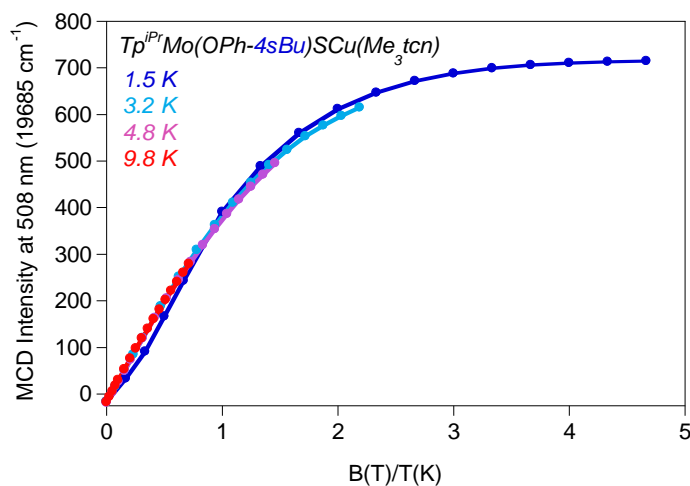


Figure 3.23: Variable-temperature-variable-magnetic-field MCD of the $\text{Tp}^{\text{iPr}}\text{Mo}(\text{OPh-4sBu})\text{SCu}(\text{Me}_3\text{tcn})$ model.

The observation of a C-term MCD signal confirms that the compound is indeed paramagnetic (as opposed to an oxidized Mo^{VI} compound). VTVH MCD was then used to confirm that the paramagnetic species is an S = ½ species. At low temperatures C-term MCD (highlighted in blue in Eq. 26) dominates the MCD signal due to the 1/T dependence of the C-term MCD intensity. VTVH effectively factors out the 1/T temperature dependence of the C-term signal by plotting MCD intensity as a function of B/T (where B is the external magnetic field, T is temperature) rather than just B.¹⁴²

$$\frac{\Delta A}{E} = \gamma\beta H \left[A_1 \left(-\frac{\partial f(E)}{\partial E} \right) + \left(B_0 + \frac{C_0}{kT} \right) f(E) \right] \quad \text{Eq. 26}$$

Thus a system whose ground state Boltzmann populations do not change as a function of temperature (i.e. an S = ½ system) should show no temperature dependence of MCD intensity plotted as a function of B/T. Figure 3.23 shows that MCD intensities for temperatures from 1.5 K to 9.8 K indeed overlay one another and thus show no temperature dependence beyond what is expected for a C-term MCD signal. The second type of control experiment involved acquiring low-temperature electronic absorption on the MCD sample after the MCD spectra were acquired without thawing the sample in the process of transferring from one instrument to another. These “post-MCD” electronic absorption spectra are included in Appendix 6.2.2. While these low-temperature absorption spectra are not as good a quality as the room-temperature electronic absorption spectra due to scattering for the frozen glass samples, they do confirm that the electronic absorption spectrum after running MCD is still that of the anaerobic model compound.

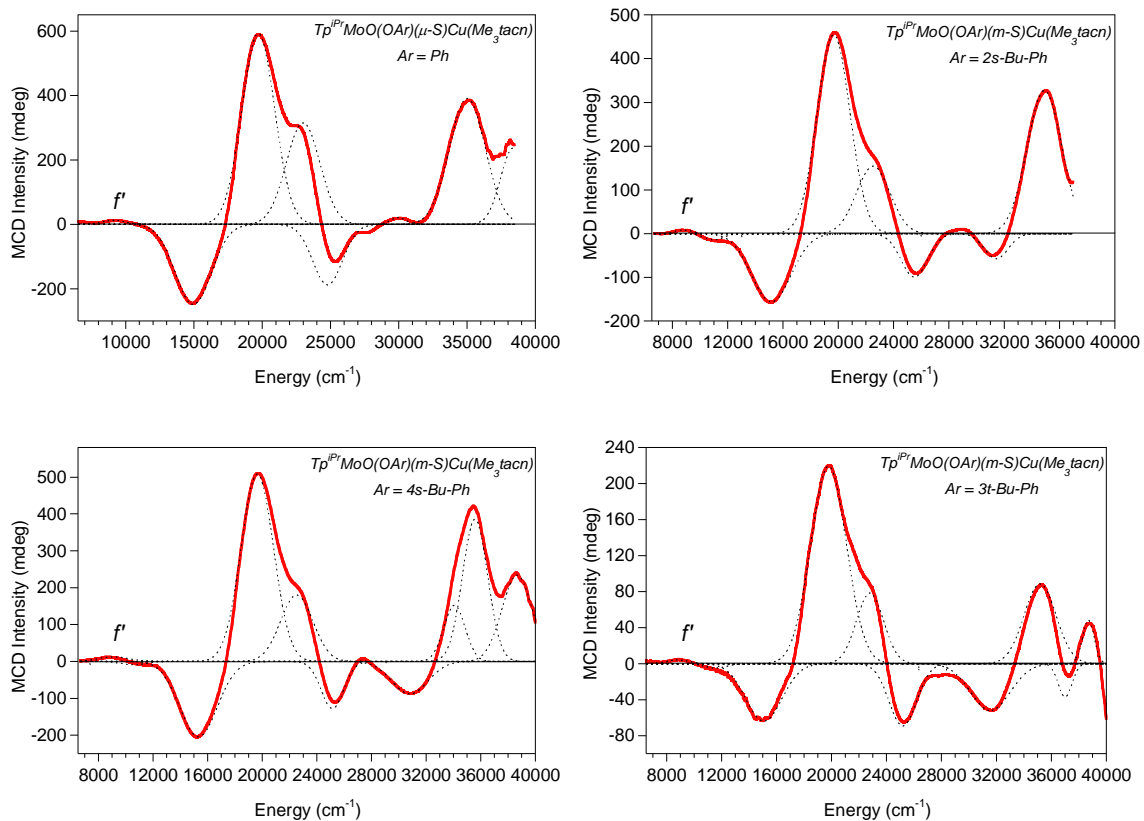


Figure 3.24: C-term MCD spectra of $Tp^{iPr}MoO(OAr)(\mu-S)Cu(Me_3tacn)$, where Ar = Ph, 2s-Bu-Ph, 4s-Bu-Ph or 3t-Bu-Ph. Spectra are 5 K, 7 T – 0 T data, where the compounds were prepared as frozen solutions in butyronitrile.

Figure 3.24 shows the C-term MCD spectra for the model compounds, and we observe that the frozen solution spectra acquired for the models are very similar to one another with only small band shifts. All observed positive and negative bands are temperature-dependent C-terms, which is confirmed by the temperature dependence of the band intensities for the 5 K, 10 K, and 20 K MCD spectra overlay (included in Appendix 6.2.1). The MCD spectra show a weak, low-energy, positive C-term band at $\sim 8800 - \sim 9100\text{ cm}^{-1}$, marked as f' in the experimental MCD spectra. This is assigned as the α SOMO-LUMO transition that is too weak to be observed in the electronic absorption spectra of the compounds. In general, d-d transitions that are too weak to be

observed in the electronic absorption spectrum (where they are dipole forbidden transition), can often be observed in the MCD spectrum, where they gain some intensity due to the fact that they are metal-based transitions, and metals have large spin-orbit coupling constants. Since the α SOMO is not a pure Mo-d orbital but is rather delocalized over the [MoSCu] unit, band f' has Cu/S \rightarrow Mo charge transfer character. An overlay of the calculated and experimental C-term MCD spectrum for $\text{Tp}^{\text{iPr}}\text{MoO}(\text{OPh})(\mu\text{-S})\text{Cu}(\text{Me}_3\text{tacn})$ is shown in Figure 3.25. As with the calculated and experimental absorption spectra, we observe that the calculated spectrum is shifted to lower energies than the experimental spectrum, by approximately 2000 cm^{-1} for most bands. The calculated spectrum shows some differences to the experimental MCD in band intensities, too, where the relative intensities of bands 4 and 5 differ in the calculated and experimental spectrum. Beyond the above mentioned differences, the calculated and experimental MCD spectra agree reasonably well.

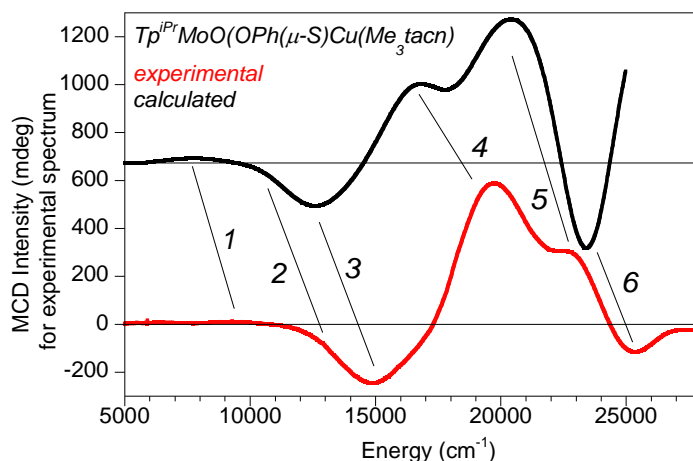


Figure 3.25: DFT-calculated (black, bandwidth 2500 cm^{-1}) and experimental (red) C-term MCD spectrum of $\text{Tp}^{\text{iPr}}\text{MoO}(\text{OPh})(\mu\text{-S})\text{Cu}(\text{Me}_3\text{tacn})$.

Table 3.17 summarizes the band assignments for the MCD transitions of the CODH model compounds, which are based on the DFT-calculated MCD spectrum. Band 1 possesses a greater MCD intensity in the DFT-calculated spectrum compared to DFT-calculated electronic absorption, just alike to the experimental electronic absorption vs. MCD intensity of band 1, and is calculated to be the α SOMO-LUMO transition in the DFT MCD spectrum, consistent with our arguments above for the assignment of band 1. Bands 2 and 3 are negative C-term features, and are not resolved at the experimental band width for $\text{Tp}^{\text{iPr}}\text{MoO}(\text{OAr})(\mu\text{-S})\text{Cu}(\text{Me}_3\text{tacn})$, but have been included as separate bands since they are resolved in the MCD spectra of the other CODH models (Figure 3.24).

Table 3.17: Energies of Gaussian resolved MCD bands of $\text{Tp}^{\text{iPr}}\text{MoO}(\text{OAr})(\mu\text{-S})\text{Cu}(\text{Me}_3\text{tacn})$.

MCD peaks	Ar =				Band	Assignment
	Ph	2s-Bu-Ph	4s-Bu-Ph	3t-Bu-Ph		
Energy (cm^{-1})	9123 +	8789 +	9096 +	8800 +	1	α SOMO-LUMO
	14946 -	10984 -	10560 -	11571 -	2	β (H-1)-SOMO
		15158 -	15329 -	15071 -	3	α HOMO-LUMO
	19705 +	19659 +	19633 +	19785 +	4	α (H-2)-LUMO
	22993 +	22524 +	22523 +	22803 +	5	β (H-5)-SOMO α (H-5)-LUMO β (H-3)-LUMO
	24784 -	25491 -	25132 -	25185 -	6	α (H-5)-(L+1)

Bands 2 and 3 are MMCT transitions that assigned as β (H-1)-SOMO (2) and α HOMO-LUMO (3) transitions. MCD band 2 corresponds to a/a' in the calculated/ experimental electronic absorption spectra, while band 3 was present with very low oscillator strength in the calculated electronic absorption spectrum. Band 4 is assigned as the α (H-2)-LUMO transition, also present with very low oscillator strength in the calculated electronic absorption spectrum. Band 4 is also a Cu \rightarrow Mo MMCT band. Band 5 is calculated to derive its positive MCD intensity from three main contributions, corresponding to calculated transitions 5, 7, and 8 from Table 3.15.

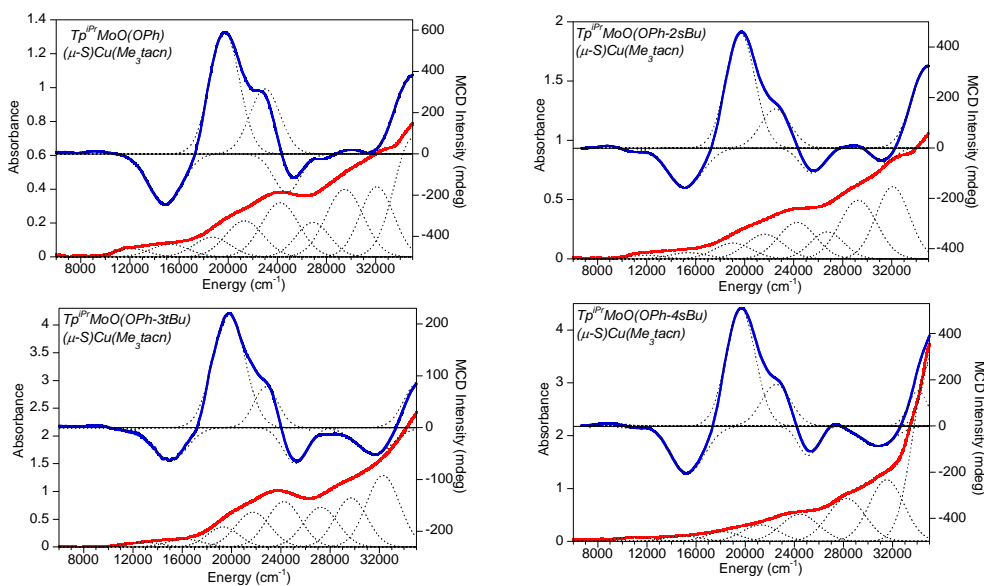


Figure 3.26: Overlay of room-temperature electronic absorption and 5 K MCD for of $\text{Tp}^{\text{iPr}}\text{MoO}(\text{OAr})(\mu\text{-S})\text{Cu}(\text{Me}_3\text{tacn})$, where $\text{Ar} = \text{Ph}, 2\text{s-Bu-Ph}, 4\text{s-Bu-Ph}$ or 3t-Bu-Ph .

These transitions are Cu/phenolate \rightarrow Mo CT transitions as well as Cu/S \rightarrow Mo CT transitions and corresponds to region c' of the electronic absorption spectrum. Band 6 is assigned as the α (H-5)-(L+1) transition, which is a Cu/Phenolate \rightarrow Mo MMCT band. Thus all MCD bands below $\sim 27000 \text{ cm}^{-1}$ are assigned as Cu \rightarrow Mo MMCT bands with S

or phenolate \rightarrow Mo LMCT character mixed in. This is what we observe in the electronic absorption of these compounds as well, and underscores the large degree of electronic communication between the metal centers of the [MoSCu] unit.

3.5 Conclusion

We have examined the electronic structure of the interesting heterobimetallic active site of the CODH enzyme computationally and compared our computed EPR parameters to the experimental EPR parameters for the enzyme available in the literature. The calculated EPR g-tensor of an equatorial oxo bound to Mo^V state strongly disagrees with the experimental g-tensor, where the g_{\min} for a dioxo Mo species is very low, a difference that should be easily experimentally measurable. Such low values of g_{\min} are also known for synthetic dioxo Mo compounds. This is very strong evidence against the presence of an equatorial oxo ligand in the EPR signal-giving species for the CODH enzyme. Calculated EPR parameters for an equatorial hydroxo or bicarbonate ligand were in good agreement with the experimental EPR parameters of the reduced enzyme, leaving both ligands as viable options for the signal-giving species.

We observed that the Cu hyperfine has a large isotropic and small dipolar component, and that the magnitude of the isotropic Cu hyperfine is tied to the amount of Cu 5 s-character in the SOMO wavefunction. We propose that the Cu 5 s character in the SOMO wavefunction derives from symmetry-allowed orbital mixing of a d_{z^2} type with the 5 s Cu orbital, where the unpaired spin population of the d_{z^2} type orbital on Cu depends on the overlap of that orbital with one of the lobes of the bridging-sulfido ligand p-orbital, which is in turn controlled by the SCuS bond angle.

CO binding at Cu induces a geometry change at Cu towards a trigonal Cu site, which will optimize to a completely trigonal Cu center in the absence of any geometric constraints. Electronic structure calculations of the enzyme active site with CO bound at Cu indicate that the trigonal Cu site (SCuS bond angle of 120°) allows for a greater activation of the CO for nucleophilic attack than a geometry with a more linear SCuS bond angle (156°). CO is activated for nucleophilic attack on the carbon by the Cu-CO bonding interaction, which is a combination of Cu-C σ bonding and Cu-CO π backbonding.

The Cu hyperfine in of synthetic CODH model compounds is also very sensitive to the Cu-S overlap, which is modulated by changes in the MoSCu bond angle in the synthetic models, similarly as for changes in the SCuS bond angle in the enzyme active site calculations. The EPR parameters of the model compounds are very similar to those observed for the enzyme active site, albeit with a larger isotropic Cu hyperfine in the models compared to the enzyme. This confirms the ability of the models to represent the electronic structure of the active site in addition to being good geometric models of the the $[\text{O}_{\text{ax}}\text{MoSCu}]$ unit.

There is a large calculated covalency across the $[\text{MoSCu}]$ unit in both the enzyme active site computational model and the model compounds. This calculated covalency is confirmed experimentally by the fact that both the electronic absorption and MCD spectra of the model compounds are dominated by Cu \rightarrow Mo MMCT (mixed with S or phenolate \rightarrow Mo CT) transitions below $\sim 27000 \text{ cm}^{-1}$. The observation of these MMCT bands is an advantage of working with the synthetic model compounds, where the

absence of the iron-sulfur cluster cofactors allows for the observation of the MMCT bands in the absorption spectra. This covalency across the [MoSCu] unit in the SOMO wavefunction of the Mo^{V} structure supports a role of the [MoSCu] unit in catalysis, where a large [MoSCu] covalency would be beneficial for electron transfer from the substrate to the Mo via the Cu and S centers.

Electronic structure calculations indicate a discrepancy between the orbital covalency of the [MoSCu] unit and the spin density distribution across the [MoSCu] unit. We have proposed a VBCI mechanism that accounts for the observed ground state spin density distribution in terms of excited state contributions to the ground state. The VBCI description of MMCT states shows how (1) MMCT from Cu orbitals into the SOMO $\text{Mo}(\text{d}_{\text{xy}})$ orbital increases positive spin density on Cu and (2) MMCT from Cu orbitals into the higher-lying empty Mo d orbitals increases alpha spin density on Mo and beta spin density on Cu (since the triplet state is energetically lower than the singlet). This leads to the net alpha spin density on Cu being lowered while the MoSCu orbital covalency/delocalization is large. Thus the VBCI description of the active site/model compounds also supports a strong Mo-Cu electronic communication. We see evidence of the Cu/Mo electronic communication via excited state contributions to the ground state even more plainly in the fact that there is any Cu hyperfine observed at all, since in the ground state Cu^{I} is a d^{10} metal and should have no net spin density (and thus no hyperfine) at all.

What we learned from our computational and experimental data thus supports catalytic mechanism II, which features CO binding at Cu and electron transfer from the

substrate to Mo through Cu and S_μ. Not only is the large covalency of the [MoSCu] unit suggestive to it having a possible role in the catalytic cycle, but CO binding at Cu can act to activate the substrate for nucleophilic attack by an equatorial ligand.

CHAPTER 4

4. SPECTROSCOPIC AND COMPUTATIONAL STUDIES OF CLASS III
VALENCE DELOCALIZED RHENIUM DIMER MOLECULES4.1 Introduction

The element rhenium was discovered less than a century ago by Walter and Ida Noddack 1925, and the existence of quadruple bonds between was recognized less than half a century ago by F. Albert Cotton *et al.* in 1964.¹⁴³ Though Russian scientists first reported the synthesis of $[\text{Re}_2\text{Cl}_8]^{2-}$, and noted that the Re-Re bond distance was shorter than that found in the rhenium metal, the existence of a quadruple bond in $[\text{Re}_2\text{Cl}_8]^{2-}$ was first recognized by Cotton *et al.*¹⁴³

Since then a large number of derivatives of $[\text{Re}_2\text{Cl}_8]^{2-}$ have been synthesized and structurally characterized.¹⁴³⁻¹⁵² These rhenium dimer complexes have bond orders of 3, 3.5 and 4, where a triple bond can either be electron-poor, corresponding to a $\sigma^2\pi^4\delta^2$ configuration, or electron-rich corresponding to a $\sigma^2\pi^4\delta^2\delta^{*2}$ configuration.¹⁴³ Likewise, rhenium dimers of Re-Re bond order 3.5 can have an electron-rich ($\sigma^2\pi^4\delta^2\delta^{*1}$) or electron-poor ($\sigma^2\pi^4\delta^1$) Re-Re bond. It is reported the Re-Re bonds are susceptible to cleavage by π donor ligands such as CO and CN^- , and there are a number of Re dimer compounds of the form $\text{Re}_2\text{X}_4(\text{LL})_2$ where LL is a bidentate ligand, such as 1,2-bis(diphenylphosphino)ethane (= dppe), and other derivatives of this bidentate ligand.¹⁵³⁻

¹⁵⁵ Another class of $[\text{Re}_2\text{Cl}_8]^{2-}$ derivatives includes a series of compounds where the chloride ligands are replaced with various phosphine ligands of form PR_3 (where R = phenyl, propyl, methyl, ethyl, or combinations thereof), following the compound formula of $\text{Re}_2\text{X}_{n+4}(\text{PR}_3)_{4-n}$.¹⁴³ These Re dimers of $\text{Re}_2\text{X}_{n+4}(\text{PR}_3)_{4-n}$ stoichiometry are very robust to both electrical and chemical oxidation or reductions, and have been interconverted by different routes of mixed chemical and electrical redox steps. Various studies have reported their syntheses,^{143–145,148,150,156,157} structural characterizations,^{143–145,148–150,152} and electrochemical behavior.^{143,147,150,157} Mixed electrochemical and chemical synthesis schemes have been published,¹⁵⁷ where the order of the electrochemical and chemical reaction steps was found to be interchangeable, such as for example in the route of $\text{Re}_2\text{Cl}_4(\text{PR}_3)_4$ to $\text{Re}_2\text{Cl}_6(\text{PR}_3)_2$, which can proceed either via an EECC or an ECEC route (E = electrochemical step, C = chemical step).

The versatile electrochemistry and chemistry of these $\text{Re}_2\text{X}_{n+4}(\text{PR}_3)_{4-n}$ compounds affords a series of Re-dimer compounds with metal-metal bond orders 3, 3.5 and 4 that have identical monodentate ligands, allowing for a direct comparison of structural parameters.¹⁵⁰ Specifically, $\text{Re}_2\text{Cl}_6(\text{PR}_3)_2$, $\text{Re}_2\text{Cl}_5(\text{PR}_3)_3^+$, $\text{Re}_2\text{Cl}_4(\text{PMe}_3)_4^{2+}$ share a $\sigma^2\pi^4\delta^2$ configuration, $\text{Re}_2\text{Cl}_6(\text{PR}_3)_2^-$, $\text{Re}_2\text{Cl}_5(\text{PR}_3)_3$, $\text{Re}_2\text{Cl}_4(\text{PMe}_3)_4^+$ share a $\sigma^2\pi^4\delta^2\delta^{*1}$ configuration, and $\text{Re}_2\text{Cl}_5(\text{PR}_3)_3^-$, $\text{Re}_2\text{Cl}_4(\text{PMe}_3)_4$ share the $\sigma^2\pi^4\delta^2\delta^{*2}$ configuration. Thus $\text{Re}_2\text{Cl}_4(\text{PMe}_2\text{Ph})_4$, $\text{Re}_2\text{Cl}_4(\text{PMe}_2\text{Ph})_4^+$, and $\text{Re}_2\text{Cl}_4(\text{PMe}_2\text{Ph})_4^{2+}$ form such a series of identical ligands but varying bond orders of 3, 3.5, and 4, respectively. Interestingly, Re-Re bond lengths changes little as the bond order changes between 3 (2.241 Å), 3.5 (2.218 Å) and 4 (2.215 Å) in this series. This has been attributed to the increase in the nuclear

charge of Re, where an ion with a larger nuclear charge will cause its valence orbitals to contract thus decreasing the contributions of the σ and π bonds to the overall Re-Re bond.¹⁴³

Starting from $[\text{Re}_2\text{Cl}_8]^{2-}$, one synthetic route involves the addition of a monodentate, basic phosphine, yielding $\text{Re}_2\text{Cl}_6(\text{PR}_3)_2$, which can then be reduced to $\text{Re}_2\text{Cl}_4(\text{PR}_3)_4$ by reflux with acetone or alcohols. NO^+PF_6^- , which is a mild oxidant, can be used to generate the $\text{Re}_2\text{Cl}_4(\text{PR}_3)_4^+$ cation.¹⁴³ Studies have been done on the role of the solvent in the reaction, where it was found that the propanol solvent itself may act as the reductant.¹⁴⁴ Alternatively, Re_3Cl_9 can react with a tertiary phosphine and give $\text{Re}_2\text{X}_4(\text{PR}_3)_4$ by reductive cleavage, where X = Cl, I, or Br.

Structural studies revealed that these $\text{Re}_2\text{X}_4(\text{PR}_3)_4$ compounds have eclipsed, noncentrosymmetric structures. Having an eclipsed, rather than a staggered, geometry allows the formation of the δ bond since the δ bonding interaction requires the overlap of all four lobes of the d-orbital that is in a plane perpendicular to the axis of the Re-Re bond. The compounds adapt noncentrosymmetric conformations to minimize steric strain between bulky tertiary phosphine ligands. Re dimer complexes of bond order 3.5 and 4 feature short Re-Re bonds, where the quadruply bonded $[\text{Re}_2\text{Cl}_8]^{2-}$ has a Re-Re bond length of $\sim 2.21\text{-}2.25$ Å depending on the nature of the counterion, and the $\text{Re}^{2+}/\text{Re}^{3+}$ core dimers with an electron-rich bond of order 3.5 has Re-Re bond lengths ranging $\sim 2.22\text{-}2.27$ Å.¹⁴³ The ligand sets can also influence Re-Re bond lengths, and Cotton *et al.* studied the effect of substituting halide ligands with weakly coordinating triflate ligands. By decreasing the σ and π donating abilities of the ligand and thus decreasing the metal-

ligand interaction, a shortened Re-Re bond was observed, 2.156 Å, the shortest reported quadruple bond.¹⁵⁸

Gas-phase photoelectron spectroscopy studies on $\text{Re}_2\text{Cl}_4(\text{PMe}_3)_4$ and the tungsten analogue of the compound allowed the authors to construct a scheme of the frontier orbitals and below and their energies. The following electronic structure was deduced from the data (in descending energy): δ^* , δ , two sets of spin-orbit split π orbitals, P σ , MM σ and Cl lone pairs. The ligand (P, Cl) orbitals in this scheme are the ones that did not have large shifts in ionization energies upon metal substitution.¹⁵⁹ Room temperature magnetic circular dichroism (MCD) data for have been reported for $[\text{Re}_2\text{Br}_8]^{2-}$ and $[\text{Re}_2\text{Cl}_8]^{2-}$, where the authors observed a weak, low-energy B-term MCD signal associated with the $\delta \rightarrow \delta^*$ band of those compounds as well as some A-terms at higher energies associated with LMCT transitions into the δ^* orbital.¹⁶⁰

Electronic absorption data was published several times for $\text{Re}_2\text{Cl}_4(\text{PPr}_3)_4\text{PF}_6$ in the literature, but the reports vary in the whether or not there are strong absorption bands between 12000 and 19000 cm^{-1} or not. In 1978, Brant *et al.*¹⁵⁷ published a report of the synthesis, electrochemical characteristics, and spectroscopic measurements (including IR, EPR, absorption, and XPS) of $\text{Re}_2\text{X}_4(\text{PPr}_3)_4$ where X = Cl or Br. The electronic absorption data was presented as a data table, but no absorption spectra, and lists the following absorption features: a strong band at $\sim 7100 \text{ cm}^{-1}$, a medium band at $\sim 16700 \text{ cm}^{-1}$, a shoulder at $\sim 20400 \text{ cm}^{-1}$ and a strong band at $\sim 23200 \text{ cm}^{-1}$ for X = Cl, and a strong band at $\sim 6900 \text{ cm}^{-1}$, shoulder at $\sim 19400 \text{ cm}^{-1}$ and strong band at $\sim 22400 \text{ cm}^{-1}$ for X = Br. The medium band at $\sim 16700 \text{ cm}^{-1}$ for $\text{Re}_2\text{Cl}_4(\text{PEt}_3)_4^+$ is what differs from other

reports and our own data (depending on the authors' interpretation of 'medium'). In 1983, Bursten *et al.*¹⁵¹ published a detailed computational and spectroscopic study of $\text{Re}_2\text{Cl}_4(\text{PPr}_3)_4\text{PF}_6$ wherein the absorption spectrum of the cation is published and has strong absorption bands at $\sim 14000\text{ cm}^{-1}$ and $\sim 17000\text{ cm}^{-1}$ (in addition to the uncontested bands at lower and higher energy, i.e. $\sim 7100\text{ cm}^{-1}$, $\sim 20400\text{ cm}^{-1}$, and $\sim 23200\text{ cm}^{-1}$). Also in 1983, Cotton *et al.*¹⁵⁰ published a report on the synthesis, and structural and spectroscopic characterization (IR, absorption and EPR) of $\text{Re}_2\text{Cl}_4(\text{PMe}_2\text{Ph})_4^{n+}$ where $n = 0, 1, \text{ or } 2$. In a data table in that paper the authors reports a weak band at $\sim 17100\text{ cm}^{-1}$ for the monocation (in addition to the strong bands at ~ 7400 and $\sim 22700\text{ cm}^{-1}$) and a very strong band at $\sim 13900\text{ cm}^{-1}$ for the dication (in addition to the strong bands at ~ 7200 and $\sim 23000\text{ cm}^{-1}$).

In the above-mentioned computational and spectroscopy paper¹⁵¹, Bursten and coworkers used relativistic SCF- α scattered-wave (SW) computational results to provide assignment for the electronic absorption bands of $\text{Re}_2\text{Cl}_4(\text{PPr}_3)_4\text{PF}_6$. Calculations modeled the n-propyl groups of the phosphine ligands as hydrogens. The energy ordering of the metal d-orbitals around the δ and δ^* frontier orbitals is reported as the σ^* and set of π^* orbitals laying just above δ^* , and just below the δ^* lie a set of π orbitals, followed by two set of Cl lone pair orbitals, then two sets of π orbitals and finally phosphine ligand orbitals. The metal character in the frontier orbitals is given as 63% for δ and 72% for δ^* , while the π set directly below the δ orbital has $\sim 20\%$ metal character, and the various other lower-lying π sets have $\sim 30\text{-}40\%$ metal character. The large band at $\sim 23700\text{ cm}^{-1}$ is

assigned as a LMCT band, while its low-energy shoulder is assigned as a $\delta \rightarrow \pi^*$ and/or σ^* transition. Most higher-lying bands are assigned as LMCT transitions.

Vibronic structure has been observed for the low-energy $\delta \rightarrow \delta^*$ band in $\text{Re}_2\text{Cl}_4(\text{PMe}_3)_4^+$, where the progression frequency observed was $275 \pm 5 \text{ cm}^{-1}$, where the sample was prepared as a KBr pellet, which brings up the question is the high concentration of Br- ions in the matrix may have influenced the stoichiometry of the compounds.¹⁵¹ Vibronic structure in related Re dimers includes are progression frequency of 247 cm^{-1} for $[\text{Re}_2\text{Cl}_8]$,¹⁶¹ and a progression frequency of 289 cm^{-1} for $\text{Re}_2\text{Cl}_6\text{P}(\text{Et}_3)_2$. Single crystal, low-temperature parallel and perpendicular polarized absorption data for $[\text{Re}_2\text{Cl}_8]^{2-}$, and $[\text{Re}_2\text{Br}_8]^{2-}$ provides more detail on the vibronic structure of the $\delta \rightarrow \delta^*$ band of these compounds.¹⁶² For $X = \text{Cl}$ the main progression had a frequency of 248 cm^{-1} (excited state, assigned as Re-Re stretch, compared to 274 cm^{-1} for the ground state) and a second progression had a frequency of 245 cm^{-1} and a vibronic origin of 115 cm^{-1} , which was assigned as a symmetric ReReCl bend. For $X = \text{Br}$ three progressions were observed, each with a frequency of 255 cm^{-1} (excited state, assigned as Re-Re stretch, compared to 277 cm^{-1} for the ground state) and origins of 98 cm^{-1} and 168 cm^{-1} (excited state, compared to 184 cm^{-1} for the ground state), which was assigned as a Re-Br stretch.

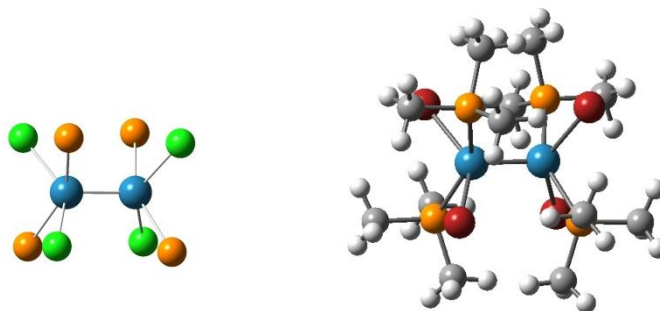


Figure 4.1: GaussView rendition of $\text{Re}_2\text{X}_4(\text{PMe}_3)_4^+$: blue = Re, orange = P, gray = C, white = H, green = Cl, maroon = Br; left: $\text{Re}_2\text{X}_4(\text{PMe}_3)_4^+$ with primary coordination to Re only (methyl groups omitted for clarity), right: complete $\text{Re}_2\text{X}_4(\text{PMe}_3)_4^+$ compound

In our work rhenium dimer complexes of the form $\text{Re}_2\text{X}_4(\text{PMe}_3)_4\text{PF}_6$, where X = Cl or Br (Figure 4.1), were synthesized by our collaborators (Dr. Frederic Poineau and Erik V. Johnstone at the Department of Chemistry, University of Nevada, Las Vegas, and Dr. Alfred Sattleberger at Argonne National Laboratory) and investigated by us spectroscopically and computationally. Figure 4.1 shows the full $\text{Re}_2\text{X}_4(\text{PMe}_3)_4^+$ cation on the right, and the “core” with the methyl groups omitted for clarity on the left. The $\text{Re}_2\text{X}_4(\text{PMe}_3)_4^+$ cations have a d^4 - d^5 metal d-orbital occupation leading to a $\sigma^2\pi^4\delta^2\delta^*1$ ground state configuration with a net bond order 3.5 (one σ bond, two π bonds, $\frac{1}{2}$ δ bond), and possess D_{2d} symmetry. In these $\text{Re}^{2+}/\text{Re}^{3+}$ dimer molecules the unpaired electron is completely delocalized between the two Re ions. The compounds are paramagnetic, and as a third row transition metal rhenium has a large spin-orbit coupling constant. We therefore expect the compounds to have a large MCD signal, however, their magnetic circular dichroism spectra have not been previously reported in the literature.

Recent interest in the chemistry of metal-metal multiple bonded complexes includes extended metal atom chain compounds (EMAC), which feature linear chains of

metal atoms held together by polydentate ligands.^{163–173} EMAC compounds have been proposed as potential candidates for molecular wires. Whereas the majority of molecular wire compounds are organic ring structures with delocalized π networks, here conductivity would be associated with delocalized metal valence electrons rather than π electrons. Scanning tunneling microscopy experiments of EMAC molecules localized onto a gold surface have shown that the conductance depends on the electronic structure of the EMAC, i.e. whether the metal bonds in the chain are localized or delocalized.¹⁶⁴

Various metals have been used to form EMAC compounds including Mo, Cr, Ni, Ru and Co. Large polydentate ligands, such as for example polypyridylamido ligands, bond the metal atoms and holds them together in a chain. A challenge in the synthesis of the metal atom chains is the synthesis of larger and more complex ligands, which can be used to lengthen the number of metal atoms in the EMAC chain and thus provide length to the prospective wire.^{163,165,166,171} Chains of up to ten Ni atoms have been reported, corresponding to a length of 24.5 Å.¹⁶³ Ligands in such complexes are necessary to hold the metal atoms in a chain, but the organic ligands are also proposed to function as insulating layers, and are useful to tune the metal-metal interactions.^{70,72} In a report on the synthesis and characterization of heptanickel and heptachromium EMAC complexes, the authors used electron-withdrawing pyrazine substituents on the polypyridylamido ligands, which allowed for the tuning of the redox behavior of the compounds.¹⁶⁷

There is some debate in the literature on whether the metal-metal bonding and bond lengths in the various EMACs are symmetric, delocalized bonding interaction or rather asymmetric, localized bonding interactions, such as for example in a

pentachromium EMAC that has an asymmetric structure with Cr-Cr quadruple bonds alternating with Cr-Cr "no bonds."¹⁶⁷ There are examples in the literature of switching from a delocalized EMAC to a localized structure using one-electron oxidations of the compounds. The oxidation leads to a change in internuclear distances and a localization of the metal-metal bonding is observed. This is proposed to be useful as an on/off switching mechanism, where the delocalized state is "on" and the localized state of the metal-metal bonding is "off."^{165,166} There is some debate on whether that localization/delocalization behavior would actually effect electron transport through an EMAC, and the results of an electron transport calculation on a Cr based EMAC have suggested that, depending on the energetic alignment of the metal bonding orbitals with respect to the Fermi level, electron transport may occur through the σ bonding orbitals rather than the π bonding orbitals of the metals.¹⁷⁰

While the role of the metal atom multiple bonding in these EMAC compounds as well as the use of EMAC compounds as molecular wires is still in question, the exploration of metal-metal multiple bonding interactions is of general interest. Understanding metal-metal higher bond order interactions and the role of the ligand-metal interaction in these higher bond order metal dimers enriches the available chemical toolbox and extends our knowledge in this area of chemistry.

4.2 Experimental Details

4.2.1 Sample Preparation

$\text{Re}_2\text{Cl}_4(\text{PMe}_3)_4\text{PF}_6$ and $\text{Re}_2\text{Br}_4(\text{PMe}_3)_4\text{PF}_6$ are olive green crystalline powders. The compounds are soluble and stable at room temperature in acetonitrile and are not air

sensitive. Even though we are not aware of any moisture-sensitivity for these compounds, the acetonitrile was dried with molecular sieves as a precaution. Alfa Aesar molecular sieves, type 3A, -8+12 beads, which are sieves with a 3 Å pore size, were baked in the oven for a minimum of three days and added to the solvent for a day or more to absorb any moisture from the solvent. Butyronitrile was used as the solvent to form low-temperature glasses and was dried likewise with molecular sieves prior to use. Mass spectra of the samples were acquired at the UNM Mass Spectrometry Facility to ensure the compounds' purity prior to spectroscopic analysis. The observed pattern was consistent with the expected pattern and no other significant ion patterns were observed.

4.2.2 Electronic Absorption Measurements

Electronic absorption spectra of the compounds were acquired in solution (acetonitrile and butyronitrile) at room temperature on a U-4100 Hitachi spectrophotometer. For liquid sample measurements the instrument employs a prism-grating double monochromator system, where the prism acts as the pre-monochromator and the diffraction grating as the main monochromator. The instrument offers a wavelength range of 185-3300 nm, and uses a deuterium lamp (for the UV wavelength range) and a 50 W tungsten-halogen lamp (for the NIR/Vis wavelength range) as the light sources. Detection is accomplished by a photomultiplier tube (for the UV/Vis wavelength range) and a cooled type PbS detector (for the NIR wavelength range). Scan speeds were 120 nm/min in the UV/Vis and 300 nm/min in the NIR, the detector switch was at 850 nm, lamp switch at 325 nm, slit-width was 2 nm in the UV/Vis, variable in the NIR. A

baseline was acquired with the same cuvette using acetonitrile or butyronitrile. The cuvettes used for measurements were masked quartz cells manufactured by Starna Cells featuring a screw cap top with a silicone rubber septum. The sample volume of the cuvettes is 100 μl and the pathlength is 10 mm.

Low-temperature electronic absorption measurements were acquired on the predecessor model of the instrument, a Hitachi U-3501 spectrophotometer, after the cuvette holder assembly was removed to accommodate the cryostat in the sample chamber. Both instruments were calibrated to the 656.1 nm deuterium line using the corresponding Hitachi software option, and spectra were resolved with Gaussian bands using Grams/AI, version 7.02 (Thermo Galactic, 1991-2002). Low-temperature electronic absorption data of frozen solutions or polystyrene films had a rising baseline due to scattering contributions, and a scattering correction was applied to the spectra following the methodology of Bendit and Ross,⁸⁸ which uses the relationship of the absorbance due to scattering, A_{sca} , with the wavelength, λ , in a non-absorbing region of the spectrum:

$$A_{sca} = y\lambda^{-x}. \quad \text{Eq. 27}$$

4.2.3 Magnetic Circular Dichroism Measurements

MCD spectra were acquired as both polystyrene film samples and frozen solutions in butyronitrile. While the film samples are easier to handle and have a smaller depolarization, frozen butyronitrile solution samples showed a better resolution for the vibrational fine-structure of the low energy $\delta \rightarrow \delta^*$ transition. By acquiring both an MCD and absorption spectrum from the same film sample, the film samples were used to convert the MCD signal intensity (mdeg) to units of $\Delta\epsilon$, where $\Delta\epsilon = \epsilon_{(LCP)} - \epsilon_{(RCP)}$, LCP =

left-circularly polarized light, and RCP = right-circularly polarized light. First the extinction coefficient (ϵ) for the absorption spectrum of the compounds is established using Beer's law to convert concentration (C) and absorbance (A) of a room temperature solution in a cuvette of 1 cm pathlength (b) to molar extinction coefficients.

$$A = \epsilon bC \quad \text{Eq. 28}$$

This now allows us to determine bC , the product of pathlength and concentration, for the film sample by simply taking an absorption spectrum of the film and using Beer's law. When the same film sample is used for the MCD experiment, which measures ΔA , we can convert the MCD signal to a $\Delta\epsilon$. This seemingly roundabout way of determining $\Delta\epsilon$ was used since we know neither the concentration of the film sample, nor can accurately measure the film thickness ($\sim 0.5 - 1$ mm) without large margins of error. For the frozen solution sample we also have a large potential margin of error determining the pathlength (1-2 mm) of the sample.

The MCD system uses JASCO spectropolarimeters, where JASCO J-810 is used for UV/Vis wavelength range (165 nm - 900 nm), and JASCO J-730 for NIR range (800 nm - 2000 nm). The J-810 unit utilizes a 150W Xenon lamp as a light source and is connected to a head-on photomultiplier tube detector. The J-730 unit utilizes a 150W halogen lamp as a light source and is connected to a liquid-nitrogen cooled InSb detector (Infrared Associates, IS-2.0 series). The polarimeter sends the linearly polarized light through a modulator that separated it into its left- and right-circularly polarized components. The light is focused by an external lens onto the sample, which sits in the liquid-helium cooled variable temperature insert of an Oxford superconducting magnet

and cryostat unit. The magnet is connected to an Oxford PS 120 power supply unit, and has a magnetic field range of 0-7 T. The temperature range of the cryostat is 1.5 – 300 K, where temperatures below 5 K require the application of a partial vacuum to the helium. Spectra were acquired at 5 K, 10 K and 20 K and at a magnetic field of 7 T. Spectra were also acquired at 0 T for each temperature and used as a baseline by subtracting them from the 7 T spectrum of each temperature. The depolarization of the nickel tartrate CD signal due to the presence of the sample is calculated by calculating the CD intensity range at a maximum (371 nm) and minimum (400 nm) with the nickel tartrate located before and after the sample with respect to the light source. Depolarizations of 10-11% were deemed acceptable for the frozen solution and polystyrene film samples.

4.2.4 Resonance Raman Measurements

Resonance Raman samples were prepared in a solid state matrix. The matrix consists of finely ground NaCl/Na₂SO₄ in an approximate 10:1 ratio by weight, and was combined with a quantity of solid Re₂Cl₄(PMe₃)₄PF₆ or Re₂Br₄(PMe₃)₄PF₆ sample and ground again to achieve a uniform, finely ground resonance Raman sample. The resonance Raman samples were put into quartz capillary tubes, which were flame-sealed to prevent sample from escaping the tube while the tube was spinning during measurements.

The amount of compound used varies: one needs to use enough compound in preparing the sample so that one can clearly see the compound's color in the resonance Raman sample. Making a concentrated, i.e. strongly colored, resonance Raman sample is often good since it improves the signal-to-noise ratio of the sample peaks and thus the

sample signal quality. However, sometimes a concentration that is too large can actually degrade the sample signal quality, where the signal will show a large, very broad fluorescence emission peak instead of or added to the resonance Raman signal. Additionally self-absorption of the photons is more likely to occur at higher sample concentrations. Self-absorption refers to a photon that has been absorbed and emitted by the sample being reabsorbed by the sample instead of travelling to the detector. Self-absorption and fluorescence emissions typically are more prevalent in solution rather than solid state samples. The ideal concentration for our resonance Raman samples was determined by trial and error, where at a good concentration one can see both reference peaks and sample peaks clearly in the spectrum without observing a large fluorescence emission signal. Reference peaks for a solid resonance Raman sample are the nine sulfate peaks, and the Raman shifts (x-axis) of the spectra are calibrated to the largest sulfate peak at 992 cm^{-1} .

Once a good resonance Raman sample has been prepared, and the best concentration for the sample has been determined, it is necessary to use the same sample (or a sample with the same concentration) for the entire experiment when obtaining a resonance Raman profile. In a resonance Raman enhancement profile the resonance Raman response of a mode of interest relative to the sulfate internal standard is plotted as a function of the excitation laser line energy. Ideally, the available laser line energies (from the Ar^+ laser: 458 nm, 488 nm, 514 nm; Kr^+ laser: 407 nm, 568 nm, 614 nm) will encompass some lines that are on resonance with an absorption band of interest, and some lines that are off resonance with the absorption band, so that the enhancement of the

Raman mode as a function of being in resonance with the absorption band can be observed. The modes that will be enhanced under a particular absorption band are those that are alike to the distortion of the molecule (i.e. the change in the nuclear coordinates) that comes from the redistribution of electrons during that electronic transition.

The resonance Raman set-up consists of a Coherent Innova I302C Ar⁺ laser or alternatively a Kr⁺ laser as the excitation source. The laser light is passed through Maxline laser line filters, which remove plasma lines from the laser output, and Razor Edge long pass filters, which cut off the Rayleigh scattering signal. These filters were obtained from Semrock. The laser light power was measured at the sample, and in order to avoid photobleaching or sample degradation in general, we chose low powers (~15 mW for 407 nm, ~20 mW for 458 nm and 488 nm, ~25 mW for 514 nm, ~35 mW for 568 nm, ~50 mW for 647 nm) as well as short exposure times. The sample is also continually spun when exposed to the laser light in order to distribute the heat throughout the sample and minimize degradation. Scattered light at a 90° angle is focused by a series of lenses and directed to the PI/Acton Spectrapro SP-2500i 500 mm focal length spectrograph with a triple-grating turret monochromator and finally the liquid-nitrogen cooled detector, PI/Acton Spec-10:100B back-illuminated 1340_100 pixel digit CCD camera.

4.2.5 Density Functional Theory Electronic Structure Calculations

Electronic structure calculations were carried out using Density Function Theory (DFT) Gaussian03 suite,^{65,71} as well as ADF.2012.^{129–134} Spin-unrestricted gas-phase calculations were carried out for Re₂Cl₄(PMe₃)₄⁺ and Re₂Br₄(PMe₃)₄⁺ on the optimized geometries of the cations. For Gaussian03 calculations, a B3LYP^{66,67} exchange-

correlation functional and a split valence, double-zeta polarized basis with added polarization functions [6-31G(d'p')] was used for all atoms, except Re, for which the LanL2DZ⁶⁸⁻⁷⁰ pseudopotential was used. Vibrational frequencies and Raman intensities were calculated in Gaussian03. ADF calculations employed a small core potential with double-zeta polarized basis (DZP) for all atoms except Re, Br, and Cl, for which a triple-zeta polarized basis (TZP) was used. Note that while Gaussian constructs its basis sets from Gaussian-type orbitals, ADF employs Slater-type orbitals. The PBE¹³⁷ functional, which employs the generalized-gradient approximation, was used (see section 3.2.3 for more detail), and a scalar ZORA¹³⁶ relativistic correction was applied. The 100 lowest energy singlet-excitations were computed for the electronic absorption spectra, and the 50 lowest energy C-term excitations were computed for the MCD spectra using the sum-over-states formalism. Electron density difference maps (EDDMs) were constructed utilizing the “EDDM, Transition Density, and Orbital Generation for ADF and Gaussian 03” written by Ben Stein at the UNM Department of Chemistry and Chemical Biology, 2011.

4.3 Spectroscopic and Computational Studies of Re Dimers: Effects of Ligand Substitution

4.3.1 Room Temperature Electronic Absorption of $\text{Re}_2\text{Cl}_4(\text{PMe}_3)_4\text{PF}_6$ and $\text{Re}_2\text{Br}_4(\text{PMe}_3)_4\text{PF}_6$

Electronic absorption spectra of $\text{Re}_2\text{Cl}_4(\text{PMe}_3)_4\text{PF}_6$ and $\text{Re}_2\text{Br}_4(\text{PMe}_3)_4\text{PF}_6$ in acetonitrile and butyronitrile show no solvatochromism in those solvents (Figure 4.2). The compounds are both stable in acetonitrile and butyronitrile in air and at room

temperature. Butyronitrile was used to form low-temperature glasses whereas acetonitrile was used for room temperature measurements. The electronic absorption spectra of these compounds in the literature vary with respect to the presence of absorption bands between 12000 and 19000 cm^{-1} . The absorption spectrum published by Bursten *et al.*¹⁵¹ for $\text{Re}_2\text{Cl}_4(\text{PPr}_3)_4\text{PF}_6$ features strong absorption bands at $\sim 14000 \text{ cm}^{-1}$ and $\sim 17000 \text{ cm}^{-1}$, which are absent in the electronic absorption spectra we obtained of the compounds shown in Figure 4.3.

When we examined an alternative preparation of $\text{Re}_2\text{Cl}_4(\text{PMe}_3)_4\text{PF}_6$ and $\text{Re}_2\text{Br}_4(\text{PMe}_3)_4\text{PF}_6$, we also observed these absorption bands (at ~ 13400 and $\sim 17200 \text{ cm}^{-1}$ for $\text{X} = \text{Br}$), while the MCD spectra of the compounds showed no corresponding bands. We infer that the absorption bands should be attributed to diamagnetic impurities, i.e. the

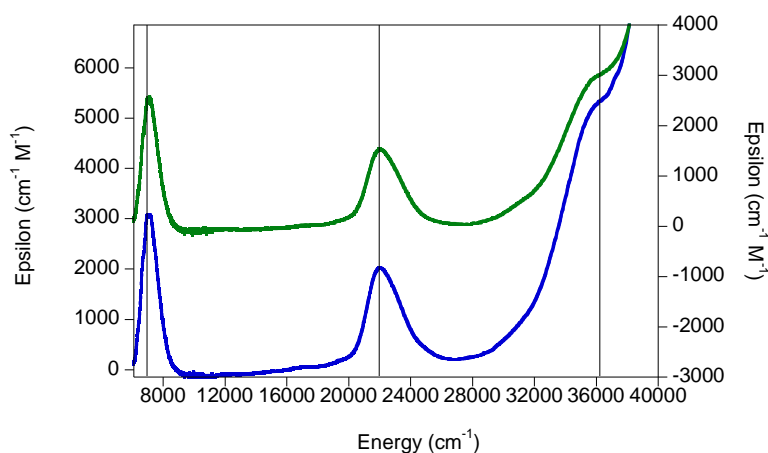


Figure 4.2: Electronic absorption spectra of $\text{Re}_2\text{Br}_4(\text{PMe}_3)_4\text{PF}_6$ at room temperature in acetonitrile (green, right y-axis) and butyronitrile (blue, left y-axis).

dications $[\text{Re}_2\text{X}_4(\text{PMe}_3)_4]^{+2}$. This is consistent with a report from Cotton *et al.* on $\text{Re}_2\text{Cl}_4(\text{PMe}_2\text{Ph})_4^+$ and $\text{Re}_2\text{Cl}_4(\text{PMe}_2\text{Ph})_4^{2+}$, which (while not showing the absorption spectra) reports a weak band at $\sim 17100 \text{ cm}^{-1}$ for the monocation (in addition to the strong

bands at $\sim 7400\text{ cm}^{-1}$ and $\sim 22700\text{ cm}^{-1}$) and a very strong band at $\sim 13900\text{ cm}^{-1}$ for the dication (in addition to the strong bands at $\sim 7200\text{ cm}^{-1}$ and $\sim 23000\text{ cm}^{-1}$).¹⁵⁰ Five years prior to the above mentioned literature reports, Brant *et al.*¹⁵⁷ had published a data table (and no absorption spectra) for $\text{Re}_2\text{X}_4(\text{PEt}_3)_4^+$ where $\text{X} = \text{Cl}, \text{Br}$ that lists the following absorption features - a strong band at $\sim 7100\text{ cm}^{-1}$, a medium band at $\sim 16700\text{ cm}^{-1}$, a shoulder at $\sim 20400\text{ cm}^{-1}$ and a strong band at $\sim 23200\text{ cm}^{-1}$ for $\text{X} = \text{Cl}$, and a strong band at $\sim 6900\text{ cm}^{-1}$, shoulder at $\sim 19400\text{ cm}^{-1}$ and strong band at $\sim 22400\text{ cm}^{-1}$ for $\text{X} = \text{Br}$. While the peaks listed for $\text{Re}_2\text{Br}_4(\text{PEt}_3)_4^+$ agree very well with the absorption spectrum we obtained for $\text{Re}_2\text{Br}_4(\text{PMe}_3)_4^+$, the medium band at $\sim 16700\text{ cm}^{-1}$ for $\text{Re}_2\text{Cl}_4(\text{PEt}_3)_4^+$ seems to suggest that the authors were perhaps looking at the dication species, though this point is not clear.

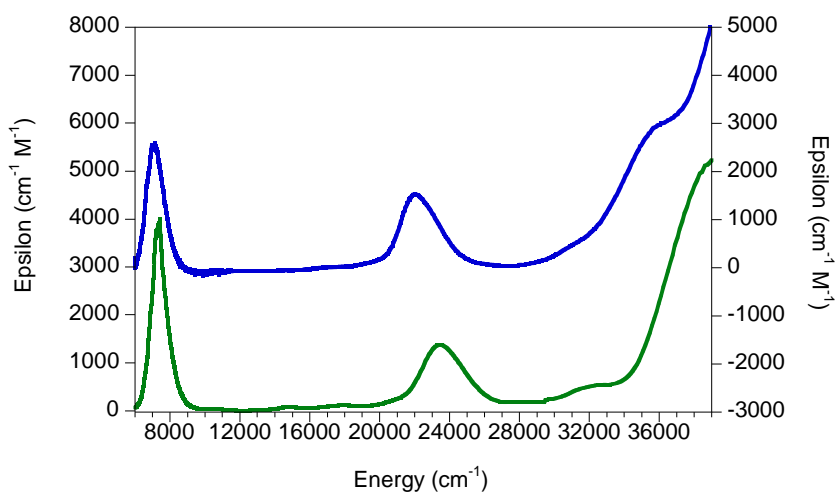


Figure 4.3: Electronic absorption spectra of $\text{Re}_2\text{Cl}_4(\text{PMe}_3)_4\text{PF}_6$ (green, left y-axis) and $\text{Re}_2\text{Br}_4(\text{PMe}_3)_4\text{PF}_6$ (blue, right y-axis) at room temperature in acetonitrile.

The Gaussian resolved room temperature electronic absorption spectra for $\text{Re}_2\text{Cl}_4(\text{PMe}_3)_4\text{PF}_6$ and $\text{Re}_2\text{Br}_4(\text{PMe}_3)_4\text{PF}_6$ are shown in Figure 4.4, while the band

assignments for the resolved bands are shown in Table 4.1. Band assignments were based on prior literature on $\text{Re}_2\text{X}_4(\text{PR}_3)_4^+$ compounds, DFT results, and a comparison of the spectra upon halide substitution. The electronic absorption spectra show an intense and energetically isolated band at low energy, which we assign as the $\delta \rightarrow \delta^*$ band in accordance to previous literature reports. This transition has vibronic fine structure, and even at room temperature we observe the peak partially resolving into a vibronic progression. Since pin-pointing the maximum of such a band is ambiguous, the table lists the energies of the resolved vibronic progression for this transition, namely the 0-0 peak, which is lowest energy peak of the progression resolved at low temperatures, and 0-1

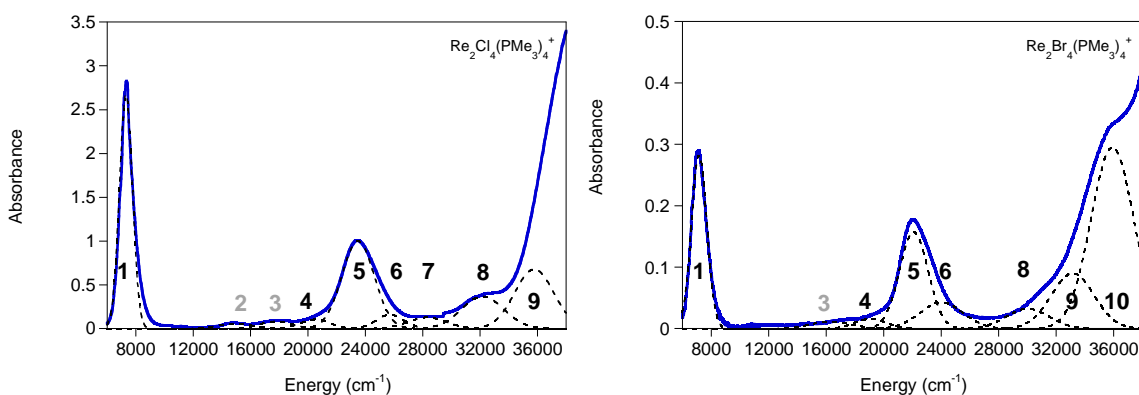


Figure 4.4: Gaussian resolved room-temperature electron electronic absorption spectra of $\text{Re}_2\text{Cl}_4(\text{PMe}_3)_4\text{PF}_6$ (left) and $\text{Re}_2\text{Br}_4(\text{PMe}_3)_4\text{PF}_6$ (right).

peak, which is the next peak in the main progression and also the peak with the highest intensity. This transition has a very small band shift upon halide substitution, $\sim 150 \text{ cm}^{-1}$ using the best-resolved progression from the 5 K MCD data (where for $\text{X} = \text{Cl}$ $0 \rightarrow 0$ is at 6890 cm^{-1} and $0 \rightarrow 1$ at 7195 cm^{-1} ; for $\text{X} = \text{Br}$ $0 \rightarrow 0$ is at 6890 cm^{-1} and $0 \rightarrow 1$ at 7195 cm^{-1}). For an electronic transition to be dipole allowed, the transition moment integral must

be non-zero. Here, D is the dipole strength, Ψ_{el} the electronic wavefunction of the ground (gs) and excited state (ex) of the molecule, and \hat{M} the dipole moment operator.⁹⁵

$$f \propto \left| \int_{-\infty}^{+\infty} \Psi_{el}^{gs} \hat{M} \Psi_{el}^{ex} \right|^2 = D \quad \text{Eq. 29}$$

$$\int \Psi_{el}^{gs} \hat{M}_z \Psi_{el}^{ex} dv, \quad \int \Psi_{el}^{gs} \hat{M}_y \Psi_{el}^{ex} dv, \quad \int \Psi_{el}^{gs} \hat{M}_x \Psi_{el}^{ex} dv \quad \text{Eq. 30 a-c}$$

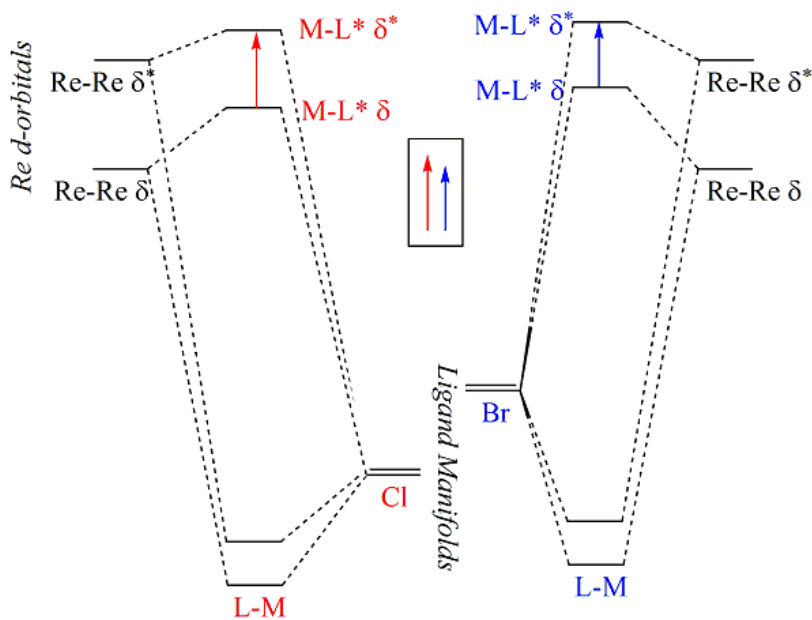


Figure 4.5: Molecular orbital diagram showing the qualitative effect of halide substitution on ligand-to-metal charge transfer bands (energy levels are not drawn to scale).

The dipole moment operator can be represented as its x, y, and z components. Using group theory, we know that the integral is non-zero when the triple product is totally symmetric, ie. A_1 in D_{2d} symmetry. In the D_{2d} point (D_{2d} character table in Appendix 6.3.2) group \hat{M}_y and \hat{M}_x are degenerate and transform as E, and \hat{M}_z transforms as B_2 . Since $A_2 * B_1 * B_2 = A_1$, the $\delta \rightarrow \delta^*$ transition from an A_2 ground state to a

B_1 excited state is dipole allowed and z-polarized. Any transitions into or out of orbitals of E symmetry will also be dipole allowed and x-y polarized.

Bands of $\text{Re}_2\text{Cl}_4(\text{PMe}_3)_4\text{PF}_6$ are at higher energies than the corresponding absorption bands of $\text{Re}_2\text{Br}_4(\text{PMe}_3)_4\text{PF}_6$, which is expected as the chloride ligand manifold is energetically lower than the bromide ligand manifold leading to higher energy transitions for $\text{Re}_2\text{Cl}_4(\text{PMe}_3)_4\text{PF}_6$ if the transitions have partial halide LMCT character, as shown in the qualitative molecular orbital diagram in Figure 4.5. Note that the $\delta \rightarrow \delta^*$ transition only shifts in energy (upon halide substitution) if the halide ligand orbitals mix more with the δ than the δ^* orbital. That is expected to be true, as the δ orbital is energetically closer to the ligand orbital manifold compared to the δ^* orbital and we assume that the ligand p-orbitals are degenerate prior to interacting with the Re d-orbitals. It is noteworthy, however, that the band shift directly depends on the LMCT character of the transition, i.e. on the difference between halide-Re δ and halide-Re δ^* mixing rather than the absolute amount. No band shifts are expected for transitions that are purely trimethyl phosphine ligand to metal charge transfer, i.e. for orbitals where neither the trimethyl phosphine nor the rhenium orbitals have mixed significantly with any halide orbitals.

The calculated oscillator strengths, f , are related to the area under an absorption band by Eq. 30,⁹⁵ where ϵ is the extinction coefficient of the absorption band and ν is its energy in cm^{-1} .

$$f = 4.315e - 9 \int \epsilon d\tilde{\nu} \quad \text{Eq. 31}$$

For a single, symmetric band f can be approximated by the product of the full width at half height of the band and its extinction coefficient according to Eq. 31.⁹⁵

$$f \approx 4.6e - 9 \varepsilon_{max} \Delta\nu_{1/2} \quad \text{Eq. 32}$$

An oscillator strength of 0.1 corresponds approximately to an extinction coefficient of 10,000 $\text{M}^{-1}\text{cm}^{-1}$.

Table 4.1: Experimental absorption band energies and molar extinction coefficients, ε , and band assignments for $\text{Re}_2\text{Cl}_4(\text{PMe}_3)_4\text{PF}_6$ and $\text{Re}_2\text{Br}_4(\text{PMe}_3)_4\text{PF}_6$.

Band	Energy (cm^{-1})		ε ($\text{M}^{-1}\text{cm}^{-1}$)		Shift (cm^{-1})	Assignment	Polarization
	X = Cl	X = Br	X = Cl	X = Br			
1	0 \rightarrow 0 6844, 0 \rightarrow 1 7150	0 \rightarrow 0 6774, 0 \rightarrow 1 7074	3750	2600	\sim 150	$\delta \rightarrow \delta^*$	z
2	14950	--	75			$\delta^* \rightarrow \pi^*(\sigma^*, \delta_b^*)$	small μ_x, μ_z
3	17790	16320	100	100			
4	20500	19090	200	200	\sim 1420	$\text{X}^{\pi^*}, \text{P}^{\sigma^*} + (\text{MM } \pi) \rightarrow \delta^*$	x, y
5	23500	22090	1400	1650	\sim 1400	$\text{X}^{\pi^*}, \text{P}^{\sigma^*} + (\text{MM } \pi) \rightarrow \delta^*$	x, y
6	25740	24030	400	600	\sim 1710	$\delta \rightarrow \pi^*$	x, y
7	28320		200				
8	32180	30020	500	400	\sim 2170	$\text{X}^{\sigma^*} + (\text{MM } \pi) \rightarrow \delta^*$	x, y
						$\text{X}, \text{P} \rightarrow \delta^*$	
						$\text{X}^{\pi} + (\text{MM } \delta) \rightarrow \delta^*$	z
9	35780	33160	2000	1400	\sim 2620	$\text{X}^{\pi^*}, \text{P}^{\sigma^*} + (\text{MM } \pi) \rightarrow \pi^*$	z
						$\text{X}^{\pi^*}, \text{P}^{\sigma^*} + (\text{MM } \pi) \rightarrow \delta_b^*$	x, y
10		35910		3100		various LMCT	x, y

Table 4.2: DFT-calculated band energies and oscillator strengths, and band assignments for $\text{Re}_2\text{Cl}_4(\text{PMe}_3)_4\text{PF}_6$ and $\text{Re}_2\text{Br}_4(\text{PMe}_3)_4\text{PF}_6$.

Band	DFT Energy (cm^{-1})		f		Assignment	Polarization
	X = Cl	X = Br	X = Cl	X = Br		
1	8913	8575	0.0160	0.0182	$\delta \rightarrow \delta^*$	z
2					$\delta^* \rightarrow \pi^*(\sigma^*, \delta_b^*)$	small μ_x, μ_z
3		16590, 16590		0.1e-4		
4	18460, 18480	17210, 17230	0.0028	0.0020	$X \pi^*, P \sigma^* + (\text{MM } \pi) \rightarrow \delta^*$	x, y
5	20450, 20490	19100, 19110	0.0117	0.0195	$X \pi^*, P \sigma^* + (\text{MM } \pi) \rightarrow \delta^*$	x, y
6	23010, 23070	22600, 22700	0.0010	0.0007	$\delta \rightarrow \pi^*$	x, y
7						
8		27440, 27450		0.0026	$X \sigma^* + (\text{MM } \pi) \rightarrow \delta^*$	x, y
	31196, 31204	28786 28790	0.0044	0.0034	$X, P \rightarrow \delta^*$	
	32070	28160, 29000	0.0077	0.0036	$X \pi + (\text{MM } \delta) \rightarrow \delta^*$	
9		32130		0.0113	$X \pi^*, P \sigma^* + (\text{MM } \pi) \rightarrow \pi^*$	z
	35730, 35770	32640, 32660	0.0161	0.0207	$X \pi^*, P \sigma^* + (\text{MM } \pi) \rightarrow \delta_b^*$	x, y
10		35470		0.0100	various LMCT	x, y

Bands 2 and 3 are very weak bands with $\epsilon < 100$, which are also extremely weak band in the calculated absorption spectra, and are assigned as transition from the $\text{Re-}\delta^* \rightarrow \text{Re-}\pi^*$ (as well as $\text{Re-}\delta^* \rightarrow \sigma^*$, $\text{Re-}\delta^* \rightarrow \delta_b^*$). All higher energy bands, i.e. bands 4-10, have varying degrees of $X \rightarrow \text{Re}$ LMCT character as evidenced by the optical electronegativity shifts observed for these bands upon halide substitution. Note that the band shifts upon halide substitution are given in Table 4.1 and Table 4.2, and are most reliable for bands 4-6. Since there are differences in how the spectra were fit at higher energies (i.e. no band 7 for X = Br), the band shifts of those higher energy bands (6, 8-10) reflect not only the optical electronegativity shifts but also effects of the choice for band

fits. For reference, the optical electronegativity for a π electron is $\chi_{\text{ligand}} = 3.0$ for Cl^- and $\chi_{\text{ligand}} = 2.8$ for Br^- , which when multiplied by $\nu_0 = 3.0 \times 10^4 \text{ cm}^{-1}$ gives an expected band shift of 6000 cm^{-1} .¹⁰⁸ Thus the $\delta\text{-}\delta^*$ transition appears to have very little halide LMCT character, whereas the higher energy transitions have significant halide LMCT character.

Bands 4, 5, 8 are assigned as $e \rightarrow a_2$ transitions from lower lying filled ligand orbitals (that also have a small amount of MM π character) into the Re δ^* orbital. These transitions are x-y polarized and thus dipole allowed. The DFT energies of two orbitals that make up a ligand e orbital set are split by a few tens of cm^{-1} up to $\sim 100 \text{ cm}^{-1}$ (see Table 4.1 and Table 4.2), and are thus never resolved in the absorption spectrum. There are numerous ligand orbital e sets that mix with the Re-Re π bonding orbital creating a block of e sets that have a small amount of Re-Re π and various amount of halide and/or phosphine character. The metal-ligand interactions in these orbitals are antibonding in nature for those e orbitals close to the frontier orbitals, and become less antibonding and more bonding in nature the further below the frontier orbitals they lie. Thus the LMCT transition assigned as band 4 originates from an e set with halide-metal π^* interaction and a phosphine-metal σ^* interaction. The next lowest ligand e set has a halide-metal π^* and a phosphine-metal σ interaction (band 5), the e set below that halide-metal σ^* and no phosphine (band 8). The e set that follows below the above has halide and phosphine character only (i.e. no Re character) and is thus non-bonding with respect to the metal (band 8). In addition to the x-y polarized LMCT transitions that contribute to band 8, a major component of band 8 is a z-polarized transition from a halide ligand orbital (also has a small Re-Re δ component) into δ^* .

Band 6 is assigned as a $\delta \rightarrow \pi^*(b_1 \rightarrow e)$ x,y-polarized transition. Band 9 is assigned as a LMCT transition from the ligand e set has a halide-metal π^* and a phosphine-metal σ interaction going to both the Re π^* and Re δ_b^* , where δ_b^* is a higher energy virtual Re d-orbital whose lobes point directly along the Re-halide and Re-P bonds (forming σ^* interactions with the ligands). Note that most of the LMCT transitions have both halide and trimethyl-phosphine LMCT character, though only the halide LMCT character contributes to band shifts between **1** and **2**.

4.3.2 C-term MCD of $\text{Re}_2\text{Cl}_4(\text{PMe}_3)_4\text{PF}_6$ and $\text{Re}_2\text{Br}_4(\text{PMe}_3)_4\text{PF}_6$

As the $\sigma^2 \pi^4 \delta^2 \delta^{*1}$ ground state configuration of these compounds has an unpaired electron with orbital character of an atom with an appreciable spin-orbit coupling constant, we expect to observe a magnetic circular dichroism signal for these compounds. Re(III), a third row transition metal atom, has a large spin-orbit coupling constant of 2500 cm^{-1} .¹⁷⁴ The MCD spectra for $\text{Re}_2\text{Cl}_4(\text{PMe}_3)_4\text{PF}_6$ and $\text{Re}_2\text{Br}_4(\text{PMe}_3)_4\text{PF}_6$, however, have not been published previously. We acquired low-temperature MCD data at 5 K, 10 K, and 20 K in order to clearly observe which MCD features represent C-term MCD, where C-term MCD has a $1/T$ temperature dependence.

Figure 4.6 shows the variable temperature MCD spectra of the cation compounds at 5, 10 and 20 K where the samples were cast into polystyrene film matrices. The spectra have a large number of temperature-dependent positive and negative MCD bands and are very similar for both compounds, in particular at energies below 24000 cm^{-1} . The spectra

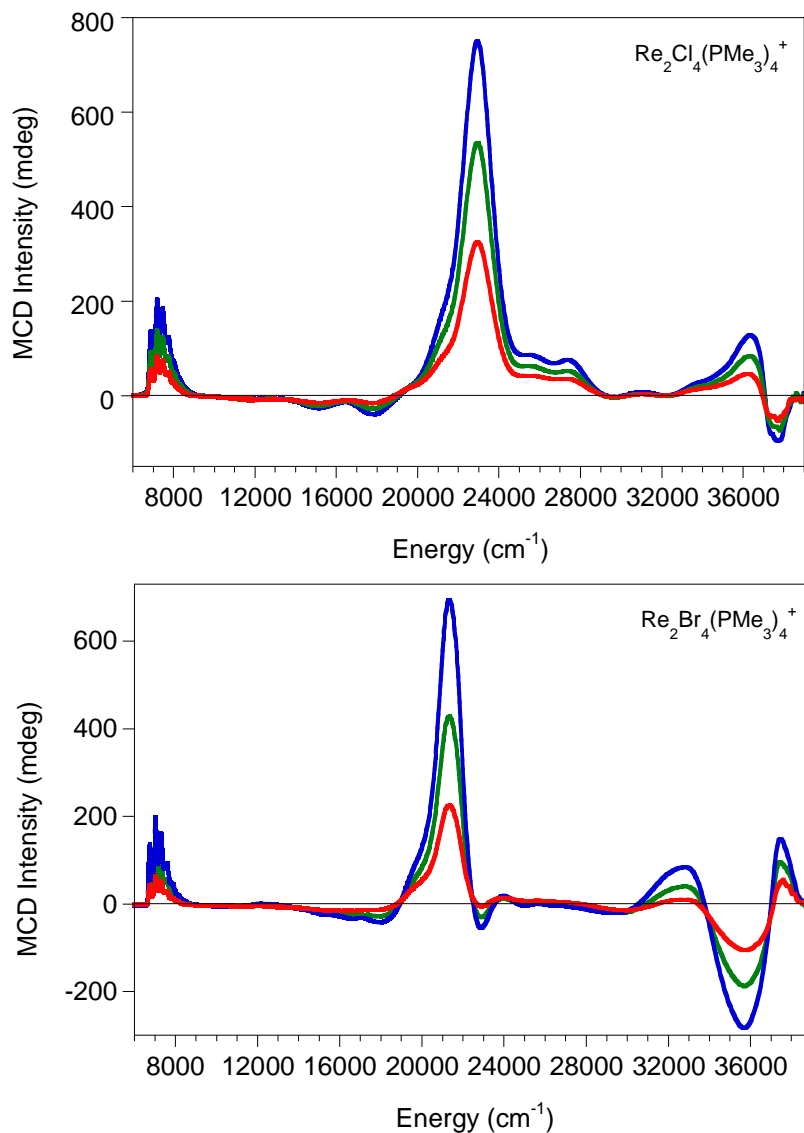


Figure 4.6: Variable temperature MCD of $\text{Re}_2\text{Cl}_4(\text{PMe}_3)_4\text{PF}_6$ (top) and $\text{Re}_2\text{Br}_4(\text{PMe}_3)_4\text{PF}_6$ (bottom) in a polystyrene film matrix. Spectra were taken at 7 T and are baseline-subtracted. 5 K (blue), 10 K (green), 20 K (red).

are dominated by a large positive band at $\sim 23000\text{ cm}^{-1}$ and $\sim 21000\text{ cm}^{-1}$ for $\text{Re}_2\text{Cl}_4(\text{PMe}_3)_4\text{PF}_6$ and $\text{Re}_2\text{Br}_4(\text{PMe}_3)_4\text{PF}_6$ respectively.

The low-energy C-term assigned as the $\delta \rightarrow \delta^*$ transition is z-polarized in D_{2d} symmetry and thus formally forbidden in MCD, where C-term intensity requires a

transition to possess two non-zero perpendicular transition moments. In order to gain intensity, the z-polarized transition can mix with either the ground state or other excited states to acquire partial x-y character. Figure 4.7 illustrates the two mechanisms that contribute to the C-term intensity of the $\delta \rightarrow \delta^*$ transition, where the C-term is proportional to the product of the two perpendicular transition dipole moments and the spin-orbit coupling integral.^{142,175} In the ground state mechanism for C-term intensity the excited state $|J\rangle$ (i.e. the $\delta \rightarrow \delta^*$ transition) spin-orbit couples with the ground state $|A\rangle$, while in the excited state mechanism the excited state $|J\rangle$ spin-orbit couples to an energetically-close excited state $|K\rangle$.

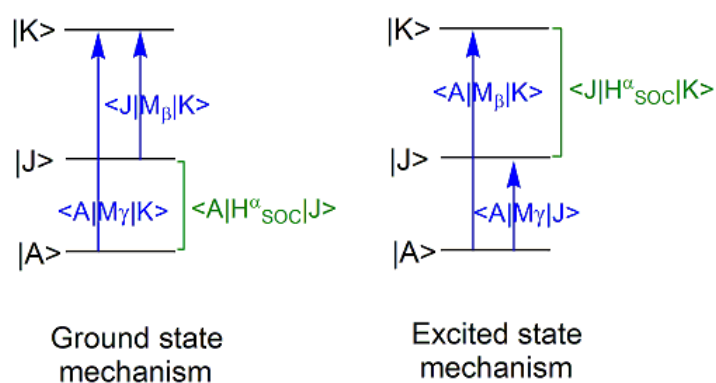


Figure 4.7: Mechanisms for gaining C-term intensity: blue = transition dipole integrals, green = spin-orbit coupling integrals, after reference¹⁴².

Typically, mixing of an excited state with other excited states dominates due to the excited states being energetically much closer to one another than the ground state. Here the low-energy C-term is energetically isolated leading to an unusual MCD intensity gaining mechanism where the spin-orbit coupling perturbation of excited state by other excited states contributes almost the same amount as the spin-orbit coupling perturbation of the excited state by the ground state as summarized in Table 4.3 extracted from the

DFT calculation of the MCD excitations. The excited states $|K\rangle$ mixing with the $\delta \rightarrow \delta^*$ transition $|J\rangle$ are in fact the $e \rightarrow \delta^*$ transitions with the largest absorption (and MCD) intensity, band 5. Note that if the calculation is run in strict D_{2d} symmetry where those e orbitals are strictly degenerate the calculated C-term intensity for the $\delta \rightarrow \delta^*$ transition becomes zero.

Table 4.3: DFT-calculated contributions to C-term intensity for the $\delta \rightarrow \delta^*$ transition.

	$\text{Re}_2\text{Cl}_4(\text{PMe}_3)_4^+$	$\text{Re}_2\text{Br}_4(\text{PMe}_3)_4^+$
Total C-term intensity for $\delta \rightarrow \delta^*$ transition $ J\rangle$	0.01253	0.01304
MCD C-term contribution from ground state mixing into $\delta \rightarrow \delta^*$ (Perturbed Orbitals) $ A\rangle$	0.00662 (52.9%)	0.00527 (40.4%)
MCD C-term contribution from excited state mixing into $\delta \rightarrow \delta^*$ (Perturbed transition densities)	0.00590 (47.1%)	0.00778 (59.6%)
Major contributing excited states $ K\rangle$	LMCT $X^{\pi^*}, P^{\sigma^+}(\text{MM } \pi)$ $e \rightarrow \delta^*$	LMCT $X^{\pi^*}, P^{\sigma^+}(\text{MM } \pi)$ $e \rightarrow \delta^*$ LMCT $X^{\sigma/\sigma^+}(\text{MM } \pi)$ $e \rightarrow \delta^*$
ΔE (cm^{-1}) $ A\rangle$ to $ J\rangle$	8913	8575
ΔE (cm^{-1}) $ J\rangle$ to $ K\rangle$	9549	8637
DFT-calculated MCD intensity of $\delta - \delta^*$ transition in strict D_{2d} symmetry	<i>None</i>	<i>None</i>

In molecules with so many x,y polarized e-orbitals it is very difficult to accurately fit the experimental MCD spectrum. The observed spectrum is of course the superposition of all positive and negative MCD bands that have appreciable oscillator strength. If a positive and negative band are close in energy, and given that the bands have a non-zero band width, the bands will cancel one another, either partially or close to completely, depending on the band width, energy separation, and relative magnitudes. At least three possible outcomes come to mind:

- a negative and a positive band that are close enough to one another in energy and have close to equal C-term intensity to cancel one another (where any remnant signal is below the noise level)
- only one band remaining after completely cancelling a band of opposite sign if the bands are close enough to one another in energy but have somewhat unequal C-term intensities
- a negative and a positive band that are close to one another in energy with somewhat unequal C-term intensities, which cancel one another partially, leaving a net feature that still shows a negative and positive component but of much lower intensity than the “original/intrinsic” bands. Note that the relative intensities of those bands now are quite unequal (even if the absolute difference remains unchanged). Also note that the band maxima after the partial cancellation appear shifted further apart in energy (i.e. at lower energy for the lower energy component of the pseudo-A term and at higher energy for the higher energy component of the pseudo-A term) as compared to the “original/intrinsic” bands.

These scenarios all occur for the present compounds due to the fact that this high symmetry molecule has a large number of orbitals of e symmetry that transitions originate from or end in. Those transitions correspond to pseudo-A (derivative-shaped) features in the MCD spectra since the transitions from (or into) one member of the e set

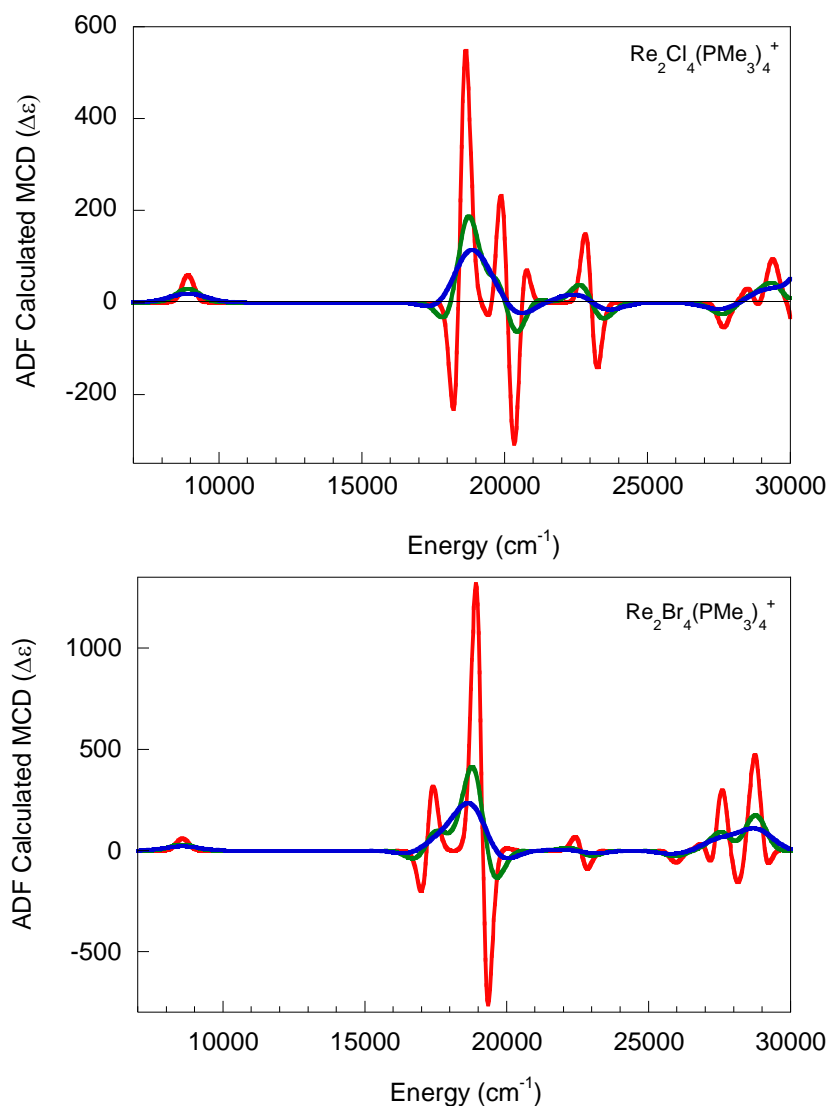


Figure 4.8: DFT-calculated MCD spectra of $\text{Re}_2\text{Cl}_4(\text{PMe}_3)_4\text{PF}_6$ (top) and $\text{Re}_2\text{Br}_4(\text{PMe}_3)_4\text{PF}_6$ (bottom) at various bandwidths: red 500 cm^{-1} , green 1000 cm^{-1} , blue 1500 cm^{-1} .

will be left-circularly polarized and the transition of the other member right-circularly polarized leading to oppositely signed MCD features. Fortunately, however, the DFT-calculated absorption and MCD spectra are very similar to the experimental spectra when using the appropriate bandwidths, so that one can correlate experimental to calculated spectral features and then use the calculation results to trace back the origins of the observed features. Figure 4.8 illustrates these cancellations, where the spectra shown are

the DFT-calculated spectra of $\text{Re}_2\text{Cl}_4(\text{PMe}_3)_4\text{PF}_6$ and $\text{Re}_2\text{Br}_4(\text{PMe}_3)_4\text{PF}_6$ plotted at different bandwidths and overlaid on one another. Note that the blue trace resembles the observed experimental MCD spectra.

Figure 4.9 shows the Gaussian resolved 5 K MCD spectra of the cations. This Gaussian resolution was based on the DFT-calculated MCD spectra as well as consideration of the high-symmetry point group and electronic structure of the compounds. The low energy C-term resolves into multiple vibronic progressions at low temperatures and its Gaussian resolved fit is presented in section 4. The MCD spectra were fitted with a number of pseudo-A term bands, i.e. bands of oppositely signed MCD intensity that are close in energy and have similar intensities. This was not so much based on the appearance of the experimental MCD spectra itself, but rather guided by the DFT MCD calculations.

In this way, we realize that the large positive feature at 22940 cm^{-1} for $\text{Re}_2\text{Cl}_4(\text{PMe}_3)_4\text{PF}_6$ and 21330 cm^{-1} for $\text{Re}_2\text{Br}_4(\text{PMe}_3)_4\text{PF}_6$ are a partially cancelled pseudo-A term, whose corresponding negative component has been cancelled in the observed MCD spectrum due to having a lower MCD intensity than its positive counterpart. For $\text{Re}_2\text{Cl}_4(\text{PMe}_3)_4\text{PF}_6$ the calculated MCD spectrum predicts the negative member of band to occur at lower energies than its positive counterpart and for $\text{Re}_2\text{Br}_4(\text{PMe}_3)_4\text{PF}_6$ the positive member of the pseudo-A term is calculated to be at lower

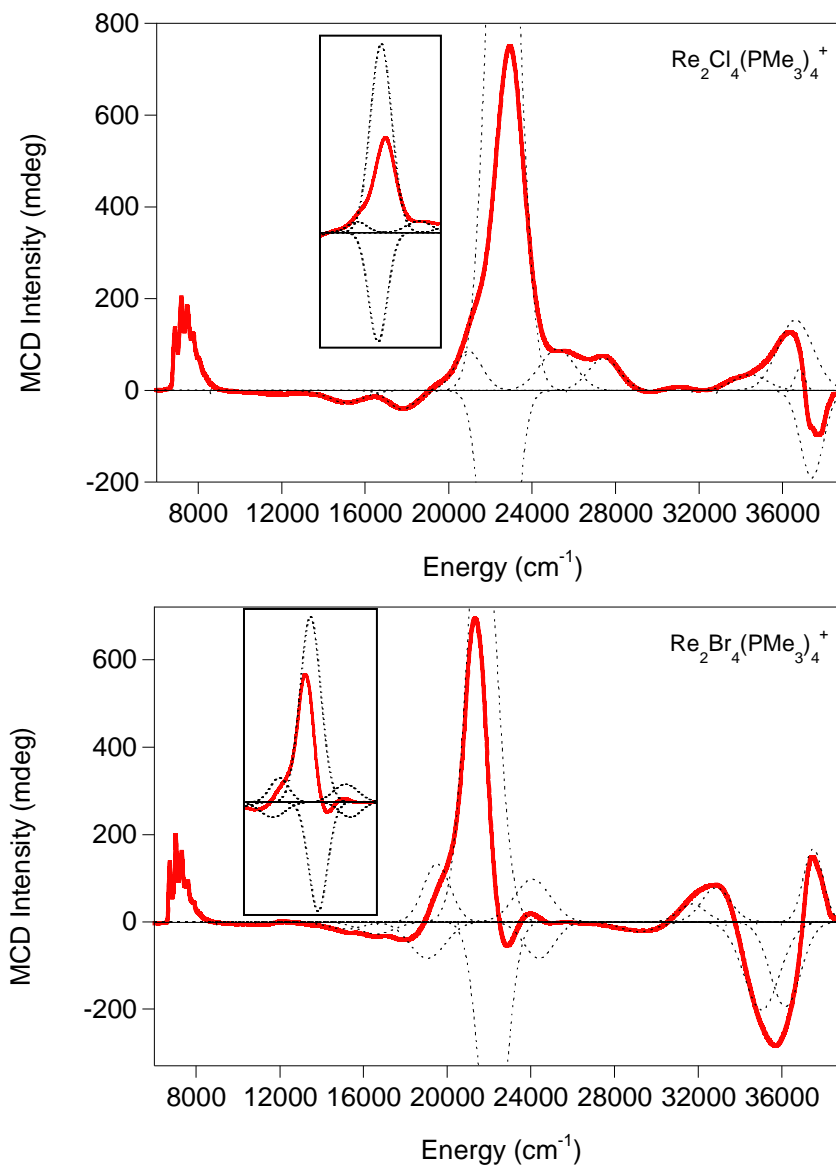


Figure 4.9: Gaussian resolved 5 K, 7 T MCD spectra of $\text{Re}_2\text{Cl}_4(\text{PMe}_3)_4\text{PF}_6$ (top) and $\text{Re}_2\text{Br}_4(\text{PMe}_3)_4\text{PF}_6$ (bottom) in a polystyrene film matrix. Inset: zoom-out of the Gaussian resolved bands.

Table 4.4: Band energies and heights of the Gaussian bands used to fit the 5 K MCD data from the Gaussian resolved MCD fit of $\text{Re}_2\text{Br}_4(\text{PMe}_3)_4\text{PF}_6$ and $\text{Re}_2\text{Cl}_4(\text{PMe}_3)_4\text{PF}_6$.

$\text{Re}_2\text{Br}_4(\text{PMe}_3)_4\text{PF}_6$		$\text{Re}_2\text{Cl}_4(\text{PMe}_3)_4\text{PF}_6$	
<i>Energy (cm⁻¹)</i>	<i>Height</i>	<i>Energy (cm⁻¹)</i>	<i>Height</i>
15130	-16	15110	-27
16610	-28	17780	-41
19060	-83	20950	86
19510	132	22400	-870
21660	1010	22610	1500
22190	-597	25220	90
24080	97	27430	70
24400	-84	34440	34
29150	-23	36630	154
31720	40	36820	47
32865	78	37410	-190
35610	-302		
37500	167		

energies. This large pseudo-A term corresponds to band 5 in the absorption spectrum and has the same band assignment. In the fitted MCD spectrum of $\text{Re}_2\text{Br}_4(\text{PMe}_3)_4\text{PF}_6$, there are smaller pseudo-A terms on either side of band 5, one at 19060 & 19510 cm^{-1} , and the other at 24080 & 24400 cm^{-1} (also shown in Table 4.4), which correspond to absorption bands 4 and 6, respectively, and have the same band assignment as bands 4 and 6 in Table 4.1. Beyond those pseudo-A terms just discussed, it is difficult to further fit the MCD spectra without perhaps overreaching what the data shows. We believe from the DFT calculations and symmetry considerations that there should, in fact, be a number of additional pseudo-A terms in the spectra, but either the negative or the positive component of the pair have been completely cancelled and do not appear in the experimental spectra. Careful comparison of the computed MCD spectra with the

experimental spectra suggests that some positive and negative bands at higher energies in the spectra ($\sim 24000 - 32,000 \text{ cm}^{-1}$) may appear to be members of a pseudo A-term but are actually the positive remnant of one pseudo-A term and the negative remnant of a different pseudo-A term. Interestingly, the MCD spectra of both compounds show weak negative bands at $15110, 17780 \text{ cm}^{-1}$ for $\text{Re}_2\text{Cl}_4(\text{PMe}_3)_4\text{PF}_6$ and $15130, 16610 \text{ cm}^{-1}$ for $\text{Re}_2\text{Br}_4(\text{PMe}_3)_4\text{PF}_6$ (see Table 4.4), which correspond energetically reasonably well to the weak bands 2 and 3 in the fitted absorption spectra of $\text{Re}_2\text{Cl}_4(\text{PMe}_3)_4\text{PF}_6$ ($14950, 17790 \text{ cm}^{-1}$) and $\text{Re}_2\text{Br}_4(\text{PMe}_3)_4\text{PF}_6$ (16315 cm^{-1}), and are assigned as $\delta^* \rightarrow \pi^*$ (or $\delta^* \rightarrow \sigma^*$, $\delta \rightarrow \sigma^*$, and $\delta^* \rightarrow \delta_b^*$) transition, i.e. bands originating from the singly occupied Re-Re δ^* orbital into the various virtual Re-Re antibonding orbitals that lie above the δ^* .

The experimental MCD spectra appear to present a huge violation of the MCD sum rule, which states that the positive and negative MCD intensity should sum to zero when integrated over the whole spectrum. Such violations can be accounted for by out-of-state spin-orbit mixing between excited states $|K_i\rangle$ and the ground state $|A\rangle$. Alternatively, we can look at the calculated absorption and MCD “stick spectra”, i.e. the calculated spectra at a 1 cm^{-1} bandwidth, which show the “intrinsic” calculated pseudo-A terms prior to any cancellation due to overlap of the bands as the bandwidth is increased. Figure 4.10 shows that the negative MCD intensity added over the spectral range is approximately equal to the positive summed MCD intensity. Certainly the relative intensities of one member of a pseudo-A term to another should be about 1:1, when rounded to the nearest integer.

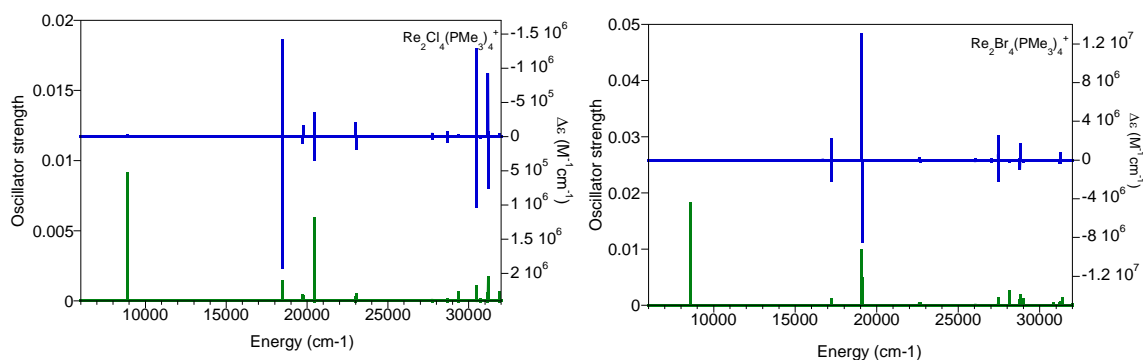


Figure 4.10: DFT-calculated electronic absorption (green) and C-term MCD (blue) spectra plotted at a 1 cm^{-1} bandwidth for $\text{Re}_2\text{Cl}_4(\text{PMe}_3)_4\text{PF}_6$ (left) and $\text{Re}_2\text{Br}_4(\text{PMe}_3)_4\text{PF}_6$ (right).

The remnant of these pseudo-A terms reflects the absolute difference between the C-term intensities, rather than their relative magnitudes. Since the intrinsic MCD intensity of these pseudo-A terms is large, the absolute difference, i.e. the remnant, is still large. Note the decrease in calculated MCD intensity of about 4-5 orders of magnitude from a band width of 1 cm^{-1} to a band width of 1500 cm^{-1} , where the 1500 cm^{-1} bandwidth calculated MCD spectra are similar to the experimental MCD spectra. Of course, one cannot know for certain how much cancellation really occurs, and what the original features truly were, if one takes into account that the calculated MCD spectra are not quantitatively accurate, and thus cannot be used as a hard-and-fast guide. With this in mind we realize that correlating the observed MCD band energies to the absorption band energies can only be of limited success. From Figure 4.10 we also notice that prior to the MCD band maxima shifting as a consequence of the cancellation of the pseudo-A terms, the MCD transitions do have corresponding absorption transitions and vice versa.

4.3.3 DFT Calculated Electronic Structure of $\text{Re}_2\text{Cl}_4(\text{PMe}_3)_4\text{PF}_6^-$ and $\text{Re}_2\text{Br}_4(\text{PMe}_3)_4\text{PF}_6^-$

DFT calculations utilized both Gaussian03 and ADF.2012, and the optimized parameters for some Re-Re and Re-L bond lengths are presented in Table 4.5.

Table 4.5: Selected bond lengths of DFT-optimized structures of $\text{Re}_2\text{Cl}_4(\text{PMe}_3)_4^+$ and $\text{Re}_2\text{Br}_4(\text{PMe}_3)_4^+$.

	$\text{Re}_2\text{Cl}_4(\text{PMe}_3)_4\text{PF}_6^-$			$\text{Re}_2\text{Br}_4(\text{PMe}_3)_4\text{PF}_6^-$		
	Re-Re (Å)	Re-Cl (Å)	Re-P (Å)	Re-Re (Å)	Re-Br (Å)	Re-P (Å)
Gaussian	2.238	2.385	2.513	2.239	2.527	2.517
ADF	2.259	2.352	2.484	2.267	2.513	2.491

The calculated Re-Re bond lengths can be compared to structural data from the literature on similar compounds, $\text{Re}_2\text{Cl}_4(\text{PMe}_3)_4\text{ReO}_4$ with Re-Re of 2.205 Å and $\text{Re}_2\text{Cl}_4(\text{PMe}_2\text{Ph})_4\text{PF}_6^-$ with Re-Re 2.218 Å. The Gaussian optimized structure has a metal-metal bond length that is closer to literature values and was chosen as the geometry on which all further calculations were carried out, i.e. the frequency calculations (Gaussian) as well as the calculation of absorption and MCD spectra (ADF). The results of the frequency calculation will be discussed in section 4.2, while in this section we continue to discuss the calculated absorption and MCD spectra and transition energies as well as the nature of the frontier orbitals.

Let us first consider the unperturbed metal orbitals shown in Figure 4.11. Without any ligands present, the metal dimer would have the orbitals to form a σ bond, a set of degenerate π bonds, a set of degenerate δ bonds and likewise for the antibonding orbitals. It is well known in the literature that $\text{Re}_2\text{Xl}_4(\text{PMe}_3)_4^+$ compounds possess a $\sigma^2\pi^4\delta^2\delta^*1$ configuration, which is due to the fact that in D_{2d} symmetry, the δ orbital sets are not

degenerate. The two sets of δ orbitals are rotate off one another along the axis of the Re-Re bond by 45° , so that one $\delta\delta^*$ set will have its lobes point directly at the ligand bonds (denoted in this document by $\delta_b\delta_b^*$), while the other one has lobes that point between the bonds. We examined the frontier and surrounding molecular orbitals to see how the halide ligands affect the energy ordering and of these metal orbitals for both $X = \text{Cl}$ and Br .

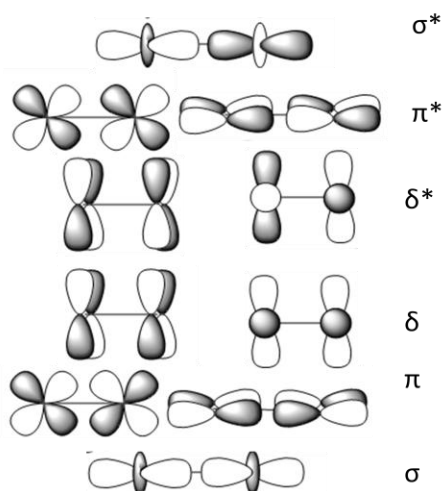


Figure 4.11: Metal dimer d-orbitals.

The summarized contributions are show in Table 4.6, and the % contributions per orbital do not total to 100% as contributions from atomic orbitals below the cut-off value were not included. The left side of the table pertains to $\text{Re}_2\text{Cl}_4(\text{PMe}_3)_4^+$, while the right side pertains to $\text{Re}_2\text{Br}_4(\text{PMe}_3)_4^+$. The center (Re-Re, Re-X, Re-P) columns are shared for

Table 4.6: Composition of molecular orbitals for $\text{Re}_2\text{Cl}_4(\text{PMe}_3)_4^+$ and $\text{Re}_2\text{Cl}_4(\text{PMe}_3)_4^+$.

β MO#	%Re	%Cl	%PMe ₃	Re-Re	Re-X	Re-P	β MO#	%Re	%Br	%PMe ₃
166	56	9	22	δ_b	σ^*	-/ σ^*	156	54	15	25
165	69	24	4	δ_b^*	σ^*	-/ σ	154	75	10	3
164	79	9	3	π^*	σ^*	σ	155	75	10	3
163	75	9	3	π^*	σ^*	σ	153	63	22	-
162	75	13	0	σ^*	π^*	-	152	75	13	-
161	75	19	0	δ^*	π^*	-	151	70	26	0
160	68	27	0	δ	π^*	-	150	64	32	0
159	23	31	32	π	π^*	σ^*	149	24	44	18
158	23	31	32	π	π^*	σ^*	148	24	42	18
157	33	45	10	π	π^*	σ	147	18	61	12
156	33	45	9	π	π^*	σ	146	18	61	12
155	30	63	-	σ	π^*	-	145	22	72	-
152	14	71	-	π	“ σ/σ^* ”	-	142	18	67	-
151	18	69	-	π	“ σ/σ^* ”	-	141	18	67	-
150	Cl, PMe ₃ only orbital			-	-	-	139	Br, PMe ₃ only orbital		
149				-	-	-	138			

both compounds and we notice that the nature of the orbitals is very similar for both $X = \text{Cl}$ and $X = \text{Br}$. The frontier δ and δ^* orbitals (highlighted in brown) have halide-metal π^* character and no phosphine contributions. The δ^* orbital composition for both compounds is very similar, while the δ orbital has more halide character when $X = \text{Br}$. The orbitals below the δ orbital are two e sets with halide-metal π^* character, phosphine-metal σ^* or σ character, and a smaller amount of metal-metal π character. Below those ligand e sets lies the halide-metal π^* orbital that has metal-metal σ character mixed in. For all these ligand orbitals, the halide character in the orbitals is larger when $X = \text{Br}$, as expected since the Br ligand manifold is energetically closer to the Re d-orbital manifold than the Cl ligand orbitals are. Below that follow more ligand based e sets which have much lower metal-character as one gets lower in energy, or no metal character at all. Not shown in Table 4.6

are e sets that follow below the pure ligand orbital listed in the table, which have metal-ligand bonding character (M-Br σ and M-P π or σ) and a small amount of MM π character.

The energy ordering of the virtual metal-dimer d-orbitals is perhaps more surprising, where the σ^* orbital is right above the δ^* orbital and below the π^* orbitals. The σ^* orbital has metal-halide π^* character, which is a weaker antibonding interaction than the metal-halide σ^* character that the higher lying π^* , δ_b^* and δ_b orbitals have. For the bromo compound, the δ_b^* and one of the π^* orbitals are switched in energy, but for both halides the δ_b^* orbital lies lower than the δ_b orbital. This is due to the fact that the δ_b^* orbital has more ligand character than the δ_b orbital, which is metal-ligand antibonding in both cases. All the orbitals examined in Table 4.6 have the same type of metal-metal and metal-ligand interactions for X = Cl vs. X = Br, except for the δ_b^* and δ_b orbitals, which differ in that for X = Cl there is no phosphine character in those orbitals and for X = Br there is metal-phosphine σ and σ^* character in those orbitals. If we compare these computational results to that published by Bursten and coworkers,¹⁵¹ we should note that their study used SCF- α SW as the computational method rather than DFT, and also that the phosphine ligands were approximated as PH₃ ligands. There are some similarities, such as the assignments of the two most notable bands (the low-energy $\delta \rightarrow \delta^*$ band as well as the intense LMCT at $\sim 23500 \text{ cm}^{-1}$), the very similar amount of metal character in the frontier orbitals and below, and some similarities in the energy ordering of these orbitals. Some of the more significant differences include the assignment of band 4, which Bursten assigned as a transition from the frontier orbitals to

virtual metal antibonding orbitals, as well as the description of some of the lower-lying orbitals, such as the presence of Cl lone pair orbitals directly underneath the highest energy metal-metal π e set.

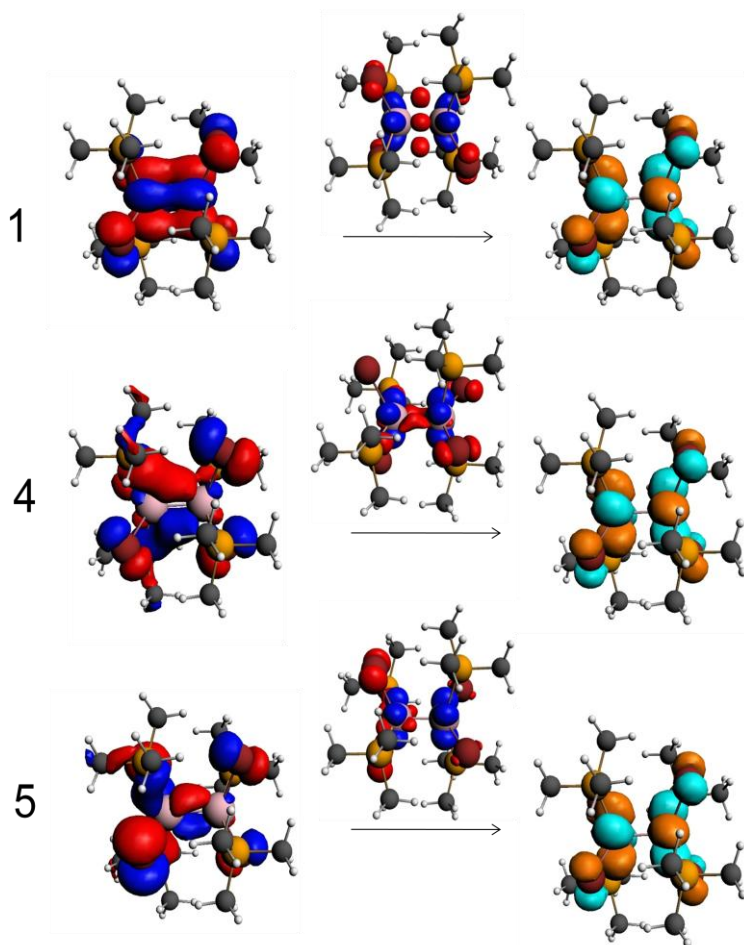


Figure 4.12: Molecular orbitals and EDDMs (electron density difference maps) for $\text{Re}_2\text{Br}_4(\text{PMe}_3)_4^+$. Molecular orbitals that the transition is originating from is on the left of the arrow, the molecular orbital that the promotion is going into (δ^*) is on the right of the arrow, and the EDDM for that transition on top of the arrow (red is electron density loss, blue is gain). Isovalues are 0.03 for molecular orbitals, 0.001 for EDDM band 1, 0.003 for EDDM bands 4 and 5.

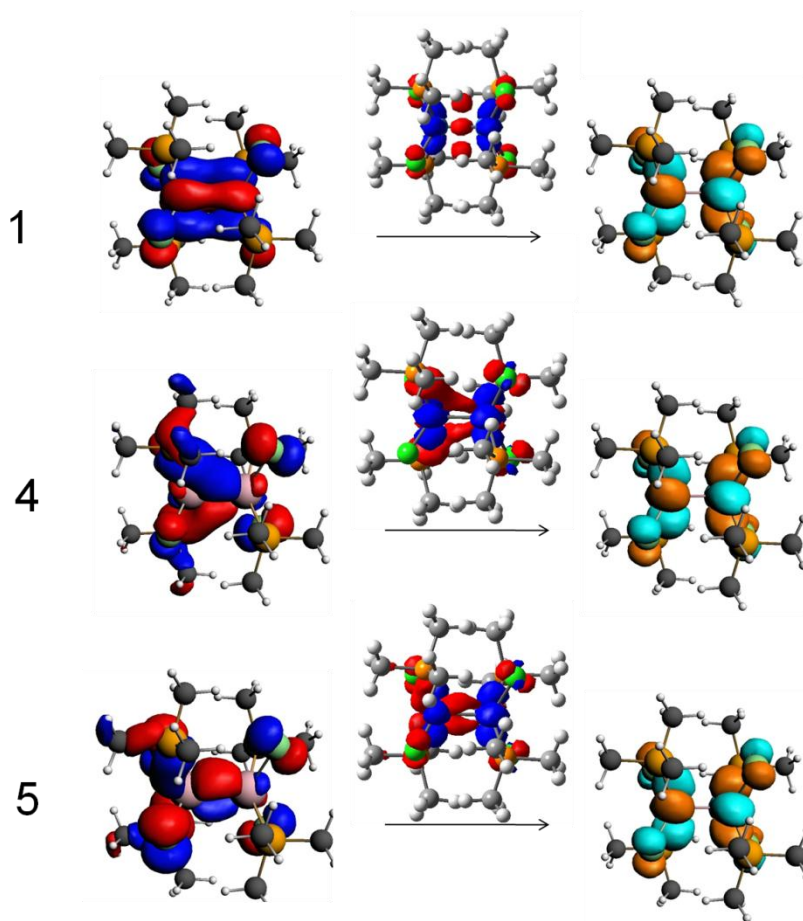


Figure 4.13: Molecular orbitals and EDDMs (electron density difference maps) for $\text{Re}_2\text{Cl}_4(\text{PMe}_3)_4^+$. Molecular orbitals that the transition is originating from is on the left of the arrow, the molecular orbital that the promotion is going into (δ^*) is on the right of the arrow, and the EDDM for that transition on top of the arrow (red is electron density loss, blue is gain). Isovalues are 0.03 for molecular orbitals, 0.001 for EDDM band 1, 0.003 for EDDM bands 4 and 5.

Figure 4.12 and Figure 4.13 show a few molecular orbitals of interest for $\text{Re}_2\text{Br}_4(\text{PMe}_3)_4^+$ and $\text{Re}_2\text{Cl}_4(\text{PMe}_3)_4^+$, respectively, namely the δ and δ^* frontier orbitals, as well as the e set ligand-type orbitals that bands 4, 5 and 6 originate from. Also shown are the electron density difference maps (EDDMs) for bands 1, 4, and 5. An EDDM for a

transition is the weighted sum of all the one-electron promotions that contribute to that transition and represents the difference in electron density before and after the transition. In this document, red is chosen to represent loss of electron density while blue is gain. The EDDMs underscore the LMCT nature of transitions 4 and 5, though the EDDM for transition 1 also has a LMCT component. While bands 4 and 5 are transitions originating from e orbitals, only one member of the e set is displayed in Figure 4.12 and Figure 4.13.

Figures 4.14 and 4.15 show a spectral overlay of calculated and experimental electronic absorption and MCD spectra for both compounds. The bandwidths used for the computed data were 3000 cm^{-1} for absorption spectra and 1500 cm^{-1} for MCD spectra. There is remarkably good qualitative agreement between the experimental absorption and MCD data and the calculated spectra in terms of the relative intensity of the bands within a spectrum and the shape of the spectrum, i.e. the number of bands in the different regions of the spectrum and the relative energies of those bands to one another within a

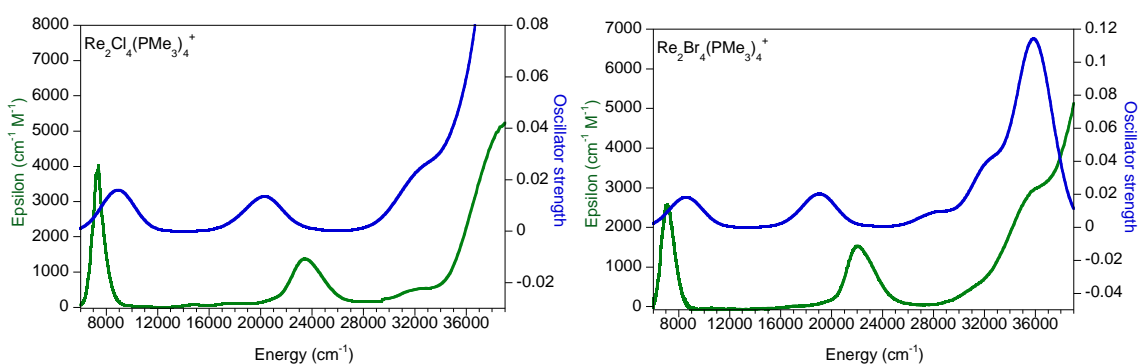


Figure 4.14: DFT-calculated (blue) and experimental (green) electronic absorption spectra of $\text{Re}_2\text{Cl}_4(\text{PMe}_3)_4\text{PF}_6$ (left) and $\text{Re}_2\text{Br}_4(\text{PMe}_3)_4\text{PF}_6$ (right).

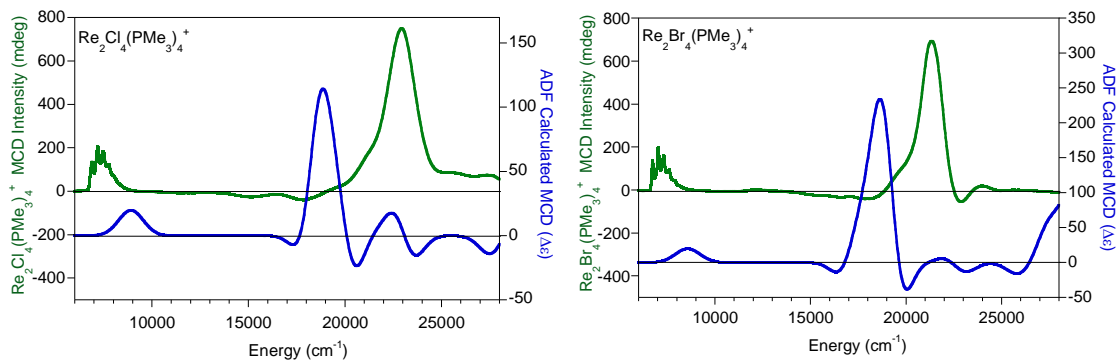


Figure 4.15: DFT-calculated (blue) and experimental (green) MCD spectra of $\text{Re}_2\text{Cl}_4(\text{PMe}_3)_4\text{PF}_6$ (left) and $\text{Re}_2\text{Br}_4(\text{PMe}_3)_4\text{PF}_6$ (right).

region of the spectrum. This is likely due to the fact that these $\text{Re}_2\text{X}_4(\text{PMe}_3)_4^+$ compounds are relatively small molecules with a high symmetry and also energetically isolated transitions.

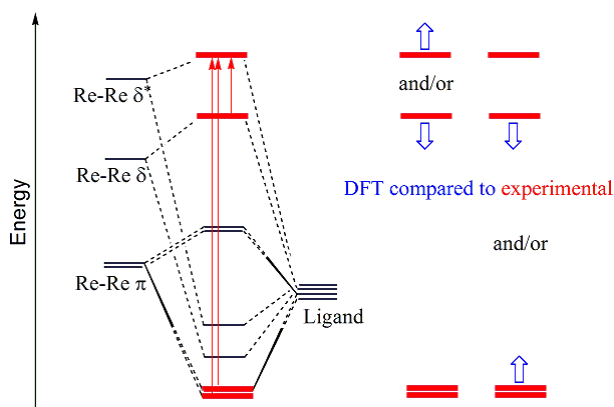


Figure 4.16: Molecular orbital diagram for $\text{Re}_2\text{X}_4(\text{PMe}_3)_4^+$ for the $\delta \rightarrow \delta^*$ band and LMCT bands (energy separations are not drawn to scale).

When comparing the experimental and calculated electronic absorption and MCD spectra of both compounds we always observe two things: that the $\delta \rightarrow \delta^*$ transition is calculated at higher energies than in the experimental data, and that the LMCT transitions originating from filled ligand-based orbitals into the δ^* orbital are calculated at lower

energies than in the experimental data. This is shown in Figure 4.16 in terms of a molecular orbital diagram. The calculations place the $\delta \rightarrow \delta^*$ band at too high an energy, which implies that either the δ orbital is too low in energy with respect to the surrounding orbitals or the δ^* too high in energy, or both. The calculations also place the LMCT bands at too high an energy, which implies that either the δ orbital is too low in energy with respect to the surrounding orbitals or the ligand (+ MM π) orbitals are too high in energy, or both. In their recent DFT study of $[\text{Re}_2\text{Cl}_8]^{2-}$ and various homo- and heterobimetallic analogues of the complex Takagi and coworkers¹⁷⁶ studied the effects of the functional on various computed quantities including Re-Re bond lengths and bond dissociation energies, and compared them with results from ab initio calculations. They concluded that GGA-type functional (GGA = generalized gradient approximation) performed the best as compared to the ab initio results, with the bond stability decreasing as more exchange is added to the functional. The energy of the $\delta \rightarrow \delta^*$ band we calculated with an exchange-correlation functional (B3LYP) is $\sim 5000 \text{ cm}^{-1}$ (for X = Cl), compared to that of the GGA functional (PBE) at $\sim 8900 \text{ cm}^{-1}$, and the experimental energy for the $\delta \rightarrow \delta^*$ band at $\sim 7300 \text{ cm}^{-1}$. The GGA functional (which was the one we used for the absorption and MCD calculations) seems to be somewhat closer to the experimental data, and we also notice that the functional with more exchange (B3LYP) does seem to correspond to a weaker δ bond for the compounds. Perhaps one could adjust the amount of exchange used in the functional and repeat the DFT calculations until the calculated $\delta \rightarrow \delta^*$ band energy matches experimental data exactly, but we have not done so.

4.4 Spectroscopic and Computational Studies of Re Dimers: the Vibronic Structure of the δ - δ^* Band

4.4.1 Vibronic Progressions Resolved in Low-Temperature Optical Spectroscopy

The low-temperature electronic absorption and MCD spectra resolve the δ - δ^* band into several vibronic progressions, which are defined as a series of equally spaced vibronic absorptions.¹⁷⁷ Figure 4.17 shows the Gaussian resolved 5 K MCD spectra of $\text{Re}_2\text{Cl}_4(\text{PMe}_3)_4\text{PF}_6$ and $\text{Re}_2\text{Br}_4(\text{PMe}_3)_4\text{PF}_6$ obtained as frozen solutions in butyronitrile.

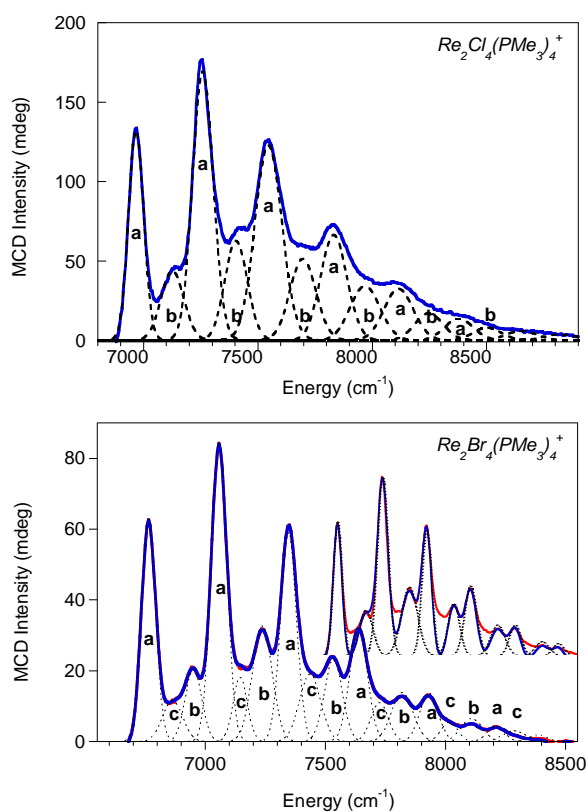


Figure 4.17: Gaussian resolved 5 K MCD $\delta \rightarrow \delta^*$ transition for $\text{Re}_2\text{Cl}_4(\text{PMe}_3)_4\text{PF}_6$ (top) and $\text{Re}_2\text{Br}_4(\text{PMe}_3)_4\text{PF}_6$ (bottom). Peaks belonging to the same progression are marked by the same letter (a, b, or c).

The vibrational fine structure is more resolved for $\text{Re}_2\text{Br}_4(\text{PMe}_3)_4\text{PF}_6$, than for $\text{Re}_2\text{Cl}_4(\text{PMe}_3)_4\text{PF}_6$. Looking at the inset on the Gaussian resolved progression of $\text{Re}_2\text{Br}_4(\text{PMe}_3)_4\text{PF}_6$, it is clear that three progressions are needed to fit the band for the bromo compound while two progressions are sufficient to fit the chloro compound. For $\text{Re}_2\text{Br}_4(\text{PMe}_3)_4\text{PF}_6$ the frequency of progression “a” (i.e. the energy spacing from one “a” peak to the next “a” peak) is 289 cm^{-1} . Progressions “b” and “c” have the same progression frequency as “a”, 289 cm^{-1} , and thus are based on the same progression forming mode. The spacing from the first “a” to the first “b” peaks is 184 cm^{-1} , and the spacing from the first “a” to the first “c” peak is 90 cm^{-1} . The first “b” and “c” peak are the vibronic origins of their progressions.

Likewise, for $\text{Re}_2\text{Cl}_4(\text{PMe}_3)_4\text{PF}_6$ the frequency of progression “a” is 286 cm^{-1} , and progressions “b” has the same progression frequency as “a”. The spacing from the first “a” to the first “b” peak is 181 cm^{-1} , which is the vibronic origin of the “b” progression for $\text{Re}_2\text{Cl}_4(\text{PMe}_3)_4\text{PF}_6$. $\text{Re}_2\text{Cl}_4(\text{PMe}_3)_4\text{PF}_6$ can be fitted with a third progression like $\text{Re}_2\text{Cl}_4(\text{PMe}_3)_4\text{PF}_6$, and in that case the vibronic origin of that progression would be $\sim 80\text{ cm}^{-1}$. Since the data, however, does not require a third progression be used in the fit, we decided not to add it.

The intensity of each peak in a progression relative to the other peaks in the progression depends on the overlap of the vibrational wavefunction of the ground electronic state potential energy surface for the progression forming mode with the vibrational wavefunctions of the excited electronic state potential energy surface for the

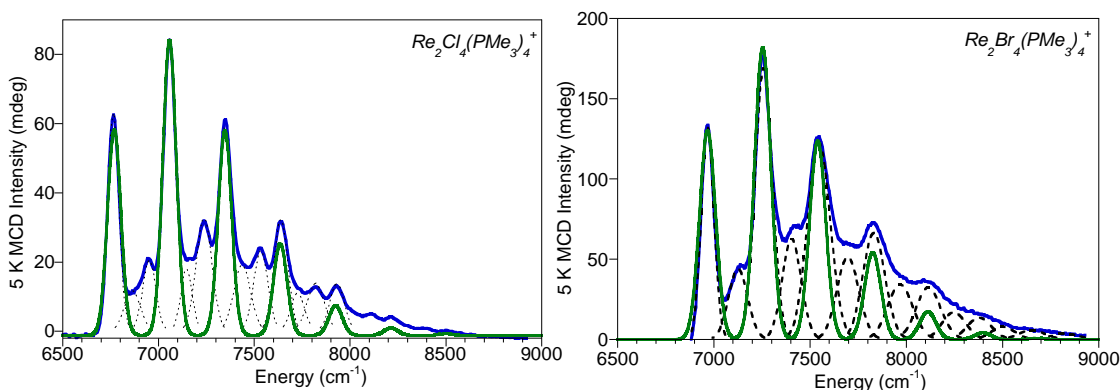


Figure 4.18: ORCA_ASA¹⁷⁸ simulated intensity patterns of the vibronic progression overlaid on the experimental resolved vibronic progression.

progression forming mode. Small displacements of the ground state potential energy surface with respect to the excited state potential energy surface will lead to a larger intensity of the $0 \rightarrow 0$ peak relative to other peaks in the progression, where the notation is (vibrational quantum level of the mode in the ground electronic state) \rightarrow (vibrational quantum level of the mode in the excited electronic state). The overlap of the vibrational wavefunctions of the ground and excited electronic states depend on the shape (force constant) of the ground state potential energy surface, the shape (force constant) of the excited state potential energy surface, and the displacement of the ground state from the excited state potential energy surface. We assume that only the lowest vibrational level is populated in the ground state since $kT \ll \nu$ at 5 K. Combining the experimental data available from low-temperature MCD spectroscopy and resonance Raman spectroscopy, we have information about the excited state vibrational levels (from 5 K MCD resolved vibronic progression), about the ground state vibrational levels (resonance Raman frequencies), and about the displacement of the excited state from the ground state

potential energy surface (intensity pattern of the 5 K resolved vibronic progression). With these data, we can use the ORCA_ASA^{79,178} fitting spectral simulation utility to fit the intensity patterns of the vibronic progressions and extract Δ , the dimensionless displacement parameter. The results of these simulations are shown in Figure 4.18.

For $\text{Re}_2\text{Cl}_4(\text{PMe}_3)_4\text{PF}_6$ we have an excited state frequency of 286 cm^{-1} and a ground state frequency of 297 cm^{-1} for the Re-Re stretch activated during the $\delta \rightarrow \delta^*$ transition. For $\text{Re}_2\text{Br}_4(\text{PMe}_3)_4\text{PF}_6$ have an excited state frequency of 289 cm^{-1} and a ground state frequency of 302 cm^{-1} for the Re-Re stretch activated during the $\delta \rightarrow \delta^*$ transition. Notice that the excited state frequencies are about 10 cm^{-1} lower than the ground state frequencies, which is reasonable since the excited state has a weaker Re-Re bond than the ground state. The ground and excited state frequency are very similar to one another, however, which implies that the curvature of the excited state surface does not differ significantly from that of the ground state surface. This also makes it probable that the first peak in the vibronic progression is indeed the $0 \rightarrow 0$ peak, rather than for example a $0 \rightarrow 1$ vibrational peak, as would be that case if the ground and excited states were displaced to such an extent that the $v = 0$ ground state vibrational level no longer had any overlap with the $v = 0$ excited state vibrational level.

The ORCA_ASA¹⁷⁸ simulation utilized the above mentioned ground and excited vibrational frequencies in the “IMDHOF A” (Independent Mode Displaced Harmonic Oscillators with Frequency Alteration) model, which assumes harmonic potential energy surfaces and a zero-temperature approximation, but allows for different frequencies in the ground and excited state, as well as the displacement of the excited state with respect to

the ground state. The results of these spectral simulations give values for $\Delta = 1.64$ for $\text{Re}_2\text{Cl}_4(\text{PMe}_3)_4\text{PF}_6$, and $\Delta = 1.66$ for $\text{Re}_2\text{Br}_4(\text{PMe}_3)_4\text{PF}_6$. We can convert Δ , the dimensionless displacement parameter, into a dimensioned parameter and thus obtain the bond length change in \AA for the Re-Re stretch of the $\delta \rightarrow \delta^*$ transition following the methodology of Gamelin *et al.*,¹⁷⁹ where ΔQ_n is the dimensioned

$$\Delta Q_n = \frac{5.8065}{\sqrt{\mu_n \nu_n}} \Delta_n \quad \& \quad \Delta r_n = \Delta Q_n * \text{calculated internal coordinate displacement}$$

Eq. 33

displacement parameter, μ_n is the reduced mass for the vibrational mode, ν_n the frequency of the vibration, and Δ_n the dimensionless normal coordinate displacement parameter. From the frequency calculation for $\text{Re}_2\text{Br}_4(\text{PMe}_3)_4\text{PF}_6$ we obtain μ_n as 35.456 amu, ν_n as 319.56 cm^{-1} , and Δ_n as 1.66 from the spectral simulation. Since the Re-Re stretching mode for $\text{Re}_2\text{Br}_4(\text{PMe}_3)_4\text{PF}_6$ is calculated as a purely Re-Re stretch with no other nuclear motions mixed into it, we can approximate the molecule during that vibration as a homo-diatomic molecule and extract the internal coordinate displacement from the frequency calculation output without having to calculate any mass-weighted eigenvectors (as there is only one vibrational mode for a homo-diatomic molecule). The calculated internal coordinate displacement for the mode is 0.60. Using these values, we calculate $\Delta Q_n = 0.095 \text{ \AA}$ in Q-space and $\Delta r_n = 0.057 \text{ \AA}$, the bond length change in \AA for the Re-Re stretch of the $\delta \rightarrow \delta^*$ transition. As discussed in the section 4.2, for $\text{Re}_2\text{Cl}_4(\text{PMe}_3)_4\text{PF}_6$ the Re-Re stretching mode is coupled to the Re-Cl stretches in the

results of the frequency calculation, and thus would require a more detailed treatment to obtain the internal coordinate displacement.

4.4.2 Resonance Raman Spectra and DFT Calculated Vibrational Frequencies of $\text{Re}_2\text{Cl}_4(\text{PMe}_3)_4\text{PF}_6$ and $\text{Re}_2\text{Br}_4(\text{PMe}_3)_4\text{PF}_6$

In this section we show the resonance Raman data of $\text{Re}_2\text{Cl}_4(\text{PMe}_3)_4\text{PF}_6$ and $\text{Re}_2\text{Br}_4(\text{PMe}_3)_4\text{PF}_6$, and use the results of DFT frequency calculations on the cations to assign key vibrational modes in the resonance Raman spectra as well as the progression forming modes and vibronic origins from section 4.1.

Resonance Raman spectra were acquired as solid state samples in a $\text{NaCl}/\text{Na}_2\text{SO}_4$ matrix for the laser excitation lines of 407 nm, 458 nm, 488 nm, 514 nm, 568 nm and 647 nm, where the data for the 407 nm line only goes as low as $\sim 600 \text{ cm}^{-1}$ due to the unavailability of the appropriate filters for this line. Since the frequency of a vibration is proportional to the square root of the reciprocal of its reduced mass, μ , we should expect a $\sim 30\%$ reduction in frequency for a pure Re-Br stretch mode as compared to a pure Re-Cl stretch mode (using the ratio of the square root of the reciprocal of the reduced masses).

$$v = \frac{1}{2\pi} \sqrt{\frac{k}{\mu}} \text{ where } \mu = \frac{m_1 m_2}{(m_1 + m_2)} \quad \text{Eq. 34}$$

$$v \propto \sqrt{\frac{1}{\mu}} \quad 0.18 \text{ for X = Cl, } 0.13 \text{ for X = Br}$$

The assumptions include that k , the force constant, is approximately the same for Re-Cl and Re-Br bonds, and also that the vibrational modes that are potentially being compared to not change themselves. What we mean by this is that the frequency of metal-

halide modes shift upon halide substitution, and that metal-halide modes of appropriate symmetry can mix/couple to metal-metal or metal-phosphine vibrational modes of like symmetry that they are energetically close to. Thus a metal-chloride mode at energy x might mix with another (metal-metal/metal-phosphine) mode y that is close by energetically, while the corresponding metal-bromide mode at energy y would be energetically close to perhaps a different metal-metal/metal phosphine mode, and mix

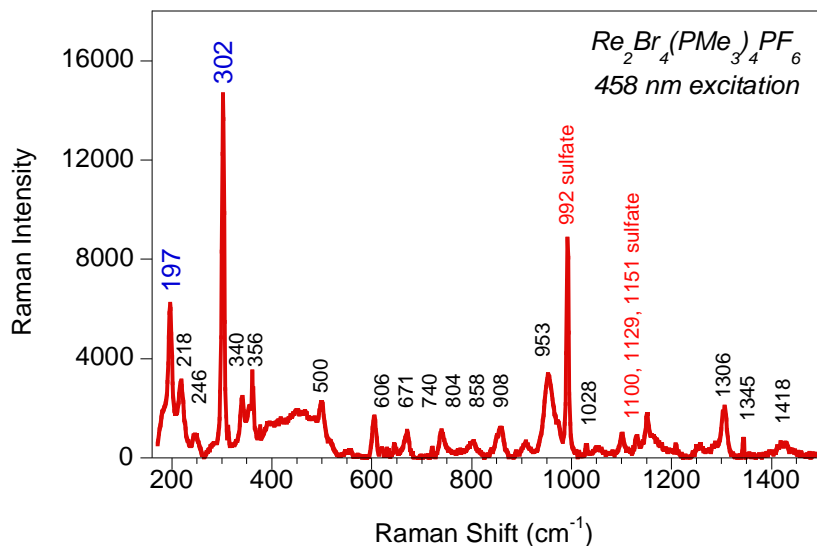


Figure 4.19: Resonance Raman spectrum of $\text{Re}_2\text{Br}_4(\text{PMe}_3)_4\text{PF}_6$ in a $\text{NaCl}/\text{Na}_2\text{SO}_4$ matrix at 458 nm excitation.

with it. The new modes are linear combinations of the original modes, but are now no longer comparable between $\text{Re}_2\text{Cl}_4(\text{PMe}_3)_4\text{PF}_6$ and $\text{Re}_2\text{Br}_4(\text{PMe}_3)_4\text{PF}_6$, and this is in fact what we observe in the results of the frequency calculations.

In resonance Raman, only modes that are totally symmetric (i.e. A_1 in D_{2d} symmetry, character table included in Appendix 6.3.2) will be resonantly enhanced,^{89,95} and in particular those vibrational modes that are alike to the distortion of the electronic

transition that is being excited by the laser light. Figure 4.19 shows the resonance Raman spectrum of $\text{Re}_2\text{Br}_4(\text{PMe}_3)_4\text{PF}_6$ at 458 nm, which is directly at the maximum of the absorption peak of band 5 for the compound, and shows the most resonance enhancement. Resonance Raman spectra for the less enhanced laser lines are included in Appendix 6.3.1. Sulfate peaks (the internal standard) are marked in red. The two most enhanced modes are at 197 cm^{-1} and 302 cm^{-1} , and the intensity of the 302 cm^{-1} mode is large enough that we can identify its overtones at 606 cm^{-1} and 908 cm^{-1} in the spectra as well. Also prominent are peaks at 218 and 953 cm^{-1} . There are a number of smaller Raman peaks at $\sim 350\text{ cm}^{-1}$, $600\text{--}900\text{ cm}^{-1}$ and $1300\text{--}1420\text{ cm}^{-1}$.

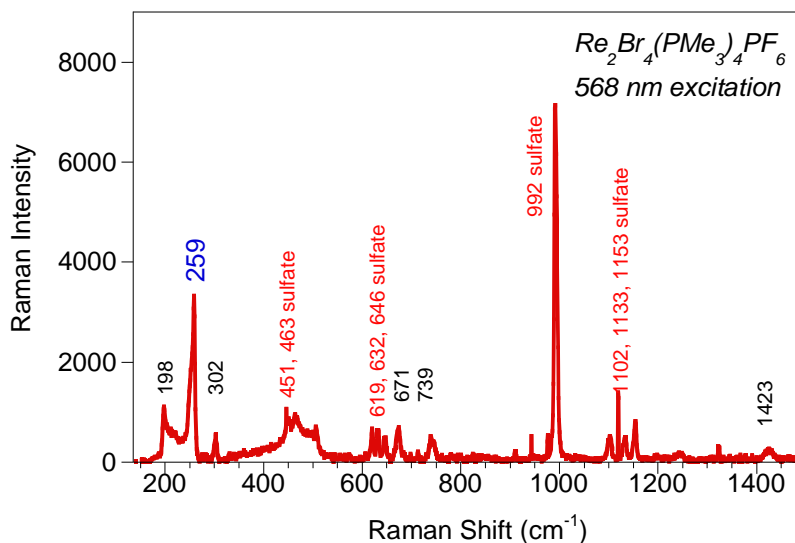


Figure 4.20: Resonance Raman spectrum of $\text{Re}_2\text{Br}_4(\text{PMe}_3)_4\text{PF}_6$ in a $\text{NaCl}/\text{Na}_2\text{SO}_4$ matrix at 568 nm excitation.

All other laser lines have overall the same peaks, but with progressively smaller intensities with respect to the internal standard as the excitation energy moves away from band 5 to lower energies. An exception to this is that at the 568 nm excitation, a mode

occurring at 259 cm^{-1} is resonantly enhanced (spectrum shown in Figure 4.20). The 568 nm excitation energy spectrum in Figure 4.20 also serves to show which modes are consistently present for all the laser line, those on-resonance and off-resonance with band 5, namely the modes at $\sim 670\text{ cm}^{-1}$, $\sim 740\text{ cm}^{-1}$, and $\sim 1423\text{ cm}^{-1}$.

DFT frequency calculations for $\text{Re}_2\text{Br}_4(\text{PMe}_3)_4^+$ show an A_1 , P-Re-P & Br-Re-Br bending mode at 94 cm^{-1} , an A_1 , Re-Br stretch at 189 cm^{-1} , and an A_1 , Re-Re stretch at 320 cm^{-1} . Notice that the totally symmetric halide-metal stretching mode (Re-Br) does not mix with any other A_1 mode, while the totally symmetric metal-halide bending mode (Br-Re-Br) mixes with an A_1 phosphine-metal bending mode. These DFT-calculated A_1 modes are in excellent agreement with the vibronic data from the low-temperature MCD data, which had vibronic origins at 90 cm^{-1} and 184 cm^{-1} and the progression frequency for all three progressions at 289 cm^{-1} . Frequencies obtained from the MCD data are excited state frequencies and as such are expected to be somewhat lower than ground state frequencies since the excited state has less Re-Re bonding character than the ground state. Resonance Raman frequencies, 197 cm^{-1} & 302 cm^{-1} , are also ground state vibrational frequencies and are thus higher than the corresponding vibronic progression frequencies. We thus assign the vibronic origin at 90 cm^{-1} as a totally symmetric P-Re-P & Br-Re-Br bending mode, the resonance Raman peak at 197 cm^{-1} and the vibronic origin at 184 cm^{-1} as the totally symmetric Re-Br stretch, and the resonance Raman peak at 302 cm^{-1} and the progression forming mode of 289 cm^{-1} as the Re-Re stretch for $\text{Re}_2\text{Br}_4(\text{PMe}_3)_4^+$. We note that for $\text{Re}_2\text{Br}_4(\text{PMe}_3)_4\text{PF}_6$ we are on resonance with band 5 at the 458 nm laser excitation energy, and that band 5 is an electronic transition that should

produce a distortion along the Re-Re bond as well as, to a lesser extent, the Re-Br bonds. This consideration further rationalizes our assignment. The assignment of the vibronic structure for $\text{Re}_2\text{Br}_4(\text{PMe}_3)_4^+$ is similar to that reported in the literature for $[\text{Re}_2\text{Br}_8]^{2-}$, where three progressions were observed at 5 K, and the progression forming mode of 255 cm^{-1} was assigned as the Re-Re stretch, while the vibronic origins at 98 cm^{-1} were assigned as the ReReBr bend (whereas we assigned a similar frequency mode for $\text{Re}_2\text{Br}_4(\text{PMe}_3)_4^+$ as the BrReBr bend), and at 184 cm^{-1} as the Re-Br stretch. The modes observed at 217 cm^{-1} and 259 cm^{-1} do not have a clear assignment based on the frequency calculations, but are in the energy range where we see bending modes of Re and its ligands.

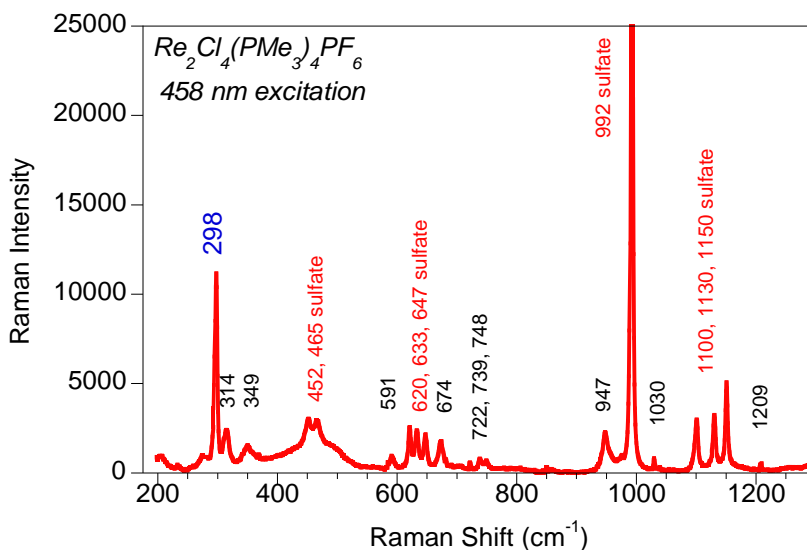


Figure 4.21: Resonance Raman spectrum of $\text{Re}_2\text{Cl}_4(\text{PMe}_3)_4\text{PF}_6$ in a $\text{NaCl}/\text{Na}_2\text{SO}_4$ matrix at 458 nm excitation.

Figure 4.21 shows the (resonance) Raman spectrum of $\text{Re}_2\text{Cl}_4(\text{PMe}_3)_4\text{PF}_6$ at 458 nm, which is not directly at the maximum of the absorption peak of band 5 for this compound. Resonance Raman spectra for the other available laser lines are included in Appendix 6.3.1. Since 458 nm is on the shoulder of band 5, we would still expect some enhancement. Sulfate peaks are marked in red, and the y-axis has been scaled such that the peaks with lower intensities are visible. The y-axis was scaled down by about a factor of two from where the 992 cm^{-1} sulfate peak would be on scale. The most enhanced mode is at 298 cm^{-1} , and the peak observed at 591 cm^{-1} is likely its overtone. Other Raman peaks are at $\sim 350\text{ cm}^{-1}$ and $600\text{--}800\text{ cm}^{-1}$. Other laser lines have overall the same peaks, and for the 514 nm line, for which the scan was extended to higher Raman shifts, we also observe a peak at 1427 cm^{-1} .

DFT frequency calculations for $\text{Re}_2\text{Cl}_4(\text{PMe}_3)_4^+$ show an A_1 , Cl-Re-Cl bending mode at 120 cm^{-1} , an A_1 , Re-Re & Re-Cl stretch at 296 cm^{-1} , and an A_1 , Re-Re, Re-Cl & Re-P stretch at 334 cm^{-1} . Notice that the totally symmetric halide-metal stretching mode (Re-Cl) mixes with the Re-Re stretch giving two totally symmetric stretches split in energy by $\sim 40\text{ cm}^{-1}$. The totally symmetric metal-halide bending mode (Cl-Re-Cl) does not mix. We assign the resonance Raman peak at 297 cm^{-1} and the progression forming mode of 286 cm^{-1} as the Re-Re stretch, which may or may not have Re-Cl stretching character in it. The experimental ground state frequency of 297 cm^{-1} is higher than the experimental excited state frequency of 286 cm^{-1} , in accordance with the loss of Re bonding character in the excited state. While the DFT frequency calculation results differ between the two compounds, their experimental data (in particular the vibronic

progression), are very similar. While the assignment is not entirely clear, a reasonable strategy is to mirror the assignment of the bromo compound and assume that the calculation may not have calculated the vibrational modes for the chloro compound accurately. We thus tentatively assign the vibronic origin 181 cm^{-1} as a Re-Cl stretch. We also note that even though the vibronic progression of the chloro compound clearly shows a vibronic origin at 181 cm^{-1} , no corresponding peak is observed in the (resonance) Raman data. One difference between the MCD data and the resonance Raman data is that they are not associated with the same electronic transition.

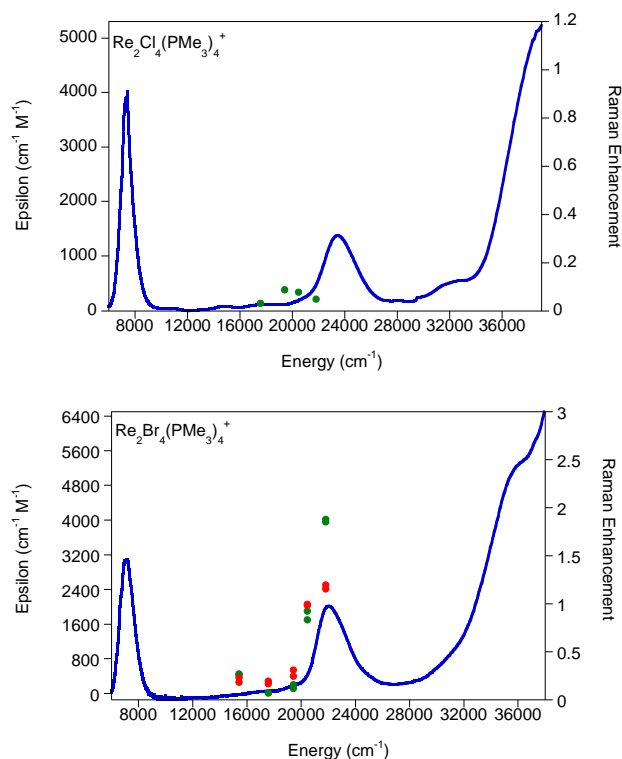


Figure 4.22: Resonance Raman enhancement profiles for $\text{Re}_2\text{Cl}_4(\text{PMe}_3)_4\text{PF}_6$ (top) and $\text{Re}_2\text{Br}_4(\text{PMe}_3)_4\text{PF}_6$ (bottom).

$\text{Re}_2\text{Cl}_4(\text{PMe}_3)_4\text{PF}_6$: area 297 cm^{-1} peak / area 992 cm^{-1} peak (green), $\text{Re}_2\text{Br}_4(\text{PMe}_3)_4\text{PF}_6$: area 301 cm^{-1} peak / area 992 cm^{-1} peak (green) and area 196 cm^{-1} peak / area 992 cm^{-1} peak (red).

The MCD data is extracted from the $\delta \rightarrow \delta^*$ band, which has Re bonding to antibonding character as well as some LMCT character. In the resonance Raman spectra in Figure 4.21 and Figure 4.19 the electronic transitions corresponding to bands 4 for X = Cl and bands 4 and 5 for X = Br were excited. These bands both have Re bonding to antibonding character and LMCT character also, which is why the data compare so well in case of $\text{Re}_2\text{Br}_4(\text{PMe}_3)_4\text{PF}_6$.

The resonance Raman enhancement profiles shown in Figure 4.22 plot the enhancement of the key modes relative to the sulfate internal standard as a function of laser excitation energy. The Raman intensity of the mode relative to the intensity of the sulfate internal standard is plotted as a function of laser excitation energy and overlaid onto the room temperature electronic absorption spectra of the compounds. For $\text{Re}_2\text{Cl}_4(\text{PMe}_3)_4\text{PF}_6$, we chose the 297 cm^{-1} mode to profile, while for $\text{Re}_2\text{Br}_4(\text{PMe}_3)_4\text{PF}_6$ we chose the 196 cm^{-1} and 301 cm^{-1} modes. Notice that while the Raman mode of chloro compound shows little resonance enhancement, the bromo compounds has both modes (Re-Re stretch and Re-Br stretch) clearly enhanced under band 5.

DFT frequency calculations show that phosphine-methyl group bending modes occur in the range of $600\text{-}800\text{ cm}^{-1}$, while carbon-hydrogen bending modes (i.e. within a methyl group) occur in the range of $1300\text{-}1450\text{ cm}^{-1}$. In particular, the totally symmetric phosphine-methyl bend is calculated at 656 cm^{-1} for the bromo compound and at 657 cm^{-1} for the chloro compound. The totally symmetric carbon-hydrogen bending bend is calculated at 1349 cm^{-1} for the bromo compound and at 1351 cm^{-1} for the chloro compound. If we examine the Raman data for modes, which do not shift upon halide

substitution, in those energy ranges, we notice modes at $\sim 670\text{ cm}^{-1}$, $\sim 740\text{ cm}^{-1}$ and $\sim 1417\text{-}1427\text{ cm}^{-1}$ that are common between both compounds and are present at all laser lines. They are more clearly seen in the off-resonance spectra, as they are not expected to be resonantly enhanced under the absorption band that is being excited. We assign the 670 cm^{-1} band as the totally symmetric bend, and the $1417\text{-}1427\text{ cm}^{-1}$ may be a totally symmetric bend. The frequency calculations also show Re-P stretching modes in the vicinity of 330 cm^{-1} , in particular the totally symmetric Re-P modes at 331 cm^{-1} for $\text{Re}_2\text{Br}_4(\text{PMe}_3)_4\text{PF}_6$ and 334 cm^{-1} for $\text{Re}_2\text{Cl}_4(\text{PMe}_3)_4\text{PF}_6$. Thus the resonance Raman peaks at $\sim 340\text{-}355\text{ cm}^{-1}$ observed for both compounds are likely totally symmetric Re-P stretches perhaps mixed with a small amount of Re-Re stretch, since they do show a small resonance enhancement (for $X = \text{Br}$ as the laser excitation moves under band 5). While the frequency calculation for $\text{Re}_2\text{Br}_4(\text{PMe}_3)_4\text{PF}_6$ does not show Re-Re and Re-P, the data would support it.

As noted in the previous section, the ground and excited state frequencies for the Re-Re stretch of both compounds are very similar, indicating that the δ bonding interaction does not contribute significantly to the total force constant of the Re-Re bond in these compounds. Moreover, the Re-Re stretch ground- and excited state frequencies are similar between the two compounds, which suggests that the progression forming mode likely has little halide character. These observations also apply to a comparison of the vibrational frequencies in the literature for $[\text{Re}_2\text{Cl}_8]^{2-}$, and $[\text{Re}_2\text{Br}_8]^{2-}$, where for the vibronic progression of the $\delta \rightarrow \delta^*$ band neither excited state vibrational frequencies (248

cm^{-1} for $X = \text{Cl}$, 255 cm^{-1} for $X = \text{Br}$) nor ground state vibrational frequencies (274 cm^{-1} for $X = \text{Cl}$, 277 cm^{-1} for $X = \text{Br}$) differ much upon halide substitutions.

4.5 Conclusion

We have employed a variety of spectroscopic and computational methods to study the effect of halide substitution for $\text{Re}_2\text{Cl}_4(\text{PMe}_3)_4\text{PF}_6$ and $\text{Re}_2\text{Br}_4(\text{PMe}_3)_4\text{PF}_6$. These compounds possess $\frac{1}{2}$ of a Re-Re δ bond in addition to one σ and two π bonds, and thus present the opportunity to investigate metal-metal δ bonding interactions, and the effect of the halide ligand orbitals on the compounds in general and the δ bond in particular. The small band shift for the $\delta \rightarrow \delta^*$ transition in both the electronic absorption and MCD data indicates that this transition possesses little LMCT character for either compound. To the best of our knowledge, the absorption and MCD spectra for these compounds presented in this document are the first reported actual electronic spectra (as opposed to data tables) for the pure monocation compounds, and the first reported C-term MCD spectra for $\text{Re}_2\text{Cl}_4(\text{PMe}_3)_4\text{PF}_6$ and $\text{Re}_2\text{Br}_4(\text{PMe}_3)_4\text{PF}_6$. The absorption and MCD data show that the $\delta \rightarrow \delta^*$ band is energetically well-isolated, and most transitions above the $\delta \rightarrow \delta^*$ band in energy are assigned as LMCT bands, based on both the observed band shifts upon halide substitution and DFT results. Analysis of the DFT-computed molecular orbitals shows that interactions with the halide and trimethylphosphine ligands control the energy ordering of the virtual metal d-orbital manifold, so that above the δ & δ^* frontier orbitals lie the σ^* , π^* , π^* , δ_b^* , δ_b orbitals for the chloro compound, and σ^* , π^* , δ_b^* , π^* , δ_b for the bromo compound. The energy ordering of these orbitals can be explained by examining the ligand-metal antibonding interactions in those orbitals, both

in terms of the % ligand character and the type of ligand-metal antibonding interaction, i.e. σ^* versus π^* . Band shifts of the LMCT bands are $\sim 1400\text{ cm}^{-1}$ for the most intense LMCT bands compared to the literature optical electronegativity data of a 6000 cm^{-1} band shift for an electron from a π Cl versus Br orbital.

MCD spectra showed $\delta \rightarrow \delta^*$ band as a positive C-term. Since the transition is z-polarized in D_{2d} symmetry, it is formally forbidden in MCD, and gains intensity by mixing other states to acquire partial x-y character. As the low-energy $\delta \rightarrow \delta^*$ band is an energetically isolated transition occurring at an energy approximately half way between the ground state and the next excited state with any appreciable oscillator strength, it mixes with both the ground state and LMCT excited state in approximately equal amounts.

Initial expectations were that the high symmetry of these molecules (D_{2d}) would make the band assignment of the MCD spectra easier, since the application of group theory would allow predictions on the allowedness of all transitions. It was found, however, that the presence of a large number of pseudo-A terms, which correspond to the numerous LMCT transitions into or out of almost-degenerate e set orbitals, reduces the information one can directly gather from the experimental MCD spectrum. Often, MCD spectra are extremely helpful for band assignments, as MCD is a signed technique and thus usually offers a greater resolution of the bands in the spectrum as compared to electronic absorption. Furthermore variable temperature MCD is a great tool to confirm whether weak features are C-term MCD or part of the baseline. The presence of these pseudo A-terms with positive and negative components that are almost degenerate due to

the high symmetry was found to lead to a large amount of cancellations in the MCD spectrum, and thus an observed experimental MCD spectrum that does not show the presence of the pseudo-A terms and appears to be violating the MCD sum rule.

For these molecules, in particular $\text{Re}_2\text{Br}_4(\text{PMe}_3)_4\text{PF}_6$, DFT-calculated electronic absorption and MCD spectra were very similar to the experimental data, albeit with some systematic band shifts between the computational and experimental data. With the aid of the DFT results, we were able to suggest a Gaussian-resolved band fit to the experimental MCD data, as well as produce band assignments for the observed bands in the electronic absorption spectra and their associated MCD counterparts.

Several vibronic progression were resolved in the $\delta \rightarrow \delta^*$ band at 5 K. The progression frequency as well as the energy of the vibronic origins was correlated to resonance Raman data and DFT-calculated vibrational frequencies. For $\text{Re}_2\text{Br}_4(\text{PMe}_3)_4\text{PF}_6$ in particular we found a very good agreement between excited states vibronic progression frequencies, ground state resonance Raman frequencies and DFT-calculated frequencies. The progression forming mode was assigned as the Re-Re stretch, while the vibronic origins were assigned as the totally symmetric Re-Br stretch and a couple P-Re-P/Br-Re-Br bend. Since the electronic absorption transition that is excited by the Raman laser has both metal bonding to antibonding character and LMCT character, it is reasonable that the Re-Re stretch as well as the totally symmetric metal-halide modes should be resonantly enhanced during that transition. The progression-forming mode itself, however, does not appear to have a large amount of halide character in it since the frequency of the progression does not change more than a few wavenumbers upon halide

substitution. Furthermore, the very close frequencies for the ground state and excited state of the Re-Re stretch suggest that the excited state distortion associated with the $\delta \rightarrow \delta^*$ transition is quite small.

The energy of the $\delta \rightarrow \delta^*$ transition, which represents a net change of one δ bond, is close to 1 eV (i.e. 6844 cm^{-1} for X = Cl, 6774 cm^{-1} for X = Br experimentally, and 8913 cm^{-1} for X = Cl, 8575 cm^{-1} for X = Br computationally). We observe that a strong interaction of the Re metal core with its ligands serves to reduce the energy of that $\delta \rightarrow \delta^*$ transition, where for a ligand that has a weaker π interaction with the metal such as X = F the DFT-computed $\delta \rightarrow \delta^*$ transition occurs at 9832 cm^{-1} . We can reconcile that the $\delta \rightarrow \delta^*$ transition energy is as large as one electron volt with the vibrational data showing that the excited state potential energy surface hardly distorts from the ground state potential energy surface for the same transition by considering the other contributions to the Re bond. Specifically, the Re-Re stretching frequency has contributions from the σ bond, the two π bonds, and the δ bonding interaction. The small change between ground- and excited state Re-Re stretching frequencies are evidence that the contribution of the δ bonding interaction to the Re-Re bond force constant is very small compared to that of the σ and π contributions. Likewise the calculated Re-Re bond length change during the $\delta \rightarrow \delta^*$ transition of 0.057 Å represents a bond length change of only ~2-3% despite the bond order changing by one whole δ bond during the $\delta \rightarrow \delta^*$ transition.

CHAPTER 5

5. CONCLUDING REMARKS

Electronic communication and delocalization between two centers is an important concept in understanding molecular electronic structure. In our work we have studied electronic coupling and electronic communication in a variety of molecular systems. In the metal-metal homodimer molecules of type $\text{Re}_2\text{X}_4(\text{PMe}_3)_4^+$, which have a direct bond between the two metal ions, we find that the unpaired electron is shared equally between the metal ions. These symmetric, homodimeric molecules, discussed in chapter four, are an example of a class III⁵ valence delocalized system. In these Re dimers of bond order 3.5 the d_{xy} and $d_{x^2-y^2}$ d-orbitals on the Re ions, which have four-lobe δ overlap, form a bonding and antibonding combination with each set of δ orbitals that are delocalized equally over both Re centers. The unpaired electron resides in the delocalized δ bonding orbital, and we observe the $\Psi_{\delta \text{ bond}} \rightarrow \Psi_{\delta \text{ antibond}}$ transition at 6844 cm^{-1} and 6774 cm^{-1} for $\text{X} = \text{Cl}$ and Br , respectively. Our spectroscopic and computational studies of these molecules were focused on understanding how the halide and phosphine ligands interact with the d-orbital manifold of the metal ions, and on understanding the nature of the Re-Re δ bond.

We found that both halide and phosphine ligand sets interact with the metal d-orbitals, and that the strength of the ligand-metal antibonding interactions for a given metal d-orbital dictates the energy of that metal d-orbital with respect to the other d-orbitals in the metal d-orbital manifold. These metal-ligand antibonding interactions lead

to an energy ordering of the d-orbital manifold that is quite different than expected when considering only the metal-metal interactions of the Re-dimer. We also found that while the energy of the $\delta \rightarrow \delta^*$ transition for the $\text{Re}_2\text{X}_4(\text{PMe}_3)_4^+$ cations is just under one electron-volt, the change in bond order of one δ bond during the $\delta \rightarrow \delta^*$ transition has very little impact on the Re-Re bond distance and Re-Re stretching frequencies. Due to the presence of three stronger bonds, i.e. one σ - and two π -bonds, a change in the δ bond order does not significantly affect the net strength of the Re-Re bonds.

We have seen several examples of the utility of using a VBCI description for a molecular system to explain and quantify observed molecular properties and electronic communication between centers. The VBCI model utilizes a description of the ground state of the molecule and low-energy excited configurations, and allows for configurational mixing of the excited configurations with the ground configurations. In the molecular systems we studied we observed that ground state properties often carry significant excited state contributions. The molecular centers that interact via ground- and excited configuration interaction can be metal ions, as in the case of the CODH enzyme active site with a catalytic $[\text{Mo-S}_\mu\text{-Cu}]$ unit in chapter Three, or organic radical ring moieties, such as in the D-B-A systems studied in chapter Two.

The case of the donor-para-bridge-acceptor biradicals in chapter Two is an excellent example of a system where the ground state ferromagnetism derives from excited state contributions, and where without the excited state interactions with the ground state no ferromagnetic coupling or donor-acceptor electronic communication would be expected. We found that the ferromagnetic exchange coupling of donor and

acceptor spins in the $\text{Tp}^{\text{Cum,Me}}\text{Zn-SQ-Bridge-NN}$ biradicals has two main contributions that both increase the net positive spin density on the NN acceptor ring: a delocalization of positive spin density from the donor to the bridge and acceptor described by donor-acceptor charge transfer excitations, and a delocalization of negative spin density from the acceptor to the bridge, which requires a spin polarization mechanism for the NN acceptor. This spin polarization on the NN acceptor is described by transitions from the NN-bridge(-SQ) HOMO to the NN-bridge LUMO. We explored how changing the nature of the bridge alters both the donor-acceptor charge transfer contribution, as well as the acceptor-bridge interaction that is based on the spin polarization within the acceptor. The donor-acceptor coupling mediated by a phenyl bridge serves as a basis for comparison to using either a thiophene bridge, a mono- or dimethylated sterically-hindered phenyl bridge, or an extended bridge consisting of two phenyl - or two thiophene rings. While magnetic susceptibility measurements provide ground state singlet-triplet gaps for the D-B-A biradicals we studied, combining magnetic susceptibility and variable-temperature electronic absorption spectroscopy allowed us to separate singlet and triplet components to the absorption spectra, and to ascertain the energy splitting between singlet and triplet optical transitions.

We used a VBCI model to elucidate the mechanism of both ferromagnetic and antiferromagnetic coupling in the DBA biradicals. Ferromagnetic coupling is due to the contribution of a donor to acceptor charge transfer excited state to the ground state, in which the unpaired spin of the SQ donor is promoted to the NN-bridge LUMO acceptor. Antiferromagnetic coupling in the meta-bridged D-B-A biradical can be explained using

a double-spin polarization mechanism between the SQ SOMO of the SQ-Ph fragment, the spin-polarized HOMO of the NN-Ph fragment, and the NN SOMO of the NN-Ph fragment. The spin-polarization in the NN-Ph HOMO arises from CI mixing of a NN-Ph HOMO \rightarrow NN-Ph LUMO excited state into the ground state. The spin-polarization of the NN-Ph HOMO is supported by the large energy splitting of the α and β components of the NN-Ph HOMO in the DFT-calculated orbitals of the open shell spin unrestricted singlet of $\text{Tp}^{\text{Cum,Me}}\text{Zn}(\text{SQ-mPh-NN})$. CASSCF calculations for $\text{Tp}^{\text{Cum,Me}}\text{Zn}(\text{SQ-mPh-NN})$ also calculate the antiferromagnetic ground state to be lowest in energy. CASSCF calculations show that the NN-Ph HOMO \rightarrow NN-Ph LUMO single excitation and the NN-Ph HOMO \rightarrow NN-Ph LUMO double excitation are the largest contribution of excited configurations to the antiferromagnetic ground state. Our computational results thus indicate that the spin polarization of the NN-Ph HOMO is significant in the antiferromagnetic ground state of $\text{Tp}^{\text{Cum,Me}}\text{Zn}(\text{SQ-mPh-NN})$. We conclude that the antiferromagnetic coupling observed in the ground state of $\text{Tp}^{\text{Cum,Me}}\text{Zn}(\text{SQ-mPh-NN})$ is a combination of the severe reduction of the ferromagnetic pathway involving the D-A CT excited state and the spin polarization of the NN-Ph HOMO leading to antiferromagnetic coupling of donor and acceptor spins in the ground state via double spin-polarization.

In the last section of chapter Two, we describe the long-range spin-spin communication in a Co valence tautomer molecule, where the diamagnetic Co^{III} ion connects/bridges a set of mixed-valent ligands. The ligands are the $[\text{SQ-pPh-NN}]^{\cdot-}$ biradical and its one-electron reduced form, $[\text{Cat-pPh-NN}]^{2-}$. Much like the symmetric mixed-valent $\text{Re}^{\text{II}}\text{Re}^{\text{III}}$ metal homo-dimers, this symmetric Co valence tautomer with

mixed valent biradical ligands actually forms a class III (Robin & Day) valence delocalized system. Here the delocalization of the unpaired electron between the catecholate and semiquinone units occurs across a Co^{III} ion, and this unpaired electron delocalized over the Co dioxolene core spin polarizes two more unpaired electrons that each reside on the nitronyl nitroxide ring of the ligand into a ferromagnetic $S = 3/2$ ground state. The mechanism of this ferromagnetic coupling involves contributions from several excited state configurations, including an excited state generated by the $\Psi_{\text{u}} \rightarrow \Psi_{\text{g}}$ transition of the delocalized electron. In this excited state, the dioxolene p-orbitals have π overlap with a Co d-orbital so that the delocalized π network extends over the entire ~ 2 nm length of the molecule. We have thus seen two examples of symmetric molecules with an unpaired electron forming a class III delocalized bonding orbital in which that electron resides.

We have also studied two examples of an asymmetric molecule with large electronic communication: the DBA biradicals which have a molecular asymmetry due to the different electronic nature of the donor and acceptor coupled to the bridge, and the heterobimetallic active site of CODH, which features two metal ions bridged covalently by a sulfido. The delocalization of electron- and spin density across the [MoSCu] unit was studied in chapter three, and is of importance to the catalytic mechanism of the CODH enzyme. EPR and DFT results indicate a large covalency across the [MoSCu] unit. We utilized a VBCI model to explain using the differences in the orbital character and the spin density distribution across the [MoSCu] unit where excited state configurations contributed to the observed ground state spin density distribution. Our

studies of model compounds with the [MoSCu] unit combined with DFT calculations of the enzyme active site highlighted the sensitivity of the Cu EPR parameters to structural perturbations of the Cu site, and allows us to evaluate the arguments for and against the mechanism for catalysis in the enzyme active site of CODH.

DFT calculations were employed for all molecular systems we studied, and the careful correlation of DFT results to experimental data allowed us to develop and solidify our understanding of the electronic structure of the molecules in question. One needs to exercise some amount of judgment when analyzing the DFT output in order to understand which factors or contributions may have been over- or underemphasized in the calculation compared to the spectroscopic data. Once the DFT results have been spectroscopically calibrated in this manner, they are a useful tool for understanding which molecular orbitals or calculated transitions contribute to a certain experimentally observed piece of data, and in what way they contribute. Specifically, one can systematically manipulate molecular structure, by changing for example a dihedral angle or substituting one ligand for another, at a larger range and speed than would be available by synthesis and spectroscopic investigation.

We utilized this approach in chapter Two where we isolated donor-bridge and donor-acceptor contributions to the spin density distribution and ferromagnetic exchange by computationally varying the dihedral angle between donor-, bridge-, and acceptor rings. In order to accept this computationally derived insight, we first established that the DFT calculations do indeed describe the biradical systems well as compared to experimental data, in terms of the optimized structure of the molecules, the ferromagnetic

exchange coupling, and electronic absorption bands calculated. We observed a solid correlation between DFT and experimental data across a range of donor-acceptor, donor-bridge-acceptor, and bridge-acceptor molecules where the computed spin populations had a linear correlation to experimentally observed isotropic nitrogen hyperfine coupling constants.

One of the most striking examples of DFT enhancing the interpretation of the experimentally observed data in our work is the interpretation of the observed MCD spectra of the Re dimer molecules. We again first established that the computational results correlated well with experimental data, and made a note of any systematic discrepancies we observed. In fact, both the DFT-calculated electronic absorption and MCD spectra reproduced the observed spectra very well, barring some systematic band shifts of the computed with respect to the experimental spectra. The computational data then allowed us to understand the origin of the experimentally observed bands by varying the bandwidth of the computed transition and overlaying the variable bandwidth MCD and electronic absorption with each other and the experimental data. This allowed us to realize that the observed MCD spectrum is largely a result of the incomplete cancellation of very larger, nearly-degenerate positive and negative pseudo A-term features, which is certainly consistent with the high symmetry and electronic structure of the Re-dimer molecules. This understanding of the experimental data would like have been missed had it not been for the DFT calculations. We found the DFT calculations to not only be an additional piece of data but rather a useful tool to complement and enhance our understanding of the experimental data.

We have utilized a VBCI description and combination of DFT and experimental data to understand delocalization and electronic communication in both symmetric and asymmetric molecular systems. Understanding the electronic communication and spin coupling in molecular systems contributes toward developing a sound basis of knowledge on which to build future molecular designs.

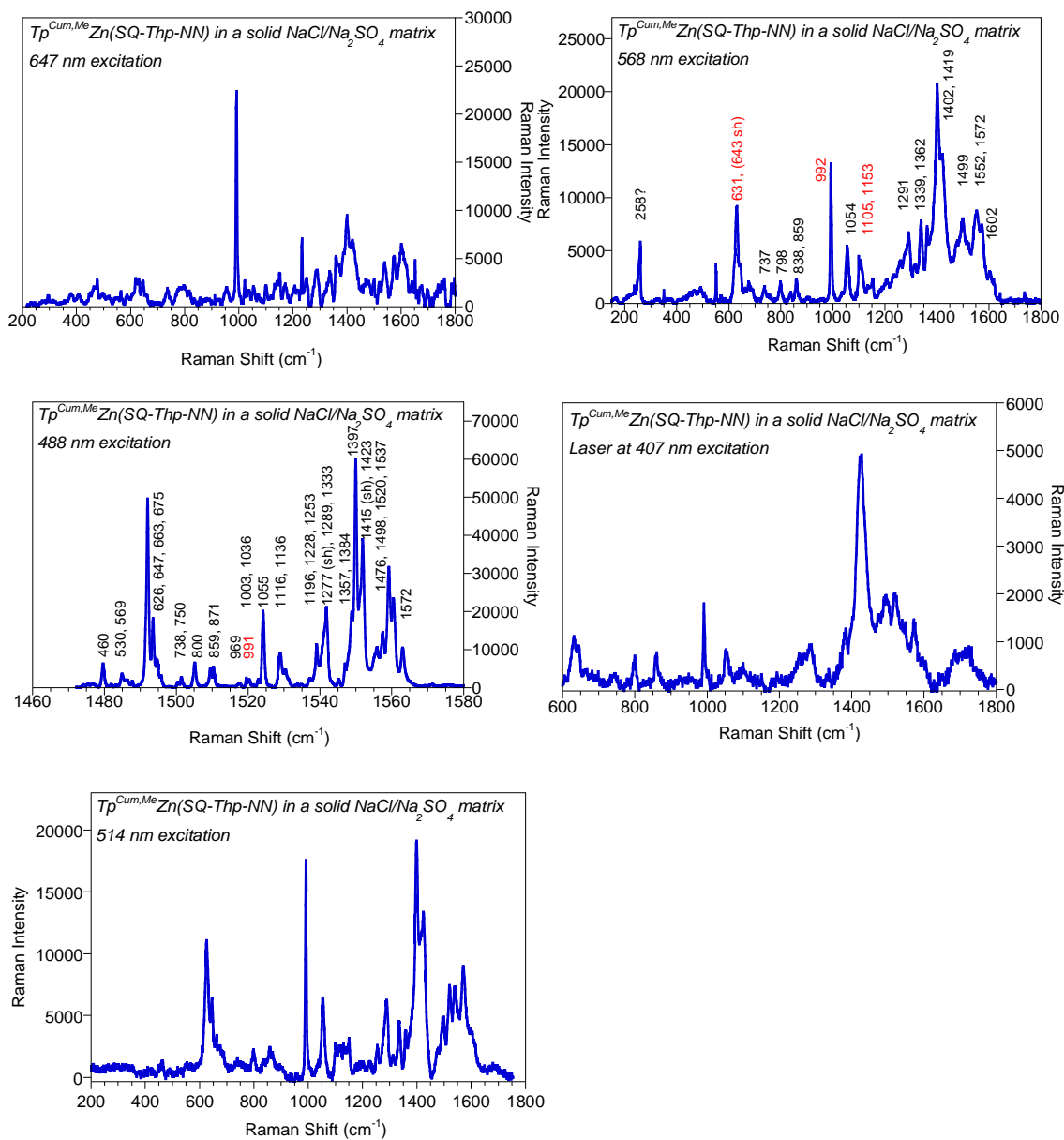
CHAPTER 6

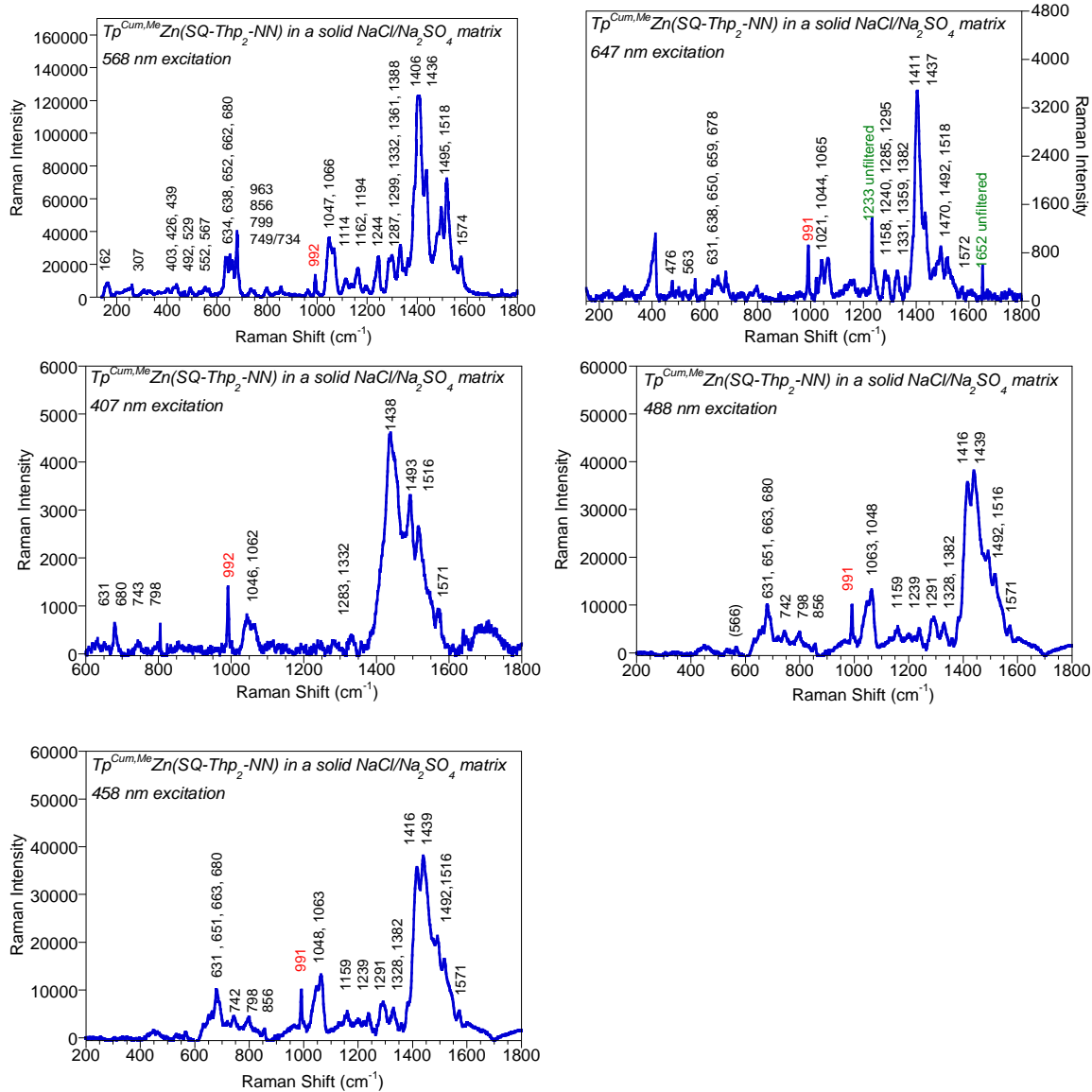
6. APPENDICES

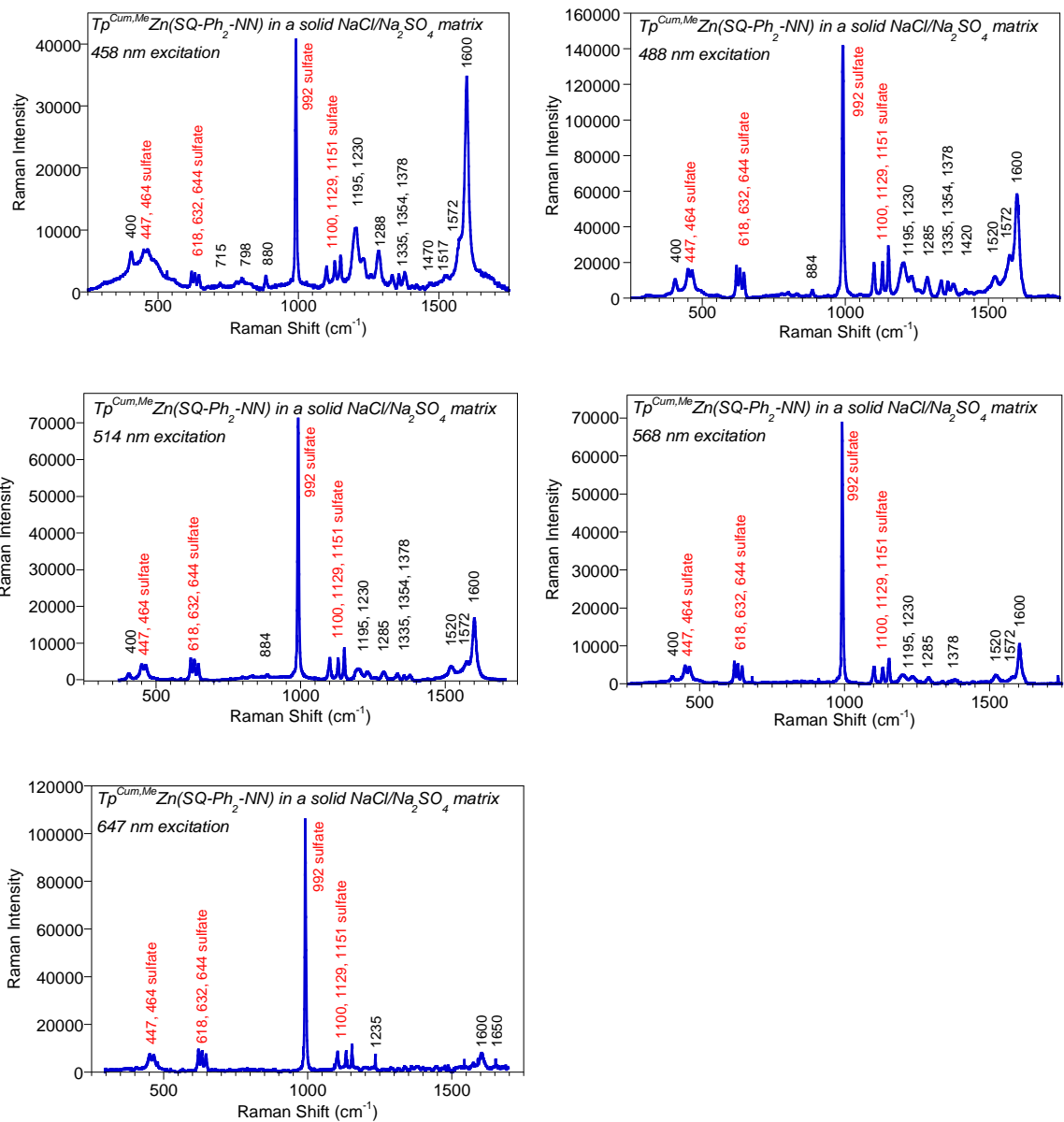
6.1 Appendix A: Supporting Information for Chapter 2

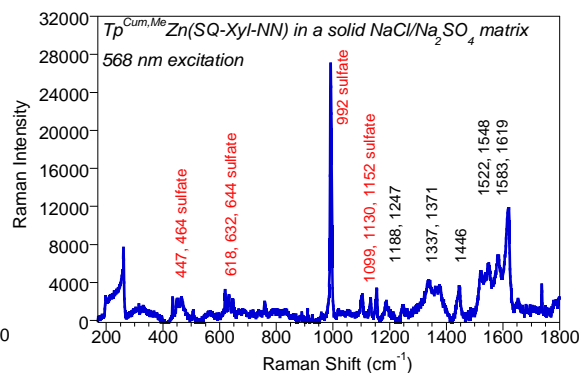
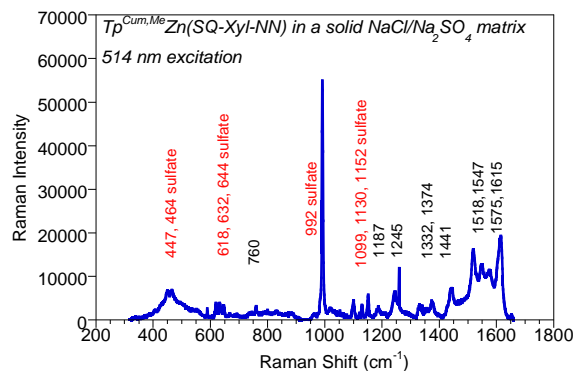
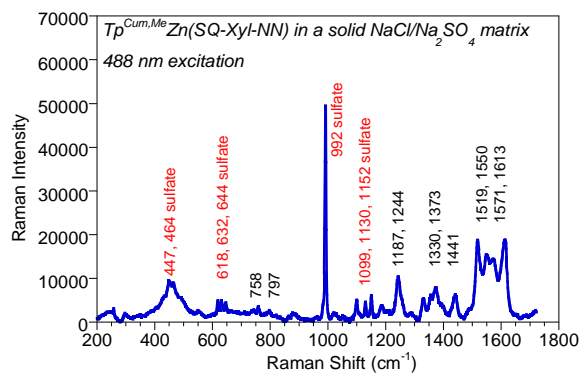
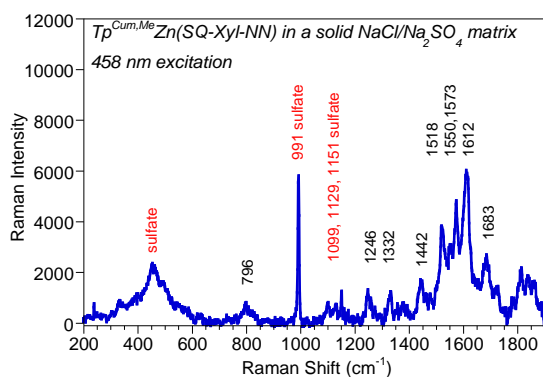
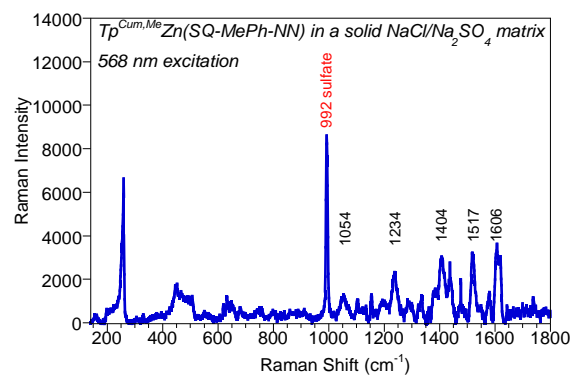
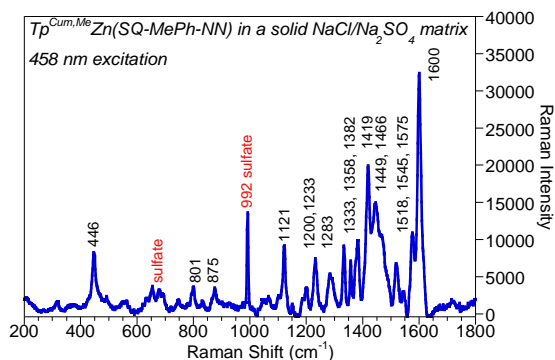
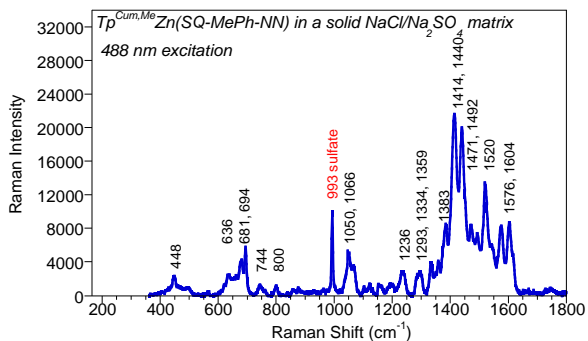
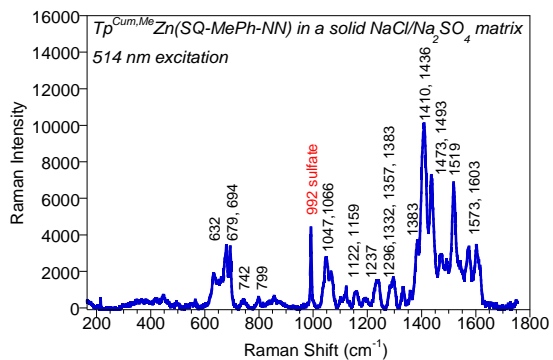
6.1.1 Resonance Raman Spectra of D-B-A Biradicals

Resonance Raman spectra of $\text{Tp}^{\text{Cum,Me}}\text{Zn}(\text{SQ-Thp-NN})$, $\text{Tp}^{\text{Cum,Me}}\text{Zn}(\text{SQ-Thp}_2\text{-NN})$, $\text{Tp}^{\text{Cum,Me}}\text{Zn}(\text{SQ-Ph}_2\text{-NN})$, $\text{Tp}^{\text{Cum,Me}}\text{Zn}(\text{SQ-MePh-NN})$, and $\text{Tp}^{\text{Cum,Me}}\text{Zn}(\text{SQ-Xyl-NN})$ in a solid state $\text{NaCl}/\text{Na}_2\text{SO}_4$ matrix.









6.1.2 Coordinates of DFT Optimized Geometries and Final Energies of D-B-A Biradicals of Table 2.4

NN (Nitronyl Nitroxide)			
N	0.00000000	0.00000000	0.00000000
O	1.26600649	0.00000000	0.00000000
C	-0.80361050	1.28737815	0.00000000
C	-2.25293051	0.74785484	-0.28548649
N	-2.11113473	-0.71154212	0.10511508
O	-3.11391276	-1.47674372	0.21406831
C	-0.81367059	-1.05887989	0.15259745
H	-0.46545611	-2.07133610	0.29685217
C	-0.61472952	1.89207480	1.40366162
H	0.33839997	2.37521917	1.45857682
H	-1.38837502	2.60709993	1.59104281
H	-0.66297810	1.11405146	2.13663621
C	-0.21988147	2.23969950	-1.06016247
H	-0.87284194	3.07818717	-1.18458534
H	0.74264929	2.58142383	-0.74132234
H	-0.12387395	1.72116500	-1.99118585
C	-3.38184991	1.38032815	0.54944974
H	-3.32447944	2.44635351	0.47734869
H	-4.32889952	1.04820156	0.17838511
H	-3.27654948	1.08587492	1.57273324
C	-2.64756333	0.74065737	-1.77404725
H	-3.60672320	0.27994005	-1.88652785
H	-2.69028992	1.74646466	-2.13657469
H	-1.91986965	0.19056655	-2.33329852
NN-Ph			
N	0.00000000	0.00000000	0.00000000
C	1.36584781	0.00000000	0.00000000
C	2.22480970	1.18698772	0.00000000
C	3.62660095	1.06221438	-0.12730736
C	4.43513877	2.19661816	-0.12864235
C	3.87716674	3.47030796	0.00012196
C	2.49287947	3.60214465	0.12882855
C	1.66807770	2.47950793	0.12738082
H	0.59486055	2.58533670	0.21652065
H	2.04552514	4.58856016	0.22935908
H	4.51494712	4.35163204	0.00015710
H	5.51197109	2.08005114	-0.22911384
H	4.06262112	0.07587126	-0.21648309
N	1.79283772	-1.29741313	0.00010270
C	0.65228518	-2.26527792	-0.21017368
C	-0.56281664	-1.38596033	0.21028596
O	-0.78388678	0.99980951	-0.00745368
O	2.98759909	-1.72943517	0.00741774
C	-0.92185718	-1.47121565	1.70536750
H	-1.39783550	-2.42832061	1.94180250
H	-1.62367465	-0.66433574	1.93705106

H	-0.04002808	-1.35126485	2.34285546
C	-1.82636586	-1.55055129	-0.63502402
H	-2.24878312	-2.55012602	-0.48440835
H	-2.56360723	-0.80669973	-0.32321110
H	-1.63587068	-1.40736910	-1.70112876
C	0.89091427	-3.51693657	0.63515757
H	0.07343457	-4.23061414	0.48461096
H	0.96743935	-3.29119859	1.70125117
H	1.82790561	-3.98477499	0.32332118
C	0.68352900	-2.63301421	-1.70525212
H	0.52176061	-1.75790717	-2.34276049
H	1.66937311	-3.04739378	-1.93694056
H	-0.07678741	-3.38437316	-1.94166034
NN-Ph (OMe)			
N	0.00000000	0.00000000	0.00000000
C	1.36574550	0.00000000	0.00000000
C	2.22494273	1.18318435	0.00000000
C	3.62195009	1.06403158	-0.12951008
C	4.44334329	2.19389581	-0.12465913
C	3.87174282	3.46805096	0.00804214
C	2.46856403	3.60134332	0.11360942
C	1.65606302	2.47053373	0.12011954
H	0.58169253	2.55704791	0.19368635
H	4.06361882	0.08016806	-0.21837479
N	1.79003671	-1.29961636	-0.00325347
C	0.64917438	-2.26337119	-0.22404724
C	-0.56520787	-1.38508246	0.19956613
O	-0.78598397	1.00136363	0.00449348
O	2.98428941	-1.73358621	0.00308482
C	-0.92881599	-1.48323369	1.69287895
H	-1.40372239	-2.44322282	1.91946997
H	-1.63231920	-0.67920481	1.92942222
H	-0.04873858	-1.36771076	2.33363455
C	-1.82676625	-1.54264775	-0.65051241
H	-2.24977402	-2.54360585	-0.51047376
H	-2.56501884	-0.80181731	-0.33407384
H	-1.63308917	-1.38970153	-1.71472204
C	0.88267392	-3.52209622	0.61242044
H	0.06426948	-4.23328797	0.45474437
H	0.95713071	-3.30452093	1.68039335
H	1.81963824	-3.98930060	0.29940370
C	0.68267191	-2.62063169	-1.72173978
H	0.52394997	-1.74026356	-2.35267476
H	1.66811261	-3.03517611	-1.95465593
H	-0.07889286	-3.36853344	-1.96457175
C	5.94105444	2.06484407	-0.26791997
H	6.46450408	2.51175915	0.58583447
H	6.23381809	1.01311374	-0.34023230
H	6.30057260	2.58819539	-1.16187382
O	1.98746277	4.87928368	0.18476392
O	4.71106059	4.54872770	-0.05182398
C	0.58036213	5.05984139	0.25232767

C	4.70864863	5.45474871	1.05555876
H	0.41840698	6.14008104	0.27989059
H	0.07650356	4.63813037	-0.62778880
H	0.15472343	4.60473836	1.15739170
H	5.53872927	6.14425504	0.87851296
H	4.88118137	4.91967836	1.99998393
H	3.76983844	6.01228759	1.11999687
Tp ^{Cum, Me} Zn (SQ-NN)			
C	0.00000000	0.00000000	0.00000000
N	1.35080933	0.00000000	0.00000000
N	1.80956289	1.27688598	0.00000000
C	0.74158364	2.07932507	-0.00476893
C	-0.43892762	1.31856046	0.00070037
B	2.35036687	-1.18376332	-0.04334704
N	3.28315603	-1.09429565	1.18629099
N	4.03849684	0.01660377	1.37035619
C	4.77241897	-0.18220096	2.46820113
C	4.48871874	-1.44324288	3.01990689
C	3.53655787	-1.98858028	2.16733931
Zn	3.88502347	1.47998820	-0.13466157
N	3.98636904	0.03023764	-1.58772158
N	3.21485321	-1.06262991	-1.34050587
C	3.34097136	-1.94161423	-2.35639306
C	4.21809743	-1.41419846	-3.29695433
C	4.59272880	-0.17319073	-2.76294209
O	3.60793829	3.43512319	-0.86765985
C	4.55711957	4.20687033	-0.51782274
C	4.61672836	5.59309732	-0.89586310
C	5.67990263	6.34951591	-0.47118021
C	6.74098784	5.80748396	0.35137255
C	6.70091313	4.46228974	0.73438727
C	5.63525400	3.63785381	0.31696321
C	7.83227435	6.66756131	0.76872312
N	8.87008566	6.30369358	1.59164089
C	9.70932557	7.48850894	2.00232192
C	9.37445123	8.49275956	0.86288848
N	8.02273974	7.98426254	0.42134804
O	9.07381246	5.17641105	2.13707159
O	7.30069761	8.71392159	-0.32566569
C	9.25034501	9.95710713	1.28514453
C	10.29081737	8.38054600	-0.37011755
C	11.17418636	7.06102419	2.10045141
C	9.19492241	7.91383230	3.39044087
C	3.50717337	6.15410613	-1.74435877
O	5.53401298	2.39363921	0.62628533
H	5.26350636	0.57657067	-3.16335479
H	4.53684384	-1.86183656	-4.22732067
H	2.79971333	-2.87779444	-2.33861650
H	1.76030032	-2.22971529	-0.05286612
H	3.02547952	-2.94173763	2.18821330
H	4.91390374	-1.89284179	3.90601748
H	5.46312766	0.58590516	2.79088615

H	-0.54918295	-0.93188813	-0.00179748
H	-1.45970258	1.67353885	0.00250384
H	0.88138171	3.15219944	-0.02175277
H	7.48183794	4.03277737	1.34607780
H	5.74029608	7.39372160	-0.75125369
H	2.53914088	6.06364033	-1.23524515
H	3.68170898	7.20921382	-1.97600036
H	3.41245663	5.59778119	-2.68516655
H	10.22501158	10.33393344	1.61435033
H	8.91533787	10.54990343	0.43061527
H	8.52937873	10.09674050	2.09391595
H	9.84200565	8.95412057	-1.18679683
H	11.28416654	8.78964994	-0.15957845
H	10.40236492	7.34293999	-0.70095563
H	11.79381113	7.91551437	2.39408822
H	11.55416667	6.65940602	1.15825411
H	11.26907733	6.28118014	2.85993821
H	8.14459420	8.22090192	3.35756564
H	9.78926510	8.74080215	3.79202366
H	9.28054432	7.05887950	4.06795688
Tp ^{Cum, Me} Zn (SQ-1, 4-Ph-NN)			
C	0.00000000	0.00000000	0.00000000
N	1.35093200	0.00000000	0.00000000
N	1.81015975	1.27653274	0.00000000
C	0.74241864	2.07923910	-0.00474521
C	-0.43839041	1.31867451	0.00061243
B	2.35245849	-1.18129843	-0.04021307
N	3.28339938	-1.08650936	1.19129828
N	4.03960977	0.02407501	1.37395145
C	4.76572247	-0.17005387	2.47788742
C	4.47592343	-1.42701173	3.03517350
C	3.52842922	-1.97533483	2.17926677
Zn	3.88987870	1.48195602	-0.13445636
N	3.98607554	0.03211951	-1.58783461
N	3.21773276	-1.06218646	-1.33661310
C	3.34804882	-1.94539317	-2.34823146
C	4.22467385	-1.41952561	-3.29008701
C	4.59474779	-0.17494466	-2.76125629
O	3.60733676	3.44952726	-0.78697351
C	4.57094388	4.21249999	-0.44066789
C	4.61114830	5.61234445	-0.76012004
C	5.69002738	6.34966514	-0.32950168
C	6.78185518	5.78175647	0.41721940
C	6.76191310	4.42754895	0.72913823
C	5.68127393	3.60830262	0.32402443
C	7.90529382	6.64399439	0.83463833
C	7.71616538	8.00728492	1.13546969
C	8.76526360	8.81979485	1.54504929
C	10.07420698	8.29870213	1.66662281
C	10.27534261	6.93216915	1.35993087
C	9.21324981	6.13448132	0.95718707
C	11.18386390	9.14510135	2.09516788

N	12.48605228	8.75158320	2.23574609
C	13.32746150	9.81600165	2.89906548
C	12.46633002	11.08526428	2.62802725
N	11.10195421	10.46895637	2.42811109
O	12.98342924	7.60202468	2.02470852
O	10.07264802	11.21350538	2.42858234
C	12.39862176	12.09860573	3.77134636
C	12.79996390	11.80833808	1.30974366
C	14.72383196	9.81640184	2.27590677
C	13.41911249	9.41586370	4.38343558
C	3.47907635	6.20196395	-1.55683304
O	5.59032600	2.35696058	0.59406696
H	5.26365492	0.57500661	-3.16448351
H	4.54589615	-1.87036091	-4.21805001
H	2.80963884	-2.88309778	-2.32687262
H	1.76524449	-2.22892423	-0.04666905
H	3.01544958	-2.92739893	2.20226326
H	4.89414181	-1.87231946	3.92673746
H	5.45628211	0.59799491	2.80073667
H	-0.54934226	-0.93181570	-0.00152349
H	-1.45912525	1.67379867	0.00247279
H	0.88288134	3.15198773	-0.02122864
H	7.54955549	3.96999908	1.32073909
H	5.74063989	7.40322398	-0.59447865
H	2.52417034	6.08190117	-1.02961566
H	3.63943000	7.26806695	-1.74653028
H	3.36536569	5.68758635	-2.51914016
H	9.40742298	5.09624670	0.70133407
H	11.27200767	6.51670674	1.43083181
H	6.71891067	8.43639058	1.08293878
H	8.58676854	9.85932556	1.78667349
H	13.38033776	12.56194251	3.91907639
H	11.67741684	12.87826438	3.51426297
H	12.07995994	11.64426466	4.71238658
H	12.00992300	12.53746799	1.10631724
H	13.75534173	12.33765028	1.38349286
H	12.84920733	11.11236139	0.46619465
H	15.34457109	10.58435086	2.75055142
H	14.69879186	10.00186792	1.19962068
H	15.18768190	8.84032726	2.43760929
H	12.43418543	9.39731859	4.86079352
H	14.06416697	10.10568631	4.93677393
H	13.84734303	8.41076318	4.44344994
Tp ^{Cum, Me} Zn (SQ-2, 5-TP-NN)			
N	0.00000000	0.00000000	0.00000000
C	1.36113613	0.00000000	0.00000000
N	1.80804549	1.29013112	0.00000000
C	0.67008456	2.26123138	0.21421469
C	-0.55875131	1.38492112	-0.20352110
C	2.17705100	-1.17029449	0.00109451
C	3.56891797	-1.22267976	0.00732580
C	4.06519525	-2.53600969	0.00242183

C	3.07639381	-3.51886251	-0.00598477
C	3.23814739	-4.96126061	-0.00690011
C	4.56933079	-5.51605092	0.00351290
C	4.81353599	-6.86742843	0.00587708
C	3.69147344	-7.76790297	0.00036670
C	2.31779854	-7.22194595	-0.01112698
C	2.14034249	-5.82552615	-0.01569481
O	3.82538671	-9.03500038	0.00062206
Zn	1.95950385	-10.01098021	-0.00050845
O	1.35372465	-8.07295377	-0.02155293
C	6.20037587	-7.45098329	0.01483685
O	3.01650464	1.67916351	0.01870828
C	0.91357359	3.51113962	-0.63285034
C	0.70349644	2.62967532	1.70893554
C	-1.81537137	1.54963534	0.65262554
C	-0.92689083	1.48021643	-1.69584134
O	-0.74056246	-1.03212101	-0.02194376
N	1.58337854	-11.23948535	1.60464718
N	1.09941435	-12.46597754	1.26991238
C	0.89320249	-13.18950980	2.38994885
C	1.25060884	-12.41987916	3.49088068
C	1.67732748	-11.20375288	2.93888669
B	0.85170762	-12.87487851	-0.21864583
N	-0.16247262	-11.88911505	-0.84355045
N	0.13320995	-10.56659001	-0.88741096
C	-0.91594631	-9.94519015	-1.43173473
C	-1.91612343	-10.87667962	-1.75869509
C	-1.39210146	-12.10119157	-1.36278209
N	2.19055080	-12.77183060	-0.99183824
N	2.84617450	-11.58594483	-1.05742752
C	3.97810830	-11.79844455	-1.73419043
C	4.06456452	-13.14387632	-2.12804880
C	2.90487606	-13.72486828	-1.62926009
H	2.04348222	-10.31232918	3.43259376
H	1.20773748	-12.69855720	4.53399081
H	0.50780340	-14.19795785	2.32530020
H	0.43016056	-13.99873954	-0.25961518
H	-1.80368484	-13.10035785	-1.41235169
H	-2.87820390	-10.68814337	-2.21362180
H	-0.89334386	-8.86959343	-1.54867126
H	2.54014716	-14.74186372	-1.68128082
H	4.85309716	-13.62387285	-2.69005202
H	4.66651706	-10.97843384	-1.89051858
H	1.12073776	-5.44938987	-0.02467475
H	5.41862670	-4.83856873	0.00987545
H	6.36928773	-8.07457919	-0.87213077
H	6.96302316	-6.66597067	0.03779522
H	6.34439405	-8.10601248	0.88285132
H	5.12664447	-2.75673383	0.00545429
H	4.17296090	-0.32452085	0.01116839
H	0.10923113	4.23745021	-0.47286408
H	1.86078372	3.96472735	-0.32977041
H	0.97596247	3.28586657	-1.69998411

H	1.68901975	3.04515137	1.93993078
H	-0.05784862	3.37971500	1.94585189
H	0.54415920	1.75461678	2.34708597
H	-2.24684090	2.54508892	0.50128332
H	-1.61490316	1.41178852	1.71759083
H	-2.55060930	0.79940275	0.34994226
H	-0.05020465	1.35272978	-2.33889265
H	-1.39263128	2.44406610	-1.92486414
H	-1.63898707	0.68254503	-1.92799742
S	1.48235328	-2.78277294	-0.01059912
Tp ^{Cum, Me} Zn (SQ-2, 5-Xyl-SQ)			
N	0.00000000	0.00000000	0.00000000
C	1.36315878	0.00000000	0.00000000
N	1.81642844	1.27636757	0.00000000
C	0.68150505	2.27013199	0.13237194
C	-0.55118000	1.38477248	-0.24727072
C	2.18392342	-1.21468225	0.07566265
C	3.28420825	-1.44614954	-0.77985033
C	4.00288272	-2.62731035	-0.58791023
C	3.67000543	-3.59549847	0.37681997
C	2.54868142	-3.36551877	1.21037742
C	1.83383871	-2.17910755	1.03296441
C	4.51626516	-4.81449495	0.46157942
C	5.94734898	-4.65951182	0.46082113
C	6.82005470	-5.72358608	0.51085012
C	6.27304815	-7.04971860	0.55493008
C	4.80800786	-7.23179939	0.54984551
C	3.96995217	-6.08783051	0.50450692
O	6.99949080	-8.10128880	0.59399915
Zn	5.85731584	-9.84667203	0.63722803
O	4.36830231	-8.43631251	0.57377845
C	8.31563715	-5.55876036	0.52741263
O	3.02167747	1.66560777	0.09216602
C	0.95564342	3.46461461	-0.78299431
C	0.70427086	2.72757183	1.60212793
C	-1.80535175	1.58476365	0.60544548
C	-0.93037739	1.42478371	-1.73923006
O	-0.76070763	-1.01409687	0.01458880
N	6.07953403	-11.06339337	2.27845770
N	6.23987910	-12.38083072	1.97911164
C	6.38175948	-13.08742370	3.11970757
C	6.31314304	-12.21318503	4.19819145
C	6.12282800	-10.95425107	3.61132513
B	6.24369169	-12.89589592	0.50316393
N	4.89630749	-12.52308516	-0.15864643
N	4.52967660	-11.22020413	-0.24152577
C	3.32464198	-11.18514194	-0.81626877
C	2.89503196	-12.48715133	-1.12387002
C	3.92798608	-13.30584051	-0.68373521
N	7.38883133	-12.19178904	-0.26679047
N	7.40450514	-10.83895618	-0.36676248
C	8.51127989	-10.50613891	-1.03655571

C	9.23134520	-11.65908504	-1.39024366
C	8.47895494	-12.70789085	-0.87536853
H	6.01595466	-9.98365642	4.07927259
H	6.38958417	-12.45286566	5.24902837
H	6.52106567	-14.15931113	3.08403050
H	6.40312829	-14.08621464	0.49590881
H	4.04190631	-14.38130920	-0.70601756
H	1.97020108	-12.78915496	-1.59457784
H	2.83587600	-10.23149901	-0.96677005
H	8.64113513	-13.77712591	-0.89764754
H	10.16148717	-11.72157904	-1.93700032
H	8.73045683	-9.46197441	-1.21687316
H	2.89697819	-6.24817630	0.46996590
H	6.34829624	-3.64799313	0.44419010
H	8.77570995	-6.06281700	-0.33195753
H	8.59931124	-4.50180101	0.50315369
H	8.75218757	-6.01844620	1.42283405
H	0.97084673	-1.99088493	1.66552349
H	4.84383206	-2.82717687	-1.24879471
H	0.17244702	4.22125811	-0.66333709
H	1.91624872	3.90586968	-0.50431744
H	1.00904021	3.18003867	-1.83641434
H	1.69050610	3.14923548	1.81657245
H	-0.05533424	3.49392941	1.78633102
H	0.53419404	1.89257933	2.28934269
H	-2.23739745	2.57360411	0.41625250
H	-1.60274292	1.48945597	1.67459181
H	-2.54011418	0.82228482	0.33422933
H	-0.06039268	1.27015492	-2.38536219
H	-1.39634428	2.38000322	-2.00157093
H	-1.64602361	0.62017238	-1.93368718
C	3.66067280	-0.50863480	-1.89990676
C	2.10992647	-4.31476714	2.30461305
H	2.80459737	-0.32321829	-2.56260214
H	3.98068903	0.46219449	-1.50591839
H	4.46505582	-0.93499765	-2.50725490
H	2.95821587	-4.82840612	2.76687996
H	1.56775407	-3.76984984	3.08481209
H	1.43245914	-5.09072139	1.92491694

NN-Ph E (UB+HF+LYP) = -765.46286924 a.u.

NN-Ph (OMe) E (UB+HF+LYP) = -1033.82092507 a.u.

Tp^{Cum,Me}Zn (SQ-NN) E (UB+HF+LYP) = -3435.63851903 a.u.

Tp^{Cum,Me}Zn (SQ-1, 4-Ph-NN) E (UB+HF+LYP) = -3666.69346056 a.u.

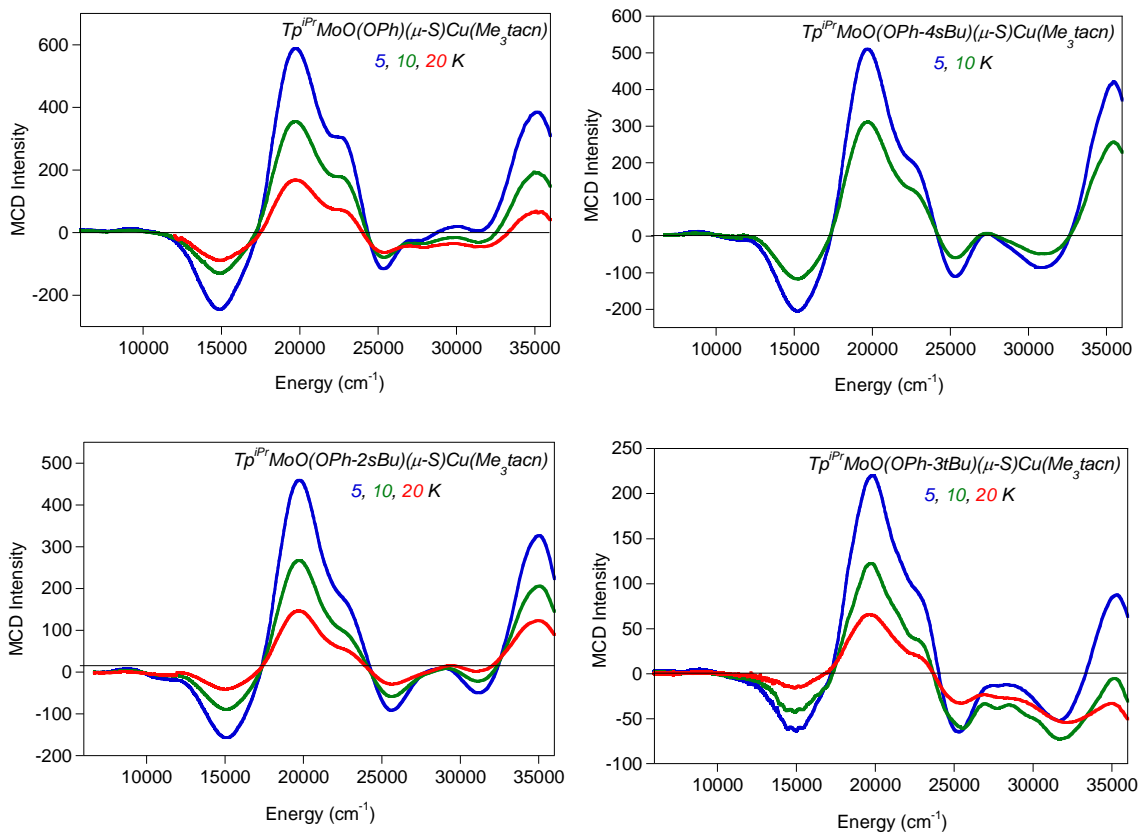
Tp^{Cum,Me}Zn (SQ-2, 5-TP-NN) E (UB+HF+LYP) = -3987.45443448 a.u.

Tp^{Cum,Me}Zn (SQ-2, 5-Xyl-SQ) E (UB+HF+LYP) = -3745.32089783 a.u.

6.2 Appendix B: Supporting Information for Chapter 3

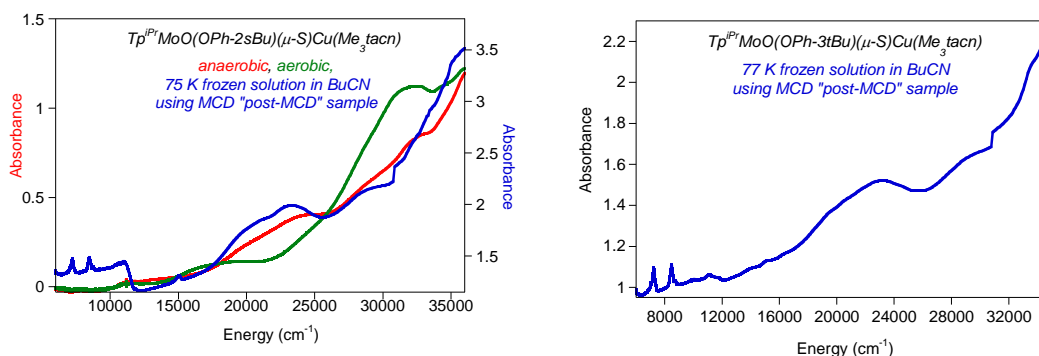
6.2.1 Variable-Temperature MCD Spectra for CODH Model Compounds

Variable-Temperature MCD of CODH models at 5 K (blue), 10 K (green), and 20 K (red) as frozen solutions in butyronitrile.



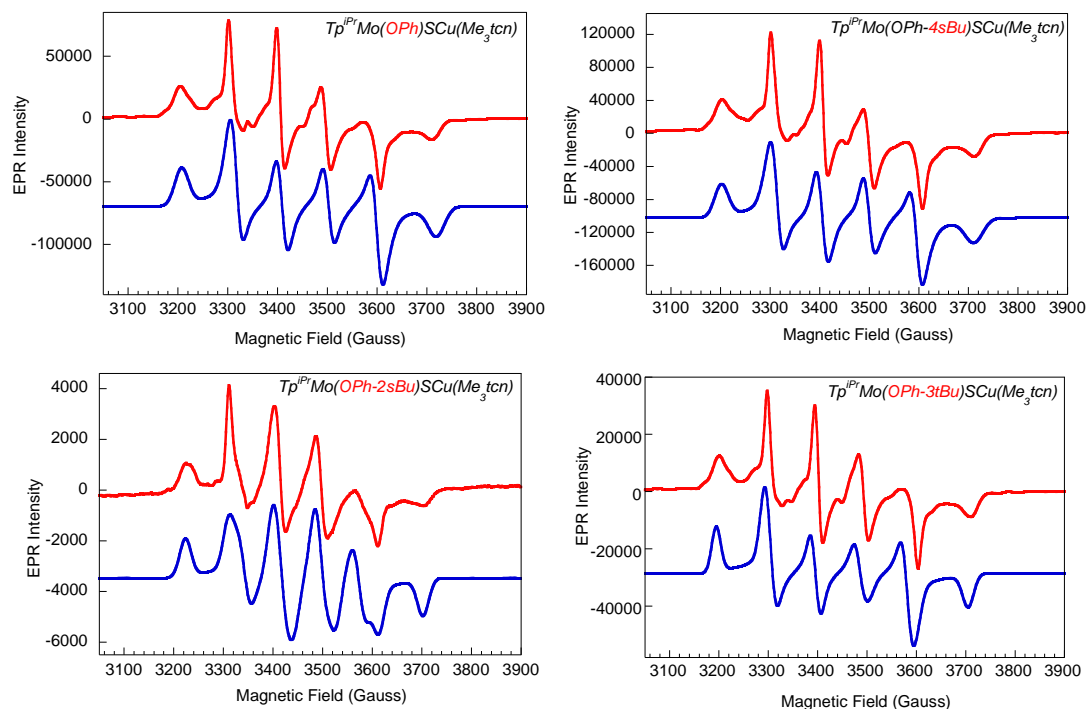
6.2.2 Low-Temperature Electronic Absorption Spectra for CODH Model Compounds “Post-MCD”

Low-temperature frozen solution spectra in butyronitrile of $\text{Tp}^{\text{iPr}}\text{MoO}(\text{OPh-3tBu})(\mu\text{-S})\text{Cu}(\text{Me}_3\text{tacn})$ and $\text{Tp}^{\text{iPr}}\text{MoO}(\text{OPh-2sBu})(\mu\text{-S})\text{Cu}(\text{Me}_3\text{tacn})$ after MCD had been acquired on the same samples. Samples were maintained frozen at all times during the transfer from the MCD to electronic absorption cryostat. An overlay of the “post-MCD” sample with anaerobic and aerobic solution electronic absorption scans shows that the MCD sample was successfully maintained anaerobic.



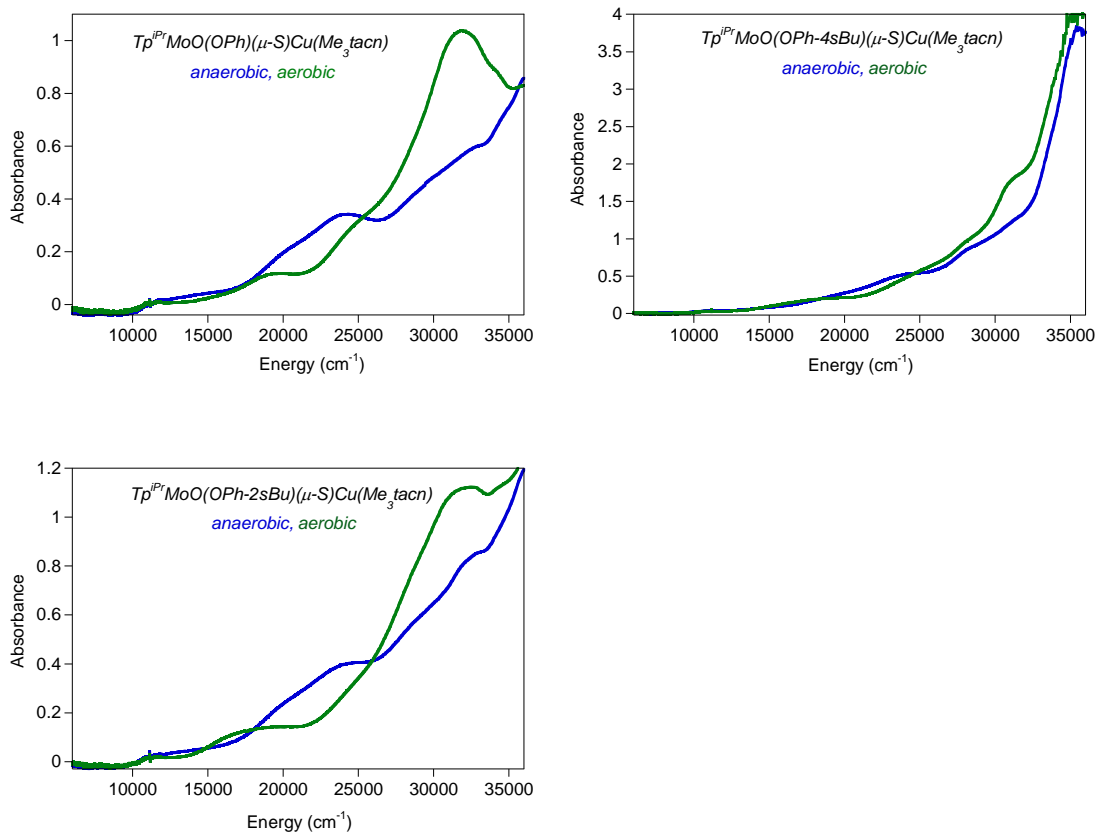
6.2.3 X-band EPR Spectra and Simulations for CODH Model Compounds

X-band EPR data of $\text{Tp}^{\text{iPr}}\text{MoO}(\text{OPh})(\mu\text{-S})\text{Cu}(\text{Me}_3\text{tacn})$, $\text{Tp}^{\text{iPr}}\text{MoO}(\text{OPh-4sBu})(\mu\text{-S})\text{Cu}(\text{Me}_3\text{tacn})$, $\text{Tp}^{\text{iPr}}\text{MoO}(\text{OPh-2sBu})(\mu\text{-S})\text{Cu}(\text{Me}_3\text{tacn})$, and $\text{Tp}^{\text{iPr}}\text{MoO}(\text{OPh-3tBu})(\mu\text{-S})\text{Cu}(\text{Me}_3\text{tacn})$ acquired at 20 K in butyronitrile. Red = data, blue = simulation.

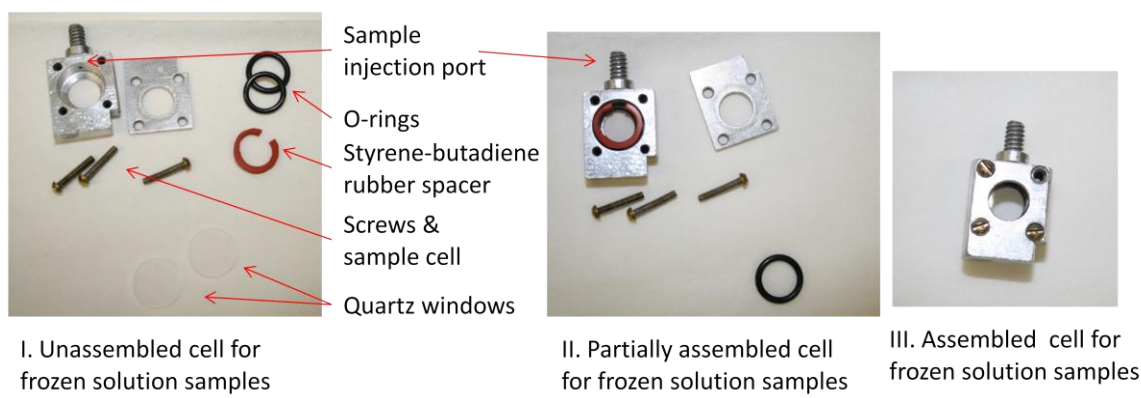


6.2.4 Aerobic and Anaerobic Electronic Absorption for CODH Model Compounds

Room temperature solution spectra of $\text{Tp}^{\text{iPr}}\text{MoO}(\text{OPh})(\mu\text{-S})\text{Cu}(\text{Me}_3\text{tacn})$, $\text{Tp}^{\text{iPr}}\text{MoO}(\text{OPh-4sBu})(\mu\text{-S})\text{Cu}(\text{Me}_3\text{tacn})$, and $\text{Tp}^{\text{iPr}}\text{MoO}(\text{OPh-2sBu})(\mu\text{-S})\text{Cu}(\text{Me}_3\text{tacn})$ in butyronitrile solution; overlay of the aerobic and anaerobic scans.



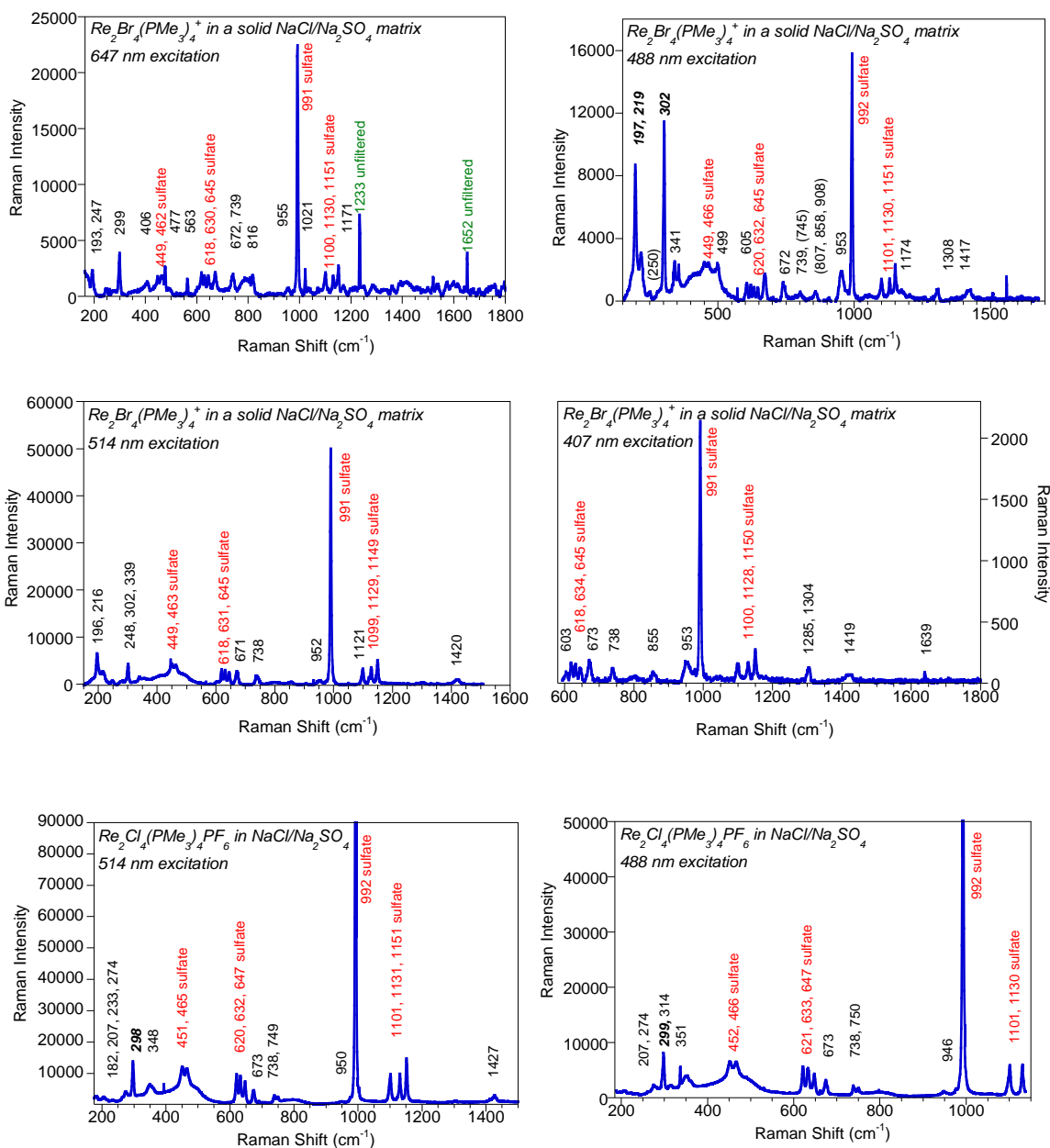
6.2.5 Variable-Temperature Sample Cell Assembly



6.3 Appendix C: Supporting Information for Chapter 4

6.3.1 Resonance Raman Spectra of $\text{Re}_2\text{Cl}_4(\text{PMe}_3)_4^+$ and $\text{Re}_2\text{Br}_4(\text{PMe}_3)_4^+$

Resonance Raman spectra acquired at room temperature in a solid $\text{NaCl}/\text{Na}_2\text{SO}_4$ matrix at laser excitation energies of 407 nm, 488 nm, 514 nm, and 647 nm ($\text{Re}_2\text{Br}_4(\text{PMe}_3)_4^+$), and 488 nm, 514 nm ($\text{Re}_2\text{Cl}_4(\text{PMe}_3)_4^+$).



6.3.2 D_{2d} Character Table

	E	$2S_4$	C_2	$2C_2'$	$2\sigma_d$	Rotation/ Translation	d-orbitals
A_1	1	1	1	1	1		x^2+y^2, z^2
A_2	1	1	1	-1	-1	R_z	
B_1	1	-1	1	1	-1		x^2-y^2
B_2	1	-1	1	-1	1	z	xy
E	2	0	-2	0	0	$(x, y), (R_x, R_y)$	(xz, yz)

Adapted from reference ¹⁸⁰

7. REFERENCES CITED

- (1) Tuczek, F.; Solomon, E. I. *Coordination Chemistry Reviews* **2001**, *219-221*, 1075–1112.
- (2) Kirk, M. L.; Shultz, D. A.; Depperman, E. C. *Polyhedron* **2005**, *24*, 2880–2884.
- (3) Kirk, M. L.; Shultz, D. A.; Depperman, E. C.; Brannen, C. L. *Journal of the American Chemical Society* **2007**, *129*, 1937–43.
- (4) Kirk, M. L.; Shultz, D. A.; Depperman, E. C.; Habel-Rodriguez, D.; Schmidt, R. D. *Journal of the American Chemical Society* **2012**, *134*, 7812–9.
- (5) Robin, M. B.; Day, P. In *Advances in Inorganic Chemistry and Radiochemistry*; Emeleus, H. J.; Sharpe, A. G., Eds.; Academic Press, 1967; pp. 248–403.
- (6) Kahn, O. *Molecular Magnetism*; VCH Publishers: New York, 1993.
- (7) Joachim, C.; Gimzewski, J. K.; Aviram, A. *Nature* **2000**, *408*, 541–8.
- (8) Joachim, C.; Ratner, M. A. *Proceedings of the National Academy of Sciences* **2005**, *102*, 8801–8808.
- (9) Goldhaber-Gordon, D.; Montemerlo, M. S.; Love, J. C.; Opiteck, G. J.; Ellenbogen, J. C. *Proceedings of the IEEE* **1997**.
- (10) Aviram, A.; Ratner, M. A. *Chemical Physics Letters* **1974**, *29*, 277–286.
- (11) Sugawara, T.; Matsushita, M. M. *Journal of Materials Chemistry* **2009**, *19*, 1738–1753.
- (12) Dougherty, D. A. *Accounts of Chemical Research* **1991**, *24*, 88–94.
- (13) Joachim, C.; Ratner, M. A. **2012**, *102*.
- (14) Kirk, M. L.; Shultz, D. A.; Schmidt, R. D.; Habel-Rodriguez, D.; Lee, H.; Lee, J. *Journal of the American Chemical Society* **2009**, *131*, 18304–13.
- (15) Kirk, M. L.; Shultz, D. A.; Habel-Rodriguez, D.; Schmidt, R. D.; Sullivan, U. *The Journal of Physical Chemistry B* **2010**, *114*, 14712–6.

- (16) Sakurai, H.; Izuoka, A.; Sugawara, T. *Journal of the American Chemical Society* **2000**, *122*, 9723–9734.
- (17) Ricks, A. B.; Solomon, G. C.; Colvin, M. T.; Scott, A. M.; Chen, K.; Ratner, M. A.; Wasielewski, M. R. *Journal of the American Chemical Society* **2010**, *132*, 15427–15434.
- (18) Weiss, E. A.; Tauber, M. J.; Kelley, R. F.; Ahrens, M. J.; Ratner, M. A.; Wasielewski, M. R. *Journal of the American Chemical Society* **2005**, *127*, 11842–50.
- (19) Redondo, A. *Los Alamos Science* **1993**, *165*, 165–171.
- (20) Venkataraman, L.; Klare, J. E.; Nuckolls, C.; Hybertsen, M. S.; Steigerwald, M. L. *Nature* **2006**, *442*, 904–7.
- (21) Hybertsen, M. S.; Venkataraman, L.; Klare, J. E.; Whalley, A. C.; Steigerwald, M. L.; Nuckolls, C. *Journal of Physics. Condensed Matter* **2008**, *20*, 374115.
- (22) Ahn, S.; Aradhya, S. V.; Klausen, R. S.; Capozzi, B.; Roy, X.; Steigerwald, M. L.; Nuckolls, C.; Venkataraman, L. *Physical Chemistry Chemical Physics : PCCP* **2012**, *14*, 13841–5.
- (23) Quek, S. Y.; Kamenetska, M.; Steigerwald, M. L.; Choi, H. J.; Louie, S. G.; Hybertsen, M. S.; Neaton, J. B.; Venkataraman, L. *Nature Nanotechnology Letters* **2009**, *4*, 230–234.
- (24) Ulrich, J.; Esrail, D.; Pontius, W.; Venkataraman, L.; Millar, D.; Doerr, L. H. *The Journal of Physical Chemistry B* **2006**, *110*, 2462–6.
- (25) Dell'Angela, M.; Kladnik, G.; Cossaro, A.; Verdini, A.; Kamenetska, M.; Tamblyn, I.; Quek, S. Y.; Neaton, J. B.; Cvetko, D.; Morgante, A.; Venkataraman, L. *Nano Letters* **2010**, *10*, 2470–4.
- (26) Reed, M. A.; Zhou, C.; Muller, C. J.; Burgin, T. P.; Tour, J. M. *Science* **1997**, *278*, 252–254.
- (27) Tran, E.; Duati, M.; Ferri, V.; Müllen, K.; Zharnikov, M.; Whitesides, G. M.; Rampi, M. A. *Advanced Materials* **2006**, *18*, 1323–1328.
- (28) Ho, G.; Heath, J. R.; Kondratenko, M.; Perepichka, D. F.; Arseneault, K.; Pézolet, M.; Bryce, M. R. *Chemistry - A European Journal* **2005**, *11*, 2914–22.

- (29) Moore, A. M.; Yeganeh, S.; Yao, Y.; Claridge, S. A.; Tour, J. M.; Ratner, M. A.; Weiss, P. S. *ACS Nano* **2010**, *4*, 7630–6.
- (30) Stokbro, K.; Taylor, J.; Brandbyge, M. *Journal of the American Chemical Society* **2003**, *125*, 3674–5.
- (31) Stokbro, K.; Taylor, J.; Brandbyge, M.; Mozos, J.-L.; Ordejon, P. *Computational Materials Science* **2003**, *27*, 151–160.
- (32) Emberly, E.; Kirczenow, G. *Nanotechnology* **1999**, *10*, 285–289.
- (33) He, H.; Pandey, R.; Mallick, G.; Karna, S. P. *The Journal of Physical Chemistry C* **2009**, *113*, 1575–1579.
- (34) Bergfield, J. P.; Solomon, G. C.; Stafford, C. A.; Ratner, M. A. *Nano Letters* **2011**, *11*, 2759–64.
- (35) Herrmann, C.; Solomon, G. C.; Ratner, M. A. *The Journal of Chemical Physics* **2011**, *134*, 224306.
- (36) Crljen, Ž.; Grigoriev, a.; Wendin, G.; Stokbro, K. *Physical Review B* **2005**, *71*, 165316.
- (37) Yeganeh, S.; Ratner, M. A.; Galperin, M.; Nitzan, A. *Nano Letters* **2009**, *9*, 1770–1774.
- (38) Liu, H.; Ni, W.; Zhao, J.; Wang, N.; Guo, Y.; Taketsugu, T.; Kiguchi, M.; Murakoshi, K. *The Journal of Chemical Physics* **2009**, *130*, 244501.
- (39) Yoshizawa, K.; Tada, T.; Staykov, A. *Journal of the American Chemical Society* **2008**, *130*, 9406–13.
- (40) Tsuji, Y.; Staykov, A.; Yoshizawa, K. *Journal of the American Chemical Society* **2011**, *133*, 5955–65.
- (41) Ke, S.-H.; Baranger, H. U.; Yang, W. *The Journal of Chemical Physics* **2005**, *122*, 074704.
- (42) Ke, S.-H.; Baranger, H.; Yang, W. *Physical Review B* **2005**, *71*, 113401.
- (43) Lahti, P. M.; Esat, B.; Liao, Y.; Serwinski, P.; Lan, J.; Walton, R. *Polyhedron* **2001**, *20*, 1647–1652.

- (44) Ullman, E. F.; Osiecki, J. H.; Boocock, D. G. B.; Darcy, R. *Journal of the American Chemical Society* **1972**, *94*, 7049–7059.
- (45) Dance, Z. E. X.; Mickley, S. M.; Wilson, T. M.; Ricks, A. B.; Scott, A. M.; Ratner, M. A.; Wasielewski, M. R. *The Journal of Physical Chemistry A* **2008**, *112*, 4194–201.
- (46) Davis, W. B.; Ratner, M. A.; Wasielewski, M. R. *Chemical Physics* **2002**, *281*, 333–346.
- (47) Goldsmith, R. H.; Vura-Weis, J.; Scott, A. M.; Borkar, S.; Sen, A.; Ratner, M. A.; Wasielewski, M. R. *Journal of the American Chemical Society* **2008**, *130*, 7659–7669.
- (48) Weiss, E. A.; Ahrens, M. J.; Sinks, L. E.; Ratner, M. A.; Wasielewski, M. R. *Journal of the American Chemical Society* **2004**, *126*, 9510–1.
- (49) Wilson, T. M.; Tauber, M. J.; Wasielewski, M. R. *Journal of the American Chemical Society* **2009**, *131*, 8952–7.
- (50) Weiss, E. A.; Tauber, M. J.; Ratner, M. A.; Wasielewski, M. R. *Journal of the American Chemical Society* **2005**, *127*, 6052–61.
- (51) Goldsmith, R. H.; Sinks, L. E.; Kelley, R. F.; Betzen, L. J.; Liu, W.; Weiss, E. A.; Ratner, M. A.; Wasielewski, M. R. *Proceedings of the National Academy of Sciences* **2005**, *102*, 3540–5.
- (52) Dance, Z. E. X.; Ahrens, M. J.; Vega, A. M.; Ricks, A. B.; McCamant, D. W.; Ratner, M. A.; Wasielewski, M. R. *Journal of the American Chemical Society* **2008**, *130*, 830–2.
- (53) Weiss, E. A.; Ahrens, M. J.; Sinks, L. E.; Gusev, A. V.; Ratner, M. A.; Wasielewski, M. R. *Journal of the American Chemical Society* **2004**, *126*, 5577–5584.
- (54) Weiss, E. A.; Ratner, M. A.; Wasielewski, M. R. *The Journal of Physical Chemistry A* **2003**, *107*, 3639–3647.
- (55) Chernick, E. T.; Mi, Q.; Vega, A. M.; Lockard, J. V.; Ratner, M. A.; Wasielewski, M. R. *The Journal of Physical Chemistry B* **2007**, *111*, 6728–37.
- (56) Miller, S. E.; Lukas, A. S.; Marsh, E.; Bushard, P.; Wasielewski, M. R. *Journal of the American Chemical Society* **2000**, *122*, 7802–7810.

- (57) Goldsmith, R. H.; DeLeon, O.; Wilson, T. M.; Finkelstein-Shapiro, D.; Ratner, M. A.; Wasielewski, M. R. *Journal of Physical Chemistry A* **2008**, *112*, 4410–4.
- (58) Kumai, R.; Matsushita, M. M.; Izuoka, A.; Sugawara, T. *Journal of the American Chemical Society* **1994**, *116*, 4523–4524.
- (59) Shultz, D. A.; Vostrikova, K. E.; Bodnar, S. H.; Koo, H.-J.; Whangbo, M.-H.; Kirk, M. L.; Depperman, E. C.; Kampf, J. W. *Journal of the American Chemical Society* **2003**, *125*, 1607–17.
- (60) Depperman, E. C.; Bodnar, S. H.; Vostrikova, K. E.; Shultz, D. A.; Kirk, M. L. *Journal of the American Chemical Society* **2001**, *123*, 3133–3134.
- (61) Kirk, M. L.; Shultz, D. A. *Coordination Chemistry Reviews* **2013**, *257*, 218–233.
- (62) Shultz, D. A. *Polyhedron* **2003**, *22*, 2423–2426.
- (63) Shultz, D. A.; Farmer, G. T. *The Journal of Organic Chemistry* **1998**, *63*, 6254–6257.
- (64) Thompson, A. L.; Ahn, T.-S.; Thomas, K. R. J.; Thayumanavan, S.; Martínez, T. J.; Bardeen, C. J. *Journal of the American Chemical Society* **2005**, *127*, 16348–9.
- (65) Frisch, M. J.; Trucks, G. W.; Schlegel, H. B.; Scuseria, G. E.; Robb, M. A.; Cheeseman, J. R. Montgomery, Jr., J. A.; Vreven, T.; Kudin, K. N.; Burant, J. C.; Millam, J. M.; Iyengar, S. S.; Tomasi, J.; Barone, V.; Mennucci, B.; Cossi, M.; Scalmani, G.; Rega, N.; Petersson, G. A.; Nakatsuji, H.; Hada, M.; Ehara, M.; Toyota, K.; Fukuda, R.; Hasegawa, J.; Ishida, M.; Nakajima, T.; Honda, Y.; Kitao, O.; Nakai, H.; Klene, M.; Li, X.; Knox, J. E.; Hratchian, H. P.; Cross, J. B.; Bakken, V.; Adamo, C.; Jaramillo, J.; Gomperts, R.; Stratmann, R. E.; Yazyev, O.; Austin, A. J.; Cammi, R.; Pomelli, C.; Ochterski, J. W.; Ayala, P. Y.; Morokuma, K.; Voth, G. A.; Salvador, P.; Dannenberg, J. J.; Zakrzewski, V. G.; Dapprich, S.; Daniels, A. D.; Strain, M. C.; Farkas, O.; Malick, D. K.; Rabuck, A. D.; Raghavachari, K.; Foresman, J. B.; Ortiz, J. V.; Cui, Q.; Baboul, A. G.; Clifford, S.; Cioslowski, J.; Stefanov, B. B.; Liu, G.; Liashenko, A.; Piskorz, P.; Komaromi, I.; Martin, R. L.; Fox, D. J.; Keith, T.; Al-Laham, M. A.; Peng, C. Y.; Nanayakkara, A.; Challacombe, M.; Gill, P. M. W.; Johnson, B.; Chen, W.; Wong, M. W.; Gonzalez, C.; Pople, J. A. *Gaussian 03* **2004**.
- (66) Becke, A. D. *The Journal of Chemical Physics* **1993**, *98*, 5648–5652.
- (67) Lee, C.; Yang, W.; Parr, R. G. *Physical Review B* **1988**, *37*, 785–789.
- (68) Wadt, W. R.; Hay, P. J. *The Journal of Chemical Physics* **1985**, *82*, 284.

- (69) Hay, P. J.; Wadt, W. R. *The Journal of Chemical Physics* **1985**, *82*, 270.
- (70) Hay, P. J.; Wadt, W. R. *The Journal of Chemical Physics* **1985**, *82*, 299.
- (71) GaussView 3.0.
- (72) Casida, M. E.; Jamorski, C.; Casida, K. C.; Salahub, D. R. *Journal of Chemical Physics* **1998**, *108*, 4439–4449.
- (73) Bauernschmitt, R.; Ahlrichs, R. *Chemical Physics Letters* **1996**, *256*, 454–464.
- (74) Neese, F. *Journal of Biological Inorganic Chemistry* **2006**, *11*, 702–711.
- (75) Burke, K.; Werschnik, J.; Gross, E. K. U. *The Journal of Chemical Physics* **2005**, *123*, 62206.
- (76) Gorelsky, S. I. AOMix: Program for Molecular Orbital Analysis; SWizard Program.
- (77) Gorelsky, S. I.; Lever, A. B. P. *Journal of Organometallic Chemistry* **2001**, *635*, 187–196.
- (78) Leach, A. R. *Molecular Modelling Principles and Applications*; Addison Wesley Longman Limited: Harlow, England, 1996.
- (79) Neese, F.; Wennmohs, F.; Becker, U.; Ganyushin, D.; Hansen, A.; Liakos, D. G.; Kollmar, C.; Kossmann, S.; Petrenko, T.; Reimann, C.; Riplinger, C.; Sivalingham, K.; Valeev, E.; Wezislá, B. *ORCA - An ab initio, DFT and semiempirical SCF-MO package*; 2.8–00 ed.; 2009.
- (80) Neese, F. *Coordination Chemistry Reviews* **2009**, *253*, 526–563.
- (81) Weltner, W. J. *Magnetic Atoms and Molecules*; Van Nostrand Reinhold Company Inc.: New York, 1983.
- (82) Hanson, G. R.; Gates, K. E.; Noble, C. J.; Griffin, M.; Mitchell, A.; Benson, S. *Journal of Inorganic Biochemistry* **2004**, *98*, 903–16.
- (83) Stoll, S.; Schweiger, A. *Chemical Physics Letters* **2003**, *380*, 464–470.
- (84) Stoll, S. PhD Thesis: Spectral Simulations in Solid-State Electron Paramagnetic Resonance, ETH Zurich, 2003.

- (85) Wang, D. M.; Hanson, G. R. *Journal of Magnetic Resonance Series A* **1995**, *117*, 1–8.
- (86) Ebert, H.; Abart, J.; Voitlaender, J. *Journal of Chemical Physics* **1983**, *79*, 4719–4723.
- (87) Van Veen, G. *Journal of Magnetic Resonance* **1978**, *30*, 91–109.
- (88) Bendit, E. G.; Ross, D. *Applied Spectroscopy* **1961**, *15*, 103–105.
- (89) Ferraro, J. R.; Nakamoto, K.; Brown, C. W. *Introductory Raman Spectroscopy*; 2nd ed.; Academic Press: San Diego, 2003.
- (90) Depperman, E. C. Spectroscopic and Theoretical Characterization of Strong Ferromagnetic Interaction in Heterospin Biradicals, University of New Mexico, 2005.
- (91) Zheludev, A.; Barone, V.; Bonnet, M.; Deuey, B.; Grand, A.; Ressouche, E.; Rey, P.; Subra, R.; Schweizer, J. *Journal of the American Chemical Society* **1994**, *116*, 2019–2027.
- (92) Aebersold, M. A.; Gillon, B.; Plantevin, O.; Pardi, L.; Kahn, O.; Bergerat, P.; Von Seggern, I.; Tuczek, F.; Lars, O.; Grand, A.; Lelievre-Berna, E. *Journal of the American Chemical Society* **1998**, *120*, 5238–5245.
- (93) Cirujeda, J.; Vidal-Gancedo, J.; Juergens, O.; Mota, F.; Novoa, J. J.; Roviro, C.; Veciana, J. *Journal of the American Chemical Society* **2000**, *122*, 11393–11405.
- (94) McConnell, H. M.; Chesnut, D. B. *The Journal of Chemical Physics* **1958**, *28*, 107–117.
- (95) Drago, R. S. *Physical Methods for Chemists*; 2nd ed.; Surfside Scientific Publishers: Gainesville, Florida, 1992.
- (96) Karafiloglou, P. *Journal of Chemical Education* **1989**, *66*, 816–818.
- (97) Ruiz-Molina, D.; Zakharov, L. N.; Rheingold, A. L.; Hendrickson, D. N. *Journal of Physics and Chemistry of Solids* **2004**, *65*, 831–837.
- (98) Jung, O.; Pierpont, C. G. *Inorganic Chemistry* **1994**, *33*, 2227–2235.
- (99) Buchanan, R. M.; Pierpont, C. G. *Journal of the American Chemical Society* **1980**, *102*, 4951–4957.

- (100) Shultz, D. a.; Kumar, R. K.; Bin-Salamon, S.; Kirk, M. L. *Polyhedron* **2005**, *24*, 2876–2879.
- (101) Evangelio, E.; Hendrickson, D. N.; Ruiz-Molina, D. *Inorganica Chimica Acta* **2008**, *361*, 3403–3409.
- (102) Schmidt, R. D.; Shultz, D. A.; Martin, J. D. *Inorganic Chemistry* **2010**, *49*, 3162–8.
- (103) Creutz, C.; Taube, H. *Journal of the American Chemical Society* **1969**, *91*, 3988–3989.
- (104) Hofmann, M.; Kassube, J. K.; Graf, T. *Journal of Biological Inorganic Chemistry* **2005**, *10*, 490–5.
- (105) Gnida, M.; Ferner, R.; Gremer, L.; Meyer, O.; Meyer-Klaucke, W. *Biochemistry* **2003**, *42*, 222–30.
- (106) Dobbek, H.; Gremer, L.; Meyer, O.; Huber, R. *Proceedings of the National Academy of Sciences* **1999**, *96*, 8884–8889.
- (107) Meyer, O. *Journal of Biological Chemistry* **1982**, *257*, 1333–1341.
- (108) Shriver, D.; Atkins, P. *Inorganic Chemistry*; W. H. Freeman and Company: New York, 1999; p. 449.
- (109) Li, Y.; Fu, Q.; Flytzani-Stephanopoulos, M. *Applied Catalysis B: Environmental* **2000**, *27*, 179–191.
- (110) Inman, R. E.; Ingersoll, R. B.; Levy, E. A. *Science* **1971**, *172*, 1229–1231.
- (111) Weinstock, B.; Niki, H. *Science* **1972**, *176*, 290–2.
- (112) Khalil, M. A. K.; Rasmussen, R. A. *Chemosphere* **1990**, *20*, 227–242.
- (113) Badr, O.; Probert, S. D. *Applied Energy* **1994**, *49*, 145–195.
- (114) Badr, O.; Probert, S. D. *Applied Energy* **1994**, *49*, 99–143.
- (115) Roberts, G. P.; Youn, H.; Kerby, R. L. *Microbiology and Molecular Biology Review* **2004**, *68*, 453–473.
- (116) Meyer, O.; Gremer, L.; Ferner, R.; Ferner, M.; Dobbek, H.; Gnida, M.; Meyer-Klaucke, W.; Huber, R. *Biological Chemistry* **2000**, *381*, 865–76.

- (117) Dobbek, H.; Gremer, L.; Kiefersauer, R.; Huber, R.; Meyer, O. *Proceedings of the National Academy of Sciences* **2002**, *99*, 15971–6.
- (118) Hille, R. *Chemical Reviews* **1996**, *96*, 2757–2816.
- (119) Pushie, M. J.; George, G. N. *Coordination Chemistry Reviews* **2011**, *255*, 1055–1084.
- (120) Siegbahn, P. E. M.; Shestakov, A. F. *Journal of Computational Chemistry* **2005**, *26*, 888–98.
- (121) Resch, M.; Dobbek, H.; Meyer, O. *Journal of Biological Inorganic Chemistry* **2005**, *10*, 518–28.
- (122) Strauss, S. H. *Journal of the Chemical Society - Dalton Transactions* **2000**, 1–6.
- (123) Wilcoxon, J.; Snider, S.; Hille, R. *Journal of the American Chemical Society Comm.* **2011**, *133*, 12934–12936.
- (124) Gremer, L.; Kellner, S.; Dobbek, H.; Huber, R.; Meyer, O. *The Journal of Biological Chemistry* **2000**, *275*, 1864–72.
- (125) Zhang, B.; Hemann, C. F.; Hille, R. *The Journal of Biological Chemistry* **2010**, *285*, 12571–8.
- (126) Gourlay, C.; Nielsen, D. J.; White, J. M.; Knottenbelt, S. Z.; Kirk, M. L.; Young, C. G. *Journal of the American Chemical Society Comm.* **2006**, *128*, 2164–5.
- (127) Groysman, S.; Holm, R. H. *Inorganic Chemistry* **2009**, *48*, 621–7.
- (128) Takuma, M.; Ohki, Y.; Tatsumi, K. *Inorganic Chemistry* **2005**, *44*, 6034–6043.
- (129) Te Velde, G.; Bickelhaupt, F. M.; Baerends, E. J.; Van Gisbergen, S. J. A.; Fonseca Guerra, C.; Snijders, J. G.; Ziegler, T. *Journal of Computational Chemistry* **2001**, *22*, 931–967.
- (130) Guerra, C. F.; Snijders, J. G.; Velde, G. te; Baerends, E. J. *Theoretical Chemistry Accounts* **1998**, *99*, 391.
- (131) Gisbergen, S. J. A. van; Snijders, J. G.; Baerends, E. J. *Computer Physics Communications* **1999**, *118*, 119.
- (132) Hernandez-Marin, E.; Seth, M.; Ziegler, T. *Inorganic Chemistry* **2009**, *48*, 2880–6.

- (133) Seth, M.; Ziegler, T.; Autschbach, J. *The Journal of Chemical Physics* **2008**, *129*, 104105.
- (134) Seth, M.; Ziegler, T. *The Journal of Chemical Physics* **2007**, *127*, 134108.
- (135) Neese, F.; Petrenko, T.; Ganyushin, D.; Olbrich, G. *Coordination Chemistry Reviews* **2007**, *251*, 288–327.
- (136) Van Wüllen, C. *The Journal of Chemical Physics* **1998**, *109*, 392.
- (137) Perdew, J. P.; Burke, K.; Ernzerhof, M. *Physical Review Letters* **1996**, *77*, 3865–3868.
- (138) Buehl, M.; Reimann, C.; Pantazis, D. A.; Bredow, T.; Neese, F. *Journal of Chemical Theory and Computation* **2008**, *4*, 1449–1459.
- (139) Xiao, Z.; Gable, R. W.; Wedd, A. G.; Young, C. G. *Journal of the American Chemical Society* **1996**, *118*, 2912–2921.
- (140) Klamt, A.; Schuurmann, G. *Journal of the Chemical Society - Perkin Transactions 2* 799–805.
- (141) Manikandan, P.; Choi, E. Y.; Hille, R.; Hoffman, B. M. *Journal of the American Chemical Society* **2001**, *123*, 2658–63.
- (142) Kirk, M. L. In *Paramagnetic Resonance of Metallobiomolecules*; Telser, J., Ed.; Oxford University Press, 2003; pp. 340–357.
- (143) Cotton, F. A.; Walton, R. A. *Multiple bonds between metal atoms*; Second Ed.; Clarendon Press: Oxford, 1993; pp. 1–120.
- (144) Cotton, F. A.; Dikarev, E. V.; Petrukhina, M. A. *Inorganic Chemistry* **1999**, *38*, 3384–3389.
- (145) Cotton, F. A.; Dikarev, E. V.; Petrukhina, M. A. *Inorganic Chemistry Communications* **1999**, 28–30.
- (146) Cole, N. F.; Cotton, F. A.; Powell, G. L.; Smith, T. J. *Inorganic Chemistry* **1983**, *22*, 2618–2621.
- (147) Cotton, F. A.; Pedersen, E. *Journal of the American Chemical Society* **1975**, *97*, 303–308.

- (148) Cotton, F. A.; Price, A. C.; Vidyasagar, K. *Inorganic Chemistry* **1990**, *29*, 5143–5147.
- (149) Cotton, F. A.; Frenz, B. A.; Ebner, J. R.; Walton, R. A. *Inorganic Chemistry* **1976**, *15*, 1630–1633.
- (150) Cotton, F. A.; Dunbar, K. R.; Falvello, L. R.; Tomas, M.; Walton, R. A. *Journal of the American Chemical Society* **1983**, *105*, 4950–4954.
- (151) Bursten, B. E.; Cotton, F. A.; Fanwick, P. E.; Stanley, G. G.; Walton, R. A. *Journal of the American Chemical Society* **1983**, *105*, 2606–2611.
- (152) Cotton, F. A.; Jennings, J. G.; Price, A. C.; Vidyasagar, K. *Inorganic Chemistry* **1990**, *29*, 4138–4143.
- (153) Beth, A. L.; Tetrick, S. M.; Walton, R. A. *Journal of the Chemical Society - Dalton Transactions* **1986**, 55–59.
- (154) Anderson, L. B.; Barder, T. J.; Esjornson, D.; Walton, R. A.; Bursten, B. E. *Journal of the Chemical Society - Dalton Transactions* **1986**, 2607–2612.
- (155) Dunbar, K. R.; Powell, D.; Walton, R. A. *Inorganic Chemistry* **1985**, *24*, 2842–2846.
- (156) Ebner, J. R.; Walton, R. A. *Inorganic Chemistry* **1975**, *14*, 1987–1992.
- (157) Brant, P.; Salmon, D. J.; Walton, R. A. *Journal of the American Chemical Society* **1978**, *100*, 4424–4430.
- (158) Cotton, F. A.; Dalal, N. S.; Huang, P.; Ibragimov, S. A.; Murillo, C. A.; Piccoli, P. M. B.; Ramsey, C. M.; Schultz, A. J.; Wang, X.; Zhao, Q. *Inorganic Chemistry* **2007**, *46*, 1718–26.
- (159) Root, D. R.; Blevins, C. H.; Lichtenberger, D. L.; Sattelberger, A. P.; Walton, R. A. *Journal of the American Chemical Society* **1986**, *108*, 953–959.
- (160) Cowman, C. D.; Trogler, W. C.; Gray, H. B. *Israel Journal of Chemistry* **1977**, *15*, 308–310.
- (161) Clark, R. J. H.; Stead, M. J. *Inorganic Chemistry* **1983**, *22*, 1214–1220.
- (162) Cowman, C. D.; Gray, H. B. *Journal of the American Chemical Society, Communications to the Editor* **1973**, *95*, 8177–8178.

- (163) Kuo, J.-H.; Tsao, T.-B.; Lee, G.-H.; Lee, H.-W.; Yeh, C.-Y.; Peng, S.-M. *European Journal of Inorganic Chemistry* **2011**, 2011, 2025–2028.
- (164) Lin, S.-Y.; Chen, I.-W. P.; Chen, C.; Hsieh, M.-H.; Yeh, C.-Y.; Lin, T.-W.; Chen, Y.-H.; Peng, S.-M. *The Journal of Physical Chemistry B* **2004**, 108, 959–964.
- (165) Tsao, T.-B.; Lo, S.-S.; Yeh, C.-Y.; Lee, G.-H.; Peng, S.-M. *Polyhedron* **2007**, 26, 3833–3841.
- (166) Chien, C.-H.; Chang, J.-C.; Yeh, C.-Y.; Lee, G.-H.; Fang, J.-M.; Peng, S.-M. *Dalton Transactions* **2006**, 2106–13.
- (167) Ismayilov, R. H.; Wang, W.-Z.; Lee, G.-H.; Chien, C.-H.; Jiang, C.-H.; Chiu, C.-L.; Yeh, C.-Y.; Peng, S.-M. *European Journal of Inorganic Chemistry* **2009**, 2009, 2110–2120.
- (168) Huang, Y.-M.; Tsai, H.-R.; Lai, S.-H.; Lee, S. J.; Chen, I.-C.; Huang, C. L.; Peng, S.-M.; Wang, W.-Z. *The Journal of Physical Chemistry C* **2011**, 115, 13919–13926.
- (169) Pantazis, D. A.; McGrady, J. E. *Journal of the American Chemical Society* **2006**, 128, 4128–35.
- (170) Georgiev, V. P.; McGrady, J. E. *Journal of the American Chemical Society* **2011**, 133, 12590–9.
- (171) Nippe, M.; Turov, Y.; Berry, J. F. *Inorganic Chemistry* **2011**, 10592–10599.
- (172) Nippe, M.; Bill, E.; Berry, J. F. *Inorganic Chemistry* **2011**, 50, 7650–7661.
- (173) Berry, J. F.; Cotton, F. A.; Fewox, C. S.; Lu, T.; Murillo, C. A.; Wang, X. *Dalton Transactions* **2004**, 2297–302.
- (174) Montalti, M.; Credi, A.; Prodi, L.; Gnanoli, M. T. *Handbook of Photochemistry*; 3rd ed.; Taylor & Francis Group, LLC: Boca Raton, 2006; pp. 617–633.
- (175) Solomon, E. I.; Hodgson, K. O.; Editors *Spectroscopic Methods in Bioinorganic Chemistry*; ACS sympos.; Oxford University Press, 1998.
- (176) Takagi, N.; Krapp, A.; Frenking, G. *Canadian Journal of Chemistry* **2010**, 88, 1079–1093.
- (177) Harris, D. C.; Bertolucci, M. D. *Symmetry and Spectroscopy*; Dover Publications, Inc.: New York, 1989.

- (178) Petrenko, T.; Neese, F. *The Journal of Chemical Physics* **2007**, *127*, 164319.
- (179) Gamelin, D. R.; Bominaar, E. L.; Mathonière, C.; Kirk, M. L.; Wieghardt, K.; Girerd, J.-J.; Solomon, E. I. *Inorganic Chemistry* **1996**, *35*, 4323–4335.
- (180) Cotton, F. A. *Chemical Applications of Group Theory*; 3rd ed.; John Wiley & Sons, Inc.: New York, 1990.